

Georg-August-Universität Göttingen
Fakultät für Mathematik und Informatik
Institut für Numerische und Angewandte Mathematik

**Robustness of High-Order Divergence-Free Finite Element
Methods for Incompressible Computational Fluid Dynamics**

Dissertation

zur Erlangung des mathematisch-naturwissenschaftlichen Doktorgrades

„DOCTOR RERUM NATURALIUM“

der Georg-August-Universität Göttingen

im Promotionsprogramm „MATHEMATICAL SCIENCES“ (SMS)

der Georg-August University School of Science (GAUSS)

vorgelegt von

Philipp W. Schroeder

geboren in Goslar

Göttingen, 2019

Betreuungsausschuss:

- Prof. Dr. Gert Lube
*Institut für Numerische und Angewandte Mathematik
Georg-August-Universität Göttingen*
- Prof. Dr. Andreas Dillmann
*Institut für Aerodynamik und Strömungsmechanik
Deutsches Zentrum für Luft- und Raumfahrt*
- Jun.-Prof. Dr. Christoph Lehrenfeld
*Institut für Numerische und Angewandte Mathematik
Georg-August-Universität Göttingen*

Prüfungskommission:

- Referent: Prof. Dr. Gert Lube
*Institut für Numerische und Angewandte Mathematik
Georg-August-Universität Göttingen*
- Korreferent: Prof. Dr. Andreas Dillmann
*Institut für Aerodynamik und Strömungsmechanik
Deutsches Zentrum für Luft- und Raumfahrt*

Externer Gutachter:

- Prof. Leo G. Rebholz, Ph.D.
*Department of Mathematical Sciences
Clemson University/USA*

Weitere Mitglieder der Prüfungskommission:

- Jun.-Prof. Dr. Christoph Lehrenfeld
*Institut für Numerische und Angewandte Mathematik
Georg-August-Universität Göttingen*
- Prof. Dr. Ingo F. Witt
*Mathematisches Institut
Georg-August-Universität Göttingen*
- Prof. Dr. Andreas Tilgner
*Institut für Geophysik
Georg-August-Universität Göttingen*
- Prof. Dr. Marcus Baum
*Institut für Informatik
Georg-August-Universität Göttingen*

Tag der mündlichen Prüfung: 1. März 2019

Dedicated to the memory of Irmgard and Kurt.

Acknowledgments

First and foremost, I would like to thank everyone who has supported me throughout my academic career. This thesis certainly would not have been possible without all your help. In particular, and without adhering to any specific order nor guarantee of completeness, I would like to express my gratitude to the individuals below for their support.

Above all others, Gert Lube undoubtedly played the most outstanding role in making this work possible. Ever since our first correspondence on 4 July 2012, he has supported me every step of the way. This included, for example, supervising both my Bachelor's and Master's thesis and introducing me to the fascinating research area known as computational fluid dynamics – my sincerest thanks for sharing your experience and knowledge with me over all these years. Secondly, my heartfelt gratitude goes out to Christoph Lehrenfeld, whose office door was always open to me and who, not least because he convinced me to use NGSolve, considerably broadened my horizons with respect to DG methods in general, not to mention hybridisation and everything else connected to increasing the computational efficiency of numerical methods. Furthermore, I would like to express my gratitude to Andreas Dillmann, whose lectures on aerodynamics – but also his passion and enthusiasm – encouraged me to appreciate fluid dynamics from a physics perspective.

In addition, I would like to thank the following people: Leo G. Rebholz and Timo Heister, for making it possible for me to have a fruitful research stay at Clemson University; Alexander Linke, for numerous insightful discussions on pressure-robustness; Joachim Schöberl and his group at TU Wien, for developing and maintaining NGSolve and their noteworthy support and encouragement in making use of it; Fabian Siggès and David A. Martin II, for proofreading and thereby improving various works I have penned; Michael Hedwig, for sharing his experience and expertise regarding numerical simulations from an engineering point of view, as well as for supervising my internship and Master's thesis from the industrial side; and, finally, Jochen Schulz, Christoph Rügge and the administrators at the HPC facilities of the GWDG, for providing a stable, user-friendly and efficient computing environment without which simulating most of the numerical examples in this work would not have been possible.

Last, but certainly not least, I am of course deeply grateful to my family and friends for their continuous support, encouragement and understanding, all of which were paramount to keeping my output levels high throughout the doctoral process. Especially my dear mother, Marion Schroeder, has always supported me selflessly from the bottom of her heart – thank you so much from the bottom of mine. My final thanks go to my partner, Karolin Krehl, whose undying care, cheerfulness and encouragement have done wonders to keeping me focused and grounded.

Robustness of High-Order Divergence-Free Finite Element Methods for Incompressible Computational Fluid Dynamics

Ph.D. Thesis in Mathematics, 2019

Author: Philipp W. Schroeder

Institute for Numerical and Applied Mathematics

Faculty of Mathematics and Computer Science

Georg-August-Universität Göttingen, Germany

Abstract

In computational fluid dynamics, obtaining exactly divergence-free approximations to the incompressible Navier–Stokes equations, by means of finite element methods, has actually not been particularly popular in the last decade. This observation is in contrast to the fact that $H(\text{div})$ -conforming finite elements indeed facilitate the flexible construction of such methods in most diverse applications. In this context, from the methodical side, Discontinuous Galerkin (DG) methods play a key role and, from the computational point of view, the concept of hybridisation can and is exploited heavily. The present work demonstrates and explains why exactly divergence-free $H(\text{div})$ methods, especially in under-resolved simulations, show an excellent performance in several laminar and turbulent test scenarios. For convection-dominated problems, the use of upwinding, which is naturally incorporated into DG methods, is evaluated and assessed. Furthermore, a careful investigation of various numerical examples is provided; this includes, for example, a Kelvin–Helmholtz instability problem, 2D and 3D freely decaying turbulence and turbulent channel flows. Especially, it is shown that $H(\text{div})$ methods provide a framework for the robust simulation of turbulent flows for basically any Reynolds number. From a theoretical perspective, it is shown that exactly divergence-free methods allow the transfer of many crucial fluid dynamics properties directly to the discrete level. In fact, they allow for a comparably straightforward numerical error analysis as well, and it turns out that this success is strongly related to the concepts of pressure- and Reynolds-semi-robustness. One important consequence of pressure-robustness is that the accuracy of the resulting velocity approximation is completely independent of the quality of the pressure approximation. Finally, the role of high-order methods is investigated which shows that in the considered examples, using a moderate order promises to deliver a good compromise between accuracy and efficiency.

Key words: computational fluid dynamics; incompressible Navier–Stokes equations; exactly divergence-free methods; $H(\text{div})$ -DG and HDG methods; structure preservation; Helmholtz decomposition; pressure- and Reynolds-semi-robustness; laminar and turbulent flows; Taylor–Green vortex; turbulent channel flow.

How to cite:

P. W. Schroeder: <i>Robustness of High-Order Divergence-Free Finite Element Methods for Incompressible Computational Fluid Dynamics</i> . Ph.D. thesis, Georg-August-Universität Göttingen, 2019.

Contents

Contents	xi
List of Figures	xiii
List of Tables	xxi
1 Introduction	1
1.1 Aim and Motivation	1
1.2 Overview of Publications	2
1.3 Outline of Thesis	7
2 Incompressible Fluid Dynamics	9
2.1 Divergence-Free Constraint	9
2.2 Navier–Stokes Equations	10
2.2.1 Weak Formulation	12
2.2.2 Essential Regularity Assumptions	13
2.2.3 Helmholtz Decomposition and Projection	16
2.3 Characteristic Quantities of Flows	17
2.4 Turbulence Theory and Spectral Analysis	20
2.5 Related Simplified Problems	22
3 Inf-Sup Stable Finite Element Methods	25
3.1 Discrete Setting	25
3.2 L^2 -DG-FEM	27
3.2.1 Classical Stokes Discretisation	28
3.2.2 Stabilisation of Divergence-Free Constraint	31
3.2.3 Upwind Convective Term	32
3.3 $H(\text{div})$ -DG-FEM	33
3.4 H^1 -FEM	36
3.5 Efficiency Aspects for High-Order Methods	38
3.5.1 From DG to Hybrid DG (HDG)	39
3.5.2 HDG Lifting Techniques	41
3.5.3 $H(\text{div})$ -HDG for Incompressible Flows	45
4 Essential Robustness Concepts	49
4.1 Structure Preservation	49
4.2 Pressure-Robustness	55
4.2.1 Potential Flows	57
4.2.2 Generalised Beltrami Flows	59
4.3 Reynolds-Semi-Robustness	63

5	Stokes Analysis with Emphasis on Pressure-Robustness	67
5.1	Divergence-Free H^1 - and $H(\text{div})$ -DG-FEM	67
5.2	The Analogue of Grad-Div for L^2 -DG-FEM	69
6	Transient Navier–Stokes: Robust Numerical Analysis	73
6.1	Divergence-Free H^1 -FEM	74
6.2	Divergence-Free $H(\text{div})$ -DG-FEM	77
7	Viscous Dissipation in DG Methods	81
7.1	Physical and Numerical Dissipation	82
7.2	A Natural Decomposition for DG Methods	84
7.3	Minimal SIP-DG Penalty Parameter on Hyperrectangles	86
7.3.1	Discrete Inverse Trace Inequality and Application	86
7.3.2	Non-Negativity of Numerical Viscous Dissipation	88
7.3.3	Minimal SIP Parameter	89
7.4	Numerical Demonstration	90
8	2D High-Order CFD Applications	93
8.1	Vortex Shedding Past Blunt Body	93
8.2	Kelvin–Helmholtz Instability	96
8.2.1	Results for $\text{Re} = 10\,000$	98
8.2.2	Helmholtz Decomposition of Convection Forces	102
8.3	Two-Dimensional Turbulence	105
8.3.1	Results for Different Reynolds Numbers	106
8.3.2	Analysis of Dissipation Processes	109
8.3.3	Long-Time Simulation	111
9	3D High-Order CFD Applications	115
9.1	Homogeneous Isotropic Turbulence: Taylor–Green Vortex	115
9.1.1	TGV Flow Topology and Characteristics for $\text{Re} = 1600$	116
9.1.2	Some Aspects of Implicit Large Eddy Simulation	119
9.1.3	Towards the Inviscid Euler Limit Case as $\text{Re} \rightarrow \infty$	123
9.1.4	Helmholtz Decomposition of Convection Forces	128
9.2	Turbulent Channel Flow	129
9.2.1	Simulations for $\text{Re}_\tau = 180$	132
9.2.2	Simulations for $\text{Re}_\tau = 395$	135
9.2.3	Simulations for $\text{Re}_\tau = 950$	138
9.2.4	Simulations for $\text{Re}_\tau = 2000$	139
10	Summary, Conclusions and Future Work	143
	References	149

List of Figures

2.1	Forward energy and enstrophy cascade processes for freely decaying turbulence in 3D (left) and 2D (right), respectively.	21
2.2	Comparison of 2D and 3D dissipation length scales against viscosity.	22
3.1	Sketch of continuity/discontinuity of normal (red) and tangential (blue) velocity components on a 2D triangular mesh for the different methods considered in this work.	26
3.2	Sketch of the different DOFs (Dirichlet, free, condensable, interface) which are important for the concept of static condensation.	38
3.3	Symmetric half of sparsity patterns: Full matrix A (left) and Schur complement S (right). Each box corresponds to a non-zero entry.	39
3.4	Cell and facet velocity in $\mathbf{H}(\text{div})$ -HDG methods for triangular ($\mathbf{BDM}_k/\mathbf{F}_k/\mathbb{P}_{k-1}^{\text{dc}}$) and quadrilateral ($\mathbf{RT}_{[k]}/\mathbf{F}_k/\mathbb{P}_k^{\text{dc}}$) meshes.	46
4.1	Evolution of vorticity $\omega_h = \nabla_h \times \mathbf{u}_h$ for the moving Gresho problem, computed with $k = 6$ and $N = 8$. Line by line: $t = 0, 1, 2, 3$. Left column: divergence-free $\mathbf{H}(\text{div})$ -DG method $\mathbf{RT}_{[6]}^{\text{red}}/\mathbb{P}_0^{\text{dc}}$; right column: textbook \mathbf{L}^2 -DG method $\mathbf{Q}_6^{\text{dc}}/\mathbf{Q}_5^{\text{dc}}$. (A video of this simulation is available at https://youtu.be/wrZTUrgxVSc ; note also the QR code.)	50
4.2	Final state of ω_h at $t = 3$ for the Gresho vortex problem computed with $\mathbf{RT}_{[k]}^{\text{red}}/\mathbb{P}_0^{\text{dc}}$ (left column) and $\mathbf{Q}_k^{\text{dc}}/\mathbf{Q}_{k-1}^{\text{dc}}$ (right column). First row: $(k, N) = (4, 14)$; second row: $(k, N) = (2, 20)$	51
4.3	Kinetic energy $\mathcal{K}(\mathbf{u}_h)$, enstrophy $\mathcal{E}(\mathbf{u}_h)$ and palinstrophy $\mathcal{P}(\mathbf{u}_h)$ monitored over time for $\mathbf{RT}_{[k]}^{\text{red}}/\mathbb{P}_0^{\text{dc}}$ (left column) and $\mathbf{Q}_k^{\text{dc}}/\mathbf{Q}_{k-1}^{\text{dc}}$ (right column).	52
4.4	Impact of DG-grad-div with parameter $\gamma \geq 0$ for the \mathbf{L}^2 -DG method on the Gresho vortex problem for low-order $(k, N) = (2, 20)$. Left column shows the final state of ω_h for $\gamma = 0.001$ (first row), $\gamma = 0.01$ (second row) and $\gamma = 0.1$ (last row). Right column shows the corresponding evolution of kinetic energy, enstrophy and palinstrophy.	53
4.5	Discrete Helmholtz decomposition of discrete convective term $\mathbf{f}_h = (\mathbf{u}_h \cdot \nabla_h) \mathbf{u}_h$. Left column: $ \mathbf{f}_h _2^2$, $ \mathbb{P}_h^{\text{div}}(\mathbf{f}_h) _2^2$ and $ \nabla \phi_h _2^2$ at $t = 3$ for $\mathbf{RT}_{[6]}/\mathbb{P}_6^{\text{dc}}$. Right column: Evolution of the corresponding norms $\ \mathbf{f}_h\ _{L^2}$, $\ \mathbb{P}_h^{\text{div}}(\mathbf{f}_h)\ _{L^2}$ and $\ \nabla \phi_h\ _{L^2}$ for $\mathbf{RT}_{[k]}/\mathbb{P}_k^{\text{dc}}$	54
4.6	No-flow in a glass. Geometry (left), tetrahedral mesh (middle) and exact pressure (right).	55
4.7	Velocity and pressure errors for the no-flow ($\mathbf{u} \equiv \mathbf{0}$) problem in a glass filled with different fluids. Non-pressure-robust method (left) and pressure-robust method (right).	56
4.8	Colliding potential flow defined by $\varphi = x^2 - y^2$. Velocity magnitude $ \mathbf{u} $ (left), cones representing the velocity field \mathbf{u} (middle) and pressure (right) on an unstructured triangular mesh. The centre of the domain corresponds to $(0, 0)$	58

4.9	Ethier–Steinman flow at $t = 0$, visualised on an unstructured tetrahedral mesh. Velocity magnitude $ \mathbf{u} $ (left) and pressure p (right).	60
4.10	Errors for the classical 3D Ethier–Steinman problem ($\nu = 0.002$). Comparison of pressure-robust $\mathbf{H}(\text{div})$ - and non-pressure-robust \mathbf{L}^2 -DG methods with $\Delta t = 10^{-4}$, both using upwinding ($\theta = 1$).	61
4.11	Errors for the 3D Ethier–Steinman problem ($\nu = 0.002$) with inaccurate BCs. Comparison of pressure-robust $\mathbf{H}(\text{div})$ - and non-pressure-robust \mathbf{L}^2 -DG methods with $\Delta t = 10^{-4}$, both using upwinding ($\theta = 1$).	62
4.12	Initial velocity of the lattice flow problem and triangular meshes without singular vertices. Left: Coarse mesh (34 triangles) with $h = 0.25$ and first component of \mathbf{u}_0 ; middle: fine mesh (902 triangles) with $h = 0.05$ and second component of \mathbf{u}_0 ; right: vorticity computed from \mathbf{u}_0	65
4.13	Evolution of \mathbf{L}^2 -norm and (broken) \mathbf{H}^1 -seminorm errors for the lattice flow problem. Results on the coarse mesh are shown by solid lines, the fine mesh is indicated by dashed lines. The $\mathbf{H}(\text{div})$ -HDG method on the coarse mesh is shown with black dots.	66
4.14	Evolution of \mathbf{L}^2 -norm and (broken) \mathbf{H}^1 -seminorm errors for the lattice flow problem under k -refinement on the $h = 0.05$ mesh with $\Delta t = 10^{-4}$. Exponential convergence can be observed. The highest orders' errors reach machine precision.	66
7.1	Kinetic energy, kinetic energy dissipation rate and viscous dissipations (physical and numerical) for $t \in [0, 20]$, computed with $k = 4$, $N = 8$. In the bottom row, using the broken gradient $\nabla_h \mathbf{u}_h$ in the definition of the physical dissipation (left) leads to negative numerical viscous dissipation while using $\boldsymbol{\sigma}_h$ from (7.8) (right) does not.	91
8.1	Periodic Kármán vortex shedding in the wake of a square. Visualisation of velocity magnitude $ \mathbf{u}_h _2$, computational mesh and underlying geometry. Unless stated otherwise, computations are done with $\mathbf{BDM}_4/\mathbb{P}_3^{\text{dc}}$ and upwinding is used ($\theta = 1$).	94
8.2	Discrete convection term $ (\mathbf{u}_h \cdot \nabla_h) \mathbf{u}_h _{3/2}^{3/2}$ computed with $\mathbf{BDM}_4/\mathbb{P}_3^{\text{dc}}$. Note that the colour bar is chosen in such a way that all values above 100 are shown red.	94
8.3	Divergence-free contribution $ \mathbb{P}_h^{\text{div}}(\mathbf{f}_h) _{3/2}^{3/2}$ of discrete Helmholtz decomposition computed with exactly divergence-free $\mathbf{BDM}_4/\mathbb{P}_3^{\text{dc}}$. Colour bar scaling identically to Fig. 8.2.	95
8.4	Gradient contribution $ \nabla \phi_h _{3/2}^{3/2}$ of discrete Helmholtz decomposition computed with exactly divergence-free $\mathbf{BDM}_4/\mathbb{P}_3^{\text{dc}}$. Colour bar scaling identically to Fig. 8.2.	95
8.5	Difference $ \mathbb{P}_h^{\text{div}}(\mathbf{f}_h) - \mathbb{P}_h^0(\mathbf{f}_h) _{3/2}^{3/2}$ of the two discrete Helmholtz projectors for $k = 4$. High values indicate advantageous regions of the pressure-robust discretisation. Note that the colour scale is chosen logarithmically.	96
8.6	Difference of discrete Helmholtz projectors $ \mathbb{P}_h^{\text{div}}(\mathbf{f}_h) - \mathbb{P}_h^0(\mathbf{f}_h) _{3/2}^{3/2}$ for different polynomial orders $k \in \{2, 4, 6, 9\}$ (from top left to bottom right).	97

8.7	Vorticity $\nabla_h \times \mathbf{u}_h$ for the $\text{Re} = 10\,000$ Kelvin–Helmholtz instability at (from left to right and top to bottom) $\bar{t} \in \{5, 10, 17, 34, 56, 200, 240, 278, 400\}$. Obtained with div-free $\mathbf{H}(\text{div})$ -HDG method $\mathbf{RT}_{[8]}^{\text{red}}/\mathbf{F}_8/\mathbb{P}_0^{\text{dc}}$ on the finest 256^2 mesh; cf. Table 8.2. (A video of this simulation is available at https://youtu.be/fXL5ULPNdbU ; note also the QR code.)	99
8.8	Evolution of kinetic energy for $\text{Re} = 10\,000$ with div-free $\mathbf{RT}_{[8]}^{\text{red}}/\mathbf{F}_8/\mathbb{P}_0^{\text{dc}}$ on a sequence of square meshes.	100
8.9	Evolution of enstrophy for $\text{Re} = 10\,000$ with div-free $\mathbf{RT}_{[8]}^{\text{red}}/\mathbf{F}_8/\mathbb{P}_0^{\text{dc}}$ on a sequence of square meshes.	101
8.10	Evolution of palinstrophy for $\text{Re} = 10\,000$ with div-free $\mathbf{RT}_{[8]}^{\text{red}}/\mathbf{F}_8/\mathbb{P}_0^{\text{dc}}$ on a sequence of square meshes.	101
8.11	Evolution of palinstrophy for $\text{Re} = 10\,000$ with divergence-free $\mathbf{RT}_{[k]}^{\text{red}}/\mathbf{F}_k/\mathbb{P}_0^{\text{dc}}$ for a sequence of polynomial orders on the 256^2 mesh.	102
8.12	Evolution of $\mathbf{L}^{3/2}$ norm of convection term for $\text{Re} = 10\,000$ with divergence-free $\mathbf{RT}_{[8]}^{\text{red}}/\mathbf{F}_8/\mathbb{P}_0^{\text{dc}}$ on a sequence of square meshes.	103
8.13	Evolution of divergence-free part of convection term for $\text{Re} = 10\,000$ with divergence-free $\mathbf{RT}_{[8]}^{\text{red}}/\mathbf{F}_8/\mathbb{P}_0^{\text{dc}}$ on a sequence of square meshes.	103
8.14	Evolution of gradient part of convection term for $\text{Re} = 10\,000$ with divergence-free $\mathbf{RT}_{[8]}^{\text{red}}/\mathbf{F}_8/\mathbb{P}_0^{\text{dc}}$ on a sequence of square meshes.	104
8.15	Snapshots of $ (\mathbf{u}_h \cdot \nabla_h)\mathbf{u}_h _{3/2}^{3/2}$ (left column), $ \mathbb{P}_h^{\text{div}}(\mathbf{f}_h) _{3/2}^{3/2}$ (middle column) and $ \nabla\phi_h _{3/2}^{3/2}$ (right column) for the $\text{Re} = 10\,000$ Kelvin–Helmholtz instability at $\bar{t} = 10$ (top row), $\bar{t} = 34$ (middle row) and $\bar{t} = 200$ (bottom row). Obtained with div-free $\mathbf{H}(\text{div})$ -HDG method $\mathbf{RT}_{[8]}^{\text{red}}/\mathbf{F}_8/\mathbb{P}_0^{\text{dc}}$ on the 128^2 mesh. Colour bar is identical in each row.	104
8.16	Initial velocity magnitude $ \mathbf{u}_h(0) $ (left) and vorticity $\nabla_h \times \mathbf{u}_h(0)$ (right) for all freely decaying 2D turbulence simulations.	105
8.17	Evolution of kinetic energy for $\nu \in \{10^{-4}, 2 \times 10^{-5}, 10^{-6}\}$, computed with the divergence-free $\mathbf{RT}_{[8]}^{\text{red}}/\mathbf{F}_8/\mathbb{P}_0^{\text{dc}}$ $\mathbf{H}(\text{div})$ - \mathbf{H}^1 -lifting-HDG method on a 64^2 mesh.	106
8.18	Evolution of enstrophy for $\nu \in \{10^{-4}, 2 \times 10^{-5}, 10^{-6}\}$, computed with the divergence-free $\mathbf{RT}_{[8]}^{\text{red}}/\mathbf{F}_8/\mathbb{P}_0^{\text{dc}}$ $\mathbf{H}(\text{div})$ - \mathbf{H}^1 -lifting-HDG method on a 64^2 mesh.	107
8.19	Evolution of palinstrophy for $\nu \in \{10^{-4}, 2 \times 10^{-5}, 10^{-6}\}$, computed with the divergence-free $\mathbf{RT}_{[8]}^{\text{red}}/\mathbf{F}_8/\mathbb{P}_0^{\text{dc}}$ $\mathbf{H}(\text{div})$ - \mathbf{H}^1 -lifting-HDG method on a 64^2 mesh.	107
8.20	Vorticity $\nabla_h \times \mathbf{u}_h(t)$ for freely decaying 2D turbulence with $\nu \in \{10^{-4}, 2 \times 10^{-5}, 10^{-6}\}$ (from left to right) at $t \in \{1, 2, 8, 24\}$ (from top to bottom). Obtained with div-free $\mathbf{H}(\text{div})$ -HDG method $\mathbf{RT}_{[8]}^{\text{red}}/\mathbf{F}_8/\mathbb{P}_0^{\text{dc}}$ on a 64^2 mesh. (A video of this simulation is available at https://youtu.be/OzUCPAD4YDQ ; note also the QR code.)	108
8.21	Energy spectra for freely decaying 2D turbulence with $\nu \in \{10^{-4}, 2 \times 10^{-5}, 10^{-6}\}$ (from left to right) at times corresponding to Fig. 8.20. Obtained with div-free $\mathbf{H}(\text{div})$ -HDG method $\mathbf{RT}_{[8]}^{\text{red}}/\mathbf{F}_8/\mathbb{P}_0^{\text{dc}}$ on a 64^2 mesh.	109
8.22	Evolution of dissipations for $\nu = 10^{-4}$ with div-free $\mathbf{RT}_{[8]}^{\text{red}}/\mathbf{F}_8/\mathbb{P}_0^{\text{dc}}$ on a 64^2 mesh.	110
8.23	Evolution of dissipations for $\nu = 2 \times 10^{-5}$ with div-free $\mathbf{RT}_{[8]}^{\text{red}}/\mathbf{F}_8/\mathbb{P}_0^{\text{dc}}$ on a 64^2 mesh.	110
8.24	Evolution of dissipations for $\nu = 10^{-6}$ with div-free $\mathbf{RT}_{[8]}^{\text{red}}/\mathbf{F}_8/\mathbb{P}_0^{\text{dc}}$ on a 64^2 mesh.	111

8.25	Long-time simulation: vorticity $\nabla_h \times \mathbf{u}_h(t)$ for freely decaying 2D turbulence with $\nu = 10^{-6}$ at $t \in \{30, 40, 60, 100, 160, 240\}$ (from left to right and top to bottom). Obtained with div-free $\mathbf{H}(\text{div})$ -HDG method $\mathbf{RT}_{[8]}^{\text{red}}/\mathbf{F}_8/\mathbb{P}_0^{\text{dc}}$ on a 64^2 mesh. (A video is available at https://youtu.be/Q1yhhF1hIOI ; note also the QR code.)	112
8.26	Long-time simulation: energy spectra for freely decaying 2D turbulence with $\nu = 10^{-6}$ at times corresponding to Fig. 8.25. Obtained with div-free $\mathbf{H}(\text{div})$ -HDG method $\mathbf{RT}_{[8]}^{\text{red}}/\mathbf{F}_8/\mathbb{P}_0^{\text{dc}}$ on a 64^2 mesh.	112
8.27	Long-time evolution of kinetic energy (top), enstrophy (middle) and palinstrophy (bottom) for $\nu = 10^{-6}$, computed with the divergence-free $\mathbf{RT}_{[8]}^{\text{red}}/\mathbf{F}_8/\mathbb{P}_0^{\text{dc}}$ $\mathbf{H}(\text{div})$ - \mathbf{H}^1 -lifting-HDG method on a 64^2 mesh.	113
8.28	Long-time evolution of physical and numerical dissipation(s) for $\nu = 10^{-6}$ with divergence-free $\mathbf{RT}_{[8]}^{\text{red}}/\mathbf{F}_8/\mathbb{P}_0^{\text{dc}}$ $\mathbf{H}(\text{div})$ - \mathbf{H}^1 -lifting-HDG method on a 64^2 mesh.	114
9.1	Upwind-stabilised high-order SIP $\mathbf{RT}_{[8]}^{\text{red}}/\mathbf{F}_8/\mathbb{P}_0^{\text{dc}}$ $\mathbf{H}(\text{div})$ -HDG results for the simulation of the $\text{Re} = 1600$ TGV under h -refinement. Evolution of kinetic energy (left) and total kinetic energy dissipation rate (right) on different meshes with $N \in \{4, 8, 16\}$	116
9.2	$\text{Re} = 1600$ TGV: Evolution of 0.1-isosurface of $Q(\mathbf{u}_h)$ -criterion coloured with velocity magnitude $ \mathbf{u}_h $, where blue corresponds to zero and red to everything above unity. Obtained with the SIP $\mathbf{RT}_{[8]}^{\text{red}}/\mathbf{F}_8/\mathbb{P}_0^{\text{dc}}$ method on a mesh with $N = 16$ cubical elements in each direction. Time instances from left to right and top to bottom: $t = 0, 2, 4, 5, 7, 9, 10, 14, 20$. (A video of this simulation is available at https://youtu.be/ENjjDUrrhwE ; note also the QR code.)	117
9.3	$\text{Re} = 1600$ TGV: kinetic energy spectra at $t = 10$ for $\mathbf{RT}_{[8]}^{\text{red}}/\mathbf{F}_8/\mathbb{P}_0^{\text{dc}}$ on different meshes with $N \in \{4, 8, 16\}$. Vertical lines correspond to $N(k + 1)$, respectively.	118
9.4	Upwind-stabilised high-order SIP $\mathbf{RT}_{[8]}^{\text{red}}/\mathbf{F}_8/\mathbb{P}_0^{\text{dc}}$ $\mathbf{H}(\text{div})$ -HDG results for the simulation of the $\text{Re} = 1600$ TGV under h -refinement. 1-isosurface of the $Q(\mathbf{u}_h)$ -criterion coloured with velocity magnitude $ \mathbf{u}_h $ at $t = 20$ on different meshes with $N \in \{4, 8, 16\}$	118
9.5	Upwind-stabilised SIP $\mathbf{RT}_{[k]}^{\text{red}}/\mathbf{F}_k/\mathbb{P}_0^{\text{dc}}$ $\mathbf{H}(\text{div})$ -HDG results for the simulation of the $\text{Re} = 1600$ TGV with a fixed, strong under-resolution. Evolution of kinetic energy (left) and total kinetic energy dissipation rate (right).	119
9.6	High-order upwind-stabilised SIP $\mathbf{RT}_{[8]}^{\text{red}}/\mathbf{F}_8/\mathbb{P}_0^{\text{dc}}$ $\mathbf{H}(\text{div})$ -HDG implicit LES mechanisms for the simulation of the $\text{Re} = 1600$ TGV under h -refinement.	120
9.7	High-order upwind-stabilised SIP $\mathbf{RT}_{[k]}^{\text{red}}/\mathbf{F}_k/\mathbb{P}_0^{\text{dc}}$ $\mathbf{H}(\text{div})$ -HDG implicit LES mechanisms for the simulation of the $\text{Re} = 1600$ TGV with a fixed level of under-resolution.	120
9.8	No upwinding: High-order SIP $\mathbf{RT}_{[8]}^{\text{red}}/\mathbf{F}_8/\mathbb{P}_0^{\text{dc}}$ $\mathbf{H}(\text{div})$ -HDG implicit LES mechanisms for the simulation of the $\text{Re} = 1600$ TGV under h -refinement.	121
9.9	High-order upwind-stabilised \mathbf{H}^1 -lifting $\mathbf{RT}_{[8]}^{\text{red}}/\mathbf{F}_8/\mathbb{P}_0^{\text{dc}}$ $\mathbf{H}(\text{div})$ -HDG implicit LES mechanisms for the simulation of the $\text{Re} = 1600$ TGV under h -refinement.	122
9.10	High-order $\mathbf{RT}_{[8]}^{\text{red}}/\mathbf{F}_8/\mathbb{P}_0^{\text{dc}}$ $\mathbf{H}(\text{div})$ -HDG implicit LES mechanisms for the under-resolved simulation of the $\text{Re} = 1600$ TGV with $N = 4$. Comparison of SIP and \mathbf{H}^1 -lifting results, with and without upwinding, respectively.	122

- 9.11 Upwind-stabilised SIP $\mathbf{RT}_{[4]}^{\text{red}}/\mathbf{F}_4/\mathbb{P}_0^{\text{dc}}$ $\mathbf{H}(\text{div})$ -HDG ($\text{Re} < \infty$) and upwind-stabilised $\mathbf{RT}_{[4]}^{\text{red}}/\mathbb{P}_0^{\text{dc}}$ $\mathbf{H}(\text{div})$ -DG ($\text{Re} = \infty$) results for the simulation of the TGV with $N = 32$. Evolution of kinetic energy (left) and kinetic energy spectra at $t = 10$ (right). The vertical line corresponds to $N(k + 1)$ and, for better clarity, for $\text{Re} = \infty$ only some spectrum values with upwinding are displayed. 123
- 9.12 Implicit LES mechanisms for upwind-stabilised SIP $\mathbf{RT}_{[4]}^{\text{red}}/\mathbf{F}_4/\mathbb{P}_0^{\text{dc}}$ $\mathbf{H}(\text{div})$ -HDG ($\text{Re} < \infty$) and upwind-stabilised $\mathbf{RT}_{[4]}^{\text{red}}/\mathbb{P}_0^{\text{dc}}$ $\mathbf{H}(\text{div})$ -DG ($\text{Re} = \infty$) for the simulation of the TGV at different Reynolds numbers with a fixed $N = 32$ mesh. 124
- 9.13 Upwind-stabilised SIP $\mathbf{RT}_{[4]}^{\text{red}}/\mathbf{F}_4/\mathbb{P}_0^{\text{dc}}$ $\mathbf{H}(\text{div})$ -HDG ($\text{Re} < \infty$) and upwind-stabilised $\mathbf{RT}_{[4]}^{\text{red}}/\mathbb{P}_0^{\text{dc}}$ $\mathbf{H}(\text{div})$ -DG ($\text{Re} = \infty$) for the simulation of the TGV at different Reynolds numbers with a fixed $N = 32$ mesh. 1-isosurface of the $Q(\mathbf{u}_h)$ -criterion coloured with velocity magnitude $|\mathbf{u}_h|$ at $t = 20$ for $\text{Re} \in \{1600, 3000, 5000, 10\,000, 100\,000, \infty\}$ (from left to right and top to bottom). 125
- 9.14 Inviscid TGV: Evolution of 0.1-isosurface of $Q(\mathbf{u}_h)$ -criterion coloured with velocity magnitude $|\mathbf{u}_h|$, where blue corresponds to zero and red to everything above unity. Obtained with the unstabilised $\mathbf{RT}_{[4]}^{\text{red}}/\mathbb{P}_0^{\text{dc}}$ method on a mesh with $N = 32$ cubical elements in each direction. Time instances from left to right and top to bottom: $t = 0, 2, 4, 5, 7, 9, 10, 14, 20$. (A video of this simulation is available at <https://youtu.be/cDXLFnR4468>; note also the QR code.) 126
- 9.15 Comparison of kinetic energy (left) and kinetic energy spectra at $t = 10$ (right), with and without upwinding for the inviscid Euler-TGV. Computed with the $\mathbf{RT}_{[4]}^{\text{red}}/\mathbb{P}_0^{\text{dc}}$ $\mathbf{H}(\text{div})$ -DG method on different meshes. For better clarity, not all spectrum values for the upwinding simulations are displayed. Vertical lines correspond to $N(k + 1)$, respectively. 127
- 9.16 Comparison of total kinetic energy dissipation rate (left) and enstrophy (right), with and without upwinding, for the inviscid Euler-TGV. Computed with the $\mathbf{RT}_{[4]}^{\text{red}}/\mathbb{P}_0^{\text{dc}}$ $\mathbf{H}(\text{div})$ -DG method on different meshes. 127
- 9.17 Evolution of Helmholtz decomposition of convection forces for $\text{Re} = 1600$ (left) and inviscid Euler limit $\text{Re} = \infty$ (right). Computed with upwind-stabilised SIP $\mathbf{RT}_{[4]}^{\text{red}}/\mathbf{F}_4/\mathbb{P}_0^{\text{dc}}$ ($\text{Re} = 1600$) and unstabilised $\mathbf{RT}_{[4]}^{\text{red}}/\mathbb{P}_0^{\text{dc}}$ ($\text{Re} = \infty$); both on a $N = 32$ mesh. All norms are normalised by the box volume $|\Omega| = (2\pi)^3$ 128
- 9.18 Sketch of streamwise profiles for laminar (top) and turbulent (bottom) channel flow. Note that the laminar profile occurs in the instantaneous flow, whereas the turbulent profile can be seen only after suitable averaging $\langle \cdot \rangle$ 131
- 9.19 Streamwise velocity profiles $\langle u_1 \rangle^+$ computed with the $\mathbf{RT}_{[3]}^{\text{red}}/\mathbb{P}_0^{\text{dc}}$ method for different friction Reynolds numbers $\text{Re}_\tau \in \{180, 395, 950, 2000\}$, together with corresponding DNS results and the law of the wall. For $\text{Re}_\tau > 180$, the results are each vertically shifted by 10 units in order to ensure better visibility. 131

- 9.20 $Re_\tau = 180$ mean velocity $\langle u_1 \rangle^+$ with linear (top left) and logarithmic (top right) scaling, cross-Reynolds stress $\langle u'_1 u'_2 \rangle^+$ (bottom left) and rms turbulence intensity $u_{1,\text{rms}}^+$ (bottom right), computed with $\mathbf{RT}_{[3]}^{\text{red}}/\mathbb{P}_0^{\text{dc}}$ on different meshes with $N \in \{4, 8, 16\}$. The indicated vertical lines visualise the underlying mesh spacing in wall-normal direction. 133
- 9.21 $Re_\tau = 180$ channel flow: 200-isosurface of $Q(\mathbf{u}_h)$ -criterion, coloured with the distance to the lower wall. Computation: $\mathbf{RT}_{[3]}^{\text{red}}/\mathbb{P}_0^{\text{dc}}$ with $N = 16$ 133
- 9.22 $Re_\tau = 180$ mean velocity $\langle u_1 \rangle^+$ (top left), cross-Reynolds stress $\langle u'_1 u'_2 \rangle^+$ (top right) and rms turbulence intensity $u_{1,\text{rms}}^+$ (bottom), computed with $\mathbf{RT}_{[2]}^{\text{red}}/\mathbb{P}_0^{\text{dc}}$ on different meshes with $N \in \{4, 8, 16\}$. The indicated vertical lines visualise the underlying mesh spacing in wall-normal direction. 134
- 9.23 Evolution of Helmholtz decomposition of convection forces in fully developed turbulent channel flow for $Re_\tau = 180$, computed with $\mathbf{RT}_{[3]}^{\text{red}}/\mathbb{P}_0^{\text{dc}}$ on the $N = 16$ mesh. All norms are normalised by the channel volume $|\Omega| = L_x L_y L_z$ 135
- 9.24 Instantaneous snapshots of velocity magnitude $|\mathbf{u}_h|$ for $Re_\tau = 395$, computed with $\mathbf{RT}_{[3]}^{\text{red}}/\mathbb{P}_0^{\text{dc}}$ on different meshes with $N \in \{4, 8, 16\}$ (from left to right). Blue colour indicates low velocity and red high velocity. 135
- 9.25 Transition from laminar to turbulent flow: instantaneous snapshots (at the same time instances) of velocity magnitude $|\mathbf{u}_h|$ for $Re_\tau = 395$ (top) and 200-isosurface of the Q -criterion (bottom; coloured with distance from lower wall), computed with $\mathbf{RT}_{[3]}^{\text{red}}/\mathbb{P}_0^{\text{dc}}$ with $N = 8$. (A video of this simulation is available at <https://youtu.be/XBwqvVxg6Dk>; note also the QR code.) 136
- 9.26 $Re_\tau = 395$ mean velocity $\langle u_1 \rangle^+$ with linear (top left) and logarithmic (top right) scaling, cross-Reynolds stress $\langle u'_1 u'_2 \rangle^+$ (bottom left) and rms turbulence intensity $u_{1,\text{rms}}^+$ (bottom right), computed with $\mathbf{RT}_{[3]}^{\text{red}}/\mathbb{P}_0^{\text{dc}}$ on different meshes with $N \in \{4, 8, 16\}$. The indicated vertical lines visualise the underlying mesh spacing in wall-normal direction. 137
- 9.27 $Re_\tau = 395$ mean velocity $\langle u_1 \rangle^+$ (top left), cross-Reynolds stress $\langle u'_1 u'_2 \rangle^+$ (top right) and rms turbulence intensity $u_{1,\text{rms}}^+$ (bottom), computed with $\mathbf{RT}_{[6]}^{\text{red}}/\mathbb{P}_0^{\text{dc}}$ on different meshes with $N \in \{4, 8, 16\}$. The indicated vertical lines visualise the underlying mesh spacing in wall-normal direction. 137
- 9.28 $Re_\tau = 950$ mean velocity $\langle u_1 \rangle^+$ with linear (top left) and logarithmic (top right) scaling, cross-Reynolds stress $\langle u'_1 u'_2 \rangle^+$ (bottom left) and rms turbulence intensity $u_{1,\text{rms}}^+$ (bottom right), computed with $\mathbf{RT}_{[3]}^{\text{red}}/\mathbb{P}_0^{\text{dc}}$ on different meshes with $N \in \{8, 16, 24\}$. The indicated vertical lines visualise the underlying mesh spacing in wall-normal direction. 138
- 9.29 No upwinding: $Re_\tau = 950$ mean velocity $\langle u_1 \rangle^+$ (top left), cross-Reynolds stress $\langle u'_1 u'_2 \rangle^+$ (top right) and rms turbulence intensity $u_{1,\text{rms}}^+$ (bottom), computed with $\mathbf{RT}_{[3]}^{\text{red}}/\mathbb{P}_0^{\text{dc}}$ on different meshes with $N \in \{8, 16, 24\}$ 139
- 9.30 Instantaneous snapshots of velocity magnitude $|\mathbf{u}_h|$ for $Re_\tau = 2000$, computed with $\mathbf{RT}_{[3]}^{\text{red}}/\mathbb{P}_0^{\text{dc}}$ on a $N = 24$ mesh. Left: with underlying mesh; right: without mesh. Blue colour indicates low velocity and red high velocity. 139

-
- 9.31 $\text{Re}_\tau = 2000$ channel flow: 200-isosurface of $Q(\mathbf{u}_h)$ -criterion, coloured with the distance to the lower wall. Computation: $\mathbf{RT}_{[3]}^{\text{red}}/\mathbb{P}_0^{\text{dc}}$ with $N = 24$ 140
- 9.32 $\text{Re}_\tau = 2000$ mean velocity $\langle u_1 \rangle^+$ with linear (top left) and logarithmic (top right) scaling, cross-Reynolds stress $\langle u'_1 u'_2 \rangle^+$ (bottom left) and rms turbulence intensity $u_{1,\text{rms}}^+$ (bottom right), computed with $\mathbf{RT}_{[3]}^{\text{red}}/\mathbb{P}_0^{\text{dc}}$ on different meshes with $N \in \{8, 16, 24\}$ 140
- 9.33 Evolution of Helmholtz decomposition of convection forces in fully developed turbulent channel flow for $\text{Re}_\tau = 2000$, computed with $\mathbf{RT}_{[3]}^{\text{red}}/\mathbb{P}_0^{\text{dc}}$ on the $N = 24$ mesh. All norms are normalised by the channel volume $|\Omega| = L_x L_y L_z$ 141

List of Tables

4.1	Material properties at 20 °C and 1 atm.	56
4.2	Errors for the colliding potential flow example. The most important numbers which show the advantages of a pressure-robust method are in bold type.	58
8.1	Convergence behaviour for $L^{3/2}$ -norms of the convection term $\mathbf{f}_h = (\mathbf{u}_h \cdot \nabla_h) \mathbf{u}_h$ and its discrete Helmholtz projections for different polynomial orders $k \in \{2, \dots, 9\}$	96
8.2	Overview of meshes, DOFs and NZEs of M^* based on a discretisation with $\mathbf{RT}_{[8]}^{\text{red}}/\mathbf{F}_8/\mathbb{P}_0^{\text{dc}}$. DOFs are counted before static condensation whereas NZEs from the Schur complement are counted after static condensation. Hybrid facet DOFs of \mathbf{F}_8 are not counted.	98

Introduction

1.1	Aim and Motivation	1
1.2	Overview of Publications	2
1.3	Outline of Thesis	7

1.1 Aim and Motivation

At present, computational fluid dynamics (CFD) is a core aspect of work carried out by a broad spectrum of individuals in academia and industry, and whose interests range from predominantly research-oriented to strongly application-oriented. This variety is also reflected in the fact that CFD is an extremely multidisciplinary field, where profound knowledge of engineering, physics, mathematics and high-performance computing is essential to success. The present thesis provides a contribution to CFD and is primarily intended to systematically investigate the role of so-called *exactly divergence-free* finite element methods (FEM). To this end, emphasis will of course be placed on mathematical precision, but the impact of the presented concepts and corresponding benefits in many practically relevant situations will be demonstrated as well. In this sense, this work is intended to address readers from all fields and backgrounds working in and with CFD.

What, then, is so special about exactly divergence-free FEM? In the context of incompressible flows, the fundamental concept of conservation of mass dictates that the velocity field be divergence-free. However, most commonly used FEM yield a velocity approximation which simply fails to honour this seemingly basic concept. Note, also, that the lack of mass conservation properties in 'classical' FEM is frequently used as a motivation to resort to finite volume methods instead. Exactly divergence-free FEM, in contrast, are perfectly mass-conserving. One of the main aims of the present work is thus to explain in which situations the deliberate violation of this physical law entails serious repercussions – the concept of *pressure-robustness* will be vital in this regard. Furthermore, it will be demonstrated that exactly divergence-free FEM provide a framework of discretisation techniques which allow various incompressible flows (laminar and turbulent, 2D and 3D) to be handled quite naturally and easily. This is the obvious meaning of a *robust* and *reliable* numerical method.

Another significant feature of this work is the usage of *high-order* methods, which can be applied comparably easily within the context of finite elements. Especially in the interest of demonstrating the performance and accuracy of exactly divergence-free FEM, we will be relying on high-order methods. However, the question as to whether they are always advantageous will be examined critically, mostly for the 3D examples given. It deserves mentioning that, in recent years, high-order space discretisations as an efficient means for the simulation of challenging flow problems – including real-world applications of CFD – have been gaining in popularity. Among others,

high-order methods are characterised by superior dissipation and dispersion properties as well as exponential convergence in certain situations.

1.2 Overview of Publications

During his time as a Ph.D. student, the author worked on several papers intended for publication in international, peer-reviewed journals. In this section, an overview of the resulting publications including a short summary and the particular relevance of each paper in the context of this thesis are explained. In order to facilitate the recognition of these contributions in the main body, their abbreviation refers to a capital ‘D’ together with Roman numerals ‘I, II, ..., X’.

Publication I

- [DI] P. W. Schroeder and G. Lube. Stabilised dG-FEM for incompressible natural convection flows with boundary and moving interior layers on non-adapted meshes. *J. Comput. Phys.*, **335**:760–779, 2017. URL: <https://doi.org/10.1016/j.jcp.2017.01.055>

Abstract: This paper presents heavily grad-div and pressure jump stabilised, equal- and mixed-order discontinuous Galerkin finite element methods for non-isothermal incompressible flows based on the Oberbeck–Boussinesq approximation. In this framework, the enthalpy-porosity model for multi-phase flow in melting and solidification problems can be employed. By considering the differentially heated cavity and the melting of pure gallium in a rectangular enclosure, it is shown that both boundary layers and sharp moving interior layers can be handled naturally by the proposed class of non-conforming methods. Due to the stabilising effect of the grad-div term and the robustness of Discontinuous Galerkin (DG) methods, it is possible to solve the underlying problems accurately on coarse, non-adapted meshes. The interaction of heavy grad-div stabilisation and DG methods significantly improves the mass conservation properties and the overall accuracy of the numerical scheme which is observed for the first time. Hence, it is inferred that stabilised discontinuous Galerkin methods are highly robust as well as computationally efficient numerical methods to deal with natural convection problems arising in incompressible computational thermo-fluid dynamics.

- *Relevance for thesis:* The basic idea of adding a grad-div mechanism to DG methods plays an important role in the concept of pressure-robustness in this work. Even though the particular mechanism used here is slightly different from the one proposed in [DI], it was nonetheless a first important step in the direction of improving DG methods for incompressible flows.

Publication II

- [DII] P. W. Schroeder and G. Lube. Pressure-robust analysis of divergence-free and conforming FEM for evolutionary incompressible Navier–Stokes flows. *J. Numer. Math.*, **25**(4):249–276, 2017. URL: <https://doi.org/10.1515/jnma-2016-1101>

Abstract: This article focusses on the analysis of a conforming finite element method for the time-dependent incompressible Navier–Stokes equations. For divergence-free approximations, in a semi-discrete formulation, error estimates for the velocity are proven that hold independently of both pressure and Reynolds number. Here, a key aspect is the use of the discrete Stokes projection for the error splitting. Optionally, edge-stabilisation can be included in the case of dominant convection. Emphasising the importance of conservation properties, the theoretical results are complemented with numerical simulations of vortex dynamics and laminar boundary layer flows.

- *Relevance for thesis:* The underlying idea of using and analysing exactly divergence-free methods in the context of incompressible flows has been taken up by the author for the first time in [DII]. Concerning the present work, the numerical analysis of \mathbf{H}^1 -conforming FEM is strongly based on it.

Publication III

- [DIII] P. W. Schroeder and G. Lube. Divergence-free $H(\text{div})$ -FEM for time-dependent incompressible flows with applications to high Reynolds number vortex dynamics. *J. Sci. Comput.*, **75**(2):830–858, 2018. URL: <https://doi.org/10.1007/s10915-017-0561-1>

Abstract: In this article, exactly divergence-free $H(\text{div})$ -conforming finite element methods for time-dependent incompressible viscous flow problems are considered. This is an extension of previous research concerning divergence-free H^1 -conforming methods; cf. [DII]. For the linearised Oseen case, the first semi-discrete numerical analysis for time-dependent flows is presented whereby special emphasis is placed on pressure- and Reynolds-semi-robustness. For convection-dominated problems, the proposed method relies on a velocity jump upwind stabilisation which is not gradient-based. Complementing the theoretical results, $H(\text{div})$ -FEM are applied to the simulation of full nonlinear Navier–Stokes problems. Focussing on dynamic high Reynolds number examples with vortical structures, the proposed method proves to be capable of reliably handling the planar lattice flow problem, Kelvin–Helmholtz instabilities and freely decaying two-dimensional turbulence.

- *Relevance for thesis:* Leaving the \mathbf{H}^1 world, the concept of exactly divergence-free FEM is considered in the framework of $\mathbf{H}(\text{div})$ -DG methods in [DIII]. While numerical analysis is provided in the Oseen case, the 2D numerical examples are based on the Navier–Stokes problem. Especially the 2D Kelvin–Helmholtz instability problem will be inspected closer in this work. Moreover, most of the techniques for analysing $\mathbf{H}(\text{div})$ methods in the context of the Stokes problem are based on the paper.

Publication IV

- [DIV] P. W. Schroeder, C. Lehrenfeld, A. Linke, and G. Lube. Towards computable flows and robust estimates for inf-sup stable FEM applied to the time-dependent incompressible Navier–Stokes equations. *SeMA J.*, **75**(4):629–653, 2018. URL: <https://doi.org/10.1007/s40324-018-0157-1>

Abstract: Inf-sup stable FEM applied to time-dependent incompressible Navier–Stokes flows are considered. The focus is on robust estimates for the kinetic and dissipation energies in a twofold sense. Firstly, pressure-robustness ensures the fulfilment of a fundamental invariance principle and velocity error estimates are not corrupted by the pressure approximability. Secondly, *Re*-semi-robustness means that constants appearing on the right-hand side of kinetic and dissipation energy error estimates (including Gronwall constants) do not explicitly depend on the Reynolds number. Such estimates rely on the essential regularity assumption $\nabla u \in L^1(L^\infty)$ which is discussed in detail. In the sense of best practice, pressure- and *Re*-semi-robust estimates for pointwise divergence-free H^1 -conforming FEM (like Scott–Vogelius pairs or certain isogeometric based FEM) and pointwise divergence-free $H(\text{div})$ -conforming DG methods are reviewed and established. For convection-dominated problems, the latter naturally includes an upwind stabilisation for the velocity.

- *Relevance for thesis:* In this paper, the pressure- and Reynolds-semi-robust error analysis for $\mathbf{H}(\text{div})$ -DG methods for the incompressible Navier–Stokes problem is performed for the first time and an attempt at treating exactly divergence-free \mathbf{H}^1 and $\mathbf{H}(\text{div})$ methods in a unified setting is made. Thus, [DIV] serves as the basis for the corresponding explanations in this work. The essential regularity assumption is discussed in more detail also here.

Publication V

- [DV] M. Akbas, A. Linke, L. G. Rebholz, and P. W. Schroeder. The analogue of grad-div stabilization in DG methods for incompressible flows: Limiting behavior and extension to tensor-product meshes. *Comput. Methods Appl. Mech. Engrg.*, **341**:917–938, 2018. URL: <https://doi.org/10.1016/j.cma.2018.07.019>

Abstract: Grad-div stabilisation is a classical remedy in conforming mixed finite element methods for incompressible flow problems, for mitigating velocity errors that are sometimes called poor mass conservation. Such errors arise due to the relaxation of the divergence constraint in classical mixed methods, and are excited whenever the spatial discretisation has to deal with comparably large and complicated pressures. In this contribution, an analogue of grad-div stabilisation for Discontinuous Galerkin methods is studied. Here, the key is the penalisation of the jumps of the normal velocities over facets of the triangulation, which controls the measure-valued part of the distributional divergence of the discrete velocity solution. The contribution is twofold. Firstly, the limit for arbitrarily large penalisation parameters is characterised, which shows that the stabilised nonconforming DG methods remain robust and accurate in this limit. Secondly, these ideas are extended to the case of non-simplicial meshes; here, broken grad-div stabilisation must be used in addition to the normal velocity jump penalisation, in order to get the desired pressure-robustness effect. The analysis is performed for the Stokes equations, and more complex flows and Crouzeix–Raviart elements are considered in numerical examples that also show the relevance of the theory in practical settings.

- *Relevance for thesis:* The idea of [DI] is picked up and, embedded into a suitable Stokes setting, the possibility of improving the pressure-robustness of L^2 -DG methods is explained in [DV]. This concept will be used at several places in this work.

Publication VI

- [DVI] P. W. Schroeder, V. John, P. L. Lederer, C. Lehrenfeld, G. Lube, and J. Schöberl. On reference solutions and the sensitivity of the 2D Kelvin–Helmholtz instability problem. *Comput. Math. Appl.*, **77**(4):1010–1028, 2019. URL: <https://doi.org/10.1016/j.camwa.2018.10.030>

Abstract: Two-dimensional Kelvin–Helmholtz instability problems are popular examples for assessing discretisations for incompressible flows at high Reynolds number. Unfortunately, the results in the literature differ considerably. This paper presents computational studies of a Kelvin–Helmholtz instability problem with high-order divergence-free FEM. Reference results in several quantities of interest are obtained for three different Reynolds numbers up to the beginning of the final vortex pairing. A mesh-independent prediction of the final pairing is not achieved due to the sensitivity of the considered problem with respect to small perturbations. Based on the theory of self-organisation of 2D turbulence, theoretical explanations for this sensitivity are provided. Possible sources of perturbations that arise in almost any numerical simulation are discussed.

- *Relevance for thesis:* The most important results from [DVI] can also be found in this work. However, most of the theoretical considerations and the comparison for different Reynolds numbers are not described in detail here.

Publication VII

- [DVII] N. R. Gauger, A. Linke, and P. W. Schroeder. On high-order pressure-robust space discretisations, their advantages for incompressible high Reynolds number generalised Beltrami flows and beyond. *arXiv:1808.10711 [math.NA]*, 2018. URL: <https://arxiv.org/abs/1808.10711>

Abstract: Recently, high-order space discretisations have been proposed for the numerical simulation of the incompressible Navier–Stokes equations at high Reynolds numbers, even for complicated domains from simulation practice. Although the overall spatial approximation order of the algorithms depends on the approximation quality of the boundary (often not better than third-order), competitively accurate and efficient results have been reported. In this contribution, first, a possible explanation for this somewhat surprising result is proposed: the velocity error of high-order space discretisations is more robust against quantitatively large and complicated pressure fields than low-order methods’. Secondly, it is demonstrated that novel pressure-robust methods are significantly more accurate than comparable classical, non-pressure-robust space discretisations, whenever the quadratic, nonlinear convection term is a nontrivial gradient field like in certain generalised Beltrami flows at high Reynolds number. Then, pressure-robust methods even allow to halve the (formal) approximation order without compromising the accuracy. Thirdly, classical high-order space discretisations are outperformed by pressure-robust methods whenever the boundary is not approximated with high-order accuracy. This improved accuracy of (low-order) pressure-robust mixed methods is explained in terms of a Helmholtz–Hodge projector, which cancels out the nonlinear convection term in any generalised Beltrami flow, since it is a gradient field. The numerical

results are illustrated by a novel numerical analysis for pressure-robust and classical space discretisations. Further, the relevance of these results is discussed for flows that are not of Beltrami type.

- *Relevance for thesis:* The concept of generalised Beltrami flows and their connection to pressure-robust discretisations has been analysed in [DVII] and plays a very important role in this work as well. For example, the usage of a discrete Helmholtz decomposition to identify and characterise forces in flows is applied at various places here.

Publication VIII

[DVIII] G. Lube and P. W. Schroeder. Implicit LES with high-order $H(\text{div})$ -conforming FEM for incompressible Navier–Stokes flows. `arXiv:1809.06558 [math.NA]`, 2018. URL: <https://arxiv.org/abs/1809.06558>. (accepted for BAIL Proceedings 2018)

Abstract: Transient incompressible Navier–Stokes flows at high Reynolds numbers are considered. A high-order $H(\text{div})$ -conforming FEM with pointwise divergence-free discrete velocities is applied to implicit large-eddy simulation in two limit cases: i) decaying turbulence in periodic domains, ii) wall-bounded turbulent channel flow.

- *Relevance for thesis:* Most of the results of the numerical experiments considered in [DVIII] are extended and explained in more detail in this work.

Publication IX

[DIX] C. Lehrenfeld, G. Lube, and P. W. Schroeder. A natural decomposition of viscous dissipation in DG methods for turbulent incompressible flows. `arXiv:1811.12769 [math.NA]`, 2018. URL: <https://arxiv.org/abs/1811.12769>

Abstract: Nowadays, (high-order) DG methods, or hybridised variants thereof, are widely used in the simulation of turbulent incompressible flow problems. For turbulence simulations, and especially in the practically relevant situation of strong under-resolution, it is important to distinguish between the resolved physical dissipation rate and the contribution of numerical dissipation originating from the underlying method. In this short article, a certain ambiguity related to such a decomposition for the viscous effects in a DG-discretised fluid flow problem, which is due to the discontinuity of the approximate solution, is addressed. A novel but rather natural definition for ‘physical’ and ‘numerical’ viscous dissipation is proposed and, based on a typical 3D benchmark problem for decaying turbulence, its meaningfulness is examined and confirmed numerically.

- *Relevance for thesis:* Basically all results from [DIX] can also be found in the present thesis. The main ideas play a crucial role for the interpretation of simulation results for (under-resolved) turbulent flows.

Publication X

- [DX] N. Fehn, M. Kronbichler, C. Lehrenfeld, G. Lube, and P. W. Schroeder. High-order DG solvers for under-resolved turbulent incompressible flows: A comparison of L^2 and $H(\text{div})$ methods, 2019. (in preparation)

Abstract: The accurate numerical simulation of turbulent flows is a challenging topic in computational fluid dynamics. For discretisation methods to be robust in the under-resolved regime, mass conservation as well as energy stability are key ingredients to obtain robust and accurate discretisations. Recently, two approaches have been proposed in the context of high-order discontinuous Galerkin (DG) discretisations that address these aspects differently. On the one hand, standard L^2 -based DG discretisations enforce mass conservation and energy stability weakly by the use of additional stabilisation terms. On the other hand, pointwise divergence-free $H(\text{div})$ -conforming approaches ensure exact mass conservation and energy stability by the use of tailored finite element function spaces. The present work raises the question whether and to which extent these two approaches are equivalent when applied to under-resolved turbulent flows. This comparative study highlights similarities and differences of these two approaches. The numerical results emphasise that both discretisation strategies are promising for under-resolved simulations of turbulent flows due to their inherent dissipation mechanisms.

- *Relevance for thesis:* In the present thesis, some of the results from [DX] can also be found in the corresponding chapter concerning 3D CFD applications. However, while the paper goes more into detail at several places, the thesis goes into more detail at several other places. In this sense, both paper and thesis complement each other. Nonetheless, the main contribution of the paper is the critical *comparison* of L^2 - and $H(\text{div})$ -based DG methods for 3D turbulent flows, whereas the thesis concentrates on $H(\text{div})$ methods in this context.

1.3 Outline of Thesis

This thesis is structured as follows:

Ch. 2 is dedicated to providing a condensed overview of fluid dynamics where, beginning with emphasising the connection between conservation of mass and the divergence-free constraint, basic mathematical and physical aspects of laminar and turbulent incompressible flow are introduced.

Then, the underlying (space) discretisation techniques are laid out in Ch. 3. This chapter provides all necessary details involved in understanding FEM for the incompressible flow problems treated in the present work. Both classical and modern concepts are explained, where the emphasis lies on Discontinuous Galerkin (DG) methods and related efficiency considerations.

Less technical, Ch. 4 is intended to give an overview of the robustness concepts which are important here: structure preservation, pressure-robustness and Reynolds-semi-robustness. Theoretical aspects are complemented with numerical examples which underline the importance of the expla-

nations.

Then, Ch. 5 and Ch. 6 provide numerical error analysis for the stationary Stokes and the time-dependent Navier–Stokes problem, respectively. Here, basically the methods introduced in Ch. 3 are considered with special regard to the robustness concepts from Ch. 4.

In preparation of the conducted numerical experiments in the following chapters, the notion of physical and numerical viscous dissipation is addressed in Ch. 7. Such a distinction is especially important in the context of DG methods, because the involved arguments are much more subtle as compared to the continuous case.

A major contribution of this work is the investigation of the performance of high-order divergence-free FEM in selected 2D and 3D applications in Ch. 8 and Ch. 9. Considerations of the flow around an obstacle, a Kelvin–Helmholtz instability problem as well as freely decaying 2D and 3D turbulence and turbulent channel flow problems conclude the main part of this thesis.

Finally, a summary along with conclusions and conceivable future research directions is provided in Ch. 10. In doing so, an attempt is made to also give some personal recommendations about certain fundamental design decisions which necessarily have to be made with regard to the particular numerical method to be used.

Incompressible Fluid Dynamics

Structure of this chapter: Beginning with a physically motivated excursion to the divergence-free constraint, the main model, namely the Navier–Stokes equations, as well as basic terminology and notation is introduced. Then, the weak formulation on the continuous level is considered together with some remarks concerning existence and regularity of weak solutions. Afterwards, essential further regularity assumptions, which will accompany us through this entire work, are introduced and the general concept of the Helmholtz decomposition is explained. Before finishing this chapter with special situations in which the governing equations can be simplified, some physically interesting flow quantities are introduced and their connection to turbulence is outlined.

2.1	Divergence-Free Constraint	9
2.2	Navier–Stokes Equations	10
2.2.1	Weak Formulation	12
2.2.2	Essential Regularity Assumptions	13
2.2.3	Helmholtz Decomposition and Projection	16
2.3	Characteristic Quantities of Flows	17
2.4	Turbulence Theory and Spectral Analysis	20
2.5	Related Simplified Problems	22

2.1 Divergence-Free Constraint

The title of this chapter is *incompressible* fluid dynamics. So our first task is to clarify what this means exactly, how it is connected to the divergence-free constraint and what it has to do with mass conservation and the continuity equation. This section is loosely based on ideas drawn from [And95; Pan13; Wie74] to which is referred for more details.

Let us assume that the continuum hypotheses (physical quantities vary continuously from point to point throughout the fluid) holds true and denote by *fluid particle* a small fluid-filled volume that possesses locally those macroscopic properties of the associated fluid in bulk.

The fundamental physical principle of conservation of mass dictates that mass can neither be created nor destroyed. In the context of fluid dynamics, the corresponding important quantities are the density ρ and the velocity \mathbf{u} of a particular flow configuration. Conservation of mass can then be reformulated mathematically as the *continuity equation* in conservation form:

$$\frac{\partial \rho}{\partial t} + \nabla \cdot (\rho \mathbf{u}) = 0.$$

Using the product rule for the divergence operator and introducing the *substantial derivative* operator $\frac{D}{Dt} = \frac{\partial}{\partial t} + \mathbf{u} \cdot \nabla$, one easily obtains the continuity equation in non-conservation form as

$$\frac{1}{\rho} \frac{D\rho}{Dt} = -\nabla \cdot \mathbf{u}.$$

This leads to our first formal definition.

Definition 2.1 (*Incompressible flow*)

Incompressible flow occurs whenever local and convective derivatives cancel each other out, i.e.

$$\frac{1}{\rho} \frac{D\rho}{Dt} = 0.$$

Physically, this means that the density of each fluid particle does not change during its motion.

One can also show that $\nabla \cdot \mathbf{u}$ has the physical meaning of the time rate of change of the volume δV of a moving fluid particle V , i.e.

$$\nabla \cdot \mathbf{u} = \frac{1}{\delta V} \frac{D(\delta V)}{Dt}.$$

Frequently, we assume that $\rho = \text{const}$. Then, the continuity equation reduces to the kinematic divergence-free constraint

$$\nabla \cdot \mathbf{u} = 0.$$

Thus, a material with constant ρ is always subject to incompressible flow. However, incompressible flow can also occur for materials with a globally variable ρ , whenever the density of each particular fluid particle is constant. For example, a mixture of oil and water is subject to incompressible flow even though ρ is obviously not constant. Moreover, in the ocean and the atmosphere, ρ varies spatially but any one fluid particle has a constant density. Hence, incompressible flow occurs as well; we also refer to [CL14, Sec. 2.4].

Remark 2.2 (Incompressible flow vs. incompressible fluid): In contrast, incompressible *fluid* is a thermodynamic term and should not be confused with incompressible *flow*. For example, low-speed aerodynamics is an illustration for an incompressible flow of a compressible fluid (actually, another phrasing for the condition of having an incompressible flow is based on a low Mach number). ▲

2.2 Navier–Stokes Equations

As the main model in this work, we consider the time-dependent and nonlinear incompressible Navier–Stokes equations (NSEs) [Dur08; SG00; Tri88], which read

$$\begin{cases} \partial_t \mathbf{u} + (\mathbf{u} \cdot \nabla) \mathbf{u} - \nu \Delta \mathbf{u} + \nabla p = \mathbf{f} & \text{in } (0, T) \times \Omega, & (2.1a) \\ \nabla \cdot \mathbf{u} = 0 & \text{in } [0, T] \times \Omega, & (2.1b) \\ \mathbf{u}(0, \cdot) = \mathbf{u}_0(\cdot) & \text{in } \Omega. & (2.1c) \end{cases}$$

For the space dimension $d \in \{2, 3\}$, $\Omega \subset \mathbb{R}^d$ denotes a connected bounded Lipschitz domain and

$T > 0$ is the end of time considered in the particular problem. Moreover, $\mathbf{u}: [0, T] \times \Omega \rightarrow \mathbb{R}^d$ indicates the velocity field, $p: [0, T] \times \Omega \rightarrow \mathbb{R}$ is the (zero-mean) kinematic pressure, $\mathbf{f}: [0, T] \times \Omega \rightarrow \mathbb{R}^d$ represents external body forces and $\mathbf{u}_0: \Omega \rightarrow \mathbb{R}^d$ stands for a suitable initial condition for the velocity. The underlying fluid is assumed to be Newtonian with constant kinematic viscosity $0 < \nu \ll 1$. In this chapter, we impose the no-slip boundary condition $\mathbf{u} = \mathbf{0}$ on $[0, T] \times \partial\Omega$. For simplicity, different boundary conditions as, for example, non-zero Dirichlet, free-slip, outflow or periodicity are not used for theoretical considerations in this subsection; however, they do appear in several remarks and numerical examples.

At this point, the probably most important quantity in fluid dynamics shall be introduced: the Reynolds number Re . A low Reynolds number indicates a relatively ‘slow’ and most likely laminar flow, whereas a flow at high Reynolds number tends to become chaotic (turbulent) and difficult to predict. Let us define this quantity [Dur08; SG00; Tri88].

Definition 2.3 (Reynolds number Re)

Given a reference length L_{ref} and a reference velocity U_{ref} , then

$$\text{Re} := \frac{U_{\text{ref}} L_{\text{ref}}}{\nu}.$$

One possible motivation for this definition, roughly speaking, is to understand Re as the ratio between inertia (convection) and viscous (diffusion) forces. Indeed, heuristically, $(\mathbf{u} \cdot \nabla)\mathbf{u} \approx U_{\text{ref}}^2/L_{\text{ref}}$ and $\nu\Delta\mathbf{u} \approx \nu U_{\text{ref}}/L_{\text{ref}}^2$ leads to

$$\frac{\text{inertia force}}{\text{viscous force}} = \frac{U_{\text{ref}}^2 L_{\text{ref}}^2}{L_{\text{ref}} \nu U_{\text{ref}}} = \frac{U_{\text{ref}} L_{\text{ref}}}{\nu} = \text{Re}.$$

Note that this interpretation does not always work. For example, in a laminar channel flow $(\mathbf{u} \cdot \nabla)\mathbf{u} = \mathbf{0}$ holds, which would always result in a zero Reynolds number. Thus, alternatively, the Reynolds number can also be interpreted as a ratio of, for example, energies or characteristic times. However, in this work, Def. 2.3 shall be sufficient.

Notation: Denote by $|\Omega|$ the volume of Ω and introduce the mean integral $f_{\Omega} = |\Omega|^{-1} \int_{\Omega}$. In what follows, for $K \subseteq \Omega$ we use the standard Sobolev spaces $W^{m,p}(K)$ for scalar-valued functions with associated norms $\|\cdot\|_{W^{m,p}(K)}$ and seminorms $|\cdot|_{W^{m,p}(K)}$ for $m \in \mathbb{N}_0$ and $1 \leq p \leq \infty$ [Eva10, Sec. 5.2]. Spaces and norms for vector- and matrix-valued functions are indicated with bold letters and their Frobenius norm is usually denoted $|\cdot|$. For example, for a vector-valued function $\mathbf{v} = (v_1, \dots, v_n)^{\dagger}$, we consider $\|\mathbf{v}\|_{L^p(\Omega)}^p = \sum_{i=1}^n \|v_i\|_{L^p(\Omega)}^p = \int_{\Omega} |\mathbf{v}|_p^p \, d\mathbf{x}$, where $|\mathbf{v}|_p^p = \sum_{i=1}^n |v_i|^p$. One obtains the Lebesgue space $W^{0,p}(K) = L^p(K)$ and the Hilbert space $W^{m,2}(K) = H^m(K)$. Note that the space H^m is still meaningful for $m \in \mathbb{R}$ [Sal16, Sec. 7.7.7]. Additionally, the closed subspaces $H_0^1(K)$ consisting of $H^1(K)$ -functions with vanishing trace on ∂K , and the set $L_0^2(K)$ of $L^2(K)$ -functions with zero mean in K play an important role. The $L^2(K)$ -inner product is denoted by $(\cdot, \cdot)_K$ and, if $K = \Omega$, we usually omit the domain completely when no confusion can arise.

Furthermore, with regard to time-dependent problems, given a Banach space \mathbf{X} and a time instance t , the Bochner space $L^p(0, t; \mathbf{X})$ for $p \in [1, \infty]$ is used [Eva10, Sec. 5.9.2]. In the case $t = T$, we frequently use the abbreviation $L^p(\mathbf{X}) = L^p(0, T; \mathbf{X})$. The dual space of \mathbf{X} is denoted by \mathbf{X}^* . With the obvious modification for $p = \infty$, and for $\|\cdot\|_{\mathbf{X}}$ denoting either a norm $\|\cdot\|_{\mathbf{X}}$ or a seminorm $|\cdot|_{\mathbf{X}}$, we define

$$\|\mathbf{v}\|_{L^p(0,t;\mathbf{X})}^p = \int_0^t \|\mathbf{v}(\tau)\|_{\mathbf{X}}^p d\tau.$$

2.2.1 Weak Formulation

Given the velocity space $\mathbf{V} = \mathbf{H}_0^1(\Omega)$ and the pressure space $Q = L_0^2(\Omega)$, the following universal weak formulation of the Navier–Stokes problem (2.1) is obtained:

$$\begin{cases} \text{Find } (\mathbf{u}, p): (0, T) \rightarrow \mathbf{V} \times Q \text{ with } \mathbf{u}(0) = \mathbf{u}_0 \text{ s.t., } \forall (\mathbf{v}, q) \in \mathbf{V} \times Q, & (2.2a) \\ \langle \partial_t \mathbf{u}, \mathbf{v} \rangle_* + \nu a(\mathbf{u}, \mathbf{v}) + c(\mathbf{w}; \mathbf{u}, \mathbf{v}) + b(\mathbf{v}, p) + b(\mathbf{u}, q) = \langle \mathbf{f}, \mathbf{v} \rangle_*. & (2.2b) \end{cases}$$

Here, $\langle \cdot, \cdot \rangle_*$ denotes the duality pairing between \mathbf{V} and its dual space $\mathbf{V}^* = \mathbf{H}^{-1}(\Omega)$. The corresponding multilinear forms are given by

$$a(\mathbf{u}, \mathbf{v}) := \int_{\Omega} \nabla \mathbf{u} : \nabla \mathbf{v} \, d\mathbf{x}, \quad b(\mathbf{u}, q) := - \int_{\Omega} q(\nabla \cdot \mathbf{u}) \, d\mathbf{x}, \quad c(\mathbf{w}; \mathbf{u}, \mathbf{v}) := \int_{\Omega} (\mathbf{w} \cdot \nabla) \mathbf{u} \cdot \mathbf{v} \, d\mathbf{x},$$

where $[\nabla \mathbf{u}]_{ij} = \partial u_i / \partial x_j$ denotes the entries of the Jacobian. The continuous bilinear form b is known to be inf-sup stable [Joh16, Thm. 3.46]; that is, there exists $\beta > 0$ such that

$$\inf_{q \in Q \setminus \{0\}} \sup_{\mathbf{v} \in \mathbf{V} \setminus \{0\}} \frac{b(\mathbf{v}, q)}{\|\mathbf{v}\|_{\mathbf{V}} \|q\|_Q} \geq \beta. \quad (2.3)$$

Let us furthermore recall some well-known properties of the trilinear form c .

Lemma 2.4 (Properties of the convection form)

Let $\mathbf{u}, \mathbf{v}, \mathbf{w} \in \mathbf{V}$ with $\nabla \cdot \mathbf{w} = 0$ and $1 \leq p, q, r \leq \infty$ with $1/p + 1/q + 1/r = 1$. Then, the trilinear form is continuous on $\mathbf{V} \times \mathbf{V} \times \mathbf{V}$ and

$$c(\mathbf{w}; \mathbf{u}, \mathbf{v}) = -c(\mathbf{w}; \mathbf{v}, \mathbf{u}), \quad c(\mathbf{w}; \mathbf{v}, \mathbf{v}) = 0, \quad |c(\mathbf{w}; \mathbf{u}, \mathbf{v})| \leq \|\mathbf{w}\|_{L^p} \|\nabla \mathbf{u}\|_{L^q} \|\mathbf{v}\|_{L^r}.$$

Proof: Cf., for example, [BF13, Lem. V.1.1] and [Lay08, Sec. 6.2, Lem. 13]. ■

For the sake of completeness, we observe that the viscous bilinear form a is coercive and bounded, which means that $a(\mathbf{v}, \mathbf{v}) = \|\mathbf{v}\|_{\mathbf{V}}^2 = \|\nabla \mathbf{v}\|_{L^2}^2$ and $a(\mathbf{u}, \mathbf{v}) \leq \|\nabla \mathbf{u}\|_{L^2} \|\nabla \mathbf{v}\|_{L^2}$ holds for all $\mathbf{u}, \mathbf{v} \in \mathbf{V}$.

Note that in problem (2.2) no precise statement or assumption is made about the regularity of either the data \mathbf{u}_0 and \mathbf{f} or the sought-after exact solution (\mathbf{u}, p) . Indeed, this is a sophisticated matter which is, in some way, related to one of the seven Millennium Problems in mathematics¹.

¹The official problem description from the Clay Mathematics Institute can be found on <http://www.claymath.org/sites/default/files/navierstokes.pdf> (retrieved 18/01/2019).

In order to be slightly more precise, we introduce the space

$$\mathbf{V}^{\text{div}} = \{\mathbf{v} \in \mathbf{V} : (q, \nabla \cdot \mathbf{v}) = 0, \forall q \in Q\} = \{\mathbf{v} \in \mathbf{V} : \nabla \cdot \mathbf{v} = 0\}$$

of weakly divergence-free velocities. The largest space in which one can work comfortably with the divergence is

$$\mathbf{H}(\text{div}; \Omega) = \{\mathbf{v} \in \mathbf{L}^2(\Omega) : \nabla \cdot \mathbf{v} \in L^2(\Omega)\}.$$

Analogously to \mathbf{V}^{div} , we define

$$\mathbf{H}^{\text{div}} = \{\mathbf{v} \in \mathbf{H}(\text{div}; \Omega) : \nabla \cdot \mathbf{v} = 0, \mathbf{v} \cdot \mathbf{n}|_{\partial\Omega} = 0\},$$

where \mathbf{n} denotes the outer unit normal vector to $\partial\Omega$. As is usual when working with Sobolev spaces, restrictions on boundaries are understood in the weak sense of traces. Note also that $\mathbf{V}^{\text{div}} \subset \mathbf{H}^{\text{div}}$.

Remark 2.5: Following [Soh01, Ch. II, Lem. 2.5.3], whenever Ω is a bounded Lipschitz domain, then \mathbf{H}^{div} is the closure of $\mathbf{C}_{0,\text{div}}^\infty(\Omega) := \{\mathbf{v} \in \mathbf{C}_0^\infty(\Omega) : \nabla \cdot \mathbf{v} = 0\}$ in $\|\cdot\|_{L^2}$. Frequently, \mathbf{H}^{div} is alternatively denoted by $\mathbf{L}_\sigma^2(\Omega)$. \blacktriangle

The known mathematical theory concerning existence and regularity of (Leray–Hopf) weak Navier–Stokes solutions to (2.2) gives the following result; see also [BF13; BIL06; Joh16; Soh01].

Theorem 2.6 (*Existence and uniqueness of weak Navier–Stokes solutions*)

Let $\Omega \subset \mathbb{R}^d$ be a connected, bounded Lipschitz domain. Then, provided $\mathbf{u}_0 \in \mathbf{H}^{\text{div}}$ and $\mathbf{f} \in L^2(0, T; \mathbf{V}^*)$, there exists a solution (\mathbf{u}, p) to (2.1) which fulfils, for all $T > 0$,

$$\mathbf{u} \in L^2(0, T; \mathbf{V}^{\text{div}}) \cap L^\infty(0, T; \mathbf{H}^{\text{div}}), \quad \partial_t \mathbf{u} \in L^{4/d}(0, T; (\mathbf{V}^{\text{div}})^*), \quad p \in W^{-1, \infty}(0, T; Q).$$

For $d = 2$ the solution is unique, whereas uniqueness is an open problem for $d = 3$. Furthermore, for all $t \in [0, T]$, the following energy inequality holds true:

$$\frac{1}{2} \|\mathbf{u}(t)\|_{L^2}^2 + \nu \int_0^t \|\nabla \mathbf{u}(\tau)\|_{L^2}^2 \, d\tau \leq \frac{1}{2} \|\mathbf{u}_0\|_{L^2}^2 + \int_0^t \langle \mathbf{f}(\tau), \mathbf{u}(t) \rangle_* \, d\tau. \quad (2.4)$$

In case of $d = 2$, in fact there holds equality in (2.4).

Proof: Cf., for example, [BF13, Ch. V, Sec. 1.3] or [Soh01, Ch. V, Sec. 3]. \blacksquare

2.2.2 Essential Regularity Assumptions

In this work we mainly deal with numerical approximations to solutions of the Navier–Stokes equations (2.1). Unfortunately, for finite element error analysis, the regularity provided in Thm. 2.6 is not sufficient. This means that if the exact solution (\mathbf{u}, p) of the problem at hand, for which an approximation is sought, has only this minimal amount of regularity, then, in general, one cannot hope to be able to construct a controllable numerical method to find a discrete solution. Therefore, we make the following additional regularity assumptions.

Assumption A: In the weak formulation (2.2), we search for $(\mathbf{u}, p) \in \mathbf{V}^T \times Q^T$, where

$$\mathbf{V}^T = \{\mathbf{v} \in L^2(0, T; \mathbf{V}) : \partial_t \mathbf{v} \in L^2(0, T; \mathbf{L}^2(\Omega))\}, \quad Q^T = L^2(0, T; Q). \quad (2.5)$$

In addition, let us assume that the right-hand side forcing term fulfils

$$\mathbf{f} \in L^2(0, T; \mathbf{L}^2), \quad (2.6)$$

which is not unrealistic in light of the assumed regularity (2.5) for the solution.

Note that the condition for $\partial_t \mathbf{u}$ in (2.5) is an assumption for the regularity both in time (only for $d = 3$) and space and implies that $\mathbf{u} \in H^1(\mathbf{L}^2)$. For p , on the other hand, it represents an assumption only for the regularity in time.

Remark 2.7: Concerning the regularity (2.6) of the forcing term \mathbf{f} , on the continuous level, the problem could be posed using the less restrictive assumption $\mathbf{f} \in L^2(\mathbf{V}^*)$. However, in this work we also deal with discretisations which are not \mathbf{H}^1 -conforming. In such a situation, rough right-hand sides lead to technical difficulties which we omit by assuming (2.6); cf. [DE12, Rem. 4.9]. Another problem with rough forcing terms, even for \mathbf{H}^1 -conforming methods, is that energy estimates can generally not be expected to be independent of ν^{-1} ; cf. [DII, Rem. 3.2]. \blacktriangle

Moreover, it is very common to additionally demand the following regularity.

Assumption B: Assume that the solution \mathbf{u} to (2.2) fulfils

$$\mathbf{u} \in L^1(0, T; \mathbf{W}^{1,\infty}(\Omega)). \quad (2.7)$$

Note that especially, this holds only if $\nabla \mathbf{u} \in L^1(\mathbf{L}^\infty)$.

We now want to highlight that incompressible flows which comply with (2.7) are relevant both from a theoretical and a practical point of view. Let us give a few arguments underlining this statement. At first, note that (2.7) guarantees unique solvability of the Navier–Stokes problem.

Lemma 2.8 (Unique solvability)

If a solution $\mathbf{u} \in \mathbf{V}^T \cap L^1(\mathbf{W}^{1,\infty})$, $p \in Q^T$ to the NSEs (2.2) exists, it is unique.

Proof: This proof is based on [MB02, Sec. 3.1] and [DII]. Let (\mathbf{u}_1, p_1) and (\mathbf{u}_2, p_2) be two solutions of (2.2) with smooth velocities according to $\mathbf{V}^T \cap L^1(\mathbf{W}^{1,\infty})$ and initial values \mathbf{u}_{0_1} and \mathbf{u}_{0_2} . Denote the difference of the solutions by $(\tilde{\mathbf{u}}, \tilde{p}) = (\mathbf{u}_1 - \mathbf{u}_2, p_1 - p_2)$.

Considering the difference of (2.1) for (\mathbf{u}_1, p_1) and (\mathbf{u}_2, p_2) , respectively, and adding a zero yields

$$\partial_t \tilde{\mathbf{u}} + (\mathbf{u}_1 \cdot \nabla) \tilde{\mathbf{u}} + (\tilde{\mathbf{u}} \cdot \nabla) \mathbf{u}_2 = -\nabla \tilde{p} + \nu \Delta \tilde{\mathbf{u}}.$$

Multiplication by $\tilde{\mathbf{u}}$ and integration over Ω results in

$$(\partial_t \tilde{\mathbf{u}}, \tilde{\mathbf{u}}) + c(\mathbf{u}_1; \tilde{\mathbf{u}}, \tilde{\mathbf{u}}) + c(\tilde{\mathbf{u}}; \mathbf{u}_2, \tilde{\mathbf{u}}) = -(\nabla \tilde{p}, \tilde{\mathbf{u}}) + \nu(\Delta \tilde{\mathbf{u}}, \tilde{\mathbf{u}}),$$

where $c(\mathbf{u}_1; \tilde{\mathbf{u}}, \tilde{\mathbf{u}}) = 0$ due to Lem. 2.4. The two terms on the right-hand side can be treated using integration by parts, where the boundary terms cancel out for no-slip (or periodic) boundary conditions on $\partial\Omega$. With the estimate in Lem. 2.4, we thus obtain

$$\frac{1}{2} \frac{d}{dt} \|\tilde{\mathbf{u}}\|_{L^2}^2 \leq \frac{1}{2} \frac{d}{dt} \|\tilde{\mathbf{u}}\|_{L^2}^2 + \nu \|\nabla \tilde{\mathbf{u}}\|_{L^2}^2 = -c(\tilde{\mathbf{u}}; \mathbf{u}_2, \tilde{\mathbf{u}}) \leq \|\nabla \mathbf{u}_2\|_{L^\infty} \|\tilde{\mathbf{u}}\|_{L^2}^2.$$

Applying the differential form of Gronwall’s lemma [Joh05, A. 54] gives, for all $0 \leq t \leq T$,

$$\|\tilde{\mathbf{u}}(t)\|_{L^2}^2 \leq \|\tilde{\mathbf{u}}(0)\|_{L^2}^2 \exp\left(2 \int_0^t \|\nabla \mathbf{u}_2(\tau)\|_{L^\infty} d\tau\right), \quad (2.8)$$

which, after taking the square root, becomes

$$\|\tilde{\mathbf{u}}\|_{L^\infty(L^2)} \leq \|\tilde{\mathbf{u}}(0)\|_{L^2} e^{|\mathbf{u}_2|_{L^1(\mathbf{W}^{1,\infty})}}. \quad (2.9)$$

The claim follows immediately whenever \mathbf{u}_{0_1} and \mathbf{u}_{0_2} coincide, since then $\|\tilde{\mathbf{u}}(0)\|_{L^2} = 0$. \blacksquare

Furthermore, the following arguments are also to be considered.

- In fact, (2.7) ensures that the velocity field \mathbf{u} is uniformly Lipschitz continuous on $[0, T]$. This can be explained as a result of Sobolev embedding theorems; cf. [BF13, Sec. 2.8]. As a consequence, the characteristic curves of the dynamical system $\frac{d}{dt} \mathbf{x}(t) = \mathbf{u}(t, \mathbf{x}(t))$ remain smooth and never intersect within $[0, T]$; cf. [BT13].
- From a physical point of view, these characteristic curves are the pathlines of the flow; cf. [Dur08, Sec. 4.3.1], and it is indeed meaningful that they never intersect.
- The symmetric part of the velocity gradient $\nabla \mathbf{u}$ encodes relevant information about the local structure of a flow; cf. [CL14, Sec. 2.5].
- At least in a periodic box and for $\mathbf{f} = \mathbf{0}$, the smallest scales of an incompressible Navier–Stokes flow behave like $\sqrt{\nu / \|\nabla \mathbf{u}\|_{L^\infty}}$; cf. [HKR90].

Remark 2.9 (Onsager’s conjecture): If $\nu = 0$ in (2.1), the *incompressible Euler equations* are recovered. Suppose $\mathbf{f} \equiv \mathbf{0}$ and $\Omega = \mathbb{R}^3$, or let $\Omega \subset \mathbb{R}^3$ be a box with periodic BCs in all directions. Then, in 1949 Onsager conjectured that energy conservation of a solution to the corresponding Euler system is guaranteed only if the velocity is Hölder continuous with exponent $> 1/3$, i.e. $\mathbf{u} \in C^{0,\alpha}(\Omega)$ for $\alpha > 1/3$ [Ons49]. In fact, Onsager’s conjecture turns out to be correct (see [BV19; CET94; Eyi94]) and energy is conserved even for $\alpha = 1/3$ [CC+08] (using Besov spaces); in this positive case, there holds equality in (2.4) ($\nu = 0$, $\mathbf{f} \equiv \mathbf{0}$). On the other hand, if $\alpha < 1/3$, the lack of smoothness results in a phenomenon called *anomalous dissipation* [BL+18]. Its occurrence is related to the notion of the so-called *zeroth law of turbulence*, which roughly states that kinetic energy dissipation is non-vanishing, even in the limit as $\nu \rightarrow 0$; see also [Fri95, Ch. 5.2]. Both experimental [PKvdW02] and numerical (DNS) evidence [KI+03] support this concept. \blacktriangle

2.2.3 Helmholtz Decomposition and Projection

The so-called *Helmholtz decomposition* is an important tool for the analysis of incompressible flows. In this thesis, we only need the very basic concept but the interested reader is, for example, referred to [JL⁺17], [Joh16, Sec. 3.7], [Soh01, Ch. II, Sec. 2.5] and [BF13, Sec. 3.3] for more information.

In order to introduce a decomposition of \mathbf{L}^2 vector fields, the following space of gradients is needed:

$$\mathbf{G}(\Omega) := \{\mathbf{v} \in \mathbf{L}^2(\Omega) : \exists \phi \in H^1(\Omega) \text{ s.t. } \mathbf{v} = \nabla\phi\}.$$

Theorem 2.10 (*Helmholtz decomposition*)

Let $\Omega \subset \mathbb{R}^d$, $d \geq 2$, be a bounded Lipschitz domain. Then, every vector field $\mathbf{f} \in \mathbf{L}^2(\Omega)$ can be decomposed uniquely into a divergence-free part \mathbf{f}_0 and a curl-free part $\nabla\phi$; that is,

$$\mathbf{f} = \mathbf{f}_0 + \nabla\phi, \quad (2.10)$$

where $\mathbf{f}_0 \in \mathbf{H}^{\text{div}}$, $\nabla\phi \in \mathbf{G}(\Omega)$, $(\mathbf{f}_0, \nabla\phi)_{\mathbf{L}^2} = 0$ and $\|\mathbf{f}\|_{\mathbf{L}^2}^2 = \|\mathbf{f}_0\|_{\mathbf{L}^2}^2 + \|\nabla\phi\|_{\mathbf{L}^2}^2$. Thus, $\mathbf{G}(\Omega) = (\mathbf{H}^{\text{div}})^\perp$, where orthogonality holds w.r.t. the \mathbf{L}^2 inner product.

Proof: Cf., for example, [BF13, Thm. IV.3.4] or [Gal11, Thm. III.1.1]. ■

In this setting, namely $\mathbf{f} = \mathbf{f}_0 + \nabla\phi$, the operator

$$\mathbb{P}: \mathbf{L}^2(\Omega) \rightarrow \mathbf{H}^{\text{div}}, \quad \mathbb{P}\mathbf{f} = \mathbf{f}_0,$$

is called *Helmholtz projector* of \mathbf{f} . Note that obtaining the Helmholtz decomposition of $\mathbf{f} \in \mathbf{L}^2(\Omega)$ can also be characterised as finding the solution $(\mathbb{P}\mathbf{f}, \phi) \in \mathbf{H}(\text{div}; \Omega) \times H^1(\Omega)$ to the PDE problem

$$\begin{cases} \mathbb{P}\mathbf{f} + \nabla\phi = \mathbf{f} & \text{in } \Omega, & (2.11a) \\ \nabla \cdot \mathbb{P}\mathbf{f} = 0 & \text{in } \Omega, & (2.11b) \\ \mathbb{P}\mathbf{f} \cdot \mathbf{n} = 0 & \text{on } \partial\Omega. & (2.11c) \end{cases}$$

The following corollary is quite obvious, but still enormously important to notice.

Corollary 2.11

For all $\phi \in H^1(\Omega)$, there holds $\mathbb{P}(\nabla\phi) = \mathbf{0}$.

Let us at this point discuss one important application of the Helmholtz decomposition. The next lemma shows that for the dynamics of the Navier–Stokes problem (2.1), only the initial condition and the Helmholtz projection of the forcing term \mathbf{f} affect the velocity solution. In other words, irrotational forces do not have an impact on the velocity of an incompressible flow [JL⁺17].

Lemma 2.12 (*Energy estimate with Helmholtz projection under smoothness*)

According to Asm. A, let $(\mathbf{u}, p) \in \mathbf{V}^T \times Q^T$ be a solution to the NSEs (2.2) with $\mathbf{f} \in L^2(\mathbf{L}^2)$. Then, for all $t \in [0, T]$, the Helmholtz decomposition $\mathbf{f}(t) = \mathbb{P}\mathbf{f}(t) + \nabla\phi(t)$ can be used to obtain the following energy estimate:

$$\|\mathbf{u}(t)\|_{\mathbf{L}^2}^2 + \nu \|\nabla\mathbf{u}\|_{L^2(\mathbf{L}^2)}^2 \leq \|\mathbf{u}_0\|_{\mathbf{L}^2}^2 + \frac{C_{\text{PF}}^2}{\nu} \|\mathbb{P}\mathbf{f}\|_{L^2(\mathbf{L}^2)}^2. \quad (2.12)$$

Proof: For all $t \in [0, T]$, testing symmetrically in (2.2), using Lem. 2.4, the Helmholtz decomposition and the fact that $\mathbf{u} \in \mathbf{V}^{\text{div}}$ leads to

$$\frac{1}{2} \frac{d}{dt} \|\mathbf{u}\|_{\mathbf{L}^2}^2 + \nu \|\nabla\mathbf{u}\|_{\mathbf{L}^2}^2 = (\mathbf{f}, \mathbf{u}) = (\mathbb{P}\mathbf{f} + \nabla\phi, \mathbf{u}) = (\mathbb{P}\mathbf{f}, \mathbf{u}) \leq C_{\text{PF}} \|\mathbb{P}\mathbf{f}\|_{\mathbf{L}^2} \|\nabla\mathbf{u}\|_{\mathbf{L}^2},$$

where the Poincaré–Friedrichs inequality has been used in the estimate. Now, applying the ideas of the proof of [Joh16, Lem. 7.21] shows the claim. \blacksquare

Remark 2.13: Whenever the Helmholtz projection of the forcing term $\mathbf{f} = \mathbf{f}_0 + \nabla\phi$ vanishes, i.e. $\mathbb{P}\mathbf{f} = \mathbf{f}_0 = \mathbf{0}$, Lem. 2.12 reveals that the only source of energy is the initial condition \mathbf{u}_0 . Worded differently, in a stationary process ($\partial_t\mathbf{u} = \mathbf{0}$), a forcing term \mathbf{f} with $\mathbb{P}\mathbf{f} = \mathbf{0}$ leads to the trivial solution $\mathbf{u} = \mathbf{0}$ (the pressure, however, does not need to vanish). We will pick up this property again in Sec. 4.2 in the context of pressure-robustness and so-called *no-flow* problems. \blacktriangle

2.3 Characteristic Quantities of Flows

Let us now take a step back from the rather technical considerations concerning regularity of Navier–Stokes solutions. In classical physical fluid dynamics theory, it is usually (sometimes implicitly) assumed that velocity and pressure are smooth enough such that carrying out basic calculus operations does not make any problems.² Taking this view, we will now introduce frequently considered and physically interesting quantities which characterise incompressible flows [Dav04; Les08].

²In order to obtain more regular solutions than provided in Thm. 2.6, one has to begin with more regular data in the first place. The corresponding notion of *strong* solutions is explained, for example, in [BF13, Ch. V, Sec. 2].

Definition 2.14

Given a velocity $\mathbf{u} = (u_1, u_2, u_3)^\dagger$, the corresponding vorticity is defined by $\boldsymbol{\omega} = (\omega_1, \omega_2, \omega_3)^\dagger = \nabla \times \mathbf{u} := \text{curl } \mathbf{u}$. For $d = 2$, we have $u_3 = 0$ and therefore, the scalar-valued analogue $\omega := \omega_3 = \partial_{x_1} u_2 - \partial_{x_2} u_1$ is usually introduced as being only the third component of the 3D curl. For $\mathbf{x} = (x_1, x_2, x_3)^\dagger$, the following quantities and their evolution are of particular interest:

$$\begin{aligned} \mathcal{K}(\mathbf{u}) &:= \frac{1}{2|\Omega|} \|\mathbf{u}\|_{L^2}^2 = \frac{1}{2} \int_{\Omega} |\mathbf{u}(\mathbf{x})|^2 \, d\mathbf{x} && \text{(kinetic energy),} \\ \varepsilon(\mathbf{u}) &:= \frac{\nu}{|\Omega|} \|\nabla \mathbf{u}\|_{L^2}^2 = \nu \int_{\Omega} |\nabla \mathbf{u}(\mathbf{x})|^2 \, d\mathbf{x} && \text{(energy dissipation rate),} \\ \mathcal{E}(\mathbf{u}) &:= \frac{1}{2|\Omega|} \|\boldsymbol{\omega}\|_{L^2}^2 = \frac{1}{2} \int_{\Omega} |\boldsymbol{\omega}(\mathbf{x})|^2 \, d\mathbf{x} && \text{(enstrophy),} \\ \mathcal{P}(\mathbf{u}) &:= \frac{1}{2|\Omega|} \|\nabla \boldsymbol{\omega}\|_{L^2}^2 = \frac{1}{2} \int_{\Omega} |\nabla \boldsymbol{\omega}(\mathbf{x})|^2 \, d\mathbf{x} && \text{(2D}^3 \text{ palinstrophy).} \end{aligned}$$

Note that recently, an increased interest, both theoretically and numerically, in using $\mathcal{K}(\mathbf{u})$, $\mathcal{E}(\mathbf{u})$ and $\mathcal{P}(\mathbf{u})$ for analysing merging processes in incompressible 2D flows at high Reynolds numbers can be observed [AP14a; AP14b; CvH17; GSS11].

In the following, we want to investigate the time evolution of kinetic energy, enstrophy and palinstrophy. The starting point for this is the momentum balance (2.1a) of the time-dependent Navier–Stokes equations (2.1). Dotting \mathbf{u} into it, integration over Ω , integration by parts of both pressure gradient and Laplacian, and then applying $\nabla \cdot \mathbf{u} = 0$ plus the no-slip boundary condition⁴ (BC) leads to the following evolution equation:

$$\frac{d}{dt} \frac{1}{2} \|\mathbf{u}(t)\|_{L^2}^2 = -\nu \|\nabla \mathbf{u}(t)\|_{L^2}^2 + \int_{\Omega} \mathbf{f}(t, \mathbf{x}) \cdot \mathbf{u}(t, \mathbf{x}) \, d\mathbf{x}. \quad (2.13)$$

Again relying essentially on $\nabla \cdot \mathbf{u} = 0$ [DG95, Sec. 1.4], one can show that at least for no-slip, stress-free ($\mathbf{u} \cdot \mathbf{n} = 0$, $(-\nu \nabla \mathbf{u}) \mathbf{n} \times \mathbf{n} = \mathbf{0}$ on $\partial\Omega$) and periodic BCs,

$$\varepsilon(\mathbf{u}) = 2\nu \mathcal{E}(\mathbf{u}) \quad (2.14)$$

holds true. Thus, after additionally dividing by $|\Omega|$, (2.13) can be rewritten as the *kinetic energy evolution equation*

$$\frac{d}{dt} \mathcal{K}(\mathbf{u}) = -2\nu \mathcal{E}(\mathbf{u}) + \int_{\Omega} \mathbf{f} \cdot \mathbf{u} \, d\mathbf{x}.$$

In order to derive a corresponding evolution equation for the enstrophy, one first has to obtain the *vorticity transport equation* [Tri88, Sec. 6.6] by taking the curl of (2.1a) which leads to

$$\partial_t \boldsymbol{\omega} + (\mathbf{u} \cdot \nabla) \boldsymbol{\omega} = \nu \Delta \boldsymbol{\omega} + (\boldsymbol{\omega} \cdot \nabla) \mathbf{u} + \text{curl } \mathbf{f}. \quad (2.15)$$

³ In the general 3D case, the palinstrophy is defined with the help of $\|\nabla \times \boldsymbol{\omega}\|_{L^2}^2$ [PL⁺75]. For the considerations in this work, however, the 2D case, in which the gradient of the (scalar-valued) vorticity is used instead, suffices.

⁴Note that periodic and stress-free BCs provide the same result [DG95, Sec. 1.3].

The term $(\boldsymbol{\omega} \cdot \nabla)\mathbf{u}$ describes the physical phenomenon of *vortex stretching* which, vanishing identically in 2D, is inherently connected to 3D turbulence and the mathematical difficulties explained in Sec. 2.2; see also [Doe09].

Now, dotting $\boldsymbol{\omega}$ into (2.15), integration over Ω , integration by parts and using $\nabla \cdot \mathbf{u} = \nabla \cdot \boldsymbol{\omega} = 0$ together with periodic and/or stress-free BCs (not under no-slip!) amounts to

$$\frac{d}{dt}\mathcal{E}(\mathbf{u}) = -2\nu\mathcal{P}(\mathbf{u}) + \int_{\Omega} (\boldsymbol{\omega} \cdot \nabla)\mathbf{u} \cdot \boldsymbol{\omega} \, dx + \int_{\Omega} \text{curl } \mathbf{f} \cdot \boldsymbol{\omega} \, dx; \quad (2.16)$$

the *enstrophy evolution equation*. The quantity $2\nu\mathcal{P}(\mathbf{u})$ is called *enstrophy dissipation rate* and is the analogue of the energy dissipation rate $\varepsilon(\mathbf{u})$. Note that even in the limit $\nu \rightarrow 0$ and without a forcing term, 3D incompressible flows hence may show a finite energy dissipation, which is a remarkable property.

Remark 2.15 (Freely decaying flows): Let us assume that $\text{curl } \mathbf{f} = \mathbf{0}$, which is, for example, the case for applications where the force field is conservative⁵. In this case, for $d = 2$ we have $(\boldsymbol{\omega} \cdot \nabla)\mathbf{u} = \mathbf{0}$ and thus, (2.16) reveals that, as a result of viscous forces only, the enstrophy (and due to (2.14) also the dissipation rate) of an incompressible flow is always monotonically (exponentially slow) decreasing in time whenever periodic and/or stress-free BCs are imposed. In contrast, under the full no-slip condition $\mathbf{u}|_{\partial\Omega} = \mathbf{0}$, vorticity and hence enstrophy can indeed be created in the vicinity of boundary layers, even in the 2D situation; cf., for example, [CMvH99; CvH17]. On the other hand, for $d = 3$, since the sign of the additional integral term in (2.16) cannot be controlled, the enstrophy might additionally either be amplified or diminished by the vortex stretching contribution. Especially, in a periodic domain, this means that if the enstrophy of a 3D incompressible flow increases in time, unavoidably the mechanism of vortex stretching has to be responsible. ▲

Rem. 2.15 highlights a fundamental difference between 2D and 3D flows: in 3D, enstrophy can increase or decrease by means of vortex stretching. Naturally, the question arises whether there exists an analogous mechanism also for 2D flows. The answer is directly connected to the 2D palinstrophy, as we will see now.

In order to obtain an evolution equation for the 2D palinstrophy, we simplify the vector-valued vorticity transport equation (2.15) for the 2D case by only considering the third component of the corresponding quantities ($\boldsymbol{\omega} \rightarrow \omega$). Now, for brevity assuming that $\mathbf{f} = \mathbf{0}$, taking the gradient⁶ of (2.15) leads to the *2D palinstrophy transport equation* [AP14a]

$$\partial_t \nabla \omega + (\mathbf{u} \cdot \nabla) \nabla \omega = \nu \Delta \nabla \omega - (\nabla \mathbf{u})^\dagger \nabla \omega.$$

Dotting $\nabla \omega$ into this equation⁷, integration over Ω and integration by parts leads to the following

⁵The probably most prominent example of a conservative force is the gravitational force.

⁶In the general 3D case, one would have to take the curl again (this is where the name ‘palinstrophy’ comes from).

⁷A different approach is to multiply (2.15) by $\Delta \omega$, integrate and use integration by parts on the left-hand side.

evolution equation [Bat69]:

$$\frac{d}{dt} \frac{1}{2} \|\nabla\omega\|_{L^2}^2 = -\nu \int_{\Omega} |\nabla(\nabla\omega)|^2 d\mathbf{x} - \int_{\Omega} (\nabla\mathbf{u})^\dagger \nabla\omega \cdot \nabla\omega d\mathbf{x}.$$

After rescaling and rewriting the term involving the Hessian of the vorticity (third derivatives of the velocity), we obtain the *2D palinstrophy evolution equation*

$$\frac{d}{dt} \mathcal{P}(\mathbf{u}) = -\frac{\nu}{|\Omega|} |\omega|_{H^2}^2 - \int_{\Omega} (\nabla\mathbf{u})^\dagger \nabla\omega \cdot \nabla\omega d\mathbf{x}. \quad (2.17)$$

Comparing the palinstrophy evolution equation (2.17) for 2D with the enstrophy evolution equation (2.16) for 3D, one can observe structural similarities. The second term on the right-hand side of (2.17) now represents the 2D analogue of 3D vortex stretching in (2.16), for it shows that palinstrophy may indeed spontaneously increase or decrease in time. Consistently, viscosity effects dampen the rate of change of palinstrophy in 2D; as they do the rate of change of enstrophy in 3D.

2.4 Turbulence Theory and Spectral Analysis

At this point, it is also useful to make a brief side note about (statistical) turbulence theory and spectral analysis; cf., for example, [DG95, Sec. 3.3]. Assuming that $\Omega \subset \mathbb{R}^n$ is a periodic box (in all directions), define by $E(\kappa)$ the amount of kinetic energy concentrated in the wavenumber $\kappa \in \mathbb{R}^n$ with $\kappa := |\kappa|$. Using Fourier analysis in spectral space allows the decomposition of a particular flow into several length scales (frequencies) which are associated with $1/\kappa$. All explanations have to be understood in the context of incompressible flows at high Reynolds numbers.

The absence of vortex stretching in 2D leads to the fact that 2D flows cannot dissipate energy at small scales, thereby giving 2D turbulence a totally different character compared to 3D turbulence [BE12; Tab02]. Therefore, there is no forward cascade of kinetic energy in 2D flows, but energy is transferred (backwards) from small to large scales. Furthermore, a typical characteristic of 2D flows is its tendency to self-organise into large-scale coherent structures [Van88]. However, 2D flows do dissipate enstrophy at small scales which means that there exists a forward cascade for enstrophy. So, very roughly speaking, 3D and 2D turbulence can be considered analogously, at least in some aspects, when the enstrophy is treated as the kinetic energy and the vorticity as the velocity.

Denote by $\langle \cdot \rangle$ a suitable averaging operator (most of the time, either time or ensemble averages are considered). In the following, we consider the *inertial range* of scales where only inertia effects from the nonlinear term are relevant and the impact of viscous diffusion is negligible. Using dimensional analysis, in this inertial range the distribution of energy across different 3D flow scales can be shown to behave according to the Kolmogorov scaling theory (see also [Les08, Ch. 6])

$$E(\kappa) \sim \langle 2\nu\mathcal{E}(\mathbf{u}) \rangle^{2/3} \kappa^{-5/3}. \quad (2.18)$$

Note that the enstrophy plays a role in this equation for the kinetic energy spectrum.

Contrary to above, and as already mentioned, the situation is fundamentally different in 2D. For large wavenumbers (small scales), kinetic energy is distributed according to

$$E(\kappa) \sim \langle 2\nu\mathcal{P}(\mathbf{u}) \rangle^{2/3} \kappa^{-3},$$

which represents the forward cascade of enstrophy [Les08, Ch. 8]. Note that now, the palinstrophy appears instead of the enstrophy. However, the so-called *inverse cascade* of kinetic energy, which is observable only for forced 2D turbulence, takes place at smaller wavenumbers and behaves analogously to (2.18); see also [Dav04, Ch. 10] and [Les08, Sec. 8.6]. A corresponding visualisation of the cascade processes in the freely decaying setting can be seen in Fig. 2.1.

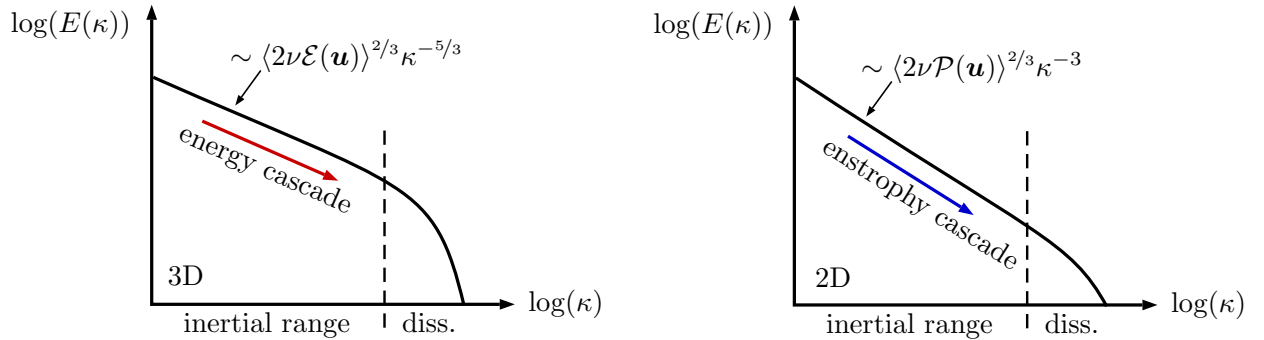


Fig. 2.1: Forward energy and enstrophy cascade processes for freely decaying turbulence in 3D (left) and 2D (right), respectively.

From these considerations concerning the distribution of energy over different scales, one can learn that asymptotically, 3D flows usually concentrate more energy in fine scales than 2D flows.

Remark 2.16 (Fourier transform, spectra and regularity): Let us briefly remark on the connection between regularity of a function and decay of its energy spectrum. Given $u \in L^2(\mathbb{R}^n)$, the Fourier transform of u for $\boldsymbol{\kappa} \in \mathbb{R}^n$ is defined as $\mathcal{F}[u](\boldsymbol{\kappa}) = \int_{\mathbb{R}^n} \exp(-i\boldsymbol{x} \cdot \boldsymbol{\kappa}) u(\boldsymbol{x}) \, d\boldsymbol{x}$ and $\mathcal{F}[u] \in L^2(\mathbb{R}^n)$ holds. More importantly, $u \in H^m(\mathbb{R}^n)$ if and only if $(1 + \kappa^2)^{m/2} \mathcal{F}[u] \in L^2(\mathbb{R}^n)$, where $\kappa = |\boldsymbol{\kappa}|$ [Sal16, Sec. 7.7.7]. Thus, $H^m(\mathbb{R}^n)$ is the space of functions $u \in L^2(\mathbb{R}^n)$ such that $\kappa^m \mathcal{F}[u] \in L^2(\mathbb{R}^n)$. Roughly speaking, this means that from the decay in wave space of the Fourier transform as $\kappa \rightarrow \infty$, one can draw conclusions concerning the regularity of the function in physical space: a steeper slope corresponds to a more regular function. This also means that, roughly speaking, a turbulent 2D flow is more regular than a turbulent 3D flow as κ^{-3} is steeper than $\kappa^{-5/3}$; cf. Fig. 2.1. Furthermore, a $\kappa^{-5/3}$ energy spectrum corresponds to the Hölder regularity $\mathcal{C}^{0,1/3}$; see [CET94], [Les08, Sec. 6.4.5] or [Fri95, Ch. 5.1, Sec. 6.3.1]. More generally, an energy spectrum decaying as $E(\kappa) \sim \kappa^{-s}$ for $1 < s \leq 3$ implies Hölder continuity $\mathcal{C}^{0, \frac{s-1}{2}}$; see [Fri95, eqn. (4.60), eqn. (4.61)] and [CET94]. With respect to Rem. 2.9, this means that any incompressible Euler flow ($\nu = 0$) which shows at least a $\kappa^{-5/3}$ decay is regular enough to be energy conserving. \blacktriangle

Another interesting point is how the fine scales react to the viscosity (equivalently the Reynolds

number) [DG95]. In 3D, the so-called *Kolmogorov dissipation length scale* λ_{3D} is defined as

$$\lambda_{3D} \sim \left(\frac{\nu^3}{\langle 2\nu\mathcal{E}(\mathbf{u}) \rangle} \right)^{1/4},$$

which indicates that below λ_{3D} , viscous dissipation dominates the dynamics of the flow. In contrast, the 2D analogue, called *Kraichnan dissipation length scale* λ_{2D} , behaves according to

$$\lambda_{2D} \sim \left(\frac{\nu^3}{\langle 2\nu\mathcal{P}(\mathbf{u}) \rangle} \right)^{1/6}.$$

In Fig. 2.2, λ_{3D} and λ_{2D} are shown exemplarily for various viscosities ν . One can observe that the dissipation length scale in 3D decreases faster for decreasing ν , which means that the amount of small-scale features of a 3D flow is asymptotically much richer. Hence, in anticipation of numerical simulations in the subsequent chapters, it can be concluded that resolving 3D flows at high Reynolds numbers is significantly more difficult and expensive than resolving 2D flows.

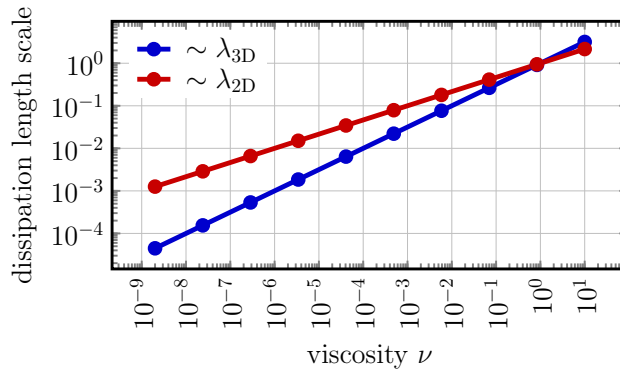


Fig. 2.2: Comparison of 2D and 3D dissipation length scales against viscosity.

2.5 Related Simplified Problems

The most obvious related simplification of the time-dependent incompressible Navier–Stokes problem (2.1) is the situation when the flow is stationary, i.e. $\partial_t \mathbf{u} = \mathbf{0}$. As a result, one obtains the stationary incompressible Navier–Stokes equations

$$\begin{cases} -\nu\Delta\mathbf{u} + (\mathbf{u}\cdot\nabla)\mathbf{u} + \nabla p = \mathbf{f} & \text{in } \Omega, \\ \nabla\cdot\mathbf{u} = 0 & \text{in } \Omega. \end{cases} \quad (2.19a)$$

$$(2.19b)$$

Due to the inertia term $(\mathbf{u}\cdot\nabla)\mathbf{u}$, this problem is still nonlinear. A linearised version can be obtained by freezing the convective velocity. Suppose that $\boldsymbol{\beta}$ is a known divergence-free velocity field, the

resulting incompressible Oseen problem then reads

$$\begin{cases} -\nu\Delta\mathbf{u} + (\boldsymbol{\beta} \cdot \nabla)\mathbf{u} + \nabla p = \mathbf{f} & \text{in } \Omega, \\ \nabla \cdot \mathbf{u} = 0 & \text{in } \Omega. \end{cases} \quad (2.20a)$$

Even more simplified is the situation where the diffusion forces $\nu\Delta\mathbf{u}$ completely dominate the inertia forces $(\mathbf{u} \cdot \nabla)\mathbf{u}$ or, equivalently, where the Reynolds number Re is small. This scenario leads to the often studied incompressible Stokes equations

$$\begin{cases} -\nu\Delta\mathbf{u} + \nabla p = \mathbf{f} & \text{in } \Omega, \\ \nabla \cdot \mathbf{u} = 0 & \text{in } \Omega. \end{cases} \quad (2.21a)$$

Remark 2.17: Concerning regularity, for the solution \mathbf{u} of the time-dependent Stokes problem

$$\begin{cases} \partial_t\mathbf{u} - \nu\Delta\mathbf{u} + \nabla p = \mathbf{0} & \text{in } (0, T) \times \Omega, \\ \nabla \cdot \mathbf{u} = 0 & \text{in } (0, T) \times \Omega. \end{cases} \quad (2.22a)$$

with inhomogeneous Dirichlet data, it has been shown that $\partial_t\mathbf{u} \in L^2(\mathbf{L}^2)$ indeed holds [CH17]. \blacktriangle

On the contrary, if viscosity effects do not play any role, the problem reduces to the incompressible Euler equations, which formally corresponds to the case $\text{Re} = \infty$ (see also Rem. 2.9):

$$\begin{cases} (\mathbf{u} \cdot \nabla)\mathbf{u} + \nabla p = \mathbf{f} & \text{in } \Omega, \\ \nabla \cdot \mathbf{u} = 0 & \text{in } \Omega. \end{cases} \quad (2.23a)$$

Inf-Sup Stable Finite Element Methods

Structure of this chapter: The various discretisation schemes which are used in this work are introduced. Mostly, the explanations are focussed on the stationary Navier–Stokes problem and its most general FE discretisation by a classical L^2 -DG method. Both $\mathbf{H}(\text{div})$ - and \mathbf{H}^1 -conforming FEM can then be characterised simply as resulting from a special choice of discrete FE spaces. Lastly, static condensation and hybridisation as techniques for improving the efficiency of high-order DG methods are introduced and applied to flow problems.

3.1	Discrete Setting	25
3.2	L^2-DG-FEM	27
	3.2.1 Classical Stokes Discretisation	28
	3.2.2 Stabilisation of Divergence-Free Constraint	31
	3.2.3 Upwind Convective Term	32
3.3	$\mathbf{H}(\text{div})$-DG-FEM	33
3.4	\mathbf{H}^1-FEM	36
3.5	Efficiency Aspects for High-Order Methods	38
	3.5.1 From DG to Hybrid DG (HDG)	39
	3.5.2 HDG Lifting Techniques	41
	3.5.3 $\mathbf{H}(\text{div})$ -HDG for Incompressible Flows	45

All computations in this thesis have been carried out using the high-order FE library `NGSolve` [Sch14], with meshes from the mesh generator `Netgen` [Sch97] – see also <https://ngsolve.org>.

3.1 Discrete Setting

In order to introduce the FE methods which are used in this work, the stationary incompressible Navier–Stokes problem (2.19) shall serve as the model problem. However, we now allow the general, possibly inhomogeneous, Dirichlet velocity boundary condition \mathbf{g}_D on $\partial\Omega$, but for the sake of presentation, analytical aspects are described only for $\mathbf{g}_D = \mathbf{0}$. With the usual adaptations, using other BCs is of course possible; see, for example, [DE12, Sec. 4.2.2]. Let $(\mathbf{V}, Q) \subset \mathbf{H}^1(\Omega) \times L^2(\Omega)$ be the appropriate velocity/pressure function spaces on the continuous level. In this work, the explanations are restricted to inf-sup stable methods since, eventually, we want to focus mainly on exactly divergence-free methods, for which inf-sup stability is mandatory.

The order of the presentation is based on the regularity across element interfaces of the particular velocity approximation: we begin with only L^2 -conformity (globally discontinuous), continue with $\mathbf{H}(\text{div})$ -DG methods (continuity of normal component) and conclude with classical \mathbf{H}^1 -conforming FEM (globally continuous). Actually, the crucial point turns out to be the continuity/discontinuity of normal and tangential velocity components across facets of the mesh; see Fig. 3.1 for a sketch.

Note that continuity of the normal component is necessary for an exactly divergence-free method.

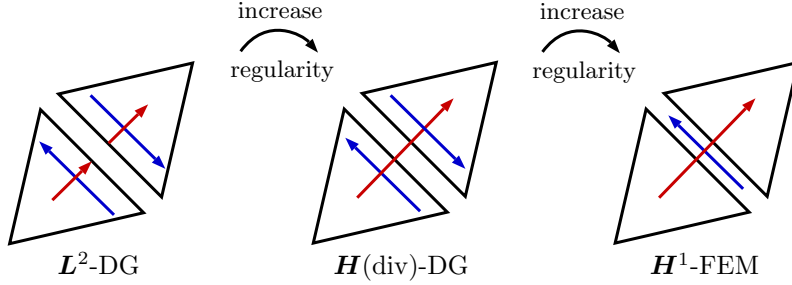


Fig. 3.1: Sketch of continuity/discontinuity of normal (red) and tangential (blue) velocity components on a 2D triangular mesh for the different methods considered in this work.

The possible choices for the pressure approximation are explained quickly, for there are only the following two basic possibilities (globally continuous and discontinuous, respectively):

$$\begin{aligned}\mathbb{P}_k &= \{v_h \in H^1(\Omega) : v_h|_K \in \mathbb{P}_k(K), \forall K \in \mathcal{T}_h\}, \\ \mathbb{P}_k^{\text{dc}} &= \{v_h \in L^2(\Omega) : v_h|_K \in \mathbb{P}_k(K), \forall K \in \mathcal{T}_h\}.\end{aligned}$$

Here, depending on the considered situation, $\mathbb{P}_k(K)$, vector-valued $\mathbb{P}_k(K)$, denotes either the local space of all polynomials on K with degree less or equal to k (simplicial mesh) or with degree less or equal to k in each variable (tensor-product elements). Note that as long as the discrete velocity is at most continuous across element interfaces, for the purpose of obtaining exactly divergence-free methods it is essential to work with a pressure space that allows for discontinuities between neighbouring elements. In case of isogeometric methods the situation is of course different; see for example [BdFS11; EH13a] for further information.

Notation: Concluding the introduction of the discrete setting, let \mathcal{T}_h be a shape-regular FE partition (either simplicial or tensor-product) of Ω without hanging nodes and mesh size $h = \max_{K \in \mathcal{T}_h} h_K$, where h_K denotes a length scale of the particular element $K \in \mathcal{T}_h$. The skeleton \mathcal{F}_h denotes the set of all facets of \mathcal{T}_h with $\mathcal{F}_K = \{F \in \mathcal{F}_h : F \subset \partial K\}$ and h_F represents a length scale of each facet $F \in \mathcal{F}_h$. Note that $h_F \leq h_K$ holds true for all $F \in \mathcal{F}_K$ and additionally, we define $N_\partial = \max_{K \in \mathcal{T}_h} \text{card}(\mathcal{F}_K)$. Moreover, $\mathcal{F}_h = \mathcal{F}_h^i \cup \mathcal{F}_h^\partial$ where \mathcal{F}_h^i is the subset of interior facets⁸ and \mathcal{F}_h^∂ collects all Dirichlet boundary facets $F \subset \partial\Omega$. To any $F \in \mathcal{F}_h$ we assign a unit normal vector \mathbf{n}_F where, for $F \in \mathcal{F}_h^\partial$, this is the outer unit normal vector \mathbf{n} . If $F \in \mathcal{F}_h^i$, there are two adjacent elements K^+ and K^- sharing the facet $F = \overline{\partial K^+} \cap \overline{\partial K^-}$ and \mathbf{n}_F points from K^+ to K^- . Let ϕ be any piecewise smooth (scalar-, vector- or matrix-valued) function with traces from within the interior of K^\pm denoted by ϕ^\pm , respectively. Then, we define the jump $[[\cdot]]_F$ and average $\{\{\cdot\}\}_F$ operator across interior facets $F \in \mathcal{F}_h^i$ by

$$[[\phi]]_F = \phi^+ - \phi^-, \quad \{\{\phi\}\}_F = \frac{1}{2}(\phi^+ + \phi^-). \quad (3.2)$$

⁸In case of periodic BCs, facets located on a periodic part of $\partial\Omega$ (not Dirichlet) are simply treated as interior facets.

For boundary facets $F \in \mathcal{F}_h^\partial$ we set $[[\phi]]_F = \{\{\phi\}\}_F = \phi$. These operators act componentwise for vector- and matrix-valued functions. Frequently, the subscript indicating the facet is omitted.

3.2 L^2 -DG-FEM

This subsection deals with ‘traditional’ DG methods and is mostly based on [DE12; Riv08]. However, we uphold the possibility of additionally adding broken grad-div and $\mathbf{H}(\text{div})$ stabilisation (also called *mass flux penalisation*) [CCQ17; DV].

The global discrete velocity/pressure spaces are given by

$$\mathbf{V}_h = \{ \mathbf{v}_h \in \mathbf{L}^2(\Omega) : \mathbf{v}_h|_K \in \mathbf{P}_k(K), \forall K \in \mathcal{T}_h \} \not\subset \mathbf{V}, \quad (3.3a)$$

$$Q_h = \mathbb{P}_{k-1}^{\text{dc}} \cap Q. \quad (3.3b)$$

As customary in DG methods, the Dirichlet boundary condition \mathbf{g}_D is not incorporated strongly in the velocity space \mathbf{V}_h but imposed weakly by means of the variational formulation itself. This FE pair is abbreviated $\mathbb{P}_k^{\text{dc}}/\mathbb{P}_{k-1}^{\text{dc}}$ and is discretely inf-sup stable; cf., for example, [Riv08, Sec. 6.4]. On tensor-product elements, the spaces $\mathbb{Q}_k^{\text{dc}}/\mathbb{Q}_{k-1}^{\text{dc}}$ are used instead.

Remark 3.1: Note that on simplicial meshes, locally we have the important property $\nabla_h \cdot \mathbb{P}_k^{\text{dc}} \subset \mathbb{P}_{k-1}^{\text{dc}}$. On tensor-product meshes, on the other hand, $\nabla_h \cdot \mathbb{Q}_k^{\text{dc}} \not\subset \mathbb{Q}_{k-1}^{\text{dc}}$, which creates an additional obstacle to handle in the analysis. \blacktriangle

Remark 3.2 (Discrete inverse inequality): It is well-known that for shape-regular decompositions \mathcal{T}_h , the discrete space \mathbf{V}_h satisfies the local inverse inequality [EG04, Lem. 1.138]

$$\forall \mathbf{v}_h \in \mathbf{V}_h: \quad \|\mathbf{v}_h\|_{\mathbf{W}^{\ell,p}(K)} \leq Ch_K^{m-\ell+d\left(\frac{1}{p}-\frac{1}{q}\right)} \|\mathbf{v}_h\|_{\mathbf{W}^{m,q}(K)}, \quad \forall K \in \mathcal{T}_h, \quad (3.4)$$

where $0 \leq m \leq \ell$ are natural numbers and $p, q \in [1, \infty]$. Such an estimate is needed for some technicalities later on. \blacktriangle

For approximating (2.19), the following DG method with broken grad-div and $\mathbf{H}(\text{div})$ stabilisation (parameter $\gamma \geq 0$) is considered:

$$\left\{ \begin{array}{l} \text{Find } (\mathbf{u}_h, p_h) \in \mathbf{V}_h \times Q_h \text{ such that, } \forall (\mathbf{v}_h, q_h) \in \mathbf{V}_h \times Q_h, \\ \nu a_h(\mathbf{u}_h, \mathbf{v}_h) + c_h(\mathbf{u}_h; \mathbf{u}_h, \mathbf{v}_h) + \gamma j_h(\mathbf{u}_h, \mathbf{v}_h) + b_h(\mathbf{v}_h, p_h) + b_h(\mathbf{u}_h, q_h) \\ = (\mathbf{f}, \mathbf{v}_h) + \nu a_h^\partial(\mathbf{g}_D; \mathbf{v}_h) + c_h^\partial(\mathbf{g}_D; \mathbf{u}_h, \mathbf{v}_h) + \gamma j_h^\partial(\mathbf{g}_D; \mathbf{v}_h) + b_h^\partial(\mathbf{g}_D, q_h). \end{array} \right. \quad (3.5a)$$

$$\quad (3.5b)$$

$$\quad (3.5c)$$

Let us now describe each of the terms appearing in the discrete weak formulation (3.5) separately. Also, their most important properties and corresponding norms are introduced for $\mathbf{g}_D = \mathbf{0}$.

We make use of the broken vector-valued Sobolev space

$$\mathbf{H}^m(\mathcal{T}_h) = \{ \mathbf{v} \in \mathbf{L}^2(\Omega) : \mathbf{v}|_K \in \mathbf{H}^m(K), \forall K \in \mathcal{T}_h \},$$

and define the (elementwise) broken gradient $\nabla_h: \mathbf{H}^1(\mathcal{T}_h) \rightarrow \mathbf{L}^2(\Omega)$ by $(\nabla_h \mathbf{v})|_K = \nabla(\mathbf{v}|_K)$ for all $K \in \mathcal{T}_h$ and the (elementwise) broken divergence $\nabla_h \cdot: \mathbf{H}^1(\mathcal{T}_h) \rightarrow L^2(\Omega)$ by $(\nabla_h \cdot \mathbf{v})|_K = \nabla \cdot (\mathbf{v}|_K)$ for all $K \in \mathcal{T}_h$.

The appearance below of certain traces of velocity facet values, and their normal derivatives, leads to the technical assumption that the involved velocities belong (at least) to $\mathbf{H}^{\frac{3}{2}+\varepsilon}(\mathcal{T}_h)$ for some $\varepsilon > 0$; cf. [Riv08, Sec. 2.1.3]. Relaxing this assumption is in general possible [Gud10], but beyond the scope of this work. We thus define the compound space

$$\mathbf{V}(h) = \mathbf{V}_h \oplus \left[\mathbf{V} \cap \mathbf{H}^{\frac{3}{2}+\varepsilon}(\mathcal{T}_h) \right].$$

Remark 3.3 (Discrete trace inequality): For $C_{\text{tr}} > 0$, independent of the mesh size h (but dependent on k), the following discrete trace inequality is valid on \mathbf{V}_h ; cf. [DE12, Rem. 1.47]:

$$\forall \mathbf{v}_h \in \mathbf{V}_h: \quad \|\mathbf{v}_h\|_{\mathbf{L}^2(\partial K)}^2 \leq C_{\text{tr}}^2 h_K^{-1} \|\mathbf{v}_h\|_{\mathbf{L}^2(K)}^2, \quad \forall K \in \mathcal{T}_h. \quad (3.6)$$

Note that the parameter C_{tr} usually scales with k^2 ; cf., for example, [DE12, Rem 1.48]. In Sec. 7.3.1, an exact expression is provided in the special context of hyperrectangles. \blacktriangle

Remark 3.4 (Approximation properties): Concerning optimal polynomial approximation properties, the following estimates are well-known [DE12, Sec. 1.4.4]. There exists a velocity approximation operator $\mathbf{j}_h: \mathbf{V} \rightarrow \mathbf{V}_h$ such that, for all $\mathbf{v} \in \mathbf{H}^r(\Omega)$ with $r > 3/2$ and $r_u = \min\{r, k+1\}$ the estimate

$$\|\mathbf{v} - \mathbf{j}_h \mathbf{v}\|_{\mathbf{L}^2(K)} + h_K \|\mathbf{v} - \mathbf{j}_h \mathbf{v}\|_{\mathbf{H}^1(K)} \leq Ch_K^{r_u} |\mathbf{v}|_{\mathbf{H}^{r_u}(K)}, \quad \forall K \in \mathcal{T}_h$$

holds. A consequence of this estimate, together with a continuous trace inequality, is the ability to bound polynomial approximation errors on facets:

$$\|\mathbf{v} - \mathbf{j}_h \mathbf{v}\|_{\mathbf{L}^2(F)} + h_K \|\nabla(\mathbf{v} - \mathbf{j}_h \mathbf{v}) \mathbf{n}_K\|_{\mathbf{L}^2(F)} \leq Ch_K^{r_u - \frac{1}{2}} |\mathbf{v}|_{\mathbf{H}^{r_u}(K)}, \quad \forall F \in \mathcal{F}_K, K \in \mathcal{T}_h.$$

Concerning the pressure, the local orthogonal L^2 -projection $\pi_0: L^2(K) \rightarrow \mathbb{P}_\ell(K)$ fulfils

$$\|q - \pi_0 q\|_{L^2(K)} \leq Ch_K^{r_p} |q|_{\mathbf{H}^{r_p}(K)}, \quad \forall K \in \mathcal{T}_h,$$

for all $q \in Q \cap H^s(\Omega)$ with $s \geq 1$ and $r_p = \min\{s, \ell+1\}$. \blacktriangle

3.2.1 Classical Stokes Discretisation

We consider the standard symmetric interior penalty (SIP) method with a jump penalisation parameter $\lambda > 0$ sufficiently large to guarantee the discrete coercivity estimates below, and define the

following bilinear form $a_h: \mathbf{V}(h) \times \mathbf{V}_h \rightarrow \mathbb{R}$ and linear form $a_h^\partial: \mathbf{V}_h \rightarrow \mathbb{R}$:

$$a_h(\mathbf{w}, \mathbf{v}_h) := \int_{\Omega} \nabla_h \mathbf{w} : \nabla_h \mathbf{v}_h \, d\mathbf{x} + \sum_{F \in \mathcal{F}_h} \frac{\lambda}{h_F} \int_F \llbracket \mathbf{w} \rrbracket \cdot \llbracket \mathbf{v}_h \rrbracket \, ds \quad (3.7a)$$

$$- \sum_{F \in \mathcal{F}_h} \int_F \{ \nabla_h \mathbf{w} \} \mathbf{n}_F \cdot \llbracket \mathbf{v}_h \rrbracket \, ds - \sum_{F \in \mathcal{F}_h} \int_F \llbracket \mathbf{w} \rrbracket \cdot \{ \nabla_h \mathbf{v}_h \} \mathbf{n}_F \, ds, \quad (3.7b)$$

$$a_h^\partial(\mathbf{g}_D; \mathbf{v}_h) := \sum_{F \in \mathcal{F}_h^\partial} \frac{\lambda}{h_F} \int_F \mathbf{g}_D \cdot \mathbf{v}_h \, ds - \sum_{F \in \mathcal{F}_h^\partial} \int_F \mathbf{g}_D \cdot (\nabla_h \mathbf{v}_h) \mathbf{n}_F \, ds. \quad (3.7c)$$

Here, $[\nabla \mathbf{w}]_{ij} = \frac{\partial w_i}{\partial x_j}$ denotes the entries of the Jacobian. In fact, we assume that $\lambda \geq 1$, which is reasonable as the choice of this parameter depends on C_{tr} , which, in turn, scales with k^2 ; cf. [DE12, Lem. 4.12, Rem. 1.48]. This behaviour is mainly a consequence of the k -dependency of the discrete trace inequality (3.6); see Rem. 3.3 and, for example, [Hil13] for more details on this topic. Corresponding to the SIP discretisation with either $\mathbf{g}_D = \mathbf{0}$ or periodic BCs, the following viscous energy norms are used:

$$\forall \mathbf{w} \in \mathbf{V}(h): \quad \|\mathbf{w}\|_e^2 := \|\nabla_h \mathbf{w}\|_{L^2}^2 + \sum_{F \in \mathcal{F}_h} h_F^{-1} \|\llbracket \mathbf{w} \rrbracket\|_{L^2(F)}^2, \quad (3.8a)$$

$$\|\mathbf{w}\|_{e,\sharp}^2 := \|\mathbf{w}\|_e^2 + \sum_{K \in \mathcal{T}_h} h_K \|(\nabla_h \mathbf{w}) \mathbf{n}_K\|_{L^2(\partial K)}^2. \quad (3.8b)$$

As the analysis in this work only deals with the case $\mathbf{g}_D = \mathbf{0}$, we restrict the subsequent presentation of norms and estimates to the no-slip situation. However, an extension to $\mathbf{g}_D \neq \mathbf{0}$ is straightforward and does not pose any essential problems.

Remark 3.5: Depending on the particular literature, sometimes the SIP penalty parameter λ is also included in the norm $\|\cdot\|_e$ defined in (3.8a). We find it more natural to not include λ in the norm; nevertheless, including it only changes the involved constants. The stronger norm $\|\cdot\|_{e,\sharp}$, defined in (3.8b), can be used conveniently in the analysis. However, both norms are uniformly equivalent on \mathbf{V}_h , which means that there exists $C > 0$ such that $C \|\mathbf{v}_h\|_{e,\sharp} \leq \|\mathbf{v}_h\|_e \leq \|\mathbf{v}_h\|_{e,\sharp}$ for all $\mathbf{v}_h \in \mathbf{V}_h$; cf., for example, [DE12, Lem. 4.20] (scalar-valued case). \blacktriangle

The key ingredients for the numerical analysis of the diffusion term are discrete coercivity and boundedness [Bra07, Ch. II, § 2].

Lemma 3.6 (Discrete coercivity and boundedness of a_h)

Assume that $\lambda > 1$ is sufficiently large (dep. on C_{tr}). Then, the SIP bilinear form a_h is coercive on \mathbf{V}_h w.r.t. the energy norm $\|\cdot\|_e$. That is, there exists $C_\lambda > 0$, independent of h , such that,

$$\forall \mathbf{v}_h \in \mathbf{V}_h: \quad a_h(\mathbf{v}_h, \mathbf{v}_h) \geq C_\lambda \|\mathbf{v}_h\|_e^2.$$

Furthermore, there exists $M > 0$, independent of h , such that

$$\forall (\mathbf{w}, \mathbf{v}_h) \in \mathbf{V}(h) \times \mathbf{V}_h: \quad |a_h(\mathbf{w}, \mathbf{v}_h)| \leq M \|\mathbf{w}\|_{e,\sharp} \|\mathbf{v}_h\|_e.$$

Proof: Cf., for example, [DE12, Sec. 6.1.2.1] or [Riv08, Lem. 6.6] for discrete coercivity. For boundedness, a scalar-valued analogue is proven, for example, in [DE12, Sec. 4.2.3]. ■

The discrete pressure-velocity coupling is defined using $b_h: \mathbf{V}(h) \times Q \rightarrow \mathbb{R}$ and $b_h^\partial: Q \rightarrow \mathbb{R}$ [MFH08]:

$$b_h(\mathbf{w}, q_h) := - \int_{\Omega} q_h (\nabla_h \cdot \mathbf{w}) \, d\mathbf{x} + \sum_{F \in \mathcal{F}_h} \int_F \{q_h\} (\llbracket \mathbf{w} \rrbracket \cdot \mathbf{n}_F) \, d\mathbf{s},$$

$$b_h^\partial(\mathbf{g}_D; q_h) := \sum_{F \in \mathcal{F}_h^\partial} \int_F q_h (\mathbf{g}_D \cdot \mathbf{n}) \, d\mathbf{s}.$$

It is known that the FE pair $\mathbb{P}_k^{\text{dc}} / \mathbb{P}_{k-1}^{\text{dc}}$ is discretely inf-sup stable; cf., for example, [Riv08]. Thus, there exists $\beta^* > 0$, independent of the mesh size h , such that

$$\inf_{q_h \in Q_h \setminus \{0\}} \sup_{\mathbf{v}_h \in \mathbf{V}_h \setminus \{0\}} \frac{b_h(\mathbf{v}_h, q_h)}{\|\mathbf{v}_h\|_e \|q_h\|_{L^2}} \geq \beta^*. \quad (3.9)$$

A well-known consequence of (3.9) (together with the closed-range theorem) is that the set of discretely divergence-free functions is non-empty [GR86]; that is,

$$\mathbf{V}_h^{\text{div}} = \{\mathbf{v}_h \in \mathbf{V}_h : b_h(\mathbf{v}_h, q_h) = 0, \forall q_h \in Q_h\} \neq \emptyset.$$

Every discretely inf-sup stable FEM for the incompressible (Navier–)Stokes problem is intrinsically connected to a particular discrete Helmholtz projector; see Sec. 2.2.3 for the continuous case. The general definition of the discrete Helmholtz projector \mathbb{P}_h of a vector field $\mathbf{g} \in \mathbf{L}^2$ is given by

$$\mathbb{P}_h: \mathbf{L}^2(\Omega) \rightarrow \mathbf{V}_h^{\text{div}}, \quad \mathbb{P}_h(\mathbf{g}) = \arg \min_{\mathbf{v}_h \in \mathbf{V}_h^{\text{div}}} \|\mathbf{g} - \mathbf{v}_h\|_{\mathbf{L}^2(\Omega)}, \quad \int_{\Omega} [\mathbb{P}_h(\mathbf{g}) - \mathbf{g}] \cdot \mathbf{v}_h \, d\mathbf{x} = 0, \quad \forall \mathbf{v}_h \in \mathbf{V}_h^{\text{div}}.$$

Equivalently, one can discretise (2.11) with a suitable finite element method. In order to accomplish this, the already known pressure-velocity coupling form b_h and additionally, a mass bilinear form defined by $m_h(\mathbf{u}_h, \mathbf{v}_h) = \int_{\Omega} \mathbf{u}_h \cdot \mathbf{v}_h \, d\mathbf{x}$ can be used to obtain the following FE problem [DVII]:

$$\begin{cases} \text{Find } (\mathbb{P}_h(\mathbf{g}), \phi_h) \in \mathbf{V}_h \times Q_h \text{ s.t., } \forall (\mathbf{v}_h, q_h) \in \mathbf{V}_h \times Q_h, & (3.10a) \\ m_h(\mathbb{P}_h(\mathbf{g}), \mathbf{v}_h) + b_h(\mathbf{v}_h, \phi_h) + b_h(\mathbb{P}_h(\mathbf{g}), q_h) = (\mathbf{g}, \mathbf{v}_h). & (3.10b) \end{cases}$$

Choosing \mathbf{V}_h according to the \mathbf{L}^2 -DG choice (3.3), the resulting discrete Helmholtz projector is denoted by \mathbb{P}_h^0 . Note that in general, $\nabla_h \cdot \mathbb{P}_h^0(\mathbf{g}) \neq 0$ since $\mathbb{P}_h^0(\mathbf{g})$ is only discretely divergence-free.

Unfortunately, it turns out that, compared to the continuous case in Cor. 2.11, the \mathbf{L}^2 -DG Helmholtz projector has the following major shortcoming.

Lemma 3.7

For the \mathbf{L}^2 -DG method (3.10) with $k_p = k - 1$, for all gradient fields $\nabla \phi$ with $\phi \in H^{k_p+1}(\Omega)$, it only holds

$$\|\mathbb{P}_h^0(\nabla \phi)\|_{\mathbf{L}^2} \leq Ch^{k_p} |\phi|_{H^{k_p+1}}.$$

Proof: See [DVII, Lem. 6.3]. ■

3.2.2 Stabilisation of Divergence-Free Constraint

Let us give a brief motivation for additionally stabilising the divergence-free constraint in this DG setting; see also [DV]. Following [JL⁺17; Sal16], recall that the *distributional divergence* of a vector field $\mathbf{v} \in \mathbf{L}^2(\Omega)$ is defined as the mapping $C_0^\infty(\Omega) \rightarrow \mathbb{R}$ given by

$$\phi \mapsto - \int_{\Omega} \nabla \phi \cdot \mathbf{v} \, d\mathbf{x}.$$

If this integral vanishes for all $\phi \in C_0^\infty(\Omega)$, i.e. if \mathbf{v} is $\mathbf{L}^2(\Omega)$ -orthogonal to all smooth gradient fields, \mathbf{v} is called *weakly divergence-free*. Suppose that we want to consider the distributional divergence of a FE function $\mathbf{v}_h \in \mathbf{V}_h$. Then, integration by parts⁹ leads to

$$\phi \mapsto - \int_{\Omega} \nabla \phi \cdot \mathbf{v}_h \, d\mathbf{x} = \int_{\Omega} \phi (\nabla_h \cdot \mathbf{v}_h) \, d\mathbf{x} - \sum_{F \in \mathcal{F}_h} \int_F \phi (\llbracket \mathbf{v}_h \rrbracket \cdot \mathbf{n}_F) \, ds.$$

Unfortunately, the pressure-velocity coupling b_h ensures $\mathbf{L}^2(\Omega)$ -orthogonality only with respect to discrete pressures $\phi \in Q_h$ (discrete divergence-free property), which is not enough in many situations. Therefore, the distributional divergence of \mathbf{v}_h vanishes only provided that $\nabla_h \cdot \mathbf{v}_h = 0$ and $\llbracket \mathbf{v}_h \rrbracket \cdot \mathbf{n}_F = 0$ for all $F \in \mathcal{F}_h$. A setting in which this holds exactly will be provided by divergence-free $\mathbf{H}(\text{div})$ -conforming approximations in Sec. 3.3.

However, as a tradeoff for L^2 -DG methods, one can introduce the following stabilisation which leads to a discrete velocity which may fulfil the elementwise divergence-free constraint and normal-continuity property across inter-element facets *more accurately*. The terms which realise broken grad-div and $\mathbf{H}(\text{div})$ stabilisation are defined by $j_h: \mathbf{V}(h) \times \mathbf{V}_h \rightarrow \mathbb{R}$ and $j_h^\partial: \mathbf{V}_h \rightarrow \mathbb{R}$, respectively:

$$\begin{aligned} j_h(\mathbf{w}, \mathbf{v}_h) &:= \int_{\Omega} (\nabla_h \cdot \mathbf{w})(\nabla_h \cdot \mathbf{v}_h) \, d\mathbf{x} + \sum_{F \in \mathcal{F}_h} h_F^{-1} \int_F (\llbracket \mathbf{w} \rrbracket \cdot \mathbf{n}_F)(\llbracket \mathbf{v}_h \rrbracket \cdot \mathbf{n}_F) \, ds, \\ j_h^\partial(\mathbf{g}_D; \mathbf{v}_h) &:= \sum_{F \in \mathcal{F}_h^\partial} h_F^{-1} \int_F (\mathbf{g}_D \cdot \mathbf{n})(\mathbf{v}_h \cdot \mathbf{n}) \, ds. \end{aligned}$$

For brevity (and for reasons which will become clear in the numerical analysis), this stabilisation is also called ‘DG-grad-div’. For all $\mathbf{w} \in \mathbf{V}(h)$ and either $\mathbf{g}_D = \mathbf{0}$ or periodic BCs, we introduce the normal jump seminorm

$$|\mathbf{w}|_{\text{nj}}^2 := \sum_{F \in \mathcal{F}_h} h_F^{-1} \int_F (\llbracket \mathbf{w} \rrbracket \cdot \mathbf{n}_F)^2 \, ds = \sum_{F \in \mathcal{F}_h} h_F^{-1} \|\llbracket \mathbf{w} \rrbracket \cdot \mathbf{n}_F\|_{L^2(F)}^2, \quad (3.11)$$

and note that comparing (3.8a) and (3.11), one directly obtains $|\mathbf{v}_h|_{\text{nj}} \leq \|\mathbf{v}_h\|_e$ for all $\mathbf{v}_h \in \mathbf{V}_h$.

It is straightforward to show that the stabilisation term j_h is a dissipative mechanism.

⁹This is actually the same procedure as in the derivation of the pressure-velocity coupling term b_h [Riv08].

Lemma 3.8 (*Dissipativity of j_h*)

The stabilisation form j_h has the following non-negativity property:

$$\forall \mathbf{v}_h \in \mathbf{V}_h: \quad j_h(\mathbf{v}_h, \mathbf{v}_h) = \|\nabla_h \cdot \mathbf{v}_h\|_{L^2}^2 + |\mathbf{v}_h|_{\text{nj}}^2.$$

Remark 3.9 (History of DG-grad-div): In the context of DG methods, the broken grad-div stabilisation $(\nabla_h \cdot \mathbf{u}_h, \nabla_h \cdot \mathbf{v}_h)$ has been used for the first time in [DI], where it has been shown that even this incomplete stabilisation can improve poor mass conservation for both inf-sup stable $\mathbb{Q}_k^{\text{dc}}/\mathbb{Q}_{k-1}^{\text{dc}}$ and equal-order methods $\mathbb{Q}_k^{\text{dc}}/\mathbb{Q}_k^{\text{dc}}$ on tensor-product meshes in practical applications of non-isothermal flows. Furthermore, [KF⁺17] shows that in DG methods the mass balance across interior facets has to be accounted for *in addition* to the broken grad-div stabilisation, but no rigorous justification by means of numerical analysis is given. Therefore, also providing a theoretical explanation why using j_h can dramatically improve results, the connection between this stabilisation and pressure-robustness has been analysed in detail in [DV]. \blacktriangle

3.2.3 Upwind Convective Term

The last physical mechanism which has to be dealt with are inertia forces. In the Navier–Stokes problem (2.19), these are represented by the nonlinear convection term $(\mathbf{u} \cdot \nabla)\mathbf{u}$. Following [DE12], a suitable discretisation is given by the terms $c_h: \mathbf{V}(h) \times \mathbf{V}(h) \times \mathbf{V}_h \rightarrow \mathbb{R}$ and $c_h^\partial: \mathbf{V}(h) \times \mathbf{V}_h \rightarrow \mathbb{R}$ with upwinding ($\theta = 1$) or without upwinding ($\theta = 0$):

$$\begin{aligned} c_h(\boldsymbol{\beta}; \mathbf{w}, \mathbf{v}_h) &:= \int_{\Omega} (\boldsymbol{\beta} \cdot \nabla_h) \mathbf{w} \cdot \mathbf{v}_h \, dx + \frac{1}{2} \int_{\Omega} (\nabla_h \cdot \boldsymbol{\beta}) \mathbf{w} \cdot \mathbf{v}_h \, dx \\ &\quad - \sum_{F \in \mathcal{F}_h^i} \int_F (\{\{\boldsymbol{\beta}\}\} \cdot \mathbf{n}_F) [\mathbf{w}] \cdot \{\{\mathbf{v}_h\}\} \, ds - \frac{1}{2} \sum_{F \in \mathcal{F}_h} \int_F ([\boldsymbol{\beta}] \cdot \mathbf{n}_F) \{\{\mathbf{w} \cdot \mathbf{v}_h\}\} \, ds \\ &\quad + \theta \sum_{F \in \mathcal{F}_h^i} \int_F \frac{1}{2} |\{\{\boldsymbol{\beta}\}\} \cdot \mathbf{n}_F| [\mathbf{w}] \cdot [\mathbf{v}_h] \, ds, \\ c_h^\partial(\mathbf{g}_D; \mathbf{w}, \mathbf{v}_h) &:= -\frac{1}{2} \sum_{F \in \mathcal{F}_h^\partial} \int_F (\mathbf{g}_D \cdot \mathbf{n}) (\mathbf{w} \cdot \mathbf{v}_h) \, ds. \end{aligned}$$

Note that this discrete term is tailored in such a way that whenever $\theta = 0$, $c_h(\boldsymbol{\beta}; \mathbf{v}_h, \mathbf{v}_h) + c_h^\partial(\mathbf{g}_D; \mathbf{v}_h, \mathbf{v}_h) = 0$ holds for all $\mathbf{v}_h \in \mathbf{V}_h$. This skew-symmetry property ensures energy-stability as the resulting discrete realisation of the convective term (without upwinding) does not interfere with the discrete energy balance.

Remark 3.10 (Upwinding): An equivalent formulation for the above discrete convective term can be found in [Riv08, Sec. 7.3.1]. Writing it in such a way as in the monograph [Riv08] (compared to [DE12]), the relationship between the DG upwind mechanism and upwinding in the context of finite volume methods is much more apparent. However, we prefer the definition of upwinding as in (3.12) because of its simplicity (the two occurring facet terms have the same structure). This especially makes numerical analysis more compact. \blacktriangle

In this work, upwinding is the only convection stabilisation which may be used for convection-dominated (high Reynolds number) problems. Thus, the typical DG upwinding is based on at least some discontinuity in the corresponding velocity field; we do not discuss or incorporate convection stabilisation in the classical \mathbf{H}^1 -conforming framework. Moreover, in order to emphasise the impact of the upwind term, we introduce the upwind seminorm

$$\forall \mathbf{w} \in \mathbf{V}(h): \quad |\mathbf{w}|_{\beta, \text{upw}}^2 := \sum_{F \in \mathcal{F}_h^i} \int_F \frac{1}{2} |\{\!\!\{ \beta \}\!\!\} \cdot \mathbf{n}_F| |\llbracket \mathbf{w} \rrbracket|^2 \, ds. \quad (3.13)$$

Remark 3.11 (Exact numerical integration): Referring to the convection term c_h , let us comment on the topic of exact numerical integration. On simplicial meshes the \mathbf{P}_k^{dc} element leads to a polynomial of degree $3k - 1$ as the integrand of the volume integral; on tensor-product meshes, \mathbf{Q}_k^{dc} generally leads to a polynomial of degree $3k$. Concerning the integrand of the facet integral, we have order $3k$ on both simplices and tensor-product elements. The effects of not integrating exactly are sometimes grouped under ‘under-integration’; cf., for example, [BF⁺16; Kop17]. \blacktriangle

The following lemma shows energy stability of the \mathbf{L}^2 -DG method with this convection term and that upwinding is a purely dissipative mechanism (non-negativity).

Lemma 3.12 (Discrete coercivity of c_h)

The convective form c_h is coercive on \mathbf{V}_h w.r.t. the upwind seminorm. That is, for all $\mathbf{w} \in \mathbf{V}(h)$,

$$c_h(\mathbf{w}; \mathbf{v}_h, \mathbf{v}_h) = \theta |\mathbf{v}_h|_{\mathbf{w}, \text{upw}}^2, \quad \forall \mathbf{v}_h \in \mathbf{V}_h.$$

Proof: Cf., for example, [DE12, Sec. 6.2]. \blacksquare

3.3 $\mathbf{H}(\text{div})$ -DG-FEM

When the underlying FE space guarantees that the normal component of the resulting discrete velocity is normal-continuous, we are dealing with $\mathbf{H}(\text{div})$ -conforming methods.

Lemma 3.13 (Characterisation of $\mathbf{H}(\text{div}; \Omega)$)

Let $\mathbf{w} \in \mathbf{H}^1(\mathcal{T}_h)$. If $\llbracket \mathbf{w} \rrbracket_F \cdot \mathbf{n}_F = 0$ for all $F \in \mathcal{F}_h^i$, then $\mathbf{w} \in \mathbf{H}(\text{div}; \Omega)$.

Proof: Cf., for example, [DE12, Lem. 1.24]. \blacksquare

The global $\mathbf{H}(\text{div})$ -DG velocity space can then be defined as

$$\mathbf{V}_h = \left\{ \mathbf{v}_h \in \mathbf{H}(\text{div}; \Omega) : \mathbf{v}_h|_K \in \mathbf{V}_k(K), \forall K \in \mathcal{T}_h; \mathbf{v}_h \cdot \mathbf{n}|_{\partial\Omega} = \mathbf{g}_D^h \cdot \mathbf{n}|_{\partial\Omega} \right\} \not\subset \mathbf{V}, \quad (3.14)$$

where \mathbf{g}_D^h denotes a projection of \mathbf{g}_D into the corresponding FE space. Contrary to \mathbf{L}^2 -DG methods, the normal component of the Dirichlet BC \mathbf{g}_D is imposed strongly in \mathbf{V}_h ; the local velocity space $\mathbf{V}_k(K)$ is a set of vector-valued piecewise polynomials of order $k \geq 1$. In the following, the particular choices for $\mathbf{V}_k(K)$ which are relevant in this thesis are introduced; see also [BBF13].

On simplicial meshes, the Brezzi–Douglas–Marini (BDM) element results from choosing the full polynomial space $\mathbf{V}_k(K) = \mathbb{P}_k(K)$ and the abbreviation \mathbf{BDM}_k shall be used. On tensor-product meshes, on the other hand, we use the Raviart–Thomas (RT) element which is defined as

$$\mathbf{V}_k(K) = \begin{cases} (\mathbb{P}_{k+1,k}(K), \mathbb{P}_{k,k+1}(K))^\dagger, & \text{for } d = 2, \\ (\mathbb{P}_{k+1,k,k}(K), \mathbb{P}_{k,k+1,k}(K), \mathbb{P}_{k,k,k+1}(K))^\dagger, & \text{for } d = 3. \end{cases}$$

Here, denoting by ψ_i 1D polynomials of order $i \in \mathbb{N}_0$, each velocity component locally has the following tensor-product structure (exemplarily for 2D):

$$\mathbb{P}_{k_1,k_2}(K) = \text{span} \left\{ \sum_{i=0}^{k_1} \sum_{j=0}^{k_2} \psi_i(x_1) \psi_j(x_2), \quad (x_1, x_2) \in K \right\}.$$

For the resulting global velocity space, the abbreviation $\mathbf{RT}_{[k]}$ is frequently used.

Regardless of whether RT or BDM elements are used, the particular pressure space $Q_h = \mathbb{P}_\ell^{\text{dc}} \cap Q$, $\ell \in \{k-1, k\}$, for $\mathbf{H}(\text{div})$ -DG methods is chosen such that $\nabla \cdot \mathbf{V}_h = Q_h$ holds true. In particular this means that $\ell = k-1$ is used on simplicials whereas $\ell = k$ is the proper choice on tensor-product meshes. The resulting FE pairs are dubbed $\mathbf{BDM}_k / \mathbb{P}_{k-1}^{\text{dc}}$ and $\mathbf{RT}_{[k]} / \mathbb{P}_k^{\text{dc}}$.

Formally, inserting either of those new FE pairs into (3.5) already describes the $\mathbf{H}(\text{div})$ -DG method. After some simplifications which are explained further afterwards, the $\mathbf{H}(\text{div})$ -DG method is defined by the following weak formulation [CKS05; CKS07]:

$$\left\{ \text{Find } (\mathbf{u}_h, p_h) \in \mathbf{V}_h \times Q_h \text{ such that, } \forall (\mathbf{v}_h, q_h) \in \mathbf{V}_h \times Q_h, \right. \quad (3.15a)$$

$$\left. \nu a_h(\mathbf{u}_h, \mathbf{v}_h) + c_h(\mathbf{u}_h; \mathbf{u}_h, \mathbf{v}_h) + b(\mathbf{v}_h, p_h) + b(\mathbf{u}_h, q_h) = (\mathbf{f}, \mathbf{v}_h) + \nu a_h^\partial(\mathbf{g}_D; \mathbf{v}_h). \right. \quad (3.15b)$$

This method is also discretely inf-sup stable (see, for example, [Riv08, Sec. 6.4]) which means that there exists $\beta^* > 0$, independent of the mesh size h , such that

$$\inf_{q_h \in Q_h \setminus \{0\}} \sup_{\mathbf{v}_h \in \mathbf{V}_h \setminus \{0\}} \frac{b(\mathbf{v}_h, q_h)}{\|\mathbf{v}_h\|_e \|q_h\|_{L^2}} \geq \beta^*.$$

A special property of the method (3.15) is that the inf-sup constant β^* is robust w.r.t. the polynomial order k ; cf. [LS18] for a rigorous analysis in 2D. Furthermore, the property $\nabla \cdot \mathbf{V}_h = Q_h$ allows to test with $q_h = \nabla \cdot \mathbf{u}_h$, which results in the desirable fact that we are obtaining an exactly divergence-free discrete velocity solution as

$$\int_{\Omega} q_h (\nabla \cdot \mathbf{u}_h) \, d\mathbf{x} = 0, \quad \forall q_h \in Q_h \quad \Rightarrow \quad \int_{\Omega} |\nabla \cdot \mathbf{u}_h|^2 \, d\mathbf{x} = 0 \quad \Rightarrow \quad \nabla \cdot \mathbf{u}_h = 0. \quad (3.16)$$

In other words, discretely divergence-free functions $\mathbf{v}_h \in \mathbf{V}_h^{\text{div}}$ are simultaneously exactly divergence-free. Concerning the discrete Helmholtz projection which comes with the $\mathbf{H}(\text{div})$ -DG method, choosing \mathbf{V}_h according to (3.14) in (3.10), the resulting projector $\mathbb{P}_h^{\text{div}}$ fulfils $\nabla \cdot \mathbb{P}_h^{\text{div}}(\mathbf{g}) = 0$. For-

tunately, the $\mathbf{H}(\text{div})$ -DG Helmholtz projector behaves similarly as the continuous one in Cor. 2.11 concerning gradient fields (note the difference compared to the \mathbf{L}^2 -DG case in Lem. 3.7).

Lemma 3.14

For the $\mathbf{H}(\text{div})$ -DG method, for all gradient fields $\nabla\phi$ with $\phi \in H^1(\Omega)$, it holds

$$\mathbb{P}_h^{\text{div}}(\nabla\phi) = \mathbf{0}.$$

Proof: From $\mathbf{v}_h \in \mathbf{V}_h^{\text{div}}$ it follows $\nabla \cdot \mathbf{v}_h = 0$ pointwise. Thus, for any $\nabla\phi \in \mathbf{L}^2(\Omega)$ it holds

$$\left(\mathbb{P}_h^{\text{div}}(\nabla\psi), \mathbf{v}_h \right) = (\nabla\psi, \mathbf{v}_h) = -(\psi, \nabla \cdot \mathbf{v}_h) = 0, \quad \forall \mathbf{v}_h \in \mathbf{V}_h^{\text{div}}.$$

Thus, the claim is proven. \blacksquare

Note that compared to the \mathbf{L}^2 -DG method (3.5), the $\mathbf{H}(\text{div})$ -DG method exploits normal-continuity and the exactly divergence-free property to induce a number of simplifications in the involved terms. Firstly, the pressure-velocity coupling b of an $\mathbf{H}(\text{div})$ -DG method coincides with the one from the continuous problem as for all $\mathbf{v}_h \in \mathbf{V}_h$, $[[\mathbf{v}_h]] \cdot \mathbf{n}_F = 0$ for all $F \in \mathcal{F}_h^i$ and $\mathbf{u}_h \cdot \mathbf{n} = \mathbf{g}_D^h \cdot \mathbf{n}$ on $\partial\Omega$. Secondly, the grad-div stabilisation and mass flux penalisation term j_h is superfluous due to normal-continuity and $\nabla \cdot \mathbf{u}_h = 0$. Thirdly, using both properties in the (upwind) convection term, we obtain the simplified form $c_h: \mathbf{V}(h) \times \mathbf{V}(h) \times \mathbf{V}_h \rightarrow \mathbb{R}$ with

$$c_h(\boldsymbol{\beta}; \mathbf{w}, \mathbf{v}_h) = \int_{\Omega} (\boldsymbol{\beta} \cdot \nabla_h) \mathbf{w} \cdot \mathbf{v}_h \, dx - \sum_{F \in \mathcal{F}_h^i} \int_F \left[(\boldsymbol{\beta} \cdot \mathbf{n}_F) [[\mathbf{w}]] \cdot \{\{\mathbf{v}_h\}\} - \frac{\theta}{2} |\boldsymbol{\beta} \cdot \mathbf{n}_F| [[\mathbf{w}]] \cdot [[\mathbf{v}_h]] \right] ds. \quad (3.17)$$

Remark 3.15 (Exact numerical integration): Referring to the convection term (3.17), note that on simplicial meshes the \mathbf{BDM}_k element leads to a polynomial of degree $3k - 1$ as the integrand of the volume integral while on tensor-product meshes, $\mathbf{RT}_{[k]}$ generally leads to a polynomial of degree $3k + 3$. Concerning the integrand of the facet integral, we are dealing with order $3k$ on simplices and order $3k + 2$ on tensor-product elements. \blacktriangle

Furthermore, the $\mathbf{H}(\text{div})$ -DG method fulfils Lem. 3.6 and Lem. 3.12 as well, and Rem. 3.4 also holds true. However, instead of the full jump across facets as in the \mathbf{L}^2 -DG method (3.5), we are now allowing only jumps of the tangential component of involved velocities.

Remark 3.16 (Reduced spaces): In order to remove some degrees of freedom (DOFs) for the velocity and all pressure unknowns except for the piecewise constants, we exploit the *a priori* knowledge that $\nabla \cdot \mathbf{u}_h = 0$ in our numerical experiments; cf. [LS16, Rem. 1] and [Leh10, Sec. 2.2.4.2]. This can be achieved with a smart choice of basis functions for \mathbf{V}_h , based on an exact sequence property¹⁰ (De Rham complex) on the discrete level; cf. [SZ05; Zag06]. The resulting discretely inf-sup stable reduced pairs are denoted $\mathbf{BDM}_k^{\text{red}}/\mathbb{P}_0^{\text{dc}}$ and $\mathbf{RT}_{[k]}^{\text{red}}/\mathbb{P}_0^{\text{dc}}$. \blacktriangle

¹⁰For example, given $\nabla \cdot \mathbf{u} = 0$ for $\mathbf{u} \in \mathbf{H}(\text{div})$, then there exists $\boldsymbol{\varphi} \in \mathbf{H}(\text{curl})$ with $\mathbf{u} = \nabla \times \boldsymbol{\varphi}$.

3.4 H^1 -FEM

Now let us increase the regularity of the discrete solution even more. When the underlying FE space guarantees that both the normal and the tangential component of the resulting discrete velocity are continuous across facets, we are dealing with classical H^1 -conforming methods.

Lemma 3.17 (Characterisation of $H^1(\Omega)$)

Let $\mathbf{w} \in \mathbf{H}^1(\mathcal{T}_h)$. If $[[\mathbf{w}]]_F = \mathbf{0}$ for all $F \in \mathcal{F}_h^i$, then $\mathbf{w} \in \mathbf{H}^1(\Omega)$.

Proof: Cf., for example, [DE12, Lem. 1.23] for a scalar-valued analogue. ■

The classical choice for an H^1 -conforming FE velocity space is

$$\mathbf{V}_h = \left\{ \mathbf{v}_h \in \mathbf{H}^1(\Omega) : \mathbf{v}_h|_K \in \mathbb{P}_k(K), \forall K \in \mathcal{T}_h; \mathbf{v}_h|_{\partial\Omega} = \mathbf{g}_D^h|_{\partial\Omega} \right\} \subset \mathbf{V}. \quad (3.18)$$

Due to Lem. 3.17, using $\mathbf{v}_h \in \mathbf{C}(\Omega)$ instead of $\mathbf{v}_h \in \mathbf{H}^1(\Omega)$ in the definition (3.18) of $\mathbf{V}_h \subset \mathbf{V}$ can also be seen frequently in the literature.

As we want to focus on discretely inf-sup stable methods, the corresponding pressure space usually contains polynomials of one degree lower than the velocity space. However, the choice between a continuous FE pressure space $Q_h = \mathbb{P}_{k-1} \cap Q$ and a discontinuous one $Q_h = \mathbb{P}_{k-1}^{\text{dc}} \cap Q$ leads to different numerical schemes with fundamentally different properties, as we will see now.

In either case, formally inserting \mathbf{V}_h/Q_h into (3.5) describes the H^1 -conforming method. Again after some simplifications, the classical weak formulation of an H^1 -FEM reads as follows:

$$\left\{ \begin{array}{l} \text{Find } (\mathbf{u}_h, p_h) \in \mathbf{V}_h \times Q_h \text{ such that, } \forall (\mathbf{v}_h, q_h) \in \mathbf{V}_h \times Q_h, \\ \nu a(\mathbf{u}_h, \mathbf{v}_h) + c_h(\mathbf{u}_h; \mathbf{u}_h, \mathbf{v}_h) + \gamma j_h(\mathbf{u}_h, \mathbf{v}_h) + b(\mathbf{v}_h, p_h) + b(\mathbf{u}_h, q_h) = (\mathbf{f}, \mathbf{v}_h). \end{array} \right. \quad (3.19a)$$

$$\quad (3.19b)$$

Compared to the L^2 -DG method (3.5), due to the increased regularity, the H^1 -FEM can exploit normal- and tangential-continuity (the discrete velocity is not necessarily divergence-free, though) which results in the following main simplification: all facet terms disappear because the discrete velocity is continuous across facets.

As a consequence, both the viscous bilinear form a and the pressure-velocity coupling b coincide with the continuous problem. Furthermore, the discrete convection term reduces to

$$c_h(\boldsymbol{\beta}; \mathbf{w}, \mathbf{v}_h) = \int_{\Omega} (\boldsymbol{\beta} \cdot \nabla) \mathbf{w} \cdot \mathbf{v}_h \, dx + \frac{1}{2} \int_{\Omega} (\nabla \cdot \boldsymbol{\beta}) \mathbf{w} \cdot \mathbf{v}_h \, dx,$$

with $c_h(\mathbf{w}; \mathbf{v}_h, \mathbf{v}_h) = 0$ for any fixed $\mathbf{w} \in \mathbf{V}(h)$ and for all $\mathbf{v}_h \in \mathbf{V}_h$ and hence, no convection stabilisation is applied anymore.

Concerning the divergence stabilisation, j_h reduces to the classical grad-div term

$$j_h(\mathbf{w}, \mathbf{v}_h) = \int_{\Omega} (\nabla \cdot \mathbf{w})(\nabla \cdot \mathbf{v}_h) \, dx.$$

The already mentioned discrete inf-sup stability of (3.19) means that there exists $\beta^* > 0$, independent of the mesh size h , such that

$$\inf_{q_h \in Q_h \setminus \{0\}} \sup_{\mathbf{v}_h \in \mathbf{V}_h \setminus \{\mathbf{0}\}} \frac{b(\mathbf{v}_h, q_h)}{\|\nabla \mathbf{v}_h\|_{L^2} \|q_h\|_{L^2}} \geq \beta^*, \quad (3.20)$$

where we notice that of course, the facet terms disappear in any already introduced norm here. In this context, let it be remarked that the \mathbf{H}^1 -conforming method also fulfils Lem. 3.6 and Lem. 3.12 – note that all jump terms vanish, though – and Rem. 3.4 also holds true.

As usual, the validity of the discrete inf-sup condition (3.20) is accompanied by certain restrictions and conditions. For continuous discrete pressures¹¹, the resulting discretisation is known as the ‘Taylor–Hood’ (TH) method, abbreviated $\mathbb{P}_k/\mathbb{P}_{k-1}$ (or $\mathbb{Q}_k/\mathbb{Q}_{k-1}$ when used on tensor-product meshes), which is discretely inf-sup stable provided $k \geq 2$ [Joh16, Sec. 3.6.2]. On simplicial meshes, the choice of a discontinuous discrete pressure leads to the so-called ‘Scott–Vogelius’ (SV) [SV85] method $\mathbb{P}_k/\mathbb{P}_{k-1}^{\text{dc}}$, which is discretely inf-sup stable on meshes without singular vertices for $k \geq 2d$ and on barycentre-refined meshes for $k \geq d$; cf. [Qim94; Zha05; Zha11].

The SV element fulfils the inclusion property $\nabla \cdot \mathbf{V}_h \subset Q_h$ which, following the same idea as (3.16) for the $\mathbf{H}(\text{div})$ -DG method, leads to the fact that $\nabla \cdot \mathbf{u}_h = 0$. On the other hand, the discrete velocity computed with a Taylor–Hood method is in general not exactly divergence-free.

Due to a guaranteed exactly divergence-free discrete velocity, the weak formulation of a SV method can be further simplified to

$$\begin{cases} \text{Find } (\mathbf{u}_h, p_h) \in \mathbf{V}_h \times Q_h \text{ such that, } \forall (\mathbf{v}_h, q_h) \in \mathbf{V}_h \times Q_h, & (3.21a) \\ \nu a(\mathbf{u}_h, \mathbf{v}_h) + c(\mathbf{u}_h; \mathbf{u}_h, \mathbf{v}_h) + b(\mathbf{v}_h, p_h) + b(\mathbf{u}_h, q_h) = (\mathbf{f}, \mathbf{v}_h). & (3.21b) \end{cases}$$

Namely, the terms in (3.21) for SV are exactly the same as in the continuous problem because the convection term c is automatically skew-symmetric and the grad-div stabilisation j_h can be dropped because it vanishes anyway.

Remark 3.18 (Disadvantages of Scott–Vogelius): In our opinion there are at least the following two arguments why exactly div-free $\mathbf{H}(\text{div})$ methods are preferable over SV methods. Firstly, SV methods can only be applied with special simplicial meshes and secondly, finding a suitable convection stabilisation for \mathbf{H}^1 -FEM is very involved and parameter-tuning is usually necessary. Upwinding in the context of DG methods, on the other hand, is natural and straightforward. \blacktriangle

¹¹Note that in the context of isogeometric analysis, several \mathbf{H}^1 -conforming and divergence-free FE spaces have been constructed using splines on tensor-product meshes [BdFS11; EH13a; EH13b; Eva11], which also use a continuous pressure.

3.5 Efficiency Aspects for High-Order Methods

In order to explain how high-order methods can be made computationally efficient, we first consider the Poisson problem with homogeneous Dirichlet BCs (directly in the weak form):

$$\begin{cases} \text{With } V = \{v \in H^1(\Omega) : v|_{\partial\Omega} = 0\} = H_0^1(\Omega), & (3.22a) \\ \text{find } u \in V \text{ s.t. } (\nabla u, \nabla v) = (f, v), \forall v \in V. & (3.22b) \end{cases}$$

The most important concept for high-order methods is *static condensation* [Guy65; Iro65], which will be explained on the basis of a classical FEM for solving (3.22) approximately. In order to understand the following concepts, let us first consider an example with $\Omega = (0, 1)^2$, a mesh consisting of 2×2 quadratic mesh elements and a \mathbb{Q}_k FEM where, at first, we choose $k = 2$.

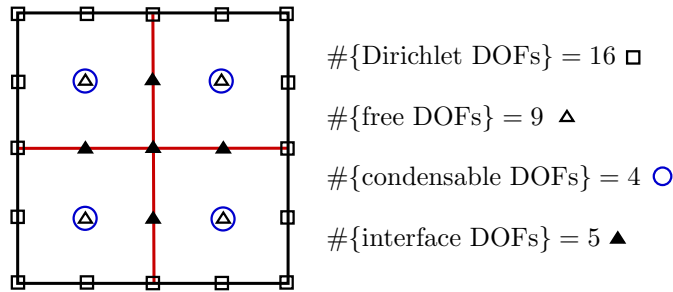


Fig. 3.2: Sketch of the different DOFs (Dirichlet, free, condensable, interface) which are important for the concept of static condensation.

Fig. 3.2 shows a sketch of the resulting situation and we first observe that the values of the 16 *Dirichlet* DOFs, which are located on $\partial\Omega$, are already known due to the Dirichlet BC. This leaves us with 9 *free* DOFs for which the particular value is not known *a priori*. However, the 4 DOFs located in the centres of the mesh elements are elementwise bubbles which means that they do not communicate with DOFs from neighbouring elements; this is what makes them *condensable* in the end. All in all, one only has to solve for the remaining 5 *interface* DOFs; the condensable DOFs can be recovered locally in each element afterwards. In the following we explain this more precisely.

Let us suppose that the resulting linear system which has to be solved can be block-partitioned using condensable (index ‘c’) and interface (index ‘i’) DOFs as follows:

$$Au = f \quad \Leftrightarrow \quad \begin{pmatrix} A_{cc} & A_{ci} \\ A_{ic} & A_{ii} \end{pmatrix} \begin{pmatrix} u_c \\ u_i \end{pmatrix} = \begin{pmatrix} f_c \\ f_i \end{pmatrix}. \quad (3.23)$$

Here, the submatrix A_{cc} is block-diagonal, which allows for cheap inversion in an element-by-element fashion. Thus, using the first row of (3.23) to solve for u_c leads to

$$u_c = A_{cc}^{-1}(f_c - A_{ci}u_i), \quad (3.24)$$

which, in turn, inserted into the second row of (3.23) leads to

$$Su_i := (A_{ii} - A_{ic}A_{cc}^{-1}A_{ci})u_i = f_i - A_{ic}A_{cc}^{-1}f_c, \quad (3.25)$$

where the matrix S is called *Schur complement*. After solving (3.25) for the interface DOFs u_i , the condensable DOFs u_c can be recovered by the matrix-vector application (3.24). As a consequence, solving the original system (3.23) using this static condensation procedure increases the efficiency of the linear solver [Coc16] when high-order methods with many elementwise bubbles are used.

Going back to the above example with a 2×2 mesh, let us now increase the polynomial order of the underlying FE space to $k = 8$. In this situation, the matrix A from the discretisation of the Poisson problem (3.22) has 13 105 non-zero entries, whereas the Schur complement has 2129. This is due to the fact that we only have 29 interface DOFs but 196 condensable DOFs. The corresponding symmetric half of the sparsity patterns can be seen in Fig. 3.3, where the importance of static condensation and, associated therewith, the possible gain in performance can be appreciated.

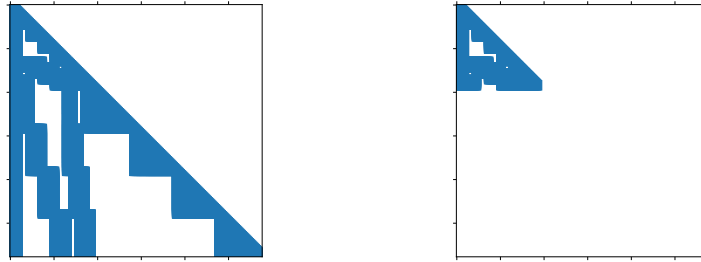


Fig. 3.3: Symmetric half of sparsity patterns: Full matrix A (left) and Schur complement S (right). Each box corresponds to a non-zero entry.

3.5.1 From DG to Hybrid DG (HDG)

A standard textbook SIP-DG method for the discretisation of the Poisson problem (3.22) reads as follows [DE12; Riv08]:

$$\left\{ \text{With } V_h = \mathbb{P}_k^{\text{dc}}, \text{ find } u_h \in V_h \text{ s.t. } a_h(u_h, v_h) = (f, v_h), \forall v_h \in V_h. \right. \quad (3.26)$$

Here, the bilinear form a_h is the scalar-valued analogue of (3.7), that is,

$$a_h(w_h, v_h) := \int_{\Omega} \nabla_h w_h \cdot \nabla_h v_h \, d\mathbf{x} + \sum_{F \in \mathcal{F}_h} \frac{\lambda}{h_F} \int_F \llbracket w_h \rrbracket \llbracket v_h \rrbracket \, d\mathbf{s} \quad (3.27a)$$

$$- \sum_{F \in \mathcal{F}_h} \int_F (\{\!\{ \nabla_h w_h \}\!\} \cdot \mathbf{n}_F) \llbracket v_h \rrbracket \, d\mathbf{s} - \sum_{F \in \mathcal{F}_h} \int_F \llbracket w_h \rrbracket (\{\!\{ \nabla_h v_h \}\!\} \cdot \mathbf{n}_F) \, d\mathbf{s}. \quad (3.27b)$$

The main criticism of standard DG methods like (3.26) is that, due to the breakup of global continuity, the number of DOFs increases compared to an H^1 -conforming method as considered above

for the introduction of static condensation. More disadvantageous, however, turns out to be that the number of couplings in the resulting stiffness matrix increases considerably¹², which results in more expensive direct (and iterative) linear systems. Furthermore, static condensation cannot be applied because also internal bubbles couple with DOFs from neighbouring elements due to (3.27).

In order to counteract these apparent disadvantages of DG methods, the concept of *hybridisation* is frequently used to improve computational efficiency in this context [CGL09; Coc16]. The resulting class of methods, called *Hybrid Discontinuous Galerkin* (HDG) methods, are designed using additional unknowns on the facets of the decomposition, which are supposed to replace direct couplings of neighbouring elements with couplings between element unknowns and facet unknowns. In this sense, one can say that HDG methods have structural similarities with non-overlapping domain decomposition techniques in the extreme case where the subdomains correspond to mesh elements. Of course, hybridisation introduces yet more DOFs, but fortunately the improved coupling structure of HDG methods allows to use static condensation for reducing the number of DOFs for which a linear system has to be solved [GM⁺18].

To make the concept of hybridisation more precise, let us define the facet FE space

$$\widehat{V}_h = \{\widehat{v}_h \in L^2(\mathcal{F}_h) : \widehat{v}_h|_F \in \mathbb{P}_k(F), \forall F \in \mathcal{F}_h; \widehat{v}_h = 0 \text{ on } \partial\Omega\}. \quad (3.28)$$

Note that usually, Dirichlet BCs are incorporated strongly into the facet space. Now, the HDG variant of the SIP method (3.26) is defined by

$$\begin{cases} \text{Find } (u_h, \widehat{u}_h) \in V_h \times \widehat{V}_h \text{ s.t., } \forall (v_h, \widehat{v}_h) \in V_h \times \widehat{V}_h, & (3.29a) \\ a_h((u_h, \widehat{u}_h), (v_h, \widehat{v}_h)) = (f, v_h). & (3.29b) \end{cases}$$

For $\lambda > 0$ sufficiently large, the SIP-HDG bilinear form is given by

$$a_h((w_h, \widehat{w}_h), (v_h, \widehat{v}_h)) := \int_{\Omega} \nabla_h w_h \cdot \nabla_h v_h \, d\mathbf{x} + \sum_{K \in \mathcal{T}_h} \int_{\partial K} \frac{\lambda}{h_{\partial K}} \llbracket w_h \rrbracket \llbracket v_h \rrbracket \, d\mathbf{s} \quad (3.30a)$$

$$- \sum_{K \in \mathcal{T}_h} \int_{\partial K} (\nabla w_h \cdot \mathbf{n}_K) \llbracket v_h \rrbracket \, d\mathbf{s} - \sum_{K \in \mathcal{T}_h} \int_{\partial K} \llbracket w_h \rrbracket (\nabla v_h \cdot \mathbf{n}_K) \, d\mathbf{s}, \quad (3.30b)$$

where $h_{\partial K} = h_{\partial K}(\mathbf{s}) = |K|_d / |F|_{d-1}$ with $\mathbf{s} \in F$ for $F \in \mathcal{F}_K$ and $|\cdot|_d$ denotes the $(d-1)$ -dimensional Lebesgue measure. In (3.30), in contrast to $\llbracket \cdot \rrbracket$, the operator $\llbracket \cdot \rrbracket$ represents the hybrid jump between cell and facet velocity; that is, $\llbracket v_h \rrbracket = v_h - \widehat{v}_h$. The natural energy norm for the HDG method is given by

$$\forall (w_h, \widehat{w}_h) \in V_h \times \widehat{V}_h: \quad \llbracket (w_h, \widehat{w}_h) \rrbracket_e^2 := \|\nabla_h w_h\|_{L^2}^2 + \sum_{K \in \mathcal{T}_h} \left\| h_{\partial K}^{-1/2} \llbracket w_h \rrbracket \right\|_{L^2(\partial K)}^2.$$

¹²For example, in the above example on the 2×2 mesh, the \mathbb{Q}_8 method leads to 225 free DOFs and 13 105 non-zero entries, whereas the corresponding \mathbb{Q}_8^{dc} DG method results in 324 free DOFs and 39 528 non-zero entries.

Remark 3.19 (Projected jumps): For elliptic problems, in order to reduce the computational effort even more, one can actually decrease the polynomial order of the facet space (3.28) by one, that is, use $\widehat{v}_h|_K \in \mathbb{P}_{k-1}(F)$; cf., for example, [Leh10, Rem. 1.2.4]. However, an additional projection operator has to be introduced which ensures that the accuracy of the resulting method is not compromised. This technique is known as ‘projected jumps’ [LS16, Sec. 2.2], also sometimes called ‘reduced stabilisation’, and we use it in every computation in this thesis. \blacktriangle

Finally, let us mention that analytical results from the DG theory carry over to HDG methods. For instance, one can eliminate the trace variables in HDG methods in order to obtain a standard DG method [Leh10]. Moreover, in the HDG literature one often finds dual mixed formulations, which also discretise the diffusive flux $\nabla \mathbf{u}$ explicitly [CGL09].

3.5.2 HDG Lifting Techniques

The main point of criticism with the SIP-DG method (3.26) is that discrete coercivity can only be guaranteed as long as the stabilisation parameter $\lambda > 0$ is chosen *sufficiently large*; cf. [DE12, Lem. 4.12]. Even more unfavourable, as already mentioned above, λ usually scales with k^2 . As the SIP jump penalisation term is non-negative, choosing λ too large results in an unnecessarily high amount of numerical dissipation which can be important in the context of implicit large-eddy simulation (ILES) for 3D turbulent flows; cf. Ch. 7. Analogously, this of course holds true for the SIP-HDG method (3.29), as well.

Therefore, in this short section we will introduce two lifting techniques in the HDG context which can be used to remove this disadvantage. An operator is called *lifting* operator when it maps a function on the skeleton to a function on mesh elements [AB⁺02; BC⁺06; DE12]. In the context of DG methods, they go back to Bassi & Rebay [BR97] and have been analysed in [BM⁺00b]; for HDG methods, we refer to [Oik10; SL13].

Lifting methods work by introducing a new variable whose DOFs can all be eliminated locally by static condensation. Therefore, their efficiency is comparable to the corresponding method without lifting. Similarly, in the context of hybrid mixed DG methods, the additional (dual) diffusive flux variable for approximating $\nabla \mathbf{u}$ can also be eliminated locally by static condensation, thereby resulting in a comparable situation in terms of global free DOFs. In fact, many mixed formulations can be expressed as primal formulations involving lifting operations [CGL09].

The ‘classical’ version of a lifting technique is what we call *L^2 -lifting*.

Definition 3.20 (*L^2 -lifting*)

Let $\mathcal{S}_h = \nabla V_h = \mathbb{P}_\ell^{\text{dc}}$ with $\ell = k - 1$ on simplicial and $\ell = k$ on tensor-product meshes. Then, for all $\varphi \in L^2(\mathcal{F}_h)$, the L^2 -lifting $\mathcal{L}(\varphi) \in \mathcal{S}_h$ is defined as the elementwise solution of

$$\int_K \mathcal{L}(\varphi) \cdot \mathbf{s}_h \, d\mathbf{x} = \int_{\partial K} \varphi(\mathbf{s}_h \cdot \mathbf{n}_K) \, d\mathbf{s}, \quad \forall \mathbf{s}_h \in \mathcal{S}_h, \quad \forall K \in \mathcal{T}_h.$$

The HDG- \mathbf{L}^2 -lifting method then reads as follows: For any $\lambda_\ell > 1$, find $(u_h, \widehat{u}_h) \in V_h \times \widehat{V}_h$ such that, for all $(v_h, \widehat{v}_h) \in V_h \times \widehat{V}_h$, there holds

$$a_h^0((u_h, \widehat{u}_h), (v_h, \widehat{v}_h)) := \quad (3.31a)$$

$$\int_{\Omega} \nabla_h u_h \cdot \nabla_h v_h \, d\mathbf{x} + \lambda_\ell \int_{\Omega} \mathcal{L}(\llbracket u_h \rrbracket) \cdot \mathcal{L}(\llbracket v_h \rrbracket) \, d\mathbf{x} + \sum_{K \in \mathcal{T}_h} \int_{\partial K} \frac{\lambda}{h_{\partial K}} \llbracket u_h \rrbracket \llbracket v_h \rrbracket \, d\mathbf{s} \quad (3.31b)$$

$$- \sum_{K \in \mathcal{T}_h} \int_{\partial K} (\nabla u_h \cdot \mathbf{n}_K) \llbracket v_h \rrbracket \, d\mathbf{s} - \sum_{K \in \mathcal{T}_h} \int_{\partial K} \llbracket u_h \rrbracket (\nabla v_h \cdot \mathbf{n}_K) \, d\mathbf{s} = (f, v_h). \quad (3.31c)$$

Usually, we set $\lambda = k$ and $\lambda_\ell = 2$. For the \mathbf{L}^2 -lifting, a natural energy norm can be defined by

$$\forall (w_h, \widehat{w}_h) \in V_h \times \widehat{V}_h: \quad \|\llbracket (w_h, \widehat{w}_h) \rrbracket\|_{e,0}^2 := \|\llbracket (w_h, \widehat{w}_h) \rrbracket\|_e^2 + \|\mathcal{L}(\llbracket w_h \rrbracket)\|_{\mathbf{L}^2}^2.$$

Now, it is straightforward to see that discrete coercivity comes without complicated restrictions (related to the underlying mesh) on the minimum size of stabilisation parameters.

Lemma 3.21 (Discrete coercivity \mathbf{L}^2 -lifting)

Let $C_{\lambda_\ell} = (\lambda_\ell - 1)(1 + \lambda_\ell)^{-1}$. Then, for all $\lambda_\ell > 1$ and $\lambda \geq C_{\lambda_\ell}$, the HDG- \mathbf{L}^2 -lifting method (3.31) is discretely coercive on $V_h \times \widehat{V}_h$ w.r.t. the norm $\|\cdot\|_{e,0}$; that is,

$$a_h^0((v_h, \widehat{v}_h), (v_h, \widehat{v}_h)) \geq C_{\lambda_\ell} \|\llbracket (v_h, \widehat{v}_h) \rrbracket\|_{e,0}^2, \quad \forall (v_h, \widehat{v}_h) \in V_h \times \widehat{V}_h.$$

Proof: Applying the definition of the \mathbf{L}^2 -lifting to the symmetry and consistency term, symmetric testing in (3.31) amounts to

$$\begin{aligned} a_h^0((v_h, \widehat{v}_h), (v_h, \widehat{v}_h)) &= \|\nabla_h v_h\|_{\mathbf{L}^2}^2 + \lambda \sum_{K \in \mathcal{T}_h} \left\| h_{\partial K}^{-1/2} \llbracket v_h \rrbracket \right\|_{L^2(\partial K)}^2 \\ &\quad + \lambda_\ell \|\mathcal{L}(\llbracket v_h \rrbracket)\|_{\mathbf{L}^2}^2 - 2 \int_{\Omega} \mathcal{L}(\llbracket v_h \rrbracket) \cdot \nabla_h v_h \, d\mathbf{x}. \end{aligned}$$

After applying Cauchy–Schwarz to the last term, we are in a situation where the estimate

$$a_h^0((v_h, \widehat{v}_h), (v_h, \widehat{v}_h)) \geq x^2 + \lambda z^2 + \lambda_\ell y^2 - 2xy \geq \frac{\lambda_\ell - 1}{1 + \lambda_\ell} (x^2 + y^2 + z^2)$$

with $x^2 = \|\nabla_h v_h\|_{\mathbf{L}^2}^2$, $y^2 = \|\mathcal{L}(\llbracket v_h \rrbracket)\|_{\mathbf{L}^2}^2$ and $z^2 = \sum_{K \in \mathcal{T}_h} \left\| h_{\partial K}^{-1/2} \llbracket v_h \rrbracket \right\|_{L^2(\partial K)}^2$ can be applied; cf. [DE12, Proof of Lem. 4.12]. This concludes the proof. \blacksquare

For the actual implementation of (3.31), however, the following equivalent formulation is used:

$$\left\{ \begin{array}{l} \text{Find } (u_h, \widehat{u}_h, \mathbf{r}_h) \in V_h \times \widehat{V}_h \times \mathbf{S}_h \text{ such that, } \forall (v_h, \widehat{v}_h, \mathbf{s}_h) \in V_h \times \widehat{V}_h \times \mathbf{S}_h, \\ a_h((u_h, \widehat{u}_h), (v_h, \widehat{v}_h)) + \ell_h^0((u_h, \widehat{u}_h, \mathbf{r}_h), (v_h, \widehat{v}_h, \mathbf{s}_h)) = (f, v_h). \end{array} \right. \quad (3.32a)$$

$$\left\{ \begin{array}{l} a_h((u_h, \widehat{u}_h), (v_h, \widehat{v}_h)) + \ell_h^0((u_h, \widehat{u}_h, \mathbf{r}_h), (v_h, \widehat{v}_h, \mathbf{s}_h)) = (f, v_h). \end{array} \right. \quad (3.32b)$$

The \mathbf{L}^2 -lifting form ℓ_h^0 in (3.32) is given by

$$\begin{aligned} \ell_h^0((u_h, \widehat{u}_h, \mathbf{r}_h), (v_h, \widehat{v}_h, \mathbf{s}_h)) &:= - \sum_{K \in \mathcal{T}_h} \lambda_\ell \int_K \mathbf{r}_h \cdot \mathbf{s}_h \, d\mathbf{x} + \sum_{K \in \mathcal{T}_h} \lambda_\ell \int_{\partial K} \llbracket u_h \rrbracket (\mathbf{s}_h \cdot \mathbf{n}_K) \, d\mathbf{s} \\ &\quad + \sum_{K \in \mathcal{T}_h} \lambda_\ell \int_{\partial K} \llbracket v_h \rrbracket (\mathbf{r}_h \cdot \mathbf{n}_K) \, d\mathbf{s}. \end{aligned}$$

Note that the two right-hand side terms in the first line express $\mathbf{r}_h = \mathcal{L}(\llbracket u_h \rrbracket)$, whereas the second line realises the original lifting term $\lambda_\ell \int_\Omega \mathcal{L}(\llbracket u_h \rrbracket) \cdot \mathcal{L}(\llbracket v_h \rrbracket) \, d\mathbf{x}$ in (3.31).

A computationally more favourable alternative is the H^1 -lifting; however, both \mathbf{L}^2 -lifting and H^1 -lifting result in the same discrete solution.

Definition 3.22 (H^1 -lifting)

Let $S_h = \{s_h \in L^2(\Omega) : s_h|_K \in V_h|_K\} \setminus \mathbb{P}_0^{\text{dc}}$. For all $\varphi \in L^2(\mathcal{F}_h)$, the H^1 -lifting $\mathcal{L}(\varphi) \in S_h$ is defined as the elementwise solution of

$$\int_K \nabla \mathcal{L}(\varphi) \cdot \nabla s_h \, d\mathbf{x} = \int_{\partial K} \varphi (\nabla s_h \cdot \mathbf{n}_K) \, d\mathbf{s}, \quad \forall s_h \in S_h, \quad \forall K \in \mathcal{T}_h.$$

The most apparent reason why the H^1 -lifting is computationally more favourable is because it is only a scalar-valued function (compared to a vector-valued one for the \mathbf{L}^2 -lifting), which eventually results in less memory consumption. Note that removing the piecewise constants in S_h is necessary because otherwise, Def. 3.22 does not lead to a unique lifting. The HDG- H^1 -lifting method then reads as follows: For any $\lambda > 0$ and $\lambda_\ell > 1$, find $(u_h, \widehat{u}_h) \in V_h \times \widehat{V}_h$ such that, for all $(v_h, \widehat{v}_h) \in V_h \times \widehat{V}_h$, there holds

$$a_h^1((u_h, \widehat{u}_h), (v_h, \widehat{v}_h)) := \int_\Omega \nabla_h u_h \cdot \nabla_h v_h \, d\mathbf{x} \tag{3.33a}$$

$$+ \lambda_\ell \int_\Omega \nabla_h \mathcal{L}(\llbracket u_h \rrbracket) \cdot \nabla_h \mathcal{L}(\llbracket v_h \rrbracket) \, d\mathbf{x} + \sum_{K \in \mathcal{T}_h} \int_{\partial K} \frac{\lambda}{h_{\partial K}} \llbracket u_h \rrbracket \llbracket v_h \rrbracket \, d\mathbf{s} \tag{3.33b}$$

$$- \sum_{K \in \mathcal{T}_h} \int_{\partial K} (\nabla u_h \cdot \mathbf{n}_K) \llbracket v_h \rrbracket \, d\mathbf{s} - \sum_{K \in \mathcal{T}_h} \int_{\partial K} \llbracket u_h \rrbracket (\nabla v_h \cdot \mathbf{n}_K) \, d\mathbf{s} = (f, v_h). \tag{3.33c}$$

For the H^1 -lifting, a natural energy norm can be defined by

$$\forall (w_h, \widehat{w}_h) \in V_h \times \widehat{V}_h: \quad \|\!\| (w_h, \widehat{w}_h) \|\!\|_{e,1}^2 := \|\!\| (w_h, \widehat{w}_h) \|\!\|_e^2 + \|\nabla_h \mathcal{L}(\llbracket w_h \rrbracket)\|\!\|_{\mathbf{L}^2}^2.$$

Analogously to Lem. 3.21, we obtain the following result.

Lemma 3.23 (Discrete coercivity H^1 -lifting)

Let $C_{\lambda_\ell} = (\lambda_\ell - 1)(1 + \lambda_\ell)^{-1}$. Then, for all $\lambda_\ell > 1$ and $\lambda \geq C_{\lambda_\ell}$, the HDG- H^1 -lifting method (3.33) is discretely coercive on $V_h \times \widehat{V}_h$ w.r.t. the norm $\|\!\| \cdot \|\!\|_{e,1}$; that is,

$$a_h^1((v_h, \widehat{v}_h), (v_h, \widehat{v}_h)) \geq C_{\lambda_\ell} \|\!\| (v_h, \widehat{v}_h) \|\!\|_{e,1}^2, \quad \forall (v_h, \widehat{v}_h) \in V_h \times \widehat{V}_h.$$

Proof: Applying the definition of the H^1 -lifting to the symmetry and consistency term, symmetric testing in (3.33) amounts to

$$\begin{aligned} a_h^0((v_h, \widehat{v}_h), (v_h, \widehat{v}_h)) &= \|\nabla_h v_h\|_{L^2}^2 + \lambda \sum_{K \in \mathcal{T}_h} \left\| h_{\partial K}^{-1/2} \llbracket v_h \rrbracket \right\|_{L^2(\partial K)}^2 \\ &\quad + \lambda_\ell \|\nabla_h \mathcal{L}(\llbracket v_h \rrbracket)\|_{L^2}^2 - 2 \int_{\Omega} \nabla_h \mathcal{L}(\llbracket v_h \rrbracket) \cdot \nabla_h v_h \, d\mathbf{x}. \end{aligned}$$

Now, exactly the same steps as in the proof of Lem. 3.21 show the claim. \blacksquare

Again, for the actual implementation, an equivalent formulation is better suited. Thus, we consider the weak formulation

$$\begin{cases} \text{Find } (u_h, \widehat{u}_h, r_h) \in V_h \times \widehat{V}_h \times S_h \text{ such that, } \forall (v_h, \widehat{v}_h, s_h) \in V_h \times \widehat{V}_h \times S_h, & (3.34a) \\ a_h((u_h, \widehat{u}_h), (v_h, \widehat{v}_h)) + \ell_h^1((u_h, \widehat{u}_h, r_h), (v_h, \widehat{v}_h, s_h)) = (f, v_h), & (3.34b) \end{cases}$$

where the H^1 -lifting form ℓ_h^1 is given by

$$\begin{aligned} \ell_h^1((u_h, \widehat{u}_h, r_h), (v_h, \widehat{v}_h, s_h)) &:= - \sum_{K \in \mathcal{T}_h} \lambda_\ell \int_K \nabla r_h \cdot \nabla s_h \, d\mathbf{x} + \sum_{K \in \mathcal{T}_h} \lambda_\ell \int_{\partial K} \llbracket u_h \rrbracket (\nabla s_h \cdot \mathbf{n}_K) \, ds \\ &\quad + \sum_{K \in \mathcal{T}_h} \lambda_\ell \int_{\partial K} \llbracket v_h \rrbracket (\nabla r_h \cdot \mathbf{n}_K) \, ds. \end{aligned}$$

Note that $r_h = \mathcal{L}(\llbracket u_h \rrbracket)$ and the second line realises $\lambda_\ell \int_{\Omega} \nabla_h \mathcal{L}(\llbracket u_h \rrbracket) \cdot \nabla_h \mathcal{L}(\llbracket v_h \rrbracket) \, d\mathbf{x}$ in (3.33).

Remark 3.24 (Uniqueness of H^1 -lifting): In order to obtain a unique H^1 -lifting in practice, the easiest solution is to add a small ($\varepsilon \ll 1$) regularisation term

$$- \sum_{K \in \mathcal{T}_h} \frac{\varepsilon}{h_K^2} \int_K r_h s_h \, d\mathbf{x}$$

to (3.34). However, we prefer the cleaner solution of projecting out the elementwise constants by introducing yet another unknown $r_h^0 \in \mathbb{P}_0^{\text{dc}}$, and adding

$$\sum_{K \in \mathcal{T}_h} \frac{1}{h_K^2} \int_K [-r_h^0 s_h^0 + r_h s_h^0 + r_h^0 s_h] \, d\mathbf{x} \quad (3.35)$$

to the left-hand side of (3.34) for all $s_h^0 \in \mathbb{P}_0^{\text{dc}}$. Note that when $\pi_0: S_h \rightarrow \mathbb{P}_0^{\text{dc}}$ denotes the L^2 -projection onto the elementwise constants, (3.35) realises the term $\sum_{K \in \mathcal{T}_h} h_K^{-2} \int_K \pi_0(r_h) \pi_0(s_h) \, d\mathbf{x}$ in a similar fashion as the lifting terms ℓ_h^1 and ℓ_h^2 are constructed. \blacktriangle

Finally, let us remark that another advantage of the H^1 -lifting method is that it essentially involves only integrals that already occur in the SIP method, plus some additional uncomplicated ones. Summarising in one sentence, lifting techniques allow to decrease the amount of stabilisation of HDG methods, whilst ensuring stability [Leh16].

3.5.3 $H(\text{div})$ -HDG for Incompressible Flows

After having explained static condensation, hybridisation and lifting techniques in the context of the scalar-valued Poisson problem, we now want to apply the ideas to the discretisation of incompressible flow problems. As those concepts are mainly interesting for the diffusion part of the method, the Stokes problem (2.21) shall now serve as the model problem. Due to the favourable combination of continuous normal component and discontinuous tangential component, we will focus on explaining a particular class of divergence-free $H(\text{div})$ -HDG methods based on [LS16]. For other possibilities of using hybridisation in the context of incompressible flow problems, we refer to [CG05a; CG05b; CG09; LW12] and especially to [Coc09; GLS18; LLS18a; LLS18b; RW17; RW18] where different approaches to exactly divergence-free HDG methods are considered.

In order to still obtain a normal-continuous and exactly divergence-free solution, the basic velocity space remains unchanged as

$$\mathbf{V}_h = \{ \mathbf{v}_h \in \mathbf{H}(\text{div}; \Omega) : \mathbf{v}_h|_K \in \mathbf{V}_k(K), \forall K \in \mathcal{T}_h; \mathbf{v}_h \cdot \mathbf{n}|_{\partial\Omega} = 0 \},$$

where the local space $\mathbf{V}_k(K)$ is based either on BDM or RT elements. Also the pressure space $Q_h = \mathbb{P}_\ell^{\text{dc}} \cap Q$ with $\ell \in \{k-1, k\}$ is the same as in the DG method. For the hybridisation, however, we introduce the space of vector-valued tangential polynomials

$$\widehat{\mathbf{V}}_h = \{ \widehat{\mathbf{v}}_h \in \mathbf{L}^2(\mathcal{F}_h) : \widehat{\mathbf{v}}_h|_F \in \mathbb{P}_k(F), \widehat{\mathbf{v}}_h \cdot \mathbf{n}_F|_F = 0, \forall F \in \mathcal{F}_h; \widehat{\mathbf{v}}_h = \mathbf{0} \text{ on } \partial\Omega \}.$$

At first, consider the weak formulation for an $H(\text{div})$ -SIP-HDG method:

$$\left\{ \begin{array}{l} \text{Find } (\mathbf{u}_h, \widehat{\mathbf{u}}_h, p_h) \in \mathbf{V}_h \times \widehat{\mathbf{V}}_h \times Q_h \text{ such that, } \forall (\mathbf{v}_h, \widehat{\mathbf{v}}_h, q_h) \in \mathbf{V}_h \times \widehat{\mathbf{V}}_h \times Q_h, \\ \nu a_h((\mathbf{u}_h, \widehat{\mathbf{u}}_h), (\mathbf{v}_h, \widehat{\mathbf{v}}_h)) + b(\mathbf{v}_h, p_h) + b(\mathbf{u}_h, q_h) = (\mathbf{f}, \mathbf{v}_h). \end{array} \right. \quad (3.36a)$$

$$(3.36b)$$

Here, the viscous bilinear form a_h is simply the extension of the scalar-valued one (3.30) for the Poisson problem to the vector-valued case; that is,

$$\begin{aligned} a_h((\mathbf{w}_h, \widehat{\mathbf{w}}_h), (\mathbf{v}_h, \widehat{\mathbf{v}}_h)) &:= \int_{\Omega} \nabla_h \mathbf{w}_h : \nabla_h \mathbf{v}_h \, dx + \sum_{K \in \mathcal{T}_h} \int_{\partial K} \frac{\lambda}{h_{\partial K}} \llbracket \mathbf{w}_h \rrbracket_{\tau} \cdot \llbracket \mathbf{v}_h \rrbracket_{\tau} \, ds \\ &\quad - \sum_{K \in \mathcal{T}_h} \int_{\partial K} (\nabla \mathbf{w}_h) \mathbf{n}_K \cdot \llbracket \mathbf{v}_h \rrbracket_{\tau} \, ds - \sum_{K \in \mathcal{T}_h} \int_{\partial K} \llbracket \mathbf{w}_h \rrbracket_{\tau} \cdot (\nabla \mathbf{v}_h) \mathbf{n}_K \, ds. \end{aligned}$$

In contrast to $\llbracket \cdot \rrbracket$ and $\llbracket \cdot \rrbracket$, the operator $\llbracket \cdot \rrbracket_{\tau}$ represents the tangential jump between cell and facet velocity; that is, using the projection onto the tangent plane $\mathbf{v}_{\tau} = \mathbf{v} - (\mathbf{v} \cdot \mathbf{n}_K) \mathbf{n}_K$,

$$\llbracket \mathbf{v} \rrbracket_{\tau} := (\mathbf{v} - \widehat{\mathbf{v}})_{\tau} = \mathbf{v}_{\tau} - \widehat{\mathbf{v}}.$$

Note that, as usual for SIP methods, λ has to be sufficiently large to guarantee discrete coercivity. In Fig. 3.4 a sketch of the situation with a continuous normal, discontinuous tangential and hybrid facet velocity can be seen for the 2D case. On simplicial meshes, the resulting method is abbrevi-

ated $\mathbf{BDM}_k/\mathbf{F}_k/\mathbb{P}_{k-1}^{\text{dc}}$ and the name $\mathbf{RT}_{[k]}/\mathbf{F}_k/\mathbb{P}_k^{\text{dc}}$ is used on tensor-product meshes.

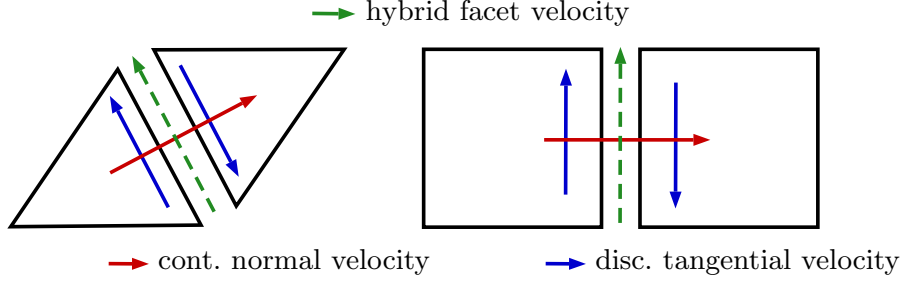


Fig. 3.4: Cell and facet velocity in $\mathbf{H}(\text{div})$ -HDG methods for triangular ($\mathbf{BDM}_k/\mathbf{F}_k/\mathbb{P}_{k-1}^{\text{dc}}$) and quadrilateral ($\mathbf{RT}_{[k]}/\mathbf{F}_k/\mathbb{P}_k^{\text{dc}}$) meshes.

Remark 3.25 (Complications on tensor-product meshes): For the $\mathbf{RT}_{[k]}/\mathbf{F}_k/\mathbb{P}_k^{\text{dc}}$ method, due to the fact that the trace of $\mathbf{RT}_{[k]}$ velocities can be a polynomial of order $k + 1$ locally, choosing the facet space \mathbf{F}_k actually introduces an additional high-order consistency error in the method. However, the stability and convergence properties are not violated. From an analysis point of view, this can be understood using the techniques described in [LLS18a]. \blacktriangle

Remark 3.26 ($\mathbf{H}(\text{div})$ -conformity through pressure hybridisation): Directly using the $\mathbf{H}(\text{div})$ -conforming velocity space \mathbf{V}_h is of course not the only possibility for obtaining a normal-continuous discrete velocity approximation. Alternatively, it is also feasible to remove all inter-element continuity requirements from the velocity space, and to introduce an additional facet Lagrange multiplier for the pressure, which ensures $\mathbf{H}(\text{div})$ -conformity of the solution; cf., for example, [LS16, Rem. 7]. More precisely, introducing the scalar-valued facet space (hybrid pressure variable)

$$\widehat{Q}_h = \{\widehat{q}_h \in L^2(\mathcal{F}_h) : \widehat{q}_h|_F \in \mathbb{P}_k(F), \forall F \in \mathcal{F}_h\},$$

and, for example on simplicial meshes, using the \mathbf{L}^2 velocity space¹³

$$\mathbf{V}'_h = \{\mathbf{v}_h \in \mathbf{L}^2(\Omega) : \mathbf{v}_h|_K \in \mathbb{P}_k(K), \forall K \in \mathcal{T}_h\},$$

another SIP $\mathbf{H}(\text{div})$ -HDG method for the Stokes problem can be formulated as follows:

$$\begin{cases} \text{Find } (\mathbf{u}_h, \widehat{\mathbf{u}}_h, p_h, \widehat{p}_h) \in \mathbf{V}'_h \times \widehat{\mathbf{V}}_h \times Q_h \times \widehat{Q}_h \text{ such that, } \forall (\mathbf{v}_h, \widehat{\mathbf{v}}_h, q_h, \widehat{q}_h) \in \mathbf{V}'_h \times \widehat{\mathbf{V}}_h \times Q_h \times \widehat{Q}_h, \\ \nu a_h((\mathbf{u}_h, \widehat{\mathbf{u}}_h), (\mathbf{v}_h, \widehat{\mathbf{v}}_h)) + b(\mathbf{v}_h, p_h) + b(\mathbf{u}_h, q_h) + d_h(\widehat{\mathbf{v}}_h, \widehat{p}_h) + d_h(\widehat{\mathbf{u}}_h, \widehat{q}_h) = (\mathbf{f}, \mathbf{v}_h). \end{cases}$$

Here, the bilinear form $d_h : \widehat{\mathbf{V}}'_h \times \widehat{Q}_h \rightarrow \mathbb{R}$ realises normal-continuity and is defined as

$$d_h(\widehat{\mathbf{v}}_h, \widehat{q}_h) := \sum_{K \in \mathcal{T}_h} \int_{\partial K} \widehat{q}_h (\widehat{\mathbf{v}}_h \cdot \mathbf{n}_K) \, ds.$$

¹³Alternatively, the space \mathbf{V}_h can be used but without strongly imposed normal-continuity, also on quads/hexes.

Note that in this formulation, all DOFs in \mathbf{V}'_h and Q_h can now be eliminated by static condensation. On simplicial meshes, the resulting velocity solution coincides with the one resulting from the $\mathbb{BDM}_k/\mathbb{F}_k/\mathbb{P}_{k-1}^{\text{dc}}$ method. However, this alternative $\mathbf{H}(\text{div})$ -conforming HDG method might be easier to implement in some software packages and it might behave differently with respect to the particular linear solver strategy. \blacktriangle

The second HDG method we consider in this work uses an \mathbf{H}^1 -lifting technique as introduced above. To be more precise, we will briefly explain how to extend the ideas to the Stokes problem. In order to compute the (now vector-valued) lifting, the space

$$\mathbf{S}_h = \{s_h \in \mathbf{L}_0^2(\Omega) : s_h|_K \in \mathbf{V}_k(K), \forall K \in \mathcal{T}_h\}$$

is used. \mathbf{S}_h is the globally discontinuous sibling of \mathbf{V}_h , without strongly imposed BCs. The vector-valued lifting is, in principle, simply defined componentwise and rewritten as follows.

Definition 3.27 (Vector-valued \mathbf{H}^1 -lifting)

For all $\varphi \in \mathbf{L}^2(\mathcal{F}_h)$, the \mathbf{H}^1 -lifting $\mathcal{L}(\varphi) \in \mathbf{S}_h$ is defined as the elementwise solution of

$$\int_K \nabla \mathcal{L}(\varphi) : \nabla s_h \, d\mathbf{x} = \int_{\partial K} \varphi \cdot (\nabla s_h) \mathbf{n}_K \, ds, \quad \forall s_h \in \mathbf{S}_h, \quad \forall K \in \mathcal{T}_h.$$

Then, our $\mathbf{H}(\text{div})$ - \mathbf{H}^1 -lifting-HDG method is based on the following weak formulation of finding $(\mathbf{u}_h, \hat{\mathbf{u}}_h, p_h) \in \mathbf{V}_h \times \hat{\mathbf{V}}_h \times Q_h$ such that

$$\begin{aligned} \nu a_h((\mathbf{u}_h, \hat{\mathbf{u}}_h), (\mathbf{v}_h, \hat{\mathbf{v}}_h)) + \nu \lambda_\ell \int_\Omega \nabla_h \mathcal{L}(\llbracket \mathbf{u}_h \rrbracket_\tau) : \nabla_h \mathcal{L}(\llbracket \mathbf{v}_h \rrbracket_\tau) \, d\mathbf{x} \\ + b(\mathbf{v}_h, p_h) + b(\mathbf{u}_h, q_h) = (\mathbf{f}, \mathbf{v}_h) \end{aligned}$$

holds for all $(\mathbf{v}_h, \hat{\mathbf{v}}_h, q_h) \in \mathbf{V}_h \times \hat{\mathbf{V}}_h \times Q_h$. Again, we usually use $\lambda = k$ and $\lambda_\ell = 2$, which is sufficient concerning stability. For the sake of completeness, however, let us state the implementation variant of the $\mathbf{H}(\text{div})$ - \mathbf{H}^1 -lifting-HDG method:

$$\left\{ \begin{array}{l} \text{Find } (\mathbf{u}_h, \hat{\mathbf{u}}_h, \mathbf{r}_h, p_h) \in \mathbf{V}_h \times \hat{\mathbf{V}}_h \times \mathbf{S}_h \times Q_h \text{ s.t., } \forall (\mathbf{v}_h, \hat{\mathbf{v}}_h, \mathbf{s}_h, q_h) \in \mathbf{V}_h \times \hat{\mathbf{V}}_h \times \mathbf{S}_h \times Q_h, \quad (3.38a) \\ \nu [a_h((\mathbf{u}_h, \hat{\mathbf{u}}_h), (\mathbf{v}_h, \hat{\mathbf{v}}_h)) + \ell_h^1((\mathbf{u}_h, \hat{\mathbf{u}}_h, \mathbf{r}_h), (\mathbf{v}_h, \hat{\mathbf{v}}_h, \mathbf{s}_h))] + b(\mathbf{v}_h, p_h) = (\mathbf{f}, \mathbf{v}_h), \quad (3.38b) \\ b(\mathbf{u}_h, q_h) = 0. \quad (3.38c) \end{array} \right.$$

Here, the \mathbf{H}^1 -lifting form ℓ_h^1 is given by

$$\begin{aligned} \ell_h^1((\mathbf{u}_h, \hat{\mathbf{u}}_h, \mathbf{r}_h), (\mathbf{v}_h, \hat{\mathbf{v}}_h, \mathbf{s}_h)) := & - \sum_{K \in \mathcal{T}_h} \lambda_\ell \int_K \nabla \mathbf{r}_h : \nabla s_h \, d\mathbf{x} + \sum_{K \in \mathcal{T}_h} \lambda_\ell \int_{\partial K} \llbracket \mathbf{u}_h \rrbracket_\tau \cdot (\nabla s_h) \mathbf{n}_K \, ds \\ & + \sum_{K \in \mathcal{T}_h} \lambda_\ell \int_{\partial K} \llbracket \mathbf{v}_h \rrbracket_\tau \cdot (\nabla \mathbf{r}_h) \mathbf{n}_K \, ds. \end{aligned}$$

Remark 3.28: Following Rem. 3.24, concerning the unique determination of the \mathbf{H}^1 -lifting in (3.38) in practice, we project out the (vector-valued) elementwise constants by introducing another un-

known $\mathbf{r}_h^0 \in \mathbb{P}_0^{\text{dc}}$, and adding

$$\sum_{K \in \mathcal{T}_h} \frac{\nu}{h_K^2} \int_K [-\mathbf{r}_h^0 \cdot \mathbf{s}_h^0 + \mathbf{r}_h \cdot \mathbf{s}_h^0 + \mathbf{r}_h^0 \cdot \mathbf{s}_h] \, d\mathbf{x}$$

to the left-hand side of (3.38) for all $\mathbf{s}_h^0 \in \mathbb{P}_0^{\text{dc}}$. ▲

For all of the computationally demanding simulations in the remainder of this thesis, we will either use the $\mathbf{H}(\text{div})$ -SIP-HDG method (3.36) with varying λ , or the $\mathbf{H}(\text{div})$ - \mathbf{H}^1 -lifting-HDG method (3.38) with $\lambda = k$ and $\lambda_\ell = 2$.

Essential Robustness Concepts

Structure of this chapter: This chapter deals with the most important robustness concepts which are fundamental in this thesis. Investigating the ability of numerical methods to sustain large-scale structures leads, by means of a discrete Helmholtz decomposition, to the central concept of pressure-robustness. After explaining this in detail and demonstrating its importance, the notion of Reynolds-semi-robust error estimates is briefly introduced and supplemented with an example.

4.1	Structure Preservation	49
4.2	Pressure-Robustness	55
4.2.1	Potential Flows	57
4.2.2	Generalised Beltrami Flows	59
4.3	Reynolds-Semi-Robustness	63

4.1 Structure Preservation

The first robustness aspect which we want to address is connected to the preservation of (large-scale/coherent) structures and, at first glance, a rather qualitative concept. Quite obviously, from a good numerical method, we expect that it is able to preserve characteristic flow structures as accurately as possible — if such structures are destroyed prematurely, a solver would not be called ‘robust’ because the solution is *de facto* unusable. In anticipation of the next subsection, we will attempt to map out a possible connection between structure preservation and pressure-robustness.

A frequently used 2D model problem for investigating how well a discretisation preserves structures is the so-called ‘Gresho vortex’ [GC90] (originally called ‘triangle vortex’). Centred at $\mathbf{c} = (c_1, c_2)^\dagger \in \mathbb{R}^2$ and with a (constant) translational velocity $\mathbf{w}_0 \in \mathbb{R}^2$, the problem setup in Cartesian coordinates is fully described by the initial condition

$$\mathbf{u}_0(\mathbf{x}) = \mathbf{w}_0 + \begin{cases} (-5\tilde{x}_2, 5\tilde{x}_1)^\dagger, & 0 \leq r < 0.2, \\ \left(-\frac{2\tilde{x}_2}{r} + 5\tilde{x}_2, \frac{2\tilde{x}_1}{r} - 5\tilde{x}_1\right)^\dagger, & 0.2 \leq r < 0.4, \\ (0, 0)^\dagger, & 0.4 \leq r, \end{cases} \quad (4.1)$$

with Euclidean distance from the vortex centre $r = |\mathbf{x} - \mathbf{c}|_2$ and $(\tilde{x}_1, \tilde{x}_2) = (x_1 - c_1, x_2 - c_2)$. The Gresho vortex (4.1) has a constant vorticity in its core for $r < 0.2$ (similar to a rigid body rotation) but then, for $0.2 \leq r < 0.4$ it decreases linearly and vanishes for $r \geq 0.4$. Thus, there are conceptual similarities with, for example, the Rankine, Lamb–Oseen or Burgers vortex [Ach90; Saf93; WMZ06], but the Gresho vortex stands out because its vorticity is discontinuous at $r \in \{0.2, 0.4\}$ which makes it especially interesting for numerically investigating robustness properties.

In the context of the incompressible Euler and Navier–Stokes equations, or even the compressible Navier–Stokes equations, the Gresho vortex is a popular test case; cf., for example, [CH⁺17; DII; GKM14; HG⁺13; LW03; Spr10; TM⁺92]. When $\mathbf{w}_0 \equiv \mathbf{0}$ is chosen, the name ‘standing vortex problem’ is also used sometimes.

Our actual simulations are done in the x_1 - and x_2 - periodic¹⁴ box $\Omega = (0, 4) \times (0, 1)$ with centre $\mathbf{c} = (0.5, 0.5)^\dagger$, a wind $\mathbf{w}_0 = (1, 0)^\dagger$ and up to an end time $T = 3$. The full time-dependent Navier–Stokes problem (2.1) with $\mathbf{f} \equiv \mathbf{0}$ governs the problem with initial condition (4.1) and $\nu = 10^{-6}$. For the spatial discretisation, a quadrilateral mesh with $4N \times N$ squares is employed, and for the time-stepping we use a constant time step $\Delta t = 0.002$ with the second-order Runge–Kutta (RK) variant ARS(2,2,2) of the implicit-explicit (IMEX) method introduced in [ARS97]; cf., for example, [Leh10] for more details about time integration for PDEs in this context. Stokes-type subproblems are treated implicitly, whereas convection is treated explicitly.

In the following, we compare the divergence-free $\mathbf{H}(\text{div})$ -DG method $\mathbf{RT}_{[k]}^{\text{red}}/\mathbb{P}_0^{\text{dc}}$ (space discretisation defined by (3.15)) with the L^2 -DG method $\mathbb{Q}_k^{\text{dc}}/\mathbb{Q}_{k-1}^{\text{dc}}$ (space discretisation defined by (3.5)). Concerning the involved parameters, we use upwinding ($\theta = 1$), a SIP parameter $\lambda = 3(k + 1)^2$ and at first no DG-grad-div ($\gamma = 0$). Note that the L^2 -DG method in this version is a standard discretisation scheme which can also be found, for example, in [DE12; Riv08].

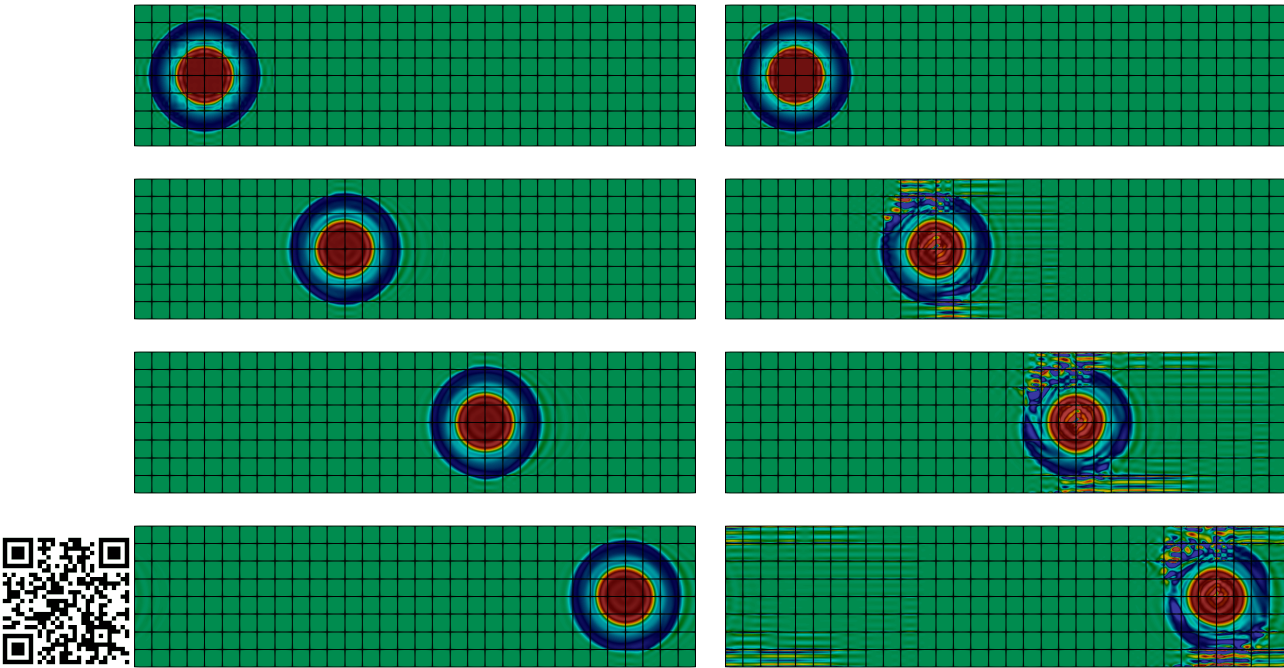


Fig. 4.1: Evolution of vorticity $\omega_h = \nabla_h \times \mathbf{u}_h$ for the moving Gresho problem, computed with $k = 6$ and $N = 8$. Line by line: $t = 0, 1, 2, 3$. Left column: divergence-free $\mathbf{H}(\text{div})$ -DG method $\mathbf{RT}_{[6]}^{\text{red}}/\mathbb{P}_0^{\text{dc}}$; right column: textbook L^2 -DG method $\mathbb{Q}_6^{\text{dc}}/\mathbb{Q}_5^{\text{dc}}$. (A video of this simulation is available at <https://youtu.be/wrZTUrgxVSc>; note also the QR code.)

¹⁴Instead of periodic BCs one could also use free-slip BCs; it is only important to not have no-slip wall interactions.

In Fig. 4.1, the evolution of the discrete vorticity $\omega_h = \nabla_h \times \mathbf{u}_h$ is displayed at $t = 0, 1, 2, 3$ for $\mathbf{RT}_{[k]}^{\text{red}}/\mathbb{P}_0^{\text{dc}}$ and $\mathbf{Q}_k^{\text{dc}}/\mathbf{Q}_{k-1}^{\text{dc}}$ with fixed $k = 6$ and $N = 8$. While the $\mathbf{H}(\text{div})$ method preserves the structure of the transported vortex very well, obviously the vortical structure computed with the L^2 method is considerably more prone to perturbations and thus significantly less well conserved. The remainder of this subsection will show why seemingly very similar numerical schemes (with the same convection stabilisation) can behave so differently in terms of structure preservation.

Concerning the underlying polynomial order, instead of choosing a high-order $k = 6$, let us consider lower-order methods with $k = 4$ ($N = 14$) and $k = 2$ ($N = 20$). Taking into consideration finer meshes for lower orders should, at least roughly, balance the different approximation properties of the spatial discretisation schemes. In the left column of Fig. 4.2, one can see qualitatively that the $\mathbf{H}(\text{div})$ -DG method is still capable of capturing and sustaining the vortex structure of the Gresho problem. Thus, the ability to maintain vortical structures is not necessarily connected to the polynomial order of the divergence-free $\mathbf{H}(\text{div})$ method. However, the right column shows that for the L^2 -DG method, decreasing the polynomial order is significantly disadvantageous. Indeed, concerning the vortex computed with $(k, N) = (4, 14)$, the structure is less damaged for the high-order method visible in Fig. 4.1. Regarding the results for the ‘Taylor–Hood’ DG sibling $\mathbf{Q}_2^{\text{dc}}/\mathbf{Q}_1^{\text{dc}}$, one cannot identify the final state as a vortex anymore. Before attempting to identify a possible source for this shortcoming of the textbook L^2 -DG method, let us take a more quantitative approach for comparing results.

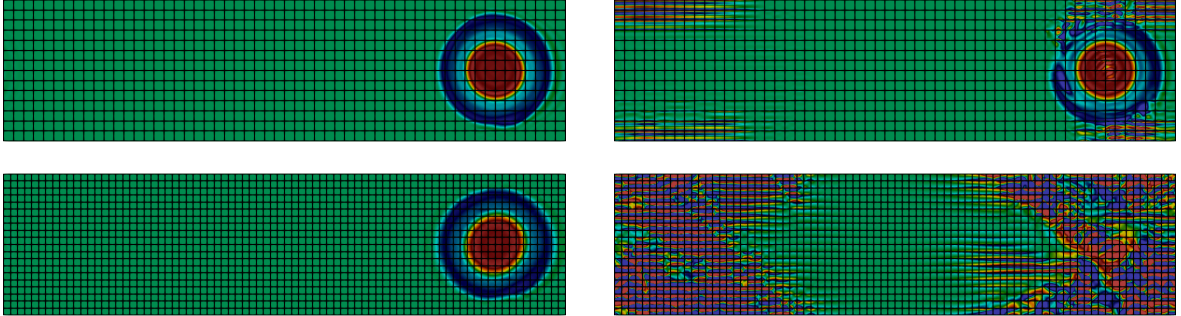


Fig. 4.2: Final state of ω_h at $t = 3$ for the Gresho vortex problem computed with $\mathbf{RT}_{[k]}^{\text{red}}/\mathbb{P}_0^{\text{dc}}$ (left column) and $\mathbf{Q}_k^{\text{dc}}/\mathbf{Q}_{k-1}^{\text{dc}}$ (right column). First row: $(k, N) = (4, 14)$; second row: $(k, N) = (2, 20)$.

Based on the quantities introduced in Sec. 2.3, Fig. 4.3 shows how kinetic energy, enstrophy and palinstrophy evolve over time for the solutions computed with both methods. We observe that $\mathcal{K}(\mathbf{u}_h)$ is nearly constant for all considered $\mathbf{RT}_{[k]}^{\text{red}}/\mathbb{P}_0^{\text{dc}}$ methods, while the $\mathbf{Q}_k^{\text{dc}}/\mathbf{Q}_{k-1}^{\text{dc}}$ solutions show a much stronger loss of kinetic energy, especially for $(k, N) = (2, 20)$. Correspondingly, one can see that both $\mathcal{E}(\mathbf{u}_h)$ and $\mathcal{P}(\mathbf{u}_h)$ are on average decreasing for the $\mathbf{H}(\text{div})$ method (we attribute the small oscillations to strong discontinuities over facets, originating in the still coarse spatial resolution). Note that in these more sensitive quantities, a difference between low-order ($k = 2$) and higher-order $k = 4, 6$ can be perceived. The solutions of the L^2 -DG method, on the other hand, behave completely different. Concerning the enstrophy, one can see that the $\mathbf{Q}_2^{\text{dc}}/\mathbf{Q}_1^{\text{dc}}$ solution ex-

plodes immediately, while for $k = 4, 6$, at least only a bounded growth is visible. Note that taking into account classical fluid dynamics, the enstrophy evolution equation (2.16) dictates that the exact quantity $\mathcal{E}(\mathbf{u})$ monotonically decreases in such a situation; see also Rem. 2.15. Therefore, we identify the global increase of the discrete enstrophy as unphysical behaviour. Lastly, even though nothing can be said about the sign of the rate of change of palinstrophy, we remark that in contrast to the $\mathbf{H}(\text{div})$ solution, the L^2 -DG's palinstrophy attains extremely large values. Thus, there is actually some evidence that this is also not a particularly robust behaviour.

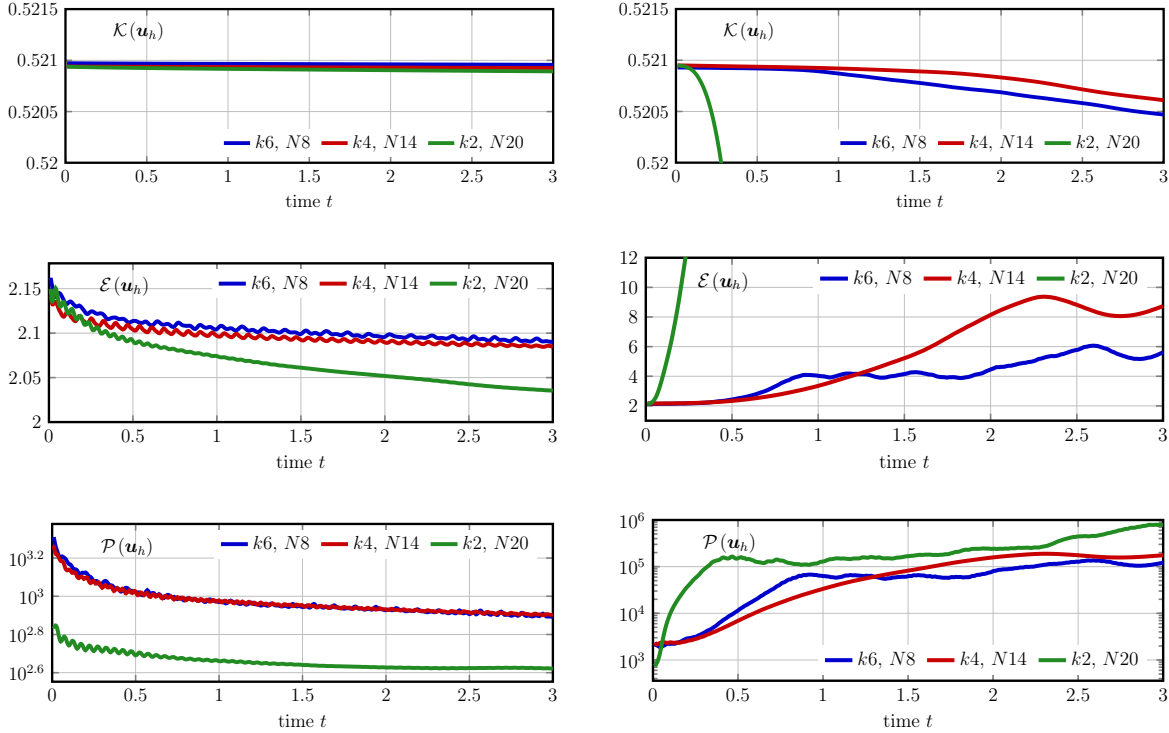


Fig. 4.3: Kinetic energy $\mathcal{K}(\mathbf{u}_h)$, enstrophy $\mathcal{E}(\mathbf{u}_h)$ and palinstrophy $\mathcal{P}(\mathbf{u}_h)$ monitored over time for $\mathbf{RT}_{[k]}^{\text{red}}/\mathbb{P}_0^{\text{dc}}$ (left column) and $\mathbf{Q}_k^{\text{dc}}/\mathbf{Q}_{k-1}^{\text{dc}}$ (right column).

Now back to the original question. Which mechanism triggers the destruction of the vortical structure and leads to the non-robustness of the L^2 -DG method? In order to answer this question, note that up to now we did not include the DG-grad-div stabilisation into the L^2 -DG method, i.e. $\gamma = 0$. Recalling Sec. 3.2.2, we will now add broken grad-div and $\mathbf{H}(\text{div})$ stabilisation by using $\gamma > 0$. As a result, both the elementwise divergence and the facetwise normal jumps of the discrete velocity decreases. Let us now try to improve the previously inadequate $\mathbf{Q}_k^{\text{dc}}/\mathbf{Q}_{k-1}^{\text{dc}}$ results in the low-order case $(k, N) = \{2, 20\}$.

Fig. 4.4 shows the impact of DG-grad-div stabilisation (see Sec. 3.2.2) on the L^2 -DG method. Regarding the vorticity, the left column shows that already using $\gamma = 0.001$ suffices such that a vortex is visible; this has not been the case with $\gamma = 0$, see Fig. 4.2. Increasing the stabilisation parameter up to $\gamma = 0.1$ continuously improves the ability of the method to preserve the vortex structure to such an extent that qualitatively, one cannot distinguish the stabilised L^2 solution from the exactly

divergence-free $\mathbf{H}(\text{div})$ one anymore. The right column of Fig. 4.4 is again aimed at a more quantitative comparison in terms of kinetic energy, enstrophy and palinstrophy. Here, we observe that the strong energy loss is sufficiently cured as γ increases. Also, the unphysical increase in $\mathcal{E}(\mathbf{u}_h)$ is rectified more and more and finally, the palinstrophy does not explode anymore. Therefore, a capable remedy which improves the structure preservation properties of the L^2 -DG method is the DG-grad-div stabilisation.

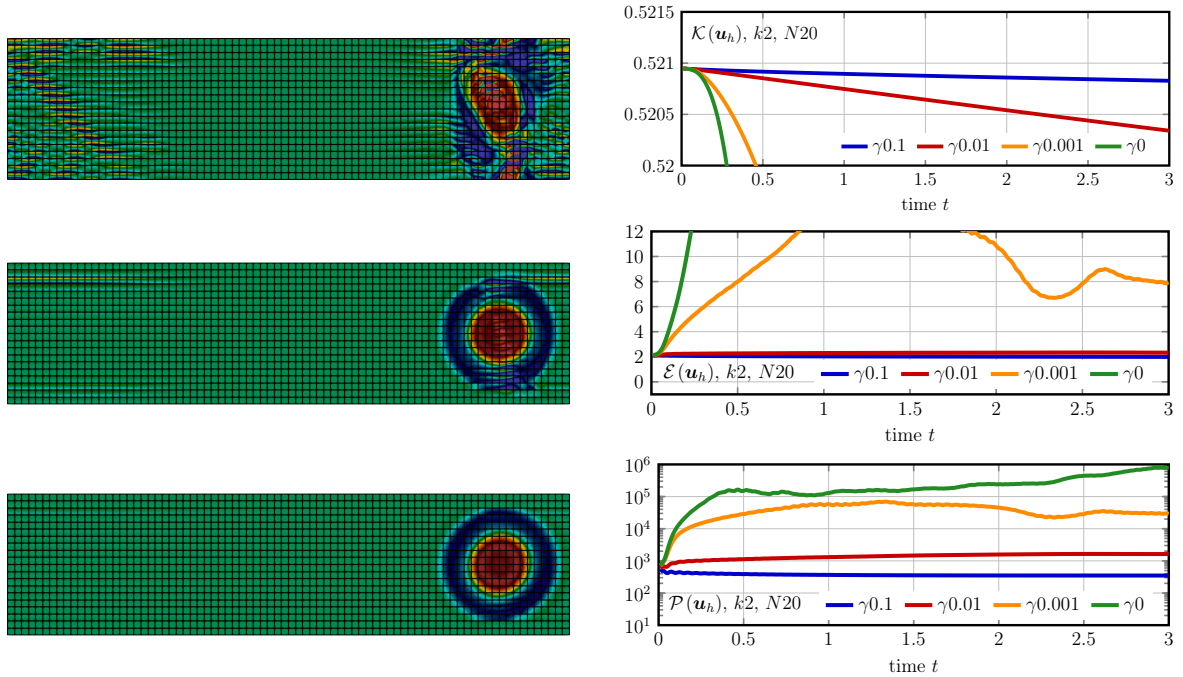


Fig. 4.4: Impact of DG-grad-div with parameter $\gamma \geq 0$ for the L^2 -DG method on the Gresho vortex problem for low-order $(k, N) = (2, 20)$. Left column shows the final state of ω_h for $\gamma = 0.001$ (first row), $\gamma = 0.01$ (second row) and $\gamma = 0.1$ (last row). Right column shows the corresponding evolution of kinetic energy, enstrophy and palinstrophy.

After having identified *how* to improve the robustness of the L^2 -DG method, one question remains. *Why* does DG-grad-div improve the robustness for the moving Gresho vortex problem? Phrased differently, what characteristic does this particular flow problem possess, which makes it so hard to simulate with the L^2 -DG method without DG-grad-div? The answer to this question is actually much more involved, and we will need the concept of pressure-robustness for it; cf. Sec. 4.2. However, at this point, let us at least give a brief motivation for it, thereby leading over smoothly to the next subsection.

For the remainder of this section, we will take a closer look at the fluid flow itself and not primarily at its discretisation anymore. Due to reasons which will become clear later on, it can be interesting to investigate the convection term $(\mathbf{u} \cdot \nabla)\mathbf{u}$ and, in particular, its (continuous) Helmholtz decomposition introduced in Sec. 2.2.3. The underlying question is what kind of forces are present in the Gresho problem. Unfortunately, the exact velocity \mathbf{u} for this problem is not known and therefore, we resort to analysing the flow by means of a discretisation. Judging from the above

demonstrations it is safe to assume that the $\mathbf{H}(\text{div})$ -DG method yields the ‘better’, or at least more reliable, approximation to this problem. Thus, let us investigate the discrete convection term $\mathbf{f}_h := (\mathbf{u}_h \cdot \nabla_h) \mathbf{u}_h$, computed with $\mathbf{RT}_{[k]}^{\text{red}}/\mathbb{P}_0^{\text{dc}}$ for $(k, N) = (6, 8)$ and its discrete Helmholtz decomposition $\mathbf{f}_h = \mathbb{P}_h^{\text{div}}(\mathbf{f}_h) + \nabla \phi_h$, computed with $\mathbf{RT}_{[k]}/\mathbb{P}_k^{\text{dc}}$; see (3.10) in Ch. 3.

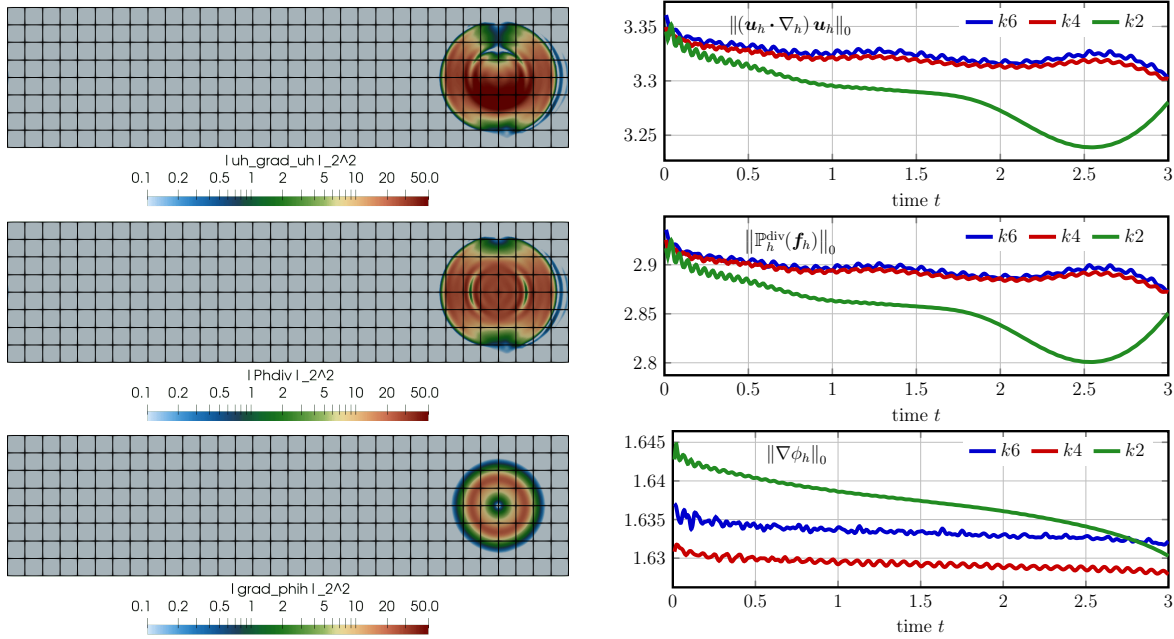


Fig. 4.5: Discrete Helmholtz decomposition of discrete convective term $\mathbf{f}_h = (\mathbf{u}_h \cdot \nabla_h) \mathbf{u}_h$. Left column: $|\mathbf{f}_h|_2^2$, $|\mathbb{P}_h^{\text{div}}(\mathbf{f}_h)|_2^2$ and $|\nabla \phi_h|_2^2$ at $t = 3$ for $\mathbf{RT}_{[6]}/\mathbb{P}_6^{\text{dc}}$. Right column: Evolution of the corresponding norms $\|\mathbf{f}_h\|_{L^2}$, $\|\mathbb{P}_h^{\text{div}}(\mathbf{f}_h)\|_{L^2}$ and $\|\nabla \phi_h\|_{L^2}$ for $\mathbf{RT}_{[k]}/\mathbb{P}_k^{\text{dc}}$.

In Fig. 4.5, the first row gives an idea of how strong the (discrete) convective part \mathbf{f}_h is in this problem. From the second row we deduce that a significant part of the force \mathbf{f}_h consists of a divergence-free part, which is represented by the discrete Helmholtz projection $\mathbb{P}_h^{\text{div}}(\mathbf{f}_h)$. However, the third row shows that nonetheless, there is a non-negligible gradient part present which stands for an irrotational force. As will be explained in the next section, irrotational forces in a fluid flow problem can cause severe problems for certain discretisation schemes which are *non-pressure-robust*, but can be handled easily with *pressure-robust* methods. The $\mathbf{H}(\text{div})$ -DG method is of the latter type, whereas the L^2 -DG method is of the former, and DG-grad-div is actually a stabilisation mechanism which improves the pressure-robustness of an otherwise non-pressure-robust method. In the remainder of this thesis, all these aspects will be explained in more detail.

Remark 4.1 (Helmholtz decomposition of $(\mathbf{u}_h \cdot \nabla_h) \mathbf{u}_h$): In this work, the distribution of convection forces according to $\mathbf{f}_h = \mathbb{P}_h^{\text{div}}(\mathbf{f}_h) + \nabla \phi_h$ will be examined at several places. Always, only the volume contribution of the discrete convection term, i.e. $\mathbf{f}_h = (\mathbf{u}_h \cdot \nabla_h) \mathbf{u}_h$, is used in the corresponding Helmholtz decomposition. Note that this approach is indeed meaningful in comparably well-resolved simulations, where the occurring facet terms in c_h (see Sec. 3.2.3) are expected to be insignificantly small. \blacktriangle

4.2 Pressure-Robustness

As has already been pointed out, the second concept which is crucial throughout this thesis is *pressure-robustness*; cf., for example, [ALM17; JL⁺17] for a more detailed explanation. Let us give the most general form of a definition.

Definition 4.2 (*Pressure-robust method*)

A numerical method is called *pressure-robust* if the following holds true: Let the exact velocity \mathbf{u} belong to the discrete approximation space, i.e. $\mathbf{u} \in \mathbf{V}_h$. Then, the approximate velocity coincides with the exact one, that is, $\mathbf{u}_h \equiv \mathbf{u}$.

At first glance, one could think that any method should honour this very basic definition. However, the fact that flow problems are mixed problems prevents this from being true. In fact, as the name suggests, it turns out that the pressure variable plays a very important role in this concept. In the following, we want to show that indeed pressure-robustness cannot be taken for granted.

The probably easiest type of flow is a fluid at rest (*hydrostatics*), i.e. $\mathbf{u} \equiv \mathbf{0}$. But yet already such a seemingly trivial situation surprisingly can be difficult for discretisation schemes which are not pressure-robust. In the context of such *no-flow* problems, it lends itself to introduce the following invariance principle (the validity of this statement is straightforward).

Lemma 4.3 (*Continuous invariance principle*)

Suppose that in the setting of the stationary Navier–Stokes equations (2.19) with no-slip BC $\mathbf{u} \equiv \mathbf{0}$ on $\partial\Omega$, the right-hand side term is a conservative (irrotational) force; that is, there exists a potential Φ such that $\mathbf{f} = \nabla\Phi$ ¹⁵. Then, independently of how large/strong the potential Φ is, the unique exact solution to the flow problem is $(\mathbf{u}, p) = (\mathbf{0}, \Phi + C)$, where $C \in \mathbb{R}$ is constant.

Note Rem. 2.13 and the close relationship of this principle with the Helmholtz projection. This is the invariance principle on the continuous level; for pressure-robust discretisations it directly transfers to the discrete case, whereas non-pressure-robust methods in general do not respect it.

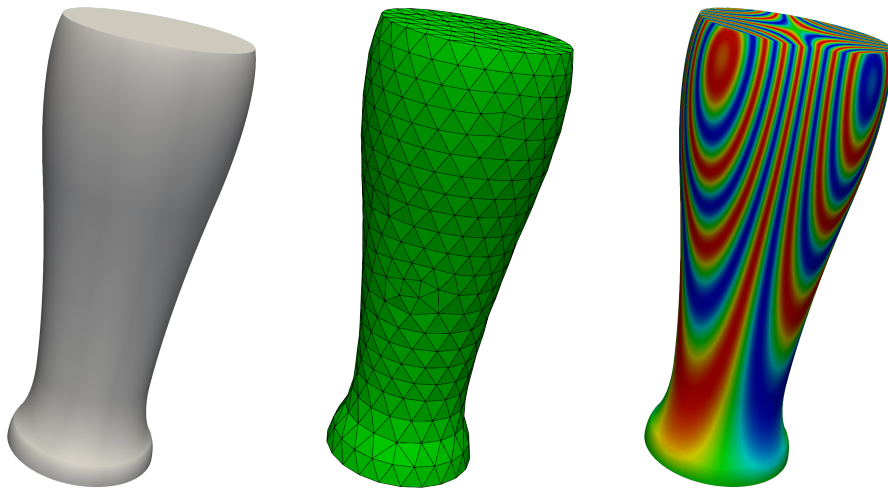


Fig. 4.6: No-flow in a glass. Geometry (left), tetrahedral mesh (middle) and exact pressure (right).

¹⁵Probably the most obvious and simple conservative force is the gravitational force.

Let us, for simplicity, consider the no-flow example only in the setting of the stationary Stokes equations (2.21) with $\mathbf{u} \equiv \mathbf{0}$ on $\partial\Omega$. The particular domain is chosen as the glass visible in Fig. 4.6 (left). This domain is decomposed into 3229 tetrahedra as shown in Fig. 4.6 (middle) and we take the exact pressure solution as $p = 10^{-4} \sin(x_1 x_2 x_3)$, see Fig. 4.6 (right). Consequently, \mathbf{f} is a gradient force and thus, the exact velocity solution is $\mathbf{u} \equiv \mathbf{0}$ (no-flow).

Table 4.1: Material properties at 20 °C and 1 atm.

Material	ρ [kg m ⁻³]	μ [Pa s] (dyn.)	ν [m ² s ⁻¹] (kin.)
Honey	1420	14.1	9.9×10^{-3}
Engine oil	850.4	0.38	4.47×10^{-4}
Hydrogen	0.083 75	8.81×10^{-6}	1.05×10^{-4}
Air	1.204	1.82×10^{-5}	1.51×10^{-5}
Water	998.2	1×10^{-3}	1.002×10^{-6}
Mercury	13 545	1.54×10^{-3}	1.14×10^{-7}

For the discretisation we fix the order $k = 3$ for the velocity FE space and compare the pressure-robust, exactly divergence-free $\mathbf{H}(\text{div})$ -DG method $\mathbf{BDM}_3/\mathbb{P}_2^{\text{dc}}$ (see (3.15)) with the classical grad-div stabilised ($\gamma = 0.1$), \mathbf{H}^1 -conforming Taylor–Hood method $\mathbb{P}_3/\mathbb{P}_2$ (see (3.19)). In order to put the following computations in a physically more realistic context, the fluid in the glass, which is supposed to rest, is varied according to the materials¹⁶ (liquid and gaseous) listed in Table 4.1.

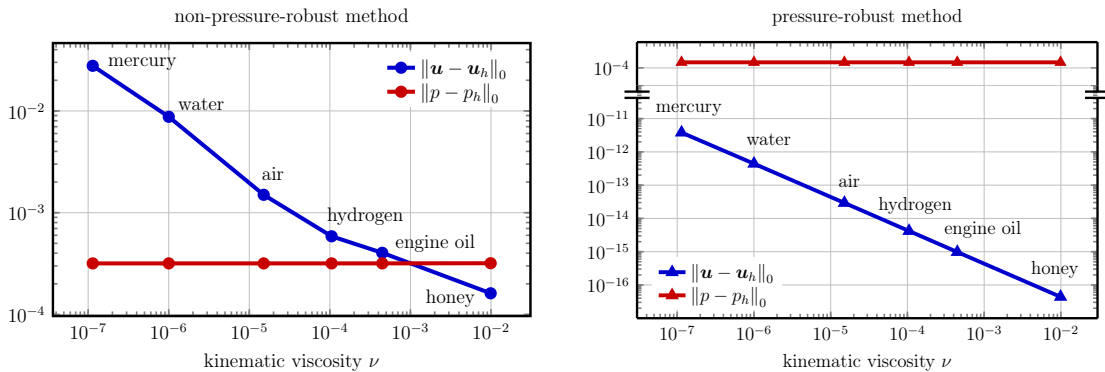


Fig. 4.7: Velocity and pressure errors for the no-flow ($\mathbf{u} \equiv \mathbf{0}$) problem in a glass filled with different fluids. Non-pressure-robust method (left) and pressure-robust method (right).

In Fig. 4.7, comparing the non-pressure-robust (left) and the pressure-robust (right) method, the resulting $L^2(\Omega)/L^2(\Omega)$ velocity and pressure errors are shown for the different materials. First of all, note that the pressure errors, regardless of pressure-robustness, are invariant against changing the viscosity. The velocity error, on the other hand, is at least ten orders of magnitude larger for the non-pressure-robust method. Indeed, the velocity error for the pressure-robust method should in fact be exactly zero, but suffers from the ‘variational crime’ of numerical integration which is especially pronounced in the context of curved boundaries here. This example shows quite powerfully the importance and advantages of pressure-robust methods, even for seemingly easy flow

¹⁶Of course, the basic assumption of a Newtonian fluid might be violated by several of these materials. But for the intended insight, this is unproblematic.

problems. The next subsections show that the exact same statement can also be made for a large number of significantly more complicated flows.

4.2.1 Potential Flows

Let us now consider one particular class of flow problems, namely *potential flows* [Dur08, Ch. 10]. Potential flows are characterised by the property that the velocity \mathbf{u} is represented as the gradient of a scalar function φ , the so-called *velocity potential*¹⁷. Thus, $\mathbf{u} = \nabla\varphi$ and such flows are also inherently irrotational (curl-free) as $\text{curl } \mathbf{u} = \text{curl}(\nabla\varphi) = \mathbf{0}$ and therefore, potential flows are closely related to inviscid, irrotational flows; cf. [Tri88, Ch. 10]. Invoking the divergence-free constraint, it also becomes clear that $\nabla \cdot \mathbf{u} = \nabla \cdot \nabla\varphi = \Delta\varphi = 0$ and thus, the vector potential of an incompressible potential flow always solves the Poisson equation. Note that also in the case of time-dependent flows, that is $\varphi = \varphi(t)$, these properties hold and thus, potential flows do not depend on the history of its motion but are completely determined by the associated boundary conditions.

Following [LM16], inserting $\mathbf{u} = \nabla\varphi$ with $\Delta\varphi = 0$ into the time-dependent incompressible Navier–Stokes equations (2.1) for $\mathbf{f} = \mathbf{0}$ and assuming sufficient regularity, one can use the identities

$$\begin{aligned} \partial_t \mathbf{u} &= \partial_t(\nabla\varphi) = \nabla(\partial_t\varphi), \\ -\nu\Delta\mathbf{u} &= -\nu\Delta(\nabla\varphi) = -\nu\nabla(\Delta\varphi) = \mathbf{0}, \\ (\mathbf{u} \cdot \nabla)\mathbf{u} &= \text{curl } \mathbf{u} \times \mathbf{u} + \frac{1}{2}\nabla(\mathbf{u} \cdot \mathbf{u}) = \frac{1}{2}\nabla|\mathbf{u}|^2 = \nabla\left(\frac{1}{2}|\nabla\varphi|^2\right), \end{aligned}$$

to obtain the following equation for the pressure:

$$\nabla\left[p + \frac{1}{2}|\nabla\varphi|^2 + \partial_t\varphi\right] = \mathbf{0}.$$

Thus, the velocity potential φ completely determines the solution of potential flows, which is given by $(\mathbf{u}, p) = \left(\nabla\varphi, -\frac{1}{2}|\nabla\varphi|^2 - \partial_t\varphi + f(t)\right)$ where $f(t)$ denotes a time-dependent function. Furthermore, the function $P = p + \frac{1}{2}|\nabla\varphi|^2 + \partial_t\varphi + f(t)$ is called *Bernoulli pressure*.

Now, let us turn to a specific two-dimensional example. Exploiting the Cauchy–Riemann equations, it can be shown that one possibility of defining a potential is by taking the real part $\Re(\cdot)$ of a so-called *complex potential* $F(z)$, $z \in \mathbb{C}$. In this setting, the imaginary part is inherently connected to the stream function of the particular flow. More precisely, let us consider $F(z) = z^2 = (x + iy)^2$, which results in the potential $\varphi = \Re(z^2) = x^2 - y^2$. This choice leads to the following solutions.

- Stokes: $\mathbf{u} = \nabla\varphi = (2x, -2y)^\dagger$, $p = 0$.
- Euler and Navier–Stokes: $\mathbf{u} = \nabla\varphi = (2x, -2y)^\dagger$, $p = -\frac{1}{2}|\nabla\varphi|^2 = -\frac{1}{2}(\mathbf{u} \cdot \mathbf{u}) = -2(x^2 + y^2)$.

Note that when it comes to potential flows, the velocity field usually coincides for the Stokes, the Euler and the Navier–Stokes problem. Only the pressure changes as a result of $(\mathbf{u} \cdot \nabla)\mathbf{u}$ being a gra-

¹⁷Note that of course, the previous no-flow example is also a potential flow with a constant potential.

dient¹⁸. Choosing a cross-shaped domain, Fig. 4.8 visualises the resulting exact flow field together with a mesh for the subsequent simulations for this problem. One can see that we basically deal with a flow which comes from both top and bottom of the domain, collides in the middle and then flows out in left/right direction. Naturally, the pressure peaks in the vicinity of the collision point in the middle. Thus, this example has some conceptual similarities with [Lin09], where a collision in a cross-shaped domain is investigated in a different setting where no analytical solution is available.

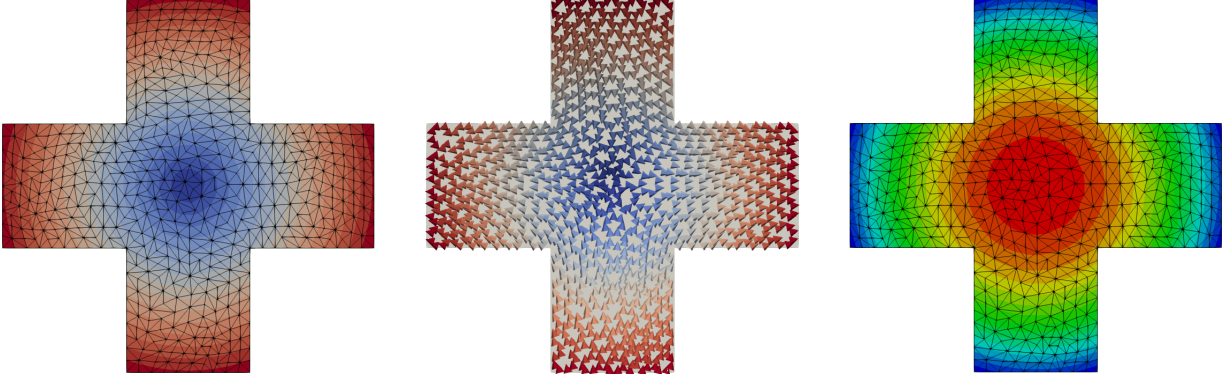


Fig. 4.8: Colliding potential flow defined by $\varphi = x^2 - y^2$. Velocity magnitude $|\mathbf{u}|$ (left), cones representing the velocity field \mathbf{u} (middle) and pressure (right) on an unstructured triangular mesh. The centre of the domain corresponds to $(0, 0)$.

For this situation we now compare the accuracy of the exactly divergence-free $\mathbf{H}(\text{div})$ method $\mathbf{BDM}_k/\mathbb{P}_{k-1}^{\text{dc}}$ (see (3.15)) with the classical grad-div stabilised ($\gamma = 0.1$), \mathbf{H}^1 -conforming Taylor–Hood method $\mathbf{P}_k/\mathbb{P}_{k-1}$ (see (3.19)). In Table 4.2, the errors for computations based on second- and third-order FEM are shown. Here, the stationary Navier–Stokes setting (2.19) with $\nu = 10^{-3}$ has been chosen, and the resulting nonlinear systems have been solved using a simple Picard iteration with tolerance 10^{-12} ; see [Riv08, Sec. 7.6].

Table 4.2: Errors for the colliding potential flow example. The most important numbers which show the advantages of a pressure-robust method are in bold type.

order	method	$\ \mathbf{u} - \mathbf{u}_h\ _{L^2}$	$\ \nabla_h(\mathbf{u} - \mathbf{u}_h)\ _{L^2}$	$\ p - p_h\ _{L^2}$
$k = 2$	<i>p</i> -robust	$5.36 \cdot 10^{-12}$	$1.2 \cdot 10^{-10}$	$4.29 \cdot 10^{-3}$
	non- <i>p</i> -robust	$2.66 \cdot 10^{-3}$	$7.82 \cdot 10^{-2}$	$5.51 \cdot 10^{-3}$
$k = 3$	<i>p</i> -robust	$2.96 \cdot 10^{-12}$	$1.24 \cdot 10^{-10}$	$2.32 \cdot 10^{-12}$
	non- <i>p</i> -robust	$1.15 \cdot 10^{-12}$	$2.18 \cdot 10^{-11}$	$1.48 \cdot 10^{-12}$

The first observation is that when using $k = 3$, then $(\mathbf{u}, p) \in \mathbf{V}_h \times Q_h$ and any method yields the exact solution $(\mathbf{u}_h, p_h) = (\mathbf{u}, p)$ (up to round-off error). However, for $k = 2$ we only have $\mathbf{u} \in \mathbf{V}_h$ but $p \notin Q_h$ and a huge difference emerges. While the pressure-robust method yields $\mathbf{u}_h = \mathbf{u}$, the non-pressure-robust method results in a large velocity error. The pressure error, on the other hand, is more or less independent of pressure-robustness here. This example thus clarifies why Def. 4.2 is fundamental.

¹⁸This fact will be investigated in more detail when we discuss generalised Beltrami flows in the next subsection.

4.2.2 Generalised Beltrami Flows

For potential flows in the last subsection, we already saw that it is possible that the nonlinear convection term is in fact the gradient of a potential. Now, let us introduce the whole corresponding family of incompressible flows.

Definition 4.4 (*Generalised Beltrami flow*)

Consider the time-dependent incompressible Navier–Stokes equations (2.1). If there exists a potential ϕ such that $(\mathbf{u} \cdot \nabla)\mathbf{u} = \nabla\phi$, then the resulting flow is called *generalised Beltrami flow*.

Note that quite generally, the velocity solution of a generalised Beltrami flow simultaneously fulfils the incompressible Stokes *and* the Navier–Stokes equations, whereas the corresponding pressures might differ. Following this definition, both the no-flow problem and the potential flow problem are generalised Beltrami flows; all Stokes solutions are trivially generalised Beltrami flows as well. Furthermore, reviving the concept of the Helmholtz decomposition/projection introduced in Sec. 2.2.3, it is clear that for any generalised Beltrami flow $\mathbb{P}((\mathbf{u} \cdot \nabla)\mathbf{u}) = \mathbf{0}$ holds true.

Remark 4.5: A more detailed introduction to generalised Beltrami flows can be found in [DVII], where, in order to pinpoint different subcategories of generalised Beltrami flows, a case differentiation based on the identity

$$(\mathbf{u} \cdot \nabla)\mathbf{u} = (\nabla \times \mathbf{u}) \times \mathbf{u} + \frac{1}{2}\nabla|\mathbf{u}|^2 = \boldsymbol{\omega} \times \mathbf{u} + \frac{1}{2}\nabla|\mathbf{u}|^2 \quad (4.2)$$

is provided. In doing so, the ‘Lamb vector’ $\boldsymbol{\omega} \times \mathbf{u}$ in (4.2) plays a crucial part. ▲

Let us give a brief motivation why investigating generalised Beltrami flows (both theoretically and numerically) is important¹⁹.

1. To the best of the author’s knowledge, all exact Navier–Stokes solutions with right-hand side $\mathbf{f} = \mathbf{0}$, whose analytical form is known, are generalised Beltrami flows, cf. [DR06].
2. Steady, maybe unstable, high Reynolds number flows ($\nu \ll 1$) with $\mathbf{f} = \mathbf{0}$ away from boundary layers, e.g. around obstacles in the fluid, fulfil the approximate momentum balance

$$(\mathbf{u} \cdot \nabla)\mathbf{u} = -\nabla p + \nu\Delta\mathbf{u} \approx -\nabla p.$$

That is, $(\mathbf{u} \cdot \nabla)\mathbf{u}$ approximates a gradient and \mathbf{u} approximates a generalised Beltrami flow; cf. [Lin09].

3. The importance of generalised Beltrami flows for turbulence is also backed up by numerical evidence from the 1980s. For example, in [PY⁺85] numerical experiments for channel flows and homogeneous decaying turbulence indicate that the large-scale turbulent features of a flow behave ‘Beltrami-like’ in regions of low dissipation. In connection therewith, the term ‘local Beltramisation’ is, for example, used in [YO87] and describes the tendency of the flow velocity and vorticity to align locally. In fact, it has even been conjectured that the coherent

¹⁹Some more arguments can again be found in [DVII].

structures of turbulent flows can be characterised as a superposition of approximate Beltrami flows; see also [CM88] for a systematic analysis of hierarchies in Beltrami flows.

In the following, some examples in the context of generalised Beltrami flows are considered which highlight the benefits a pressure-robust discretisation yields; in [DVII], more examples can be found.

Classical 3D Ethier–Steinman Problem

We now want to compare the performance of the pressure-robust $\mathbf{H}(\text{div})$ -DG method $\mathbb{BDM}_k/\mathbb{P}_{k-1}^{\text{dc}}$ and the non-pressure-robust \mathbf{L}^2 -DG method $\mathbb{P}_k^{\text{dc}}/\mathbb{P}_{k-1}^{\text{dc}}$ (both with upwinding, $\theta = 1$) in terms of accuracy and efficiency in the following three-dimensional, time-dependent incompressible Navier–Stokes setting. Fix $\nu = 0.002$, $\mathbf{f} \equiv \mathbf{0}$, $T = 1$ and consider the Ethier–Steinman problem [ES94] with exact velocity

$$\mathbf{u}_0(\mathbf{x}) = -a \begin{bmatrix} e^{ax_1} \sin(ax_2 + bx_3) + e^{ax_3} \cos(ax_1 + bx_2) \\ e^{ax_2} \sin(ax_3 + bx_1) + e^{ax_1} \cos(ax_2 + bx_3) \\ e^{ax_3} \sin(ax_1 + bx_2) + e^{ax_2} \cos(ax_3 + bx_1) \end{bmatrix}, \quad \mathbf{u}(t, \mathbf{x}) = \mathbf{u}_0(\mathbf{x})e^{-\nu d^2 t}. \quad (4.3)$$

Here, the parameters $a = \pi/4$ and $b = \pi/2$ are used and the domain is given as the cube $\Omega = (-1, 1)^3$ with time-dependent Dirichlet BC \mathbf{g}_D according to the exact generalised Beltrami²⁰ solution (4.3). For the simulation, only the initial velocity \mathbf{u}_0 is prescribed and the evolution of the flow is observed; see Fig. 4.9 for a visualisation of the initial flow configuration. Varying polynomial orders $k \in \{2, 3, 4, 6\}$ of the FE spaces are used, the resolution of the particular method is controlled via an unstructured tetrahedral mesh and the SIP penalty parameter $\lambda = 8k^2$ is chosen.

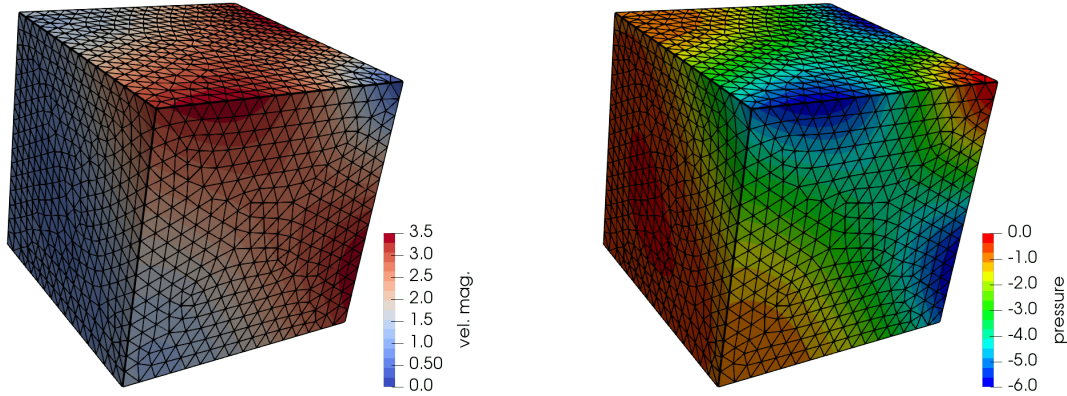


Fig. 4.9: Ethier–Steinman flow at $t = 0$, visualised on an unstructured tetrahedral mesh. Velocity magnitude $|\mathbf{u}|$ (left) and pressure p (right).

The time-stepping is based on the second-order multistep implicit-explicit (IMEX) scheme SBDF2 [ARW95] with a constant time step of $\Delta t = 10^{-4}$, where the Stokes part of the problem is discretised implicitly with a BDF2 method and the convection part relies on an explicit treatment with second-order accurate extrapolation in time. The system matrix of the Stokes part is called M^* and note

²⁰In fact, we are dealing with the special case of a *Beltrami flow*, which is characterised by the property that vorticity and velocity are aligned, $\boldsymbol{\omega} \times \mathbf{u} = \mathbf{0}$, which can only happen in 3D; cf. [DVII].

that in such an IMEX scheme, only linear systems associated with M^* have to be solved in every time step.

Remark 4.6 (Choice of time-discretisation): At this point, a brief remark about the particular choice of time-discretisation is in order. Note that while for the Ethier–Steinman problem the SBDF2-IMEX method is chosen here, for the moving Gresho vortex in Sec. 4.1 the RK2-IMEX method has been used. Depending on what kind of problem is considered, mostly one of these two IMEX schemes is used in this thesis. Practical experience showed that the RK2 method is usually stable (note that a CFL condition due to the explicit treatment appears) for roughly a twice larger time step than the SBDF2 method, but the RK2 method is also roughly twice as expensive to apply per time step (more linear systems have to be solved and more operator applications for the explicit part have to be performed). On the other hand, time-dependent Dirichlet BCs might be easier to implement in a multistep context. Thus, it is mainly a matter of taste which one is used. A systematic investigation concerning IMEX methods in the context of incompressible flows, which basically comes to the same conclusion, can be found in [vWah18]. \blacktriangle

We will compare the following two different quantities: total (velocity plus pressure) number of degrees of freedom (DOFs) and number of non-zero entries (NZE) of M^* . While the DOFs indicate how rich the approximation space is, the NZEs are a reasonable measure of how efficient a particular discretisation is. The NZEs of M^* indicate how expensive solving linear systems is; usually, this is the most time consuming part of a flow solver (especially in 3D).

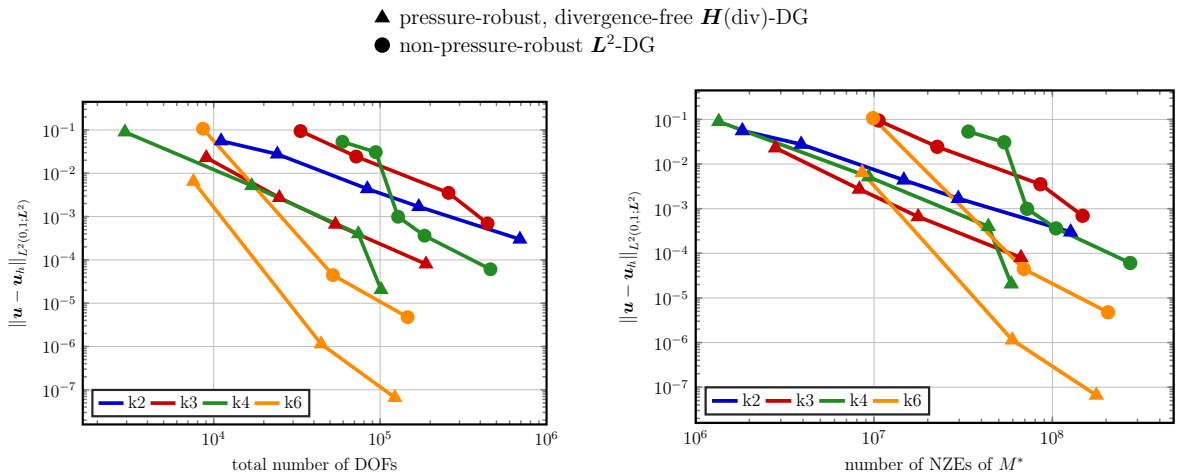


Fig. 4.10: Errors for the classical 3D Ethier–Steinman problem ($\nu = 0.002$). Comparison of pressure-robust $\mathbf{H}(\text{div})$ - and non-pressure-robust L^2 -DG methods with $\Delta t = 10^{-4}$, both using upwinding ($\theta = 1$).

The resulting $L^2(0, T; L^2(\Omega))$ errors can be seen in Fig. 4.10. Firstly, for each fixed k , one can observe that the divergence-free and pressure-robust $\mathbf{H}(\text{div})$ -DG method always yields an at least ten times smaller error, both in terms of DOFs and NZEs. On the finest mesh and with $k = 6$, this offset increases to such an extent that the $\mathbf{H}(\text{div})$ -DG method’s solution has an error which is almost a hundred times smaller. Concerning efficiency, the plot of the number of NZEs shows that by using a pressure-robust method, a significant amount of computational effort can be saved

while maintaining the same level of accuracy.

More precisely, in terms of fixing DOFs, at least on coarse meshes the pressure-robust $k = 2$ $\mathbf{H}(\text{div})$ -DG method is more accurate than the $k = 4$ L^2 -DG method while, at the same time, it leads to fewer NZEs. A similar observation holds for $\mathbf{BDM}_3/\mathbb{P}_2^{\text{dc}}$ and $\mathbb{P}_6^{\text{dc}}/\mathbb{P}_5^{\text{dc}}$. In practice, as higher-order methods usually lead to more NZEs, being able to use a method of order k instead of $2k$, without losing accuracy, means a considerable improvement with respect to performance. However, for sufficiently fine meshes, higher-order methods will always be superior because of the smoothness of the problem and thus, exponential convergence behaviour; cf., for example, [KS05; XC⁺18]. This observation directly leads to the next numerical example.

3D Ethier–Steinman with Inaccurate BCs

In applications, it is very rare that one has an exact geometry description of the underlying domain. For example, curved boundaries make it necessary to approximate also the geometry to a certain accuracy. Therefore, the imposition of the *correct* Dirichlet BCs is usually made on the *approximated* boundary. Unavoidably, this is a source for errors and in this section we want to mimic such a situation in the following equivalent way. Instead of prescribing the correct Dirichlet BCs on the approximated boundary, we will impose inaccurate BCs on the correct boundary.

Let us revisit the 3D Ethier–Steinman problem. The exact solution is also given by (4.3), exactly the same parameters are used and again, time-dependent Dirichlet boundary conditions are imposed. However, now, instead of choosing \mathbf{g}_D according to the exact solution \mathbf{u} , we will use a piecewise quadratic approximation of it instead, such that $\mathbf{g}_D \approx \mathbf{u}$.

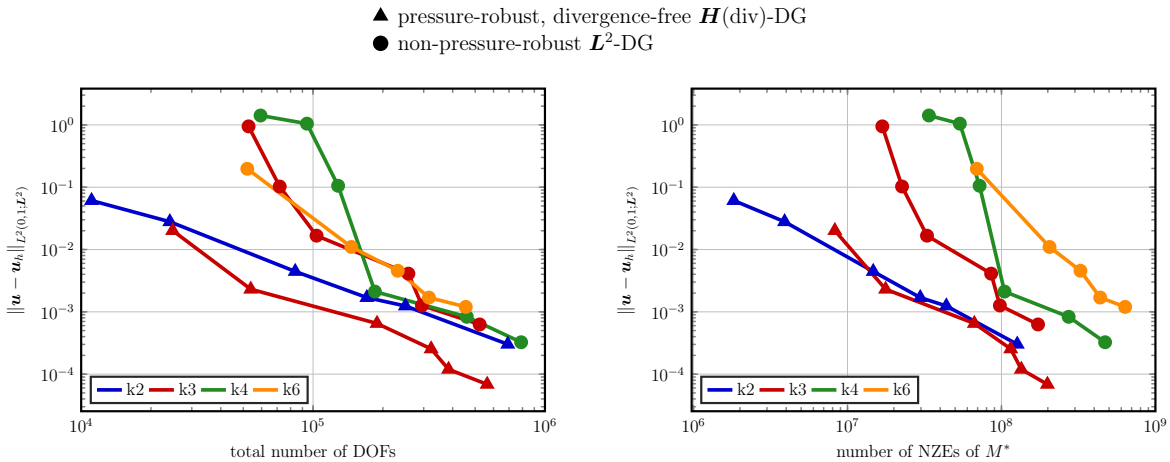


Fig. 4.11: Errors for the 3D Ethier–Steinman problem ($\nu = 0.002$) with inaccurate BCs. Comparison of pressure-robust $\mathbf{H}(\text{div})$ - and non-pressure-robust L^2 -DG methods with $\Delta t = 10^{-4}$, both using upwinding ($\theta = 1$).

Fig. 4.11 shows the resulting $L^2(0, T; L^2(\Omega))$ errors. First of all, note that the pressure-robust method is again always more accurate for a fixed number of DOFs and a fixed number of NZEs. In contrast to the classical Ethier–Steinman problem, the asymptotical behaviour for higher k and

finer meshes is now, by construction, dominated by the accuracy of \mathbf{g}_D . Thus, one can see that all methods roughly lead to the same result when the resolution is high enough; but high-order methods can simply not achieve high-order convergence anymore. The interesting fact now is that on coarse meshes, the pressure-robust method is always significantly more accurate and efficient. Superiority in under-resolved flow settings is actually a very desirable property.

Remark 4.7 (Beyond generalised Beltrami flows): Summarising, we believe that it has now been made abundantly clear that pressure-robust methods are significantly superior whenever generalised Beltrami flows are considered and/or strong gradient forces are present in the underlying motion. What remains to investigate is whether such a statement can be extended to more general flow problems. In this context it is worth to recall the results from Sec. 4.1, where the ability of numerical methods to preserve large-scale/coherent structures has been considered. We have seen that in the transport of a vortex, the nonlinear convective term features a large gradient contribution, see Fig. 4.5. Having the concept of pressure-robustness at our disposal, we have now explained why the $\mathbf{H}(\text{div})$ -DG method gives satisfying results for this problem. Similar investigations for different flow problems, underlining the potential of pressure-robust methods, will appear in the remainder of this thesis. Finally, in Sec. 5.2, we will understand why the DG-grad-div stabilisation actually improves the pressure-robustness of the L^2 -DG method. ▲

Note that in Sec. 8.1, we conduct another 2D numerical experiment which shows that the flow around a blunt body and the associated von Kármán vortex street behaves locally in space like a generalised Beltrami flow, and thus has a strong gradient contribution in $(\mathbf{u} \cdot \nabla)\mathbf{u}$. Moreover, for a 2D Kelvin–Helmholtz problem, Sec. 8.2.2 shows that by investigating the evolution of divergence-free and curl-free contributions to the (discrete) convection term, one can identify their respective roles for vortex dynamics problems. As it turns out, such a free-shear flow can behave like a generalised Beltrami flow in time. Finally, a related study for 3D turbulent flows can be found in Sec. 9.1.4 for a Taylor–Green vortex problem and in Sec. 9.2 for turbulent channel flows.

Remark 4.8 (Div-free methods and p -robustness): In this chapter, most explanations concerning the comparison of p -robust against non- p -robust methods are actually based on comparing exactly divergence-free $\mathbf{H}(\text{div})$ - against L^2 -based DG methods. Most exactly divergence-free methods are naturally also pressure-robust. However, using exactly divergence-free methods is not the decisive factor here and all the qualitative statements which have been made above also hold for other pressure-robust/non-pressure-robust methods (for example, Scott–Vogelius vs. Taylor–Hood). ▲

4.3 Reynolds-Semi-Robustness

The last concept which we want to discuss at this point is much more subtle and connected to numerical error analysis. More precisely, it is related to the worst case behaviour of the velocity error due to the nonlinearity of the convection term in the time-dependent setting. This behaviour is reflected in the numerical error analysis by Gronwall constants depending at least exponentially on time. The following definition is inspired by the original proposal for scalar diffusion-advection problems presented in [RST08].

Definition 4.9

A numerical method is called *Reynolds-semi-robust*, short *Re-semi-robust*, if in its error estimates for the time-dependent incompressible Navier–Stokes equations, the constants appearing on the right-hand side (including Gronwall constants) do not explicitly depend on the Reynolds number or, equivalently, on ν^{-1} .

Indeed, in case of $0 < \nu \ll 1$, in many estimates available in the literature the constant C in the exponential growth $\exp(Ct)$ in fact depends on the Reynolds number Re (respectively, on ν^{-1}) or even higher positive powers of Re . Obviously, such error estimates can describe a sensible error behaviour only for ultra short time intervals. Partially, the problems in the numerical analysis come from very weak assumptions on the exact solution \mathbf{u} and the data. It turns out that error estimates can be improved considerably under the essential regularity condition $\nabla \mathbf{u} \in L^1(\mathbf{L}^\infty)$, which has been introduced and discussed already in Sec. 2.2.2 in detail²¹.

Remark 4.10 (Some history): Let us briefly comment on some milestones in the development of this analysis technique. Concerning Re-semi-robust error estimates, [BF07] is presumably the first work which takes advantage of the regularity assumption $\nabla \mathbf{u} \in L^1(\mathbf{L}^\infty)$ in the analysis of a CIP-stabilised \mathbf{H}^1 -FEM with equal-order approximation of velocity and pressure. For an equal-order method with local projection stabilisation (LPS), we refer to the recent work [dFG+18b]²². For \mathbf{H}^1 -conforming inf-sup stable FEM, in [ADL15] the combination with grad-div stabilisation in some different energy norm led to Re-semi-robust error estimates, which have been sharpened in [DA16] and, in particular concerning optimal pressure estimates, deepened in [dFG+18a]. Re-semi-robustness for divergence-free \mathbf{H}^1 -FEM has been shown for the first time in [DII], and for divergence-free $\mathbf{H}(\text{div})$ -DG methods in [DIII; DIV]. Results for $\mathbf{H}(\text{div})$ methods in the case of the incompressible Euler equations ($\nu = 0$) can be found, for example, in [GSS17; NC18]. ▲

Before considering error analysis for the full Navier–Stokes problem in Ch. 6 in more detail, we want to show exemplarily already now that for a 2D vortex problem, the exponential growth of the Re-semi-robust Gronwall-based error estimates can indeed be observed at least qualitatively in practice; cf. [DIV].

The so-called ‘planar lattice flow’ problem [Ber88] consists of four vortices which are oppositely rotating at a fixed position in the periodic domain $\Omega = (0, 1)^2$. A freely-decaying exact solution of (2.1) with $\mathbf{f} = \mathbf{0}$ which describes such a flow is given by

$$\mathbf{u}_0(\mathbf{x}) = \begin{bmatrix} \sin(2\pi x_1) \sin(2\pi x_2) \\ \cos(2\pi x_1) \cos(2\pi x_2) \end{bmatrix}, \quad \mathbf{u}(t, \mathbf{x}) = \mathbf{u}_0(\mathbf{x}) e^{-8\pi^2 \nu t}. \quad (4.4)$$

This example also represents a generalised Beltrami flow (see Sec. 4.2.2) and has been investigated (in this or slightly different form) in detail, also qualitatively, in [DII; DIII; DIV; DVII; DVIII]²³. Only the initial velocity \mathbf{u}_0 is prescribed in the simulation and induces a flow structure which, due to its saddle point character, is ‘*dynamically unstable so that small perturbations result in a very*

²¹Actually, flows which fulfil this regularity condition are dubbed ‘computable’ in [DIV].

²²Note, however, that using non-inf-sup stable methods excludes the possibility of obtaining pressure-robustness.

²³A 3D extension of (4.4) in form of an unstable Beltrami flow has been considered in [DVIII].

chaotic motion' [MB02]. In Fig. 4.12 the initial flow configuration, together with the two triangular meshes which will be used for this problem, are shown. Note that the meshes are unstructured and therefore do not exploit the saddle-point structure of the flow.

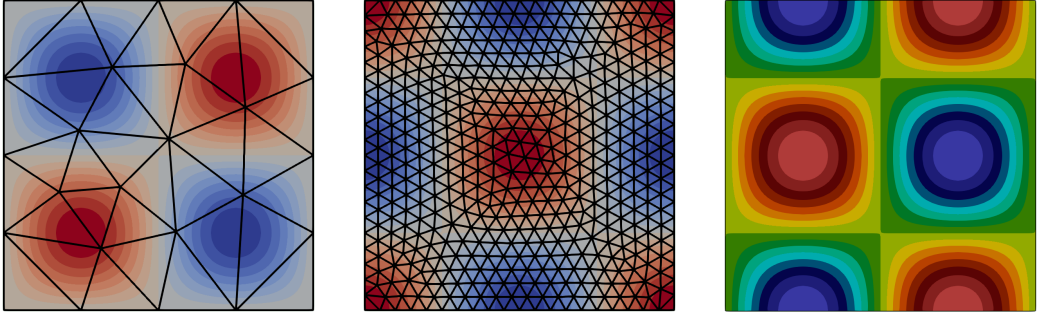


Fig. 4.12: Initial velocity of the lattice flow problem and triangular meshes without singular vertices. Left: Coarse mesh (34 triangles) with $h = 0.25$ and first component of \mathbf{u}_0 ; middle: fine mesh (902 triangles) with $h = 0.05$ and second component of \mathbf{u}_0 ; right: vorticity computed from \mathbf{u}_0 .

For the time-integration, the second-order multistep implicit-explicit (IMEX) scheme SBDF2 from [ARW95] with a constant time step of $\Delta t = 10^{-4}$ is again employed. The small time step makes it possible to neglect errors stemming from the time discretisation. Our aim is to demonstrate the role of the Gronwall factor for simulations over $(0, T)$ for ‘large’ T and for high Reynolds numbers; we choose $T = 26$ and $\nu = 10^{-5}$.

On the shown meshes we consider different high-order methods. The \mathbf{H}^1 -conforming methods under comparison are the pure Galerkin formulation of the Taylor–Hood method $\mathbb{P}_8/\mathbb{P}_7$ (Galerkin-TH8), Taylor–Hood with additional grad-div stabilisation (grad-div-TH8) with $\gamma = 0.1$ (both non-divergence-free) and the divergence-free Scott–Vogelius element $\mathbb{P}_8^{\text{dc}}/\mathbb{P}_7$ (SV8). Concerning $\mathbf{H}(\text{div})$ -conforming methods, the divergence-free DG method $\mathbb{BDM}_8^{\text{red}}/\mathbb{P}_0^{\text{dc}}$ (BDM8) and the also divergence-free hybridised variant $\mathbb{BDM}_8^{\text{red}}/\mathbf{F}_8/\mathbb{P}_0^{\text{dc}}$ (hBDM8) are chosen; see Sec. 3.5.3. For the DG variant we choose $\lambda = 4k^2$ for the SIP penalty and make a corresponding choice for HDG.

A visualisation of the performance of the different methods can be seen in Fig. 4.13. Let us comment on some aspects of the results. For classical Taylor–Hood elements, one observes an immediate blow-up of the Gronwall factor due to the fact that without grad-div stabilisation, the method is not Re-semi-robust. However, grad-div stabilisation can considerably improve the results of the Galerkin variant. Non-div-free grad-div stabilised Taylor–Hood, div-free Scott–Vogelius FEM and div-free $\mathbf{H}(\text{div})$ -(H)DG show the theoretical qualitative behaviour of the exponential Gronwall factor. No immediate blow-up occurs. On the coarse mesh, $\mathbf{H}(\text{div})$ -conforming methods provide much better results than \mathbf{H}^1 -FEM. On the fine mesh, all Re-semi-robust methods perform similarly.

In addition to considering the situation when the mesh is refined, one can of course also increase the polynomial order of the underlying FE spaces. The results of such an approach, using the $\mathbb{BDM}_k^{\text{red}}/\mathbf{F}_k/\mathbb{P}_0^{\text{dc}}$ with $k \in \{2, \dots, 9\}$ and for which the mesh with $h = 0.05$ has been fixed, can

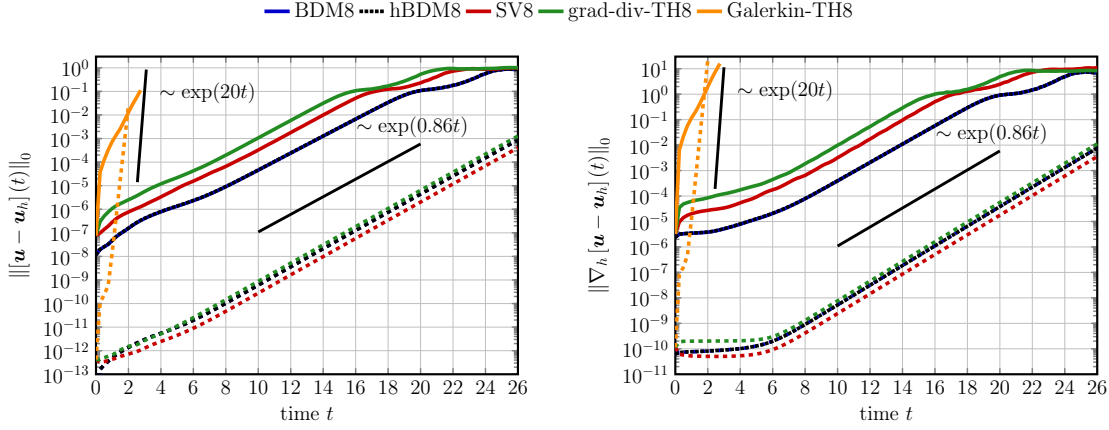


Fig. 4.13: Evolution of L^2 -norm and (broken) H^1 -seminorm errors for the lattice flow problem. Results on the coarse mesh are shown by solid lines, the fine mesh is indicated by dashed lines. The $H(\text{div})$ -HDG method on the coarse mesh is shown with black dots.

be seen in Fig. 4.14. First of all, the exponential growth of the error due to the Gronwall term is still visible, and also the slope remains the same for all considered orders. The overall level of the error, on the other hand, displays exponential convergence as can be expected from such a smooth flow problem. Note that the results with even polynomial orders systematically seem to be slightly better than the corresponding ones with odd orders. Furthermore, one can observe that with $k = 8$ the error is already in the order of magnitude of machine precision, which means that increasing the resolution to $k = 9$, even at $t = 0$, does not further improve the results anymore²⁴.

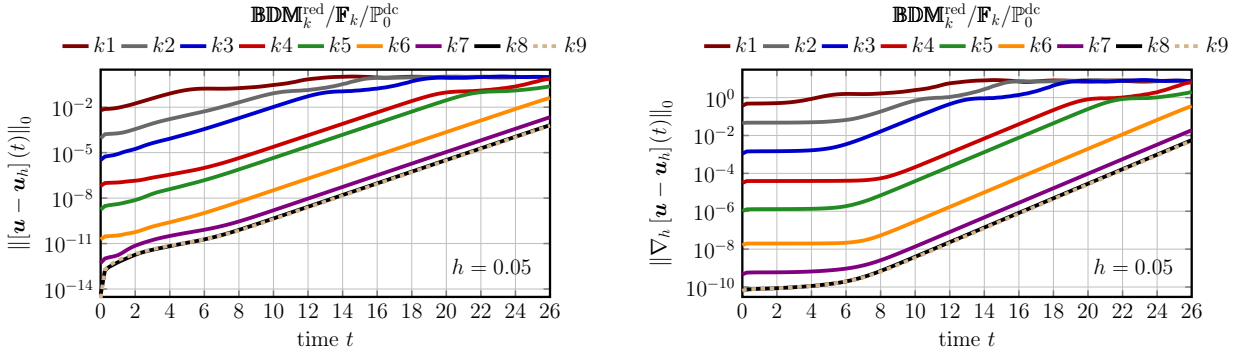


Fig. 4.14: Evolution of L^2 -norm and (broken) H^1 -seminorm errors for the lattice flow problem under k -refinement on the $h = 0.05$ mesh with $\Delta t = 10^{-4}$. Exponential convergence can be observed. The highest orders' errors reach machine precision.

²⁴We also confirmed this using smaller Δt , so it does not seem to be the time error which dominates the overall error.

Stokes Analysis with Emphasis on Pressure-Robustness

Structure of this chapter: We begin with numerical analysis for the simplest problem in Sec. 2.5 – the stationary incompressible Stokes problem (2.21) with no-slip BC $\mathbf{u} = \mathbf{0}$ on $\partial\Omega$. The most basic case of divergence-free \mathbf{H}^1 methods is discussed first (more details can be found in [DII]), then the divergence-free $\mathbf{H}(\text{div})$ -DG case is explained (more details can be found in [DIII; DIV]), and we finish with analysis for the DG-grad-div stabilisation of L^2 -DG methods, which reveals some important connections between the $\mathbf{H}(\text{div})$ solution and the stabilised L^2 one, cf. [DV] for more details. Having velocity error estimates for the Stokes discretisation is essential in the context of the so-called ‘Stokes projection’ for the analysis of the Navier–Stokes problem in Ch. 6. We only present velocity estimates here, since pressure-robustness allows for a clean splitting.

5.1	Divergence-Free \mathbf{H}^1- and $\mathbf{H}(\text{div})$-DG-FEM	67
5.2	The Analogue of Grad-Div for L^2-DG-FEM	69

In order to obtain optimal L^2 -estimates for the velocity, we always make the following assumption which is called ‘elliptic regularity’, ‘Cattabriga’s regularity’ or ‘smoothing property’, depending on the particular literature.

Assumption C: Assume that Ω is either a convex polygon for $d = 2$ or of class $C^{1,1}$ for $d \in \{2, 3\}$. Then, for all $\mathbf{f} \in \mathbf{L}^2(\Omega)$, the solution $(\mathbf{u}, p) \in \mathbf{V} \times Q$ of the Stokes problem (2.21) additionally fulfils the regularity property $(\mathbf{u}, p) \in \mathbf{H}^2(\Omega) \times H^1(\Omega)$ and the energy estimate $\sqrt{\nu} \|\mathbf{u}\|_{\mathbf{H}^2} + \|p\|_{H^1} \leq C \|\mathbf{f}\|_{L^2}$; cf. [EG04, Lem. 4.17] or [BF13, Thm. IV.5.8].

5.1 Divergence-Free \mathbf{H}^1 - and $\mathbf{H}(\text{div})$ -DG-FEM

Consider the same setting as in Sec. 3.4, with the additional assumption that $\nabla \cdot \mathbf{V}_h \subset Q_h$, thereby guaranteeing an exactly divergence-free velocity approximation $\nabla \cdot \mathbf{u}_h = 0$. For example, one can think of the Scott–Vogelius element. The following error estimate can then be obtained.

Theorem 5.1 (*Div-free \mathbf{H}^1 Stokes error estimate*)

Under Asm. C, and provided $\mathbf{u} \in \mathbf{H}^r(\Omega)$, the error estimate

$$\|\mathbf{u} - \mathbf{u}_h\|_{L^2} + h \|\nabla[\mathbf{u} - \mathbf{u}_h]\|_{L^2} \leq Ch \inf_{\mathbf{v}_h \in \mathbf{V}_h^{\text{div}}} \|\nabla[\mathbf{u} - \mathbf{v}_h]\|_{L^2} \leq Ch^{r_u} \|\mathbf{u}\|_{\mathbf{H}^{r_u}}$$

holds true with $r_u = \min\{r, k + 1\}$.

Proof: The first estimate is a simple adaption to the \mathbf{H}^1 case of [DIII, Thm. 3.3], while the convergence rate can be shown to hold using [JL⁺17, Lem. 4.3] together with the optimal polynomial

approximation properties of the FE spaces; cf. Rem. 3.4. We also refer to the explanations in [Joh16, Rem. 4.38] for more details. \blacksquare

The most important property of Thm. 5.1 is that the error estimate does not involve the pressure term in any way. In other words, the optimal error estimate for the velocity is guaranteed *independently* of how good (or bad) the corresponding pressure is approximated. This is another advantage of working with a pressure-robust method.

Remark 5.2 (Non- p -robust Stokes estimates): In order to underline the importance of pressure-robust error estimates, let us consider the corresponding results for non-pressure-robust methods. For example, a classical Galerkin Taylor–Hood method²⁵ leads to [EG04; GR86; JL⁺17; Joh16]

$$\|\nabla[\mathbf{u} - \mathbf{u}_h]\|_{L^2} \leq C \left[\inf_{\mathbf{v}_h \in \mathbf{V}_h^{\text{div}}} \|\nabla[\mathbf{u} - \mathbf{v}_h]\|_{L^2} + \frac{1}{\nu} \inf_{q_h \in Q_h} \|p - q_h\|_{L^2} \right].$$

Thus, whenever ν is small and/or the pressure is large/complicated, the velocity approximation can be corrupted by a poor pressure approximation. The most popular remedy for improving this result is the classical grad-div stabilisation with parameter $\gamma > 0$. Following [JL⁺17], there are certain situations in which the error estimate can then become

$$\|\nabla[\mathbf{u} - \mathbf{u}_h]\|_{L^2} \leq C \left[\inf_{\mathbf{v}_h \in \mathbf{V}_h^{\text{div}}} \|\nabla[\mathbf{u} - \mathbf{v}_h]\|_{L^2} + \frac{1}{\sqrt{\nu\gamma}} \inf_{q_h \in Q_h} \|p - q_h\|_{L^2} \right].$$

Hence, the factor in front of the pressure term changed from ν^{-1} to $\nu^{-1/2}\gamma^{-1/2}$. Such an improvement becomes important again in the context of DG-grad-div stabilisation in Sec. 5.2, since basically the same phenomenon can be observed there. \blacktriangle

For the analysis of the Navier–Stokes problem in Ch. 6, the following lemma is essential for dealing with estimates for the nonlinear convection term $(\mathbf{u} \cdot \nabla)\mathbf{u}$. Concerning the necessary regularity, note again the connection to Sec. 2.2.2.

Lemma 5.3 (*Div-free H^1 Stokes max-norm stability*)

Let Ω be a convex domain. If the solution to the Stokes problem (2.21) fulfils $\mathbf{u} \in \mathbf{W}^{1,\infty}(\Omega)$, then one obtains the stability estimate

$$\|\nabla \mathbf{u}_h\|_{L^\infty} \leq C \|\nabla \mathbf{u}\|_{L^\infty}.$$

Proof: In [GNS15], an analogue of Lem. 5.3 has been shown in the context of non-divergence-free H^1 -conforming methods, which also involve the pressure. The analysis in [GNS15] simplifies for the divergence-free H^1 case, thereby leading to Lem. 5.3. \blacksquare

Leaving the H^1 world, the pressure-robust Stokes error estimate for the exactly divergence-free $\mathbf{H}(\text{div})$ -DG method, introduced in Sec. 3.3, reads as follows.

²⁵Note that $\mathbf{v}_h \in \mathbf{V}_h^{\text{div}}$ is now of course not necessarily exactly divergence-free anymore.

Theorem 5.4 (Div-free $H(\text{div})$ Stokes error estimate)

Under Asm. C, and provided $\mathbf{u} \in \mathbf{H}^r(\Omega)$ for $r > 3/2$, the error estimate

$$\|\mathbf{u} - \mathbf{u}_h\|_{L^2} + h\|\mathbf{u} - \mathbf{u}_h\|_{e,\sharp} \leq Ch \inf_{\mathbf{v}_h \in \mathbf{V}_h^{\text{div}}} \|\mathbf{u} - \mathbf{v}_h\|_{e,\sharp} \leq Ch^{r_u} \|\mathbf{u}\|_{\mathbf{H}^{r_u}}$$

holds true with $r_u = \min\{r, k+1\}$ and a constant $C > 0$.

Proof: The proof of the first estimate can be found in [DIII, Thm. 3.3], while the convergence rate again follows from optimal approximation properties of the $H(\text{div})$ spaces; cf. [BBF13]. ■

Concerning the max-norm properties, however, we have to make the following assumption.

Assumption D: For the $H(\text{div})$ method, we assume max-norm stability and linear convergence for the L^∞ error, that is,

$$\|\mathbf{u} - \mathbf{u}_h\|_{L^\infty} + h\|\nabla_h \mathbf{u}_h\|_{L^\infty} \leq Ch\|\nabla \mathbf{u}\|_{L^\infty}.$$

The validity of this estimate is an open problem although, in principle, similar techniques as in [GNS15] seem to be applicable.

5.2 The Analogue of Grad-Div for L^2 -DG-FEM

The remainder of this chapter is intended to explain why the DG-grad-div stabilisation with parameter $\gamma > 0$, introduced in Sec. 3.2.2, indeed improves the pressure-robustness of the L^2 -DG method; see again Sec. 4.1. Moreover, providing more details, we identify the connection between the $H(\text{div})$ solution and the stabilised L^2 solution as $\gamma \rightarrow \infty$.

Only the main ideas are presented here with a restriction to the simplicial case $\mathbb{P}_k^{\text{dc}}/\mathbb{P}_{k-1}^{\text{dc}}$, and the corresponding velocity estimates; for a much more detailed treatment, see [DV]. As it turns out, on simplicial meshes it is completely sufficient to use

$$j_h(\mathbf{w}_h, \mathbf{v}_h) = \sum_{F \in \mathcal{F}_h} \frac{1}{h_F} \int_F (\llbracket \mathbf{w}_h \rrbracket \cdot \mathbf{n}_F)(\llbracket \mathbf{v}_h \rrbracket \cdot \mathbf{n}_F) \, ds$$

as the only stabilisation mechanism. The addition of the broken grad-div term is necessary only on tensor-product meshes, which is due to the fact that there, $\nabla_h \cdot \mathbb{Q}_k^{\text{dc}} \not\subset \mathbb{Q}_{k-1}^{\text{dc}}$.

For the sake of presentation, let us repeat the weak formulation on the continuous level:

$$\begin{cases} \text{Find } (\mathbf{u}, p) \in \mathbf{V} \times Q \text{ such that, } \forall (\mathbf{v}, q) \in \mathbf{V} \times Q, \\ \nu(\nabla \mathbf{u}, \nabla \mathbf{v}) - (p, \nabla \cdot \mathbf{v}) + (q, \nabla \cdot \mathbf{u}) = (\mathbf{f}, \mathbf{v}). \end{cases}$$

The DG-grad-div stabilised method reads as follows:

$$\begin{cases} \text{Find } (\mathbf{u}_h, p_h) \in \mathbf{V}_h \times Q_h \text{ such that, } \forall (\mathbf{v}_h, q_h) \in \mathbf{V}_h \times Q_h, & (5.2a) \\ \nu a_h(\mathbf{u}_h, \mathbf{v}_h) + \gamma j_h(\mathbf{u}_h, \mathbf{v}_h) + b_h(\mathbf{v}_h, p_h) - b_h(\mathbf{u}_h, q_h) = (\mathbf{f}, \mathbf{v}_h). & (5.2b) \end{cases}$$

Concerning stability, the following energy estimates are straightforward to prove.

Lemma 5.5 (Energy estimate)

Let $\mathbf{f} \in \mathbf{L}^2(\Omega)$. Then, with a constant $C > 0$, one obtains the following estimates for the stabilised \mathbf{L}^2 -DG solution (\mathbf{u}_h, p_h) to the Stokes problem (2.21):

$$\begin{aligned} \frac{\nu C_\lambda}{2} \|\mathbf{u}_h\|_e^2 + \gamma |\mathbf{u}_h|_{\text{nj}}^2 &\leq C \nu^{-1} \|\mathbf{f}\|_{\mathbf{L}^2(\Omega)}^2, \\ \|\nabla_h \cdot \mathbf{u}_h\|_{L^2(\Omega)}^2 &\leq C |\mathbf{u}_h|_{\text{nj}}^2 \leq C \gamma^{-1} \nu^{-1} \|\mathbf{f}\|_{\mathbf{L}^2(\Omega)}^2. \end{aligned}$$

Proof: The complete proof can be found in [DV, Lem. 3.2]. ■

Here, one can directly see that this stabilisation procedure indirectly also penalises both the elementwise divergence and the normal discontinuity of discrete velocities; cf. Sec. 3.2.2.

Concerning error estimates, at first we introduce the stationary error decomposition

$$\begin{aligned} \mathbf{u} - \mathbf{u}_h &= (\mathbf{u} - \boldsymbol{\pi}_h \mathbf{u}) - (\mathbf{u}_h - \boldsymbol{\pi}_h \mathbf{u}) = \boldsymbol{\eta}^u - \mathbf{e}_h^u, \\ p - p_h &= (p - \pi_0 p) - (p_h - \pi_0 p) = \eta^p - e_h^p, \end{aligned}$$

where $(\boldsymbol{\pi}_h, \pi_0): \mathbf{V} \times Q \rightarrow \mathbf{V}_h \times Q_h$ represent appropriate approximation operators, and we refer to $(\boldsymbol{\eta}^u, \eta^p)$ and (\mathbf{e}_h^u, e_h^p) as approximation and discretisation errors, respectively. Without going into detail, note that $\boldsymbol{\pi}_h$ is chosen as the $\mathbf{H}(\text{div})$ BDM interpolator [BBF13], thus revealing a strong relationship also from a theoretical perspective²⁶. The following error estimate can be shown.

Theorem 5.6 (DG-grad-div \mathbf{L}^2 Stokes error estimate)

Let $\mathbf{f} \in \mathbf{L}^2(\Omega)$. Then, there exists a constant $C > 0$ such that

$$\|\mathbf{u} - \mathbf{u}_h\|_e \leq C \left[\|\boldsymbol{\eta}^u\|_{e, \sharp} + \frac{1}{\sqrt{\nu \gamma}} \|\eta^p\|_{L^2(\Omega)} \right].$$

Proof: The entire proof can be found in [DV, Lem. 3.4]. ■

This theorem reveals that, analogously to classical grad-div for \mathbf{H}^1 methods, the DG-grad-div stabilisation term j_h also leads to an improved factor $\nu^{-1/2} \gamma^{-1/2}$ in front of the pressure term; cf. Rem. 5.2. Also analogously, the unstabilised \mathbf{L}^2 -DG method shows a ν^{-1} factor in front of the

²⁶Note that one can show discrete inf-sup stability of the \mathbf{L}^2 method by first showing discrete inf-sup stability of the $\mathbf{H}(\text{div})$ method, and then essentially exploiting that $\mathbf{H}(\text{div}; \Omega) \subset \mathbf{L}^2(\Omega)$ [Riv08].

pressure term [Riv08, Thm. 6.10].

In contrast to Thm. 5.6 which predicts an error reduction with rate $\gamma^{-1/2}$, numerical experiments in [DV] indicate a better (linear) reduction behaving like γ^{-1} . The purpose of the remainder of this section is to consider the limiting behaviour of the method as $\gamma \rightarrow \infty$, and to resolve this issue of scaling with γ .

In order to do so, we utilise the corresponding $\mathbf{H}(\text{div})$ method $\mathbf{BDM}_k/\mathbb{P}_{k-1}^{\text{dc}}$, abbreviated as \mathbf{W}_h/Q_h , and consider another discretisation of the Stokes problem²⁷:

$$\begin{cases} \text{Find } (\hat{\mathbf{u}}_h, \hat{p}_h) \in \mathbf{W}_h \times Q_h \text{ such that, } \forall (\mathbf{w}_h, q_h) \in \mathbf{W}_h \times Q_h, & (5.3a) \\ \nu a_h(\hat{\mathbf{u}}_h, \mathbf{w}_h) + b(\mathbf{w}_h, \hat{p}_h) - b(\hat{\mathbf{u}}_h, q_h) = (\mathbf{f}, \mathbf{w}_h). & (5.3b) \end{cases}$$

Note again that the L^2 method uses the same pressure space Q_h as the $\mathbf{H}(\text{div})$ method (at least on simplicial meshes). The next aim is to show that the solution \mathbf{u}_h of the DG-grad-div stabilised method \mathbf{V}_h/Q_h converges to the exactly divergence-free solution $\hat{\mathbf{u}}_h$ of the $\mathbf{H}(\text{div})$ method \mathbf{W}_h/Q_h as $\gamma \rightarrow \infty$.

The subspaces of discretely divergence-free velocities are denoted $\mathbf{V}_h^{\text{div}}$ and $\mathbf{W}_h^{\text{div}}$, respectively. Due to the fact that $\mathbf{W}_h \subset \mathbf{V}_h$, one can easily convince oneself that $\mathbf{W}_h^{\text{div}} \subset \mathbf{V}_h^{\text{div}}$. We obtain the following main result.

Theorem 5.7 (Convergence to div-free $\mathbf{H}(\text{div})$ solution)

Let $\mathbf{f} \in L^2(\Omega)$. Then, there exists a constant $C > 0$, independent of γ , such that

$$\|\mathbf{u}_h - \hat{\mathbf{u}}_h\|_e \leq C\gamma^{-1} \|\mathbf{f}\|_{L^2(\Omega)}.$$

Proof: All details of the proof can be found in [DV, Sec. 3.4], but let us give a brief sketch here.

Based on the fact that a_h defines a symmetric bilinear form on \mathbf{V}_h , the orthogonal complement

$$\mathbf{R}_h^\perp = \left(\mathbf{W}_h^{\text{div}}\right)^{\perp \mathbf{V}_h^{\text{div}}} = \left\{ \mathbf{v}_h \in \mathbf{V}_h^{\text{div}} : a_h(\mathbf{v}_h, \mathbf{w}_h) = 0, \forall \mathbf{w}_h \in \mathbf{W}_h^{\text{div}} \right\}$$

makes it possible to obtain the following inner direct sum decomposition:

$$\mathbf{V}_h^{\text{div}} = \mathbf{W}_h^{\text{div}} \oplus \mathbf{R}_h^\perp, \quad \mathbf{W}_h^{\text{div}} \cap \mathbf{R}_h^\perp = \{\mathbf{0}\}, \quad (\perp \text{ w.r.t. } a_h \text{ inner product}).$$

Based on this, decomposing the L^2 solution $\mathbf{u}_h = \mathbf{u}_h^0 + \mathbf{u}_h^\perp$ with $(\mathbf{u}_h^0, \mathbf{u}_h^\perp) \in \mathbf{W}_h^{\text{div}} \times \mathbf{R}_h^\perp$ and the L^2 test functions $\mathbf{v}_h = \mathbf{v}_h^0 + \mathbf{v}_h^\perp$ with $(\mathbf{v}_h^0, \mathbf{v}_h^\perp) \in \mathbf{W}_h^{\text{div}} \times \mathbf{R}_h^\perp$, inserting in (5.2) then leads to the

²⁷Apologies for the abuse of notation that $\hat{\mathbf{u}}_h$ does not denote a facet velocity in this section.

decoupled system

$$\nu a_h(\mathbf{u}_h^0, \mathbf{v}_h^0) = (\mathbf{f}, \mathbf{v}_h^0), \quad \forall \mathbf{v}_h^0 \in \mathbf{W}_h^{\text{div}}, \quad (5.4a)$$

$$\nu a_h(\mathbf{u}_h^\perp, \mathbf{v}_h^\perp) + \gamma j_h(\mathbf{u}_h^\perp, \mathbf{v}_h^\perp) = (\mathbf{f}, \mathbf{v}_h^\perp), \quad \forall \mathbf{v}_h^\perp \in \mathbf{R}_h^\perp. \quad (5.4b)$$

Now, (5.4a) represents exactly the equivalent pressure-free formulation of (5.3) and thus, $\mathbf{u}_h^0 = \widehat{\mathbf{u}}_h$. Testing symmetrically with $\mathbf{v}_h^\perp = \mathbf{u}_h^\perp$ in (5.4b), using discrete coercivity (Lem. 3.6) on the left-hand side and Cauchy–Schwarz on the right-hand side leads to

$$\nu C_\lambda \left\| \left\| \mathbf{u}_h^\perp \right\|_e \right\|_e^2 + \gamma \left| \mathbf{u}_h^\perp \right|_{\text{nj}}^2 \leq \|\mathbf{f}\|_{L^2} \left\| \mathbf{u}_h^\perp \right\|_{L^2}. \quad (5.5)$$

Next, one can show that the mapping $|\cdot|_{\text{nj}}: \mathbf{V}_h \rightarrow \mathbb{R}$ defines a norm on \mathbf{R}_h^\perp which, by means of norm equivalence on finite-dimensional spaces, after dropping the viscous energy norm term multiplied by ν , applying the DG analogue of Poincaré–Friedrichs (cf., for example, [DE12, Cor. 5.4]), allows to obtain the following estimate from (5.5):

$$\gamma C \left\| \left\| \mathbf{u}_h^\perp \right\|_e \right\|_e^2 \leq \nu C_\lambda \left\| \left\| \mathbf{u}_h^\perp \right\|_e \right\|_e^2 + \gamma \left| \mathbf{u}_h^\perp \right|_{\text{nj}}^2 \leq \|\mathbf{f}\|_{L^2} \left\| \mathbf{u}_h^\perp \right\|_{L^2} \leq C_{\text{PF}} \|\mathbf{f}\|_{L^2} \left\| \left\| \mathbf{u}_h^\perp \right\|_e \right\|_e.$$

Reordering the last inequality and noting that

$$\left\| \mathbf{u}_h - \widehat{\mathbf{u}}_h \right\|_e = \left\| \mathbf{u}_h - \mathbf{u}_h^0 \right\|_e = \left\| \left\| \mathbf{u}_h^\perp \right\|_e \right\|_e$$

concludes the proof. ■

Transient Navier–Stokes: Robust Numerical Analysis

Structure of this chapter: In this chapter, a numerical analysis for the time-dependent, incompressible Navier–Stokes problem (2.1) with $\mathbf{u} = \mathbf{0}$ on $\partial\Omega$ is performed, taking into consideration pressure- and Re-semi-robustness; see Ch. 4. More details on several aspects of this analysis can be found in [DII; DIII; DIV]. The considered FEMs are the divergence-free \mathbf{H}^1 from Sec. 3.4 and the divergence-free $\mathbf{H}(\text{div})$ -DG method from Sec. 3.3. Note that the Stokes results from Ch. 5 play a crucial role. We only present velocity estimates here, since pressure-robustness allows for a clean splitting of velocity and pressure.

6.1	Divergence-Free \mathbf{H}^1-FEM	74
6.2	Divergence-Free $\mathbf{H}(\text{div})$-DG-FEM	77

The first task is to introduce a suitable error splitting for the velocity for which we will use the so-called ‘discrete stationary Stokes projection’²⁸ [dFG+18a; EG04; Ing13]. Independently of the method to be analysed, the following definition is stated directly in $\mathbf{V}_h^{\text{div}}$, which suffices because we exclusively consider pressure-robust methods.

Definition 6.1 (Stationary Stokes projection)

Let $\mathbf{w} \in \mathbf{H}^{\frac{3}{2}+\varepsilon}(\mathcal{T}_h)$ for $\varepsilon > 0$ fulfil $\nabla \cdot \mathbf{w} = 0$ pointwise. Then, we define the stationary discrete Stokes projection $\mathbb{S}_h \mathbf{w} \in \mathbf{V}_h^{\text{div}}$ of \mathbf{w} to be the unique FE solution to the problem

$$a_h(\mathbb{S}_h \mathbf{w}, \mathbf{v}_h) = a_h(\mathbf{w}, \mathbf{v}_h), \quad \forall \mathbf{v}_h \in \mathbf{V}_h^{\text{div}}.$$

A careful inspection of Def. 6.1 reveals that the Stokes projection $\mathbb{S}_h \mathbf{w}$ is actually only the discrete solution of a stationary Stokes problem, where the right-hand side forcing term is chosen as $-\Delta \mathbf{w}$; cf., for example, [DII] for more details. Especially, this means that whenever a divergence-free method is used to compute the discrete Stokes projection, we have $\nabla \cdot \mathbb{S}_h \mathbf{w} = 0$, provided that $\nabla \cdot \mathbf{w} = 0$, since discretely divergence-free velocities are exactly divergence-free in this case. This is an important property of exactly divergence-free methods.

Let $\mathbf{u}(t)$ be the exact Navier–Stokes solution and $\mathbf{u}_h(t)$ its approximation by means of the considered FEM. We are now able to define the following error splitting:

$$\mathbf{u} - \mathbf{u}_h = [\mathbf{u} - \mathbb{S}_h \mathbf{u}] - [\mathbf{u}_h - \mathbb{S}_h \mathbf{u}] = \boldsymbol{\eta} - \mathbf{e}_h. \tag{6.1}$$

Note that $\nabla \cdot \boldsymbol{\eta} = \nabla \cdot \mathbf{e}_h = 0$ whenever an exactly divergence-free method is considered.

²⁸In the context of more general problems, it is also frequently called ‘elliptic projection’ or ‘Ritz projection’.

Remark 6.2 (Helmholtz projection for error splitting): Instead of the discrete Stokes projection \mathbb{S}_h , an interesting alternative is using the discrete Helmholtz projection \mathbb{P}_h for the error splitting; for example, see [DVII]. An advantage is that usually, no terms involving the time derivative of the approximation error $\boldsymbol{\eta}$ will appear on the right-hand side of error estimates. However, in the context of the Navier–Stokes problem, the dominating error contribution usually stems from the nonlinear convective term, which is why such a modification involving the discrete Helmholtz projection would not improve the overall convergence rate of the estimate. For the sake of presentation we thus adhere to (6.1). \blacktriangle

Using Ch. 5, it is straightforward to analyse the approximation properties of the Stokes projection.

Corollary 6.3 (Stokes projection approximation properties)

Under Asm. C, and provided $\mathbf{u}, \partial_t \mathbf{u} \in \mathbf{H}^r(\Omega)$ (for $r > 3/2$ in the $\mathbf{H}(\text{div})$ case), the Stokes projection has the following approximation properties with $r_{\mathbf{u}} = \min\{r, k + 1\}$ and a constant $C > 0$:

$$\begin{aligned} \|\boldsymbol{\eta}\|_{\mathbf{L}^2} + h\|\boldsymbol{\eta}\|_{e,\sharp} &\leq Ch^{r_{\mathbf{u}}} \|\mathbf{u}\|_{\mathbf{H}^{r_{\mathbf{u}}}}, \\ \|\partial_t \boldsymbol{\eta}\|_{\mathbf{L}^2} &\leq Ch^{r_{\mathbf{u}}} \|\partial_t \mathbf{u}\|_{\mathbf{H}^{r_{\mathbf{u}}}}. \end{aligned}$$

In the \mathbf{H}^1 case, $\|\boldsymbol{\eta}\|_{e,\sharp}$ reduces to $\|\nabla \boldsymbol{\eta}\|_{\mathbf{L}^2}$.

Proof: Basically, this is a direct consequence of Thm. 5.4. Concerning the commutation of Stokes projection and time derivative, we refer, for example, to [Joh16, Sec. 4.2.2]. \blacksquare

Another important property of the considered methods basically results from its consistency (note that $\llbracket \mathbf{u} \rrbracket = \mathbf{0}$ for the exact solution).

Corollary 6.4 (Galerkin orthogonality)

For a.e. $t \in (0, T)$ and for all $\mathbf{v}_h \in \mathbf{V}_h^{\text{div}}$,

$$(\partial_t[\mathbf{u} - \mathbf{u}_h], \mathbf{v}_h) + \nu a_h(\mathbf{u} - \mathbf{u}_h, \mathbf{v}_h) + c_h(\mathbf{u}; \mathbf{u}, \mathbf{v}_h) - c_h(\mathbf{u}_h; \mathbf{u}_h, \mathbf{v}_h) = 0.$$

The main problem usually is the estimation of the difference of discrete convective terms appearing in Cor. 6.4. Opposed to [DIV], in the following, the \mathbf{H}^1 - and the $\mathbf{H}(\text{div})$ -conforming analysis is carried out separately. This separation makes it easier to understand the involved techniques.

6.1 Divergence-Free H^1 -FEM

Consider the same setting as in Sec. 3.4, with the additional assumption that $\nabla \cdot \mathbf{V}_h \subset Q_h$, thereby guaranteeing an exactly divergence-free velocity approximation $\nabla \cdot \mathbf{u}_h = 0$ (for example Scott–Vogelius). Note that in this case, concerning the occurring forms, $a_h = a$ and $c_h = c$ holds true.

Lemma 6.5 (Difference of div-free \mathbf{H}^1 convective terms)

Assume that $\mathbf{u} \in L^1(\mathbf{W}^{1,\infty})$. Then, for all $\varepsilon_1, \varepsilon_2 > 0$, one obtains the following estimate:

$$\begin{aligned} c(\mathbf{u}; \mathbf{u}, \mathbf{e}_h) - c(\mathbf{u}_h; \mathbf{u}_h, \mathbf{e}_h) &\leq \frac{1}{2\varepsilon_1} \|\mathbf{u}\|_{L^\infty} \|\nabla \boldsymbol{\eta}\|_{L^2}^2 + \frac{1}{2\varepsilon_2} \|\nabla \mathbb{S}_h \mathbf{u}\|_{L^\infty} \|\boldsymbol{\eta}\|_{L^2}^2 \\ &\quad + \left[\frac{\varepsilon_1}{2} \|\mathbf{u}\|_{L^\infty} + \left(1 + \frac{\varepsilon_2}{2}\right) \|\nabla \mathbb{S}_h \mathbf{u}\|_{L^\infty} \right] \|\mathbf{e}_h\|_{L^2}^2. \end{aligned}$$

Remark 6.6: Note that it is essential that the discrete Stokes projection has the max-norm stability property stated in Lem. 5.3. Otherwise, terms as $\|\nabla \mathbb{S}_h \mathbf{u}\|_{L^\infty}$ would not make any sense. \blacktriangle

Proof of Lem. 6.5: This proof is an adaption of [DIV, Lem. 5.5] to the \mathbf{H}^1 case. Begin with inserting the definition of c , then subtract and add $(\mathbf{u} \cdot \nabla \mathbb{S}_h \mathbf{u}, \mathbf{e}_h)$, and then replace $\mathbf{u}_h = \mathbb{S}_h \mathbf{u} + \mathbf{e}_h$ and apply Lem. 2.4 ($(\mathbf{u}_h \cdot \nabla \mathbf{e}_h, \mathbf{e}_h) = 0$):

$$\begin{aligned} c(\mathbf{u}; \mathbf{u}, \mathbf{e}_h) - c(\mathbf{u}_h; \mathbf{u}_h, \mathbf{e}_h) &= (\mathbf{u} \cdot \nabla \mathbf{u}, \mathbf{e}_h) - (\mathbf{u}_h \cdot \nabla \mathbf{u}_h, \mathbf{e}_h) \\ &= (\mathbf{u} \cdot \nabla \mathbf{u}, \mathbf{e}_h) - (\mathbf{u} \cdot \nabla \mathbb{S}_h \mathbf{u}, \mathbf{e}_h) - [(\mathbf{u}_h \cdot \nabla \mathbf{u}_h, \mathbf{e}_h) - (\mathbf{u} \cdot \nabla \mathbb{S}_h \mathbf{u}, \mathbf{e}_h)] \\ &= (\mathbf{u} \cdot \nabla \boldsymbol{\eta}, \mathbf{e}_h) + [(\mathbf{u} - \mathbf{u}_h) \cdot \nabla \mathbb{S}_h \mathbf{u}, \mathbf{e}_h]. \end{aligned}$$

Now, using Hölder's inequality, the triangle inequality, and Young's inequality with $\varepsilon_1, \varepsilon_2 > 0$ leads to the claim

$$\begin{aligned} c(\mathbf{u}; \mathbf{u}, \mathbf{e}_h) - c(\mathbf{u}_h; \mathbf{u}_h, \mathbf{e}_h) &\leq \|\mathbf{u}\|_{L^\infty} \|\nabla \boldsymbol{\eta}\|_{L^2} \|\mathbf{e}_h\|_{L^2} + \|\boldsymbol{\eta} - \mathbf{e}_h\|_{L^2} \|\nabla \mathbb{S}_h \mathbf{u}\|_{L^\infty} \|\mathbf{e}_h\|_{L^2} \\ &\leq \frac{1}{2\varepsilon_1} \|\mathbf{u}\|_{L^\infty} \|\nabla \boldsymbol{\eta}\|_{L^2}^2 + \frac{1}{2\varepsilon_2} \|\nabla \mathbb{S}_h \mathbf{u}\|_{L^\infty} \|\boldsymbol{\eta}\|_{L^2}^2 + \left[\frac{\varepsilon_1}{2} \|\mathbf{u}\|_{L^\infty} + \left(1 + \frac{\varepsilon_2}{2}\right) \|\nabla \mathbb{S}_h \mathbf{u}\|_{L^\infty} \right] \|\mathbf{e}_h\|_{L^2}^2. \end{aligned}$$

The estimate of the difference of convective terms is the crucial component of the following error estimate. Furthermore, note that due to the arbitrariness of ε_i in Lem. 6.5, there are also infinitely many possible error estimates which can be deduced.

Theorem 6.7 (\mathbf{H}^1 discretisation error estimate)

If $\mathbf{u} \in L^1(\mathbf{W}^{1,\infty})$, $\partial_t \mathbf{u} \in L^2(\mathbf{L}^2)$ and $\mathbf{u}_h(0) = \mathbb{S}_h \mathbf{u}_0$, we obtain the following error estimate for a constant $C > 0$:

$$\|\mathbf{e}_h\|_{L^\infty(L^2)}^2 + \nu \|\nabla \mathbf{e}_h\|_{L^2(L^2)}^2 \leq C e^{G_u(T)} \int_0^T \left[\|\nabla \mathbf{u}\|_{L^\infty} \|\boldsymbol{\eta}\|_{L^2}^2 + \|\partial_t \boldsymbol{\eta}\|_{L^2}^2 + \|\mathbf{u}\|_{L^\infty} \|\nabla \boldsymbol{\eta}\|_{L^2}^2 \right] d\tau.$$

Here, the Gronwall constant is given by

$$G_u(T) = T + \|\mathbf{u}\|_{L^1(L^\infty)} + C \|\nabla \mathbf{u}\|_{L^1(L^\infty)}.$$

Proof: This proof is an adaption of [DIV, Thm. 5.6] to the \mathbf{H}^1 case. Cor. 6.4 with $\mathbf{v}_h = \mathbf{e}_h(t) \in \mathbf{V}_h^{\text{div}}$

together with the error splitting (6.1) leads to

$$(\partial_t \mathbf{e}_h, \mathbf{e}_h) + \nu a(\mathbf{e}_h, \mathbf{e}_h) = (\partial_t \boldsymbol{\eta}, \mathbf{e}_h) + \nu a(\boldsymbol{\eta}, \mathbf{e}_h) + c(\mathbf{u}; \mathbf{u}, \mathbf{e}_h) - c(\mathbf{u}_h; \mathbf{u}_h, \mathbf{e}_h).$$

In order to treat this equation further, we use $(\partial_t \mathbf{e}_h, \mathbf{e}_h) = \frac{1}{2} \frac{d}{dt} \|\mathbf{e}_h\|_{\mathbf{L}^2}^2$ and discrete coercivity of a on the left-hand side (note that $\nabla \cdot \mathbf{e}_h = 0$). On the right-hand side, apply Cauchy–Schwarz plus Young ($\varepsilon_3 > 0$), and use the Stokes projection (Def. 6.1) to observe that $a(\boldsymbol{\eta}, \mathbf{e}_h) = 0$. Thus,

$$\begin{aligned} \frac{1}{2} \frac{d}{dt} \|\mathbf{e}_h\|_{\mathbf{L}^2}^2 + \nu \|\nabla \mathbf{e}_h\|_{\mathbf{L}^2}^2 &\leq \frac{1}{2\varepsilon_3} \|\partial_t \boldsymbol{\eta}\|_{\mathbf{L}^2}^2 + \frac{\varepsilon_3}{2} \|\mathbf{e}_h\|_{\mathbf{L}^2}^2 + [c(\mathbf{u}; \mathbf{u}, \mathbf{e}_h) - c(\mathbf{u}_h; \mathbf{u}_h, \mathbf{e}_h)] \\ &\leq \frac{1}{2\varepsilon_2} \|\nabla \mathbb{S}_h \mathbf{u}\|_{\mathbf{L}^\infty} \|\boldsymbol{\eta}\|_{\mathbf{L}^2}^2 + \frac{1}{2\varepsilon_3} \|\partial_t \boldsymbol{\eta}\|_{\mathbf{L}^2}^2 + \frac{1}{2\varepsilon_1} \|\mathbf{u}\|_{\mathbf{L}^\infty} \|\nabla \boldsymbol{\eta}\|_{\mathbf{L}^2}^2 \\ &\quad + \left[\frac{\varepsilon_1}{2} \|\mathbf{u}\|_{\mathbf{L}^\infty} + \left(1 + \frac{\varepsilon_2}{2}\right) \|\nabla \mathbb{S}_h \mathbf{u}\|_{\mathbf{L}^\infty} + \frac{\varepsilon_3}{2} \right] \|\mathbf{e}_h\|_{\mathbf{L}^2}^2, \end{aligned}$$

where the second estimate makes use of Lem. 6.5. The factors ε_i can be chosen arbitrarily, and we simply choose to consider $\varepsilon_1 = \varepsilon_2 = \varepsilon_3 = 1$ which, after multiplying by two and applying Lem. 5.3, results in

$$\begin{aligned} \frac{d}{dt} \|\mathbf{e}_h\|_{\mathbf{L}^2}^2 + \nu \|\nabla \mathbf{e}_h\|_{\mathbf{L}^2}^2 &\leq C \|\nabla \mathbf{u}\|_{\mathbf{L}^\infty} \|\boldsymbol{\eta}\|_{\mathbf{L}^2}^2 + \|\partial_t \boldsymbol{\eta}\|_{\mathbf{L}^2}^2 + \|\mathbf{u}\|_{\mathbf{L}^\infty} \|\nabla \boldsymbol{\eta}\|_{\mathbf{L}^2}^2 \\ &\quad + [1 + \|\mathbf{u}\|_{\mathbf{L}^\infty} + C \|\nabla \mathbf{u}\|_{\mathbf{L}^\infty}] \|\mathbf{e}_h\|_{\mathbf{L}^2}^2. \end{aligned}$$

In such a situation, Gronwall’s lemma [Joh16, Lem. A.54] states that for a.e. $t \in [0, T]$ ²⁹,

$$\frac{d}{dt} \|\mathbf{e}_h(t)\|_{\mathbf{L}^2}^2 \leq \alpha(t) + \beta(t) \|\mathbf{e}_h(t)\|_{\mathbf{L}^2}^2 \quad \Rightarrow \quad \|\mathbf{e}_h(t)\|_{\mathbf{L}^2}^2 \leq \int_0^t \alpha(s) \exp\left(\int_s^t \beta(\tau) d\tau\right) ds. \quad (6.2)$$

The essential regularity assumption $\mathbf{u} \in L^1(\mathbf{W}^{1,\infty})$ (see Sec. 2.2.2) ensures that

$$G_{\mathbf{u}}(t) = \int_0^t \beta(\tau) d\tau = \int_0^t [1 + \|\mathbf{u}(\tau)\|_{\mathbf{L}^\infty} + C \|\nabla \mathbf{u}(\tau)\|_{\mathbf{L}^\infty}] d\tau < \infty.$$

Application of Gronwall’s lemma (6.2) together with $\mathbf{u}_h(0) = \mathbb{S}_h \mathbf{u}_0$ concludes the proof. \blacksquare

Corollary 6.8 (H^1 convergence rate)

Under the assumptions of the previous theorem, assume a smooth solution according to

$$\mathbf{u} \in L^2(0, T; \mathbf{H}^r(\Omega)), \quad \partial_t \mathbf{u} \in L^2(0, T; \mathbf{H}^r(\Omega)), \quad r > \frac{3}{2}.$$

Then, with $r_{\mathbf{u}} = \min\{r, k + 1\}$ and a constant $C > 0$, we obtain the following convergence rate:

$$\begin{aligned} &\|\mathbf{e}_h\|_{\mathbf{L}^\infty(\mathbf{L}^2)}^2 + \nu \|\nabla \mathbf{e}_h\|_{\mathbf{L}^2(\mathbf{L}^2)}^2 \\ &\leq Ch^{2(r_{\mathbf{u}}-1)} e^{G_{\mathbf{u}}(T)} \int_0^T \left[h^2 \|\partial_t \mathbf{u}\|_{\mathbf{H}^{r_{\mathbf{u}}}}^2 + (\|\mathbf{u}\|_{\mathbf{L}^\infty} + h^2 \|\nabla \mathbf{u}\|_{\mathbf{L}^\infty}) \|\mathbf{u}\|_{\mathbf{H}^{r_{\mathbf{u}}}}^2 \right] d\tau. \end{aligned}$$

²⁹Cf., for example, [DVII, Proof of Thm. 4.1] for more details on how Gronwall can be applied in such a setting.

Proof: Apply Cor. 6.3 on the right-hand side of Thm. 6.7. \blacksquare

Note that by using the triangle inequality, the estimates of both Thm. 6.7 and Cor. 6.8 also hold true (only the constant C changes) for the full error $\mathbf{u} - \mathbf{u}_h$.

The next lemma is interesting, because it shows that for the discrete solution, and under some additional conditions, $\mathbf{u}_h \in L^\infty(\mathbf{L}^\infty)$ holds; to the best of the author's knowledge, no other \mathbf{H}^1 -conforming and inf-sup stable FEM has this property³⁰.

Lemma 6.9 (H^1 max-norm estimate)

Under the assumptions of the previous corollary, for simplicity, additionally assume that $\mathbf{u} \in L^\infty(\mathbf{W}^{1,\infty} \cap \mathbf{H}^{r_u})$. Then, with $r_u = \min\{r, k+1\}$, the estimate

$$\begin{aligned} \|\mathbf{u} - \mathbf{u}_h\|_{L^\infty(\mathbf{L}^\infty)} &\leq Ch \|\mathbf{u}\|_{L^\infty(\mathbf{W}^{1,\infty})} + Ch^{r_u-d/2} \|\mathbf{u}\|_{L^\infty(\mathbf{H}^{r_u})} \\ &\quad + Ch^{r_u-(d/2+1)} e^{G_{\mathbf{u}}(T)/2} \sqrt{H_{\mathbf{u}}^h(T)}, \end{aligned}$$

holds, where

$$H_{\mathbf{u}}^h(T) = \int_0^T \left[h^2 \|\partial_t \mathbf{u}\|_{\mathbf{H}^{r_u}}^2 + (\|\mathbf{u}\|_{\mathbf{L}^\infty} + h^2 \|\nabla \mathbf{u}\|_{\mathbf{L}^\infty}) \|\mathbf{u}\|_{\mathbf{H}^{r_u}}^2 \right] d\tau.$$

Especially provided $r_u > \frac{d}{2} + 1$, this ensures that $\mathbf{u}_h \in L^\infty(\mathbf{L}^\infty)$ also under mesh-refinement.

Proof: This is basically shown in [DII, Lem. 4.2] with the help of the orthogonal \mathbf{L}^2 -projection onto \mathbf{V}_h ; here, only some cosmetic changes have been performed. Note that a global discrete inverse inequality is necessary to show this max-norm estimate and thus, a quasi-uniform mesh has to be assumed. An alternative proof could use the discrete Stokes projection $\mathbb{S}_h \mathbf{u}$, but the convergence statement of Asm. D would have to be valid also in the \mathbf{H}^1 -conforming case. The corresponding proof for the $\mathbf{H}(\text{div})$ -DG method is presented with all details in the next subsection. \blacksquare

6.2 Divergence-Free $\mathbf{H}(\text{div})$ -DG-FEM

Let us now perform the numerical analysis for the exactly divergence-free $\mathbf{H}(\text{div})$ -DG method of Sec. 3.3. We will proceed analogously to the \mathbf{H}^1 -conforming case, and exploit the fact that only additional facet terms have to be treated now.

Lemma 6.10 (Difference of div-free $\mathbf{H}(\text{div})$ convective terms)

Assume that $\mathbf{u} \in L^1(\mathbf{W}^{1,\infty})$. Then, for all $\varepsilon_1, \varepsilon_2, \varepsilon_4 > 0$, we obtain the following estimate:

$$\begin{aligned} c_h(\mathbf{u}; \mathbf{u}, \mathbf{e}_h) - c_h(\mathbf{u}_h; \mathbf{u}_h, \mathbf{e}_h) &\leq -|\mathbf{e}_h|_{\mathbf{u}_h, \text{upw}}^2 \\ &\quad + \frac{1}{2\varepsilon_1} \|\mathbf{u}\|_{\mathbf{L}^\infty} \|\nabla_h \boldsymbol{\eta}\|_{\mathbf{L}^2}^2 + \left[\frac{1}{2\varepsilon_2} \|\nabla_h \mathbb{S}_h \mathbf{u}\|_{\mathbf{L}^\infty} + \frac{1}{2\varepsilon_4} h^{-1} \|\mathbb{S}_h \mathbf{u}\|_{\mathbf{L}^\infty} \right] \|\boldsymbol{\eta}\|_{\mathbf{L}^2}^2 \\ &\quad + \left[\frac{\varepsilon_1}{2} \|\mathbf{u}\|_{\mathbf{L}^\infty} + \left(1 + \frac{\varepsilon_2}{2}\right) \|\nabla_h \mathbb{S}_h \mathbf{u}\|_{\mathbf{L}^\infty} + \|\nabla \mathbf{u}\|_{\mathbf{L}^\infty} + \frac{\varepsilon_4}{2} h^{-1} \|\mathbb{S}_h \mathbf{u}\|_{\mathbf{L}^\infty} \right] \|\mathbf{e}_h\|_{\mathbf{L}^2}^2. \end{aligned}$$

³⁰For an equal-order \mathbf{H}^1 -FEM, a corresponding result is proven in [BF07, Cor. 4].

Proof (Sketch): This proof is basically taken from [DIV, Lem. 5.5], but for the sake of presentation we provide a sketch of it here with minor modifications. Let us write down the terms which are involved in the difference of convective terms for the $\mathbf{H}(\text{div})$ -DG method, using $[[\mathbf{u}]]_F = \mathbf{0}$ for all facets $F \in \mathcal{F}_h^i$:

$$\begin{aligned} c_h(\mathbf{u}; \mathbf{u}, \mathbf{e}_h) - c_h(\mathbf{u}_h; \mathbf{u}_h, \mathbf{e}_h) &= \int_{\Omega} [(\mathbf{u} \cdot \nabla_h) \mathbf{u} \cdot \mathbf{e}_h - (\mathbf{u}_h \cdot \nabla_h) \mathbf{u}_h \cdot \mathbf{e}_h] \, d\mathbf{x} \\ &\quad - \sum_{F \in \mathcal{F}_h^i} \int_F (\mathbf{u}_h \cdot \mathbf{n}_F) [[\mathbf{u} - \mathbf{u}_h]] \cdot \{\{\mathbf{e}_h\}\} \, ds + \sum_{F \in \mathcal{F}_h^i} \int_F \frac{1}{2} |\mathbf{u}_h \cdot \mathbf{n}_F| [[\mathbf{u} - \mathbf{u}_h]] \cdot [[\mathbf{e}_h]] \, ds \\ &= \mathfrak{T}_1 + \mathfrak{T}_2 + \mathfrak{T}_3. \end{aligned}$$

Now, \mathfrak{T}_1 has already been estimated in Lem. 6.5 ($\varepsilon_1, \varepsilon_2 > 0$), which can be taken over with the slight modification that $0 \neq (\mathbf{u}_h \cdot \nabla_h \mathbf{e}_h, \mathbf{e}_h) = \sum_{F \in \mathcal{F}_h^i} \int_F (\mathbf{u}_h \cdot \mathbf{n}_F) [[\mathbf{e}_h]] \cdot \{\{\mathbf{e}_h\}\} \, ds$ (see Lem. 3.12):

$$\begin{aligned} |\mathfrak{T}_1| &\leq - \sum_{F \in \mathcal{F}_h^i} \int_F (\mathbf{u}_h \cdot \mathbf{n}_F) [[\mathbf{e}_h]] \cdot \{\{\mathbf{e}_h\}\} \, ds + \frac{1}{2\varepsilon_1} \|\mathbf{u}\|_{\mathbf{L}^\infty} \|\nabla_h \boldsymbol{\eta}\|_{\mathbf{L}^2}^2 + \frac{1}{2\varepsilon_2} \|\nabla_h \mathbb{S}_h \mathbf{u}\|_{\mathbf{L}^\infty} \|\boldsymbol{\eta}\|_{\mathbf{L}^2}^2 \\ &\quad + \left[\frac{\varepsilon_1}{2} \|\mathbf{u}\|_{\mathbf{L}^\infty} + \left(1 + \frac{\varepsilon_2}{2}\right) \|\nabla_h \mathbb{S}_h \mathbf{u}\|_{\mathbf{L}^\infty} \right] \|\mathbf{e}_h\|_{\mathbf{L}^2}^2. \end{aligned}$$

For the facet terms $\mathfrak{T}_2, \mathfrak{T}_3$, inserting the error splitting $\mathbf{u} - \mathbf{u}_h = \boldsymbol{\eta} - \mathbf{e}_h$ (6.1) leads to

$$\begin{aligned} \mathfrak{T}_2 &= - \sum_{F \in \mathcal{F}_h^i} \int_F (\mathbf{u}_h \cdot \mathbf{n}_F) [[\boldsymbol{\eta}]] \cdot \{\{\mathbf{e}_h\}\} \, ds + \sum_{F \in \mathcal{F}_h^i} \int_F (\mathbf{u}_h \cdot \mathbf{n}_F) [[\mathbf{e}_h]] \cdot \{\{\mathbf{e}_h\}\} \, ds = \mathfrak{T}_{2,1} + \mathfrak{T}_{2,2}, \\ \mathfrak{T}_3 &= \sum_{F \in \mathcal{F}_h^i} \int_F \frac{1}{2} |\mathbf{u}_h \cdot \mathbf{n}_F| [[\boldsymbol{\eta}]] \cdot [[\mathbf{e}_h]] \, ds - \sum_{F \in \mathcal{F}_h^i} \int_F \frac{1}{2} |\mathbf{u}_h \cdot \mathbf{n}_F| [[\mathbf{e}_h]] \cdot [[\mathbf{e}_h]] \, ds = \mathfrak{T}_{3,1} - |\mathbf{e}_h|_{\mathbf{u}_h, \text{upw}}^2. \end{aligned}$$

Note that $\mathfrak{T}_{2,2}$ cancels out with its corresponding part from \mathfrak{T}_1 . Using the \mathbf{L}^∞ approximation properties (Asm. D) of the discrete Stokes projection, the discrete trace inequality (Rem. 3.3) and Young's inequality ($\varepsilon_4 > 0$), one can show that

$$|\mathfrak{T}_{2,1}| + |\mathfrak{T}_{3,1}| \leq C \left[\|\nabla \mathbf{u}\|_{\mathbf{L}^\infty} + \frac{\varepsilon_4}{2} h^{-1} \|\mathbb{S}_h \mathbf{u}\|_{\mathbf{L}^\infty} \right] \|\mathbf{e}_h\|_{\mathbf{L}^2}^2 + C \frac{1}{2\varepsilon_4} h^{-1} \|\mathbb{S}_h \mathbf{u}\|_{\mathbf{L}^\infty} \|\boldsymbol{\eta}\|_{\mathbf{L}^2}^2.$$

For more technical details, we refer to [DIV, Lem. 5.5]. Collecting and reordering the estimates concludes the proof. \blacksquare

Now, the following discretisation error estimate can be proven.

Theorem 6.11 (*$\mathbf{H}(\text{div})$ discretisation error estimate*)

If $\mathbf{u} \in L^2(\mathbf{H}^{\frac{3}{2}+\varepsilon}(\mathcal{T}_h))$ for $\varepsilon > 0$, $\mathbf{u} \in L^1(\mathbf{W}^{1,\infty})$, $\partial_t \mathbf{u} \in L^2(\mathbf{L}^2)$ and $\mathbf{u}_h(0) = \mathbb{S}_h \mathbf{u}_0$, we obtain the following error estimate for a constant $C > 0$:

$$\begin{aligned} \|\mathbf{e}_h\|_{L^\infty(\mathbf{L}^2)}^2 + \int_0^T \left[\nu C_\lambda \|\mathbf{e}_h\|_e^2 + |\mathbf{e}_h|_{\mathbf{u}_h, \text{upw}}^2 \right] d\tau \\ \leq C e^{G_u(T)} \int_0^T \left[(1 + h^{-2}) \|\nabla \mathbf{u}\|_{\mathbf{L}^\infty} \|\boldsymbol{\eta}\|_{\mathbf{L}^2}^2 + \|\partial_t \boldsymbol{\eta}\|_{\mathbf{L}^2}^2 + \|\mathbf{u}\|_{\mathbf{L}^\infty} \|\nabla_h \boldsymbol{\eta}\|_{\mathbf{L}^2}^2 \right] d\tau. \end{aligned}$$

The Gronwall constant is again given by $G_u(T) = T + \|\mathbf{u}\|_{L^1(\mathbf{L}^\infty)} + C \|\nabla \mathbf{u}\|_{L^1(\mathbf{L}^\infty)}$.

Remark 6.12: In contrast to the \mathbf{H}^1 case in Thm. 6.7, this error estimate for the $\mathbf{H}(\text{div})$ DG method has two important new aspects. On the left-hand side, additional control over the error in the upwind seminorm can be achieved, and on the right-hand side, the factor h^{-2} originates from the application of a discrete trace inequality (Rem. 3.3) for the additional facet terms. The exponential Gronwall factor, however, basically remains the same (up to constants). \blacktriangle

Proof of Thm. 6.11: Proceeding analogously as in the proof of Thm. 6.7 (this time using discrete coercivity of the DG method on the left-hand side), with the help of Lem. 6.10, one obtains the following estimate:

$$\begin{aligned} \frac{1}{2} \frac{d}{dt} \|\mathbf{e}_h\|_{\mathbf{L}^2}^2 + \nu C_\lambda \|\mathbf{e}_h\|_e^2 + |\mathbf{e}_h|_{\mathbf{u}_h, \text{upw}}^2 &\leq \frac{1}{2\varepsilon_3} \|\partial_t \boldsymbol{\eta}\|_{\mathbf{L}^2}^2 + \frac{\varepsilon_3}{2} \|\mathbf{e}_h\|_{\mathbf{L}^2}^2 \\ &+ \frac{1}{2\varepsilon_1} \|\mathbf{u}\|_{\mathbf{L}^\infty} \|\nabla_h \boldsymbol{\eta}\|_{\mathbf{L}^2}^2 + \left[\frac{1}{2\varepsilon_2} \|\nabla_h \mathbb{S}_h \mathbf{u}\|_{\mathbf{L}^\infty} + \frac{1}{2\varepsilon_4} h^{-1} \|\mathbb{S}_h \mathbf{u}\|_{\mathbf{L}^\infty} \right] \|\boldsymbol{\eta}\|_{\mathbf{L}^2}^2 \\ &+ \left[\frac{\varepsilon_1}{2} \|\mathbf{u}\|_{\mathbf{L}^\infty} + \left(1 + \frac{\varepsilon_2}{2}\right) \|\nabla_h \mathbb{S}_h \mathbf{u}\|_{\mathbf{L}^\infty} + \|\nabla \mathbf{u}\|_{\mathbf{L}^\infty} + \frac{\varepsilon_4}{2} h^{-1} \|\mathbb{S}_h \mathbf{u}\|_{\mathbf{L}^\infty} \right] \|\mathbf{e}_h\|_{\mathbf{L}^2}^2. \end{aligned}$$

Note that in contrast to the \mathbf{H}^1 case, additional control over the upwind seminorm on the left-hand side can be achieved, and on the right-hand side, the terms involving ε_4 (stemming from facets) have to be added. In order to keep the exponential Gronwall term clear from scalings involving negative powers of h , we choose $\varepsilon_4 = h$ and $\varepsilon_1 = \varepsilon_2 = \varepsilon_3 = 1$ which, after applying Asm. D, multiplying by two and rearranging amounts to

$$\begin{aligned} \frac{d}{dt} \|\mathbf{e}_h\|_{\mathbf{L}^2}^2 + \nu C_\lambda \|\mathbf{e}_h\|_e^2 + |\mathbf{e}_h|_{\mathbf{u}_h, \text{upw}}^2 &\leq C(1 + h^{-2}) \|\nabla \mathbf{u}\|_{\mathbf{L}^\infty} \|\boldsymbol{\eta}\|_{\mathbf{L}^2}^2 + \|\partial_t \boldsymbol{\eta}\|_{\mathbf{L}^2}^2 + \|\mathbf{u}\|_{\mathbf{L}^\infty} \|\nabla_h \boldsymbol{\eta}\|_{\mathbf{L}^2}^2 \\ &+ [1 + \|\mathbf{u}\|_{\mathbf{L}^\infty} + C \|\nabla \mathbf{u}\|_{\mathbf{L}^\infty}] \|\mathbf{e}_h\|_{\mathbf{L}^2}^2. \end{aligned}$$

Again, Gronwall's lemma together with $\mathbf{u}_h(0) = \mathbb{S}_h \mathbf{u}_0$ concludes the proof. \blacksquare

Under suitable smoothness assumptions on the exact solution, one obtains the usual convergence rates as follows.

Corollary 6.13 ($H(\text{div})$ convergence rate)

Under the assumptions of the previous theorem, assume a smooth solution according to

$$\mathbf{u} \in L^2(0, T; \mathbf{H}^r(\Omega)), \quad \partial_t \mathbf{u} \in L^2(0, T; \mathbf{H}^r(\Omega)), \quad r > \frac{3}{2}.$$

Then, with $r_{\mathbf{u}} = \min \{r, k + 1\}$ and a constant $C > 0$, we obtain the following convergence rate:

$$\begin{aligned} & \|e_h\|_{L^\infty(\mathbf{L}^2)}^2 + \int_0^T \left[\nu C_\lambda \|e_h\|_e^2 + |e_h|_{\mathbf{u}_h, \text{upw}}^2 \right] d\tau \\ & \leq Ch^{2(r_{\mathbf{u}}-1)} e^{G_{\mathbf{u}}(T)} \int_0^T \left[h^2 \|\partial_t \mathbf{u}\|_{\mathbf{H}^{r_{\mathbf{u}}}}^2 + [\|\mathbf{u}\|_{\mathbf{L}^\infty} + (h^2 + 1) \|\nabla \mathbf{u}\|_{\mathbf{L}^\infty}] \|\mathbf{u}\|_{\mathbf{H}^{r_{\mathbf{u}}}}^2 \right] d\tau. \end{aligned}$$

Proof: Apply Cor. 6.3 on the right-hand side of Thm. 6.11. ■

Note again that by using the triangle inequality, the estimates of both Thm. 6.11 and Cor. 6.13 also hold true (only the constant C changes) for the full error $\mathbf{u} - \mathbf{u}_h$.

Lemma 6.14 ($H(\text{div})$ max-norm estimate)

Under the assumptions of the previous corollary, for simplicity, additionally assume that $\mathbf{u} \in L^\infty(\mathbf{W}^{1, \infty})$. Then, with $r_{\mathbf{u}} = \min \{r, k + 1\}$,

$$\|\mathbf{u} - \mathbf{u}_h\|_{L^\infty(\mathbf{L}^\infty)} \leq Ch \|\mathbf{u}\|_{L^\infty(\mathbf{W}^{1, \infty})} + Ch^{r_{\mathbf{u}} - (d/2 + 1)} e^{G_{\mathbf{u}}(T)/2} \sqrt{H_{\mathbf{u}}^h(T)},$$

where

$$H_{\mathbf{u}}^h(T) = \int_0^T \left[h^2 \|\partial_t \mathbf{u}\|_{\mathbf{H}^{r_{\mathbf{u}}}}^2 + [\|\mathbf{u}\|_{\mathbf{L}^\infty} + (h^2 + 1) \|\nabla \mathbf{u}\|_{\mathbf{L}^\infty}] \|\mathbf{u}\|_{\mathbf{H}^{r_{\mathbf{u}}}}^2 \right] d\tau.$$

Epecially, provided $r_{\mathbf{u}} > \frac{d}{2} + 1$, this ensures that $\mathbf{u}_h \in L^\infty(\mathbf{L}^\infty)$ also under mesh-refinement.

Proof: In contrast to the \mathbf{H}^1 -conforming case in Lem. 6.9, the Stokes projection $\mathbb{S}_h \mathbf{u}$ is the most elegant tool to show the claim. Recalling Asm. D, we have assumed that

$$\|\mathbf{u}(t) - \mathbb{S}_h \mathbf{u}(t)\|_{\mathbf{L}^\infty} \leq Ch \|\nabla \mathbf{u}\|_{L^\infty(\mathbf{L}^\infty)},$$

for a.e. $t \in [0, T]$. Thus, with the triangle inequality, one obtains

$$\|\mathbf{u}(t) - \mathbf{u}_h(t)\|_{\mathbf{L}^\infty} \leq \|\mathbf{u}(t) - \mathbb{S}_h \mathbf{u}(t)\|_{\mathbf{L}^\infty} + \|\mathbb{S}_h \mathbf{u}(t) - \mathbf{u}_h(t)\|_{\mathbf{L}^\infty} \leq Ch \|\nabla \mathbf{u}\|_{L^\infty(\mathbf{L}^\infty)} + \|e_h(t)\|_{\mathbf{L}^\infty}.$$

Due to $e_h \in \mathbf{V}_h$, the global analogue of the inverse inequality (3.4) can be applied³¹. Indeed, for a.e. $t \in [0, T]$, choosing $\ell = m = 0$, $p = \infty$ and $q = 2$ leads to

$$\|e_h(t)\|_{\mathbf{L}^\infty} \leq Ch^{-d/2} \|e_h\|_{L^\infty(\mathbf{L}^\infty)} \leq Ch^{r_{\mathbf{u}} - (d/2 + 1)} e^{G_{\mathbf{u}}(T)/2} \sqrt{H_{\mathbf{u}}^h(T)},$$

where the last estimate results from Cor. 6.13. Collecting the estimates concludes the proof. ■

³¹Note that for simplicity, quasi-uniformity of the mesh is assumed at this point in order to be able to use a global inverse inequality.

Viscous Dissipation in DG Methods

Structure of this chapter: We aim at a characterisation of the discretisation of viscous dissipation, which allows to distinguish ‘physical’ (also frequently called ‘molecular’, or ‘resolved’) from ‘numerical’ dissipation in DG-discretised incompressible flow simulations; this chapter is based on [DIX]. In order to propose a suitable decomposition, the concept of a DG lifting operator (see Sec. 3.5.2 for more information about HDG lifting techniques) is used. Furthermore, we provide the background for the selection of minimal SIP-DG penalty parameters on tensor-product meshes (1D/2D/3D) for \mathbf{Q}_k^{dc} and $\mathbf{RT}_{[k]}$ FE spaces. The chapter is complemented with numerical demonstrations based on a typical 3D benchmark problem for decaying turbulence (the 3D Taylor–Green vortex at $\text{Re} = 1600$).

7.1	Physical and Numerical Dissipation	82
7.2	A Natural Decomposition for DG Methods	84
7.3	Minimal SIP-DG Penalty Parameter on Hyperrectangles	86
7.3.1	Discrete Inverse Trace Inequality and Application	86
7.3.2	Non-Negativity of Numerical Viscous Dissipation	88
7.3.3	Minimal SIP Parameter	89
7.4	Numerical Demonstration	90

Let us consider an incompressible Navier–Stokes problem with periodic or no-stress boundary conditions, and without acting outer forcing terms, i.e. without any additional volume forces. Given a physical domain $\Omega \subset \mathbb{R}^d$, the strong form of such a problem, equipped with a suitable initial condition $\mathbf{u}_0: \Omega \rightarrow \mathbb{R}^d$, reads (cf. (2.1))

$$\partial_t \mathbf{u} - \nu \Delta \mathbf{u} + (\mathbf{u} \cdot \nabla) \mathbf{u} + \nabla p = \mathbf{0}, \quad \nabla \cdot \mathbf{u} = 0. \tag{7.1}$$

We are especially interested in the situation where the corresponding Reynolds number is large enough such that a turbulent flow is expected, and its approximation is performed in a strongly under-resolved setting. In praxis, a strongly under-resolved simulation may be recognised, for example, by a comparably large amount of numerical dissipation.

Recalling Ch. 3, for a FE pair \mathbf{V}_h/Q_h for velocity/pressure, and assuming that the simulation is performed up to the time instance $T > 0$, a typical DG scheme (in primal form) for discretising (7.1) is written as follows:

$$\left\{ \begin{array}{l} \text{Find } (\mathbf{u}_h, p_h): (0, T] \rightarrow \mathbf{V}_h \times Q_h \text{ with } \mathbf{u}_h(0) = \mathbf{u}_{0h} \text{ s.t., } \forall (\mathbf{v}_h, q_h) \in \mathbf{V}_h \times Q_h, \\ (\partial_t \mathbf{u}_h, \mathbf{v}_h) + \nu a_h(\mathbf{u}_h, \mathbf{v}_h) + c_h(\mathbf{u}_h, \mathbf{v}_h) + j_h(\mathbf{u}_h, \mathbf{v}_h) + b_h(\mathbf{v}_h, p_h) - b_h(\mathbf{u}_h, q_h) = 0. \end{array} \right. \tag{7.2a}$$

$$\tag{7.2b}$$

The bilinear form a_h treats the viscosity effects, c_h the nonlinear convection term, b_h connects pressure and incompressibility condition and j_h is a possible additional stabilisation and/or turbulence model [DE12; Riv08]; see also Sec. 3.2. In this chapter, we will focus on the viscous term a_h .

7.1 Physical and Numerical Dissipation

Testing (7.2) symmetrically with $(\mathbf{v}_h, q_h) = (\mathbf{u}_h, p_h)$ leads to the discrete kinetic energy balance

$$-\partial_t \mathcal{K}(\mathbf{u}_h) = -\frac{d}{dt} \frac{1}{2} \|\mathbf{u}_h\|_{\mathbf{L}^2(\Omega)}^2 = \nu a_h(\mathbf{u}_h, \mathbf{u}_h) + c_h(\mathbf{u}_h; \mathbf{u}_h, \mathbf{u}_h) + j_h(\mathbf{u}_h, \mathbf{u}_h), \quad (7.3)$$

whereas on the continuous level, the counterpart for the exact solution \mathbf{u} is (see also Sec. 2.3)

$$-\partial_t \mathcal{K}(\mathbf{u}) = -\frac{1}{2} \frac{d}{dt} \|\mathbf{u}\|_{\mathbf{L}^2(\Omega)}^2 = \nu \|\nabla \mathbf{u}\|_{\mathbf{L}^2(\Omega)}^2.$$

Hence, the only physical dissipation process in the original Navier–Stokes model is due to viscosity. Therefore, in our opinion, every additional energy-dissipating (or energy-producing) mechanism, which is frequently incorporated in c_h and j_h , has to be characterised as artificial (numerical).

The purpose of this chapter can be explained compactly as follows. *We want to distinguish physical and numerical viscous dissipation in a_h , and aim for an additive decomposition $a_h = a_h^{\text{phy}} + a_h^{\text{num}}$ where both quantities a_h^{phy} and a_h^{num} are non-negative (possibly zero) in order to justify the term ‘dissipation’.* In the DG literature, denoting by ∇_h the broken, i.e. element-wise gradient, the choice $a_h^{\text{phy}}(\mathbf{u}_h, \mathbf{u}_h) = \|\nabla_h \mathbf{u}_h\|_{\mathbf{L}^2}^2$ can be found most frequently (see, e.g. [CH⁺13]). We will demonstrate that this definition can be misleading when an under-resolved simulation is performed, and propose an alternative for a large class of DG methods.

In order to introduce a mathematically rigorous notion of viscous dissipation processes, let a_h^{phy} denote the non-negative part in the discretisation of the viscous term that represents *physical dissipation*, which is supposed to fulfil $a_h^{\text{phy}}(\mathbf{u}, \mathbf{u}) = \|\nabla \mathbf{u}\|_{\mathbf{L}^2}^2$ for the exact solution \mathbf{u} . We assume that the remainder of a_h is a non-negative bilinear form a_h^{num} , which describes *numerical dissipation* in the discretisation of the viscous term, and require that the decomposition is consistent in the sense that $a_h^{\text{num}}(\mathbf{u}_h, \mathbf{u}_h)$ vanishes for $h/k \rightarrow 0$, with \mathbf{u}_h being a discrete solution converging to \mathbf{u} as $h/k \rightarrow 0$. Here, h denotes again the underlying mesh size and k is the polynomial order of discrete velocities belonging to \mathbf{V}_h .

Note that the requirement that both parts of the decomposition be non-negative is a restriction and disallows some choices for a_h^{phy} , which may seem intuitive at first glance. Being able to identify the physical dissipation, the total numerical dissipation $\varepsilon_h^{\text{tot}}$ of the scheme can be defined as

$$\varepsilon_h^{\text{tot}}(\mathbf{u}_h) := -\partial_t \mathcal{K}(\mathbf{u}_h) - \nu a_h^{\text{phy}}(\mathbf{u}_h, \mathbf{u}_h).$$

This total numerical dissipation $\varepsilon_h^{\text{tot}}$ then fulfils the reasonable and widely accepted expectation (for a meaningful discretisation) that it is non-negative; that is, $\varepsilon_h^{\text{tot}}(\mathbf{v}_h) \geq 0$ for all $\mathbf{v}_h \in \mathbf{V}_h$.

Example 7.1 (H^1 -FEM): In an H^1 -conforming setting (see, e.g. [HSF18]) the physical (viscous) dissipation is simply the seminorm $a^{\text{phy}}(\mathbf{u}_h, \mathbf{u}_h) = \|\nabla \mathbf{u}_h\|_{L^2}^2$ while $a_h^{\text{num}}(\mathbf{u}_h, \mathbf{u}_h) = 0$. This definition is unproblematic since the discrete velocity \mathbf{u}_h is continuous here. Numerical dissipation in H^1 -conforming schemes is thus only contained in explicitly added terms such as turbulence modelling and/or convection stabilisation, which are collected in j_h , or are part of c_h . \blacktriangle

Example 7.2 (NIP): The viscous bilinear form of the *non-symmetric* interior penalty (NIP) method [Riv08] for a scalar problem reads

$$a_h(u_h, v_h) := \int_{\Omega} \nabla_h u_h \cdot \nabla_h v_h \, d\mathbf{x} + \sum_{F \in \mathcal{F}_h} \frac{\lambda}{h_F} \int_F \llbracket u_h \rrbracket \llbracket v_h \rrbracket \, d\mathbf{s} \quad (7.4a)$$

$$- \sum_{F \in \mathcal{F}_h} \int_F (\{\!\{ \nabla_h u_h \}\!\} \cdot \mathbf{n}_F) \llbracket v_h \rrbracket \, d\mathbf{s} + \sum_{F \in \mathcal{F}_h} \int_F \llbracket u_h \rrbracket (\{\!\{ \nabla_h v_h \}\!\} \cdot \mathbf{n}_F) \, d\mathbf{s}, \quad (7.4b)$$

where $\lambda > 0$ is the NIP stabilisation parameter. In this case we have a simple decomposition with

$$a_h(u_h, u_h) = \int_{\Omega} |\nabla_h u_h|^2 \, d\mathbf{x} + \sum_{F \in \mathcal{F}_h} \frac{\lambda}{h_F} \int_F \llbracket u_h \rrbracket^2 \, d\mathbf{s} = a_h^{\text{phy}}(u_h, u_h) + a_h^{\text{num}}(u_h, u_h). \quad \blacktriangle$$

In contrast to the decomposition in the previous examples, the decomposition in most other DG schemes is more involved. Especially, $a_h^{\text{phy}}(\mathbf{u}_h, \mathbf{u}_h) = \|\nabla_h \mathbf{u}_h\|_{L^2}^2$ is frequently not a valid option as the remainder of a_h is not necessarily non-negative, as the following example shows.

Example 7.3 (1D SIP): Let us consider the scalar 1D example (with $\nu = 1$), where the domain $\Omega = (0, h)$ with $h = 1$ is only one element with periodic boundary conditions, and use the symmetric interior penalty (SIP) DG discretisation [DE12] with scalar-valued polynomial space V_h of order $k = 1$. The set of facets is only $\mathcal{F}_h = \{1\}$ (due to periodicity). Using $\llbracket v_h \rrbracket = v_h(1) - v_h(0)$ and $\{\!\{ v_h \}\!\} = \frac{1}{2}v_h(0) + \frac{1}{2}v_h(1)$, the symmetrically tested bilinear form in this case is

$$a_h(u_h, u_h) = \int_0^1 |u_h'(x)|^2 \, dx - 2\llbracket u_h \rrbracket(1) \{\!\{ u_h' \}\!\}(1) + \lambda \llbracket u_h \rrbracket^2(1).$$

Here, $\lambda > 0$ is the SIP penalty parameter which needs to be sufficiently large (depending on the constant of a discrete trace inequality) such that a_h defines an inner product on $V_h \setminus \mathbb{R}$ and discrete coercivity is ensured; cf. Ch. 3. Choosing $\lambda = 3/2 > C_{\text{tr},0}^2/2 = 1$ is sufficient as shown in Sec. 7.3. Taking $u_h^* = x$, we obtain $u_h' = 1$, $\{\!\{ u_h' \}\!\}(1) = 1$ and $\llbracket u_h \rrbracket(1) = 1$, which results in $a_h(u_h^*, u_h^*) = \frac{1}{2}$ and $\|\nabla_h u_h^*\|_{L^2(\Omega)}^2 = 1$. Now, the choice $a_h^{\text{phy}}(u_h^*, u_h^*) = \|\nabla_h u_h^*\|_{L^2}^2 = 1$ renders $a_h^{\text{num}}(u_h^*, u_h^*) = -\frac{1}{2}$ negative, thereby contradicting our intuitive understanding that both physical and numerical dissipation should be non-negative. \blacktriangle

We conclude that the choice $a_h^{\text{phy}}(\mathbf{u}_h, \mathbf{u}_h) = \|\nabla_h \mathbf{u}_h\|_{L^2}^2$ can be misleading in DG methods. However, let us mention that the difference between individual notions of physical dissipation in DG methods is only relevant in the under-resolved case. The remainder of this chapter will demonstrate that a lifting technique can be used to define a more suitable decomposition of the total viscous dissipation

into a physical and a numerical contribution. In doing so, we restrict ourselves to the SIP method as a very frequently used DG method.

7.2 A Natural Decomposition for DG Methods

For the sake of presentation, let us recall the SIP bilinear form [DE12] (cf. Sec. 3.2.1)

$$a_h(\mathbf{u}_h, \mathbf{v}_h) := \int_{\Omega} \nabla_h \mathbf{u}_h : \nabla_h \mathbf{v}_h \, d\mathbf{x} + \sum_{F \in \mathcal{F}_h} \frac{\lambda}{h_F} \int_F \llbracket \mathbf{u}_h \rrbracket \cdot \llbracket \mathbf{v}_h \rrbracket \, ds \quad (7.5a)$$

$$- \sum_{F \in \mathcal{F}_h} \int_F \{ \nabla_h \mathbf{u}_h \} \mathbf{n}_F \cdot \llbracket \mathbf{v}_h \rrbracket \, ds - \sum_{F \in \mathcal{F}_h} \int_F \llbracket \mathbf{u}_h \rrbracket \cdot \{ \nabla_h \mathbf{v}_h \} \mathbf{n}_F \, ds, \quad (7.5b)$$

where $\lambda > 0$ is a sufficiently large (due to a discrete inverse inequality) penalty parameter.

One can interpret the DG formulation (7.5) in a mixed setting, cf. [AB⁺02], which gives a natural definition of a discrete diffusive flux (scaled with ν^{-1}) $\boldsymbol{\sigma}_h = \boldsymbol{\sigma}_h(\mathbf{u}_h)$, which is defined element-wise for all $\boldsymbol{\tau}_h \in \nabla_h \mathbf{V}_h|_K$ by the following operation on any $K \in \mathcal{T}_h$, cf. [AB⁺02, eqn. (1.2)]:

$$\int_K \boldsymbol{\sigma}_h : \boldsymbol{\tau}_h \, d\mathbf{x} = - \int_K \mathbf{u}_h \cdot (\nabla \cdot \boldsymbol{\tau}_h) \, d\mathbf{x} + \int_{\partial K} \hat{\mathbf{u}}_h \cdot (\boldsymbol{\tau}_h \mathbf{n}_K) \, ds \quad (7.6a)$$

$$= \int_K \nabla \mathbf{u}_h : \boldsymbol{\tau}_h \, d\mathbf{x} + \int_{\partial K} (\hat{\mathbf{u}}_h - \mathbf{u}_h) \cdot (\boldsymbol{\tau}_h \mathbf{n}_K) \, ds. \quad (7.6b)$$

Here, the second equality is due to integration by parts and $\hat{\mathbf{u}}_h$ denotes a ‘numerical trace’, which characterises different DG methods, see [AB⁺02, Table 3.1]. In the following, for the sake of simplicity, we exclusively want to consider the SIP method where $\hat{\mathbf{u}}_h = \{ \mathbf{u}_h \}$. For SIP, $\hat{\mathbf{u}}_h - \mathbf{u}_h = \{ \mathbf{u}_h \} - \mathbf{u}_h = -1/2 \llbracket \mathbf{u}_h \rrbracket$ and thus we define the DG lifting operator $\mathcal{L}: \mathbf{V}_h|_{\partial K} \rightarrow \nabla_h \mathbf{V}_h|_K$ by

$$\int_{\partial K} (\hat{\mathbf{u}}_h - \mathbf{u}_h) \cdot (\boldsymbol{\tau}_h \mathbf{n}_K) \, ds = - \int_{\partial K} \llbracket \mathbf{u}_h \rrbracket \cdot \frac{1}{2} (\boldsymbol{\tau}_h \mathbf{n}_K) \, ds = - \int_K \mathcal{L}(\llbracket \mathbf{u}_h \rrbracket) : \boldsymbol{\tau}_h \, d\mathbf{x}, \quad \forall K \in \mathcal{T}_h. \quad (7.7)$$

Remark 7.4 (HDG): Note that for HDG methods, the numerical trace $\hat{\mathbf{u}}_h$ simply coincides with the hybrid facet variable. Using the hybrid jump operator $\llbracket \cdot \rrbracket$, this actually leads to a matrix-valued L^2 -HDG lifting $\mathcal{L}(\llbracket \mathbf{u}_h \rrbracket)$, similar to the vector-valued one introduced in Sec. 3.5.2. \blacktriangle

With the notion (7.7) of the lifting operator \mathcal{L} , (7.6) can also finally be used to gain the characterisation

$$\boldsymbol{\sigma}_h(\mathbf{u}_h) = \nabla_h \mathbf{u}_h - \mathcal{L}(\llbracket \mathbf{u}_h \rrbracket), \quad (7.8)$$

for which one directly obtains

$$\begin{aligned} \int_{\Omega} |\boldsymbol{\sigma}_h|^2 \, d\mathbf{x} &= (\boldsymbol{\sigma}_h, \boldsymbol{\sigma}_h)_{L^2} = (\nabla_h \mathbf{u}_h - \mathcal{L}(\llbracket \mathbf{u}_h \rrbracket), \nabla_h \mathbf{u}_h - \mathcal{L}(\llbracket \mathbf{u}_h \rrbracket))_{L^2} \\ &= \int_{\Omega} |\nabla_h \mathbf{u}_h|^2 \, d\mathbf{x} - 2 \int_{\Omega} \nabla_h \mathbf{u}_h : \mathcal{L}(\llbracket \mathbf{u}_h \rrbracket) \, d\mathbf{x} + \int_{\Omega} |\mathcal{L}(\llbracket \mathbf{u}_h \rrbracket)|^2 \, d\mathbf{x}. \end{aligned}$$

For the middle term in this equality, the following DG procedure can be performed after using

definition (7.7) of the lifting $\mathcal{L}(\llbracket \mathbf{u}_h \rrbracket)$:

$$\int_{\Omega} \nabla_h \mathbf{u}_h : \mathcal{L}(\llbracket \mathbf{u}_h \rrbracket) \, d\mathbf{x} = \sum_{K \in \mathcal{T}_h} \int_{\partial K} \frac{1}{2} (\nabla_h \mathbf{u}_h) \mathbf{n}_K \cdot \llbracket \mathbf{u}_h \rrbracket \, d\mathbf{s} \quad (7.9a)$$

$$= \sum_{F \in \mathcal{F}_h} \int_F \frac{1}{2} (\nabla_h \mathbf{u}_h) \mathbf{n}|_{K_1} \cdot \llbracket \mathbf{u}_h \rrbracket + \frac{1}{2} (\nabla_h \mathbf{u}_h) \mathbf{n}|_{K_2} \cdot (-\llbracket \mathbf{u}_h \rrbracket) \, d\mathbf{s} \quad (7.9b)$$

$$= \sum_{F \in \mathcal{F}_h} \int_F \frac{1}{2} [(\nabla_h \mathbf{u}_h)|_{K_1} + (\nabla_h \mathbf{u}_h)|_{K_2}] \mathbf{n}_F \cdot \llbracket \mathbf{u}_h \rrbracket \, d\mathbf{s} \quad (7.9c)$$

$$= \sum_{F \in \mathcal{F}_h} \int_F \{ \nabla_h \mathbf{u}_h \} \mathbf{n}_F \cdot \llbracket \mathbf{u}_h \rrbracket \, d\mathbf{s}. \quad (7.9d)$$

Note the minus sign in front of the jump term in the second line, which stems from the transition of boundary element integrals to the skeleton formulation.

Thus, with the help of (7.9) and definition (7.8) of σ_h , one can decompose the symmetrically tested bilinear form a_h from (7.5) as follows:

$$a_h(\mathbf{u}_h, \mathbf{u}_h) = \underbrace{\int_{\Omega} |\sigma_h|^2 \, d\mathbf{x}}_{=a_h^{\text{phy}}(\mathbf{u}_h, \mathbf{u}_h)} + \underbrace{\sum_{F \in \mathcal{F}_h} \frac{\lambda}{h_F} \int_F |\llbracket \mathbf{u}_h \rrbracket|^2 \, d\mathbf{s} - \int_{\Omega} |\mathcal{L}(\llbracket \mathbf{u}_h \rrbracket)|^2 \, d\mathbf{x}}_{=a_h^{\text{num}}(\mathbf{u}_h, \mathbf{u}_h)}. \quad (7.10)$$

We notice that the usual assumption on the parameter λ guarantees that both parts $a_h^{\text{phy}}(\mathbf{u}_h, \mathbf{u}_h)$ and $a_h^{\text{num}}(\mathbf{u}_h, \mathbf{u}_h)$ are non-negative for any discrete function $\mathbf{u}_h \in \mathbf{V}_h$; a detailed explanation for this statement can be found in Sec. 7.3. Further, note that $a_h^{\text{num}}(\mathbf{u}_h, \mathbf{u}_h) \rightarrow 0$ as $h/k \rightarrow 0$.

Interestingly, as shown above, one can rewrite $a_h^{\text{phy}}(\mathbf{u}_h, \mathbf{u}_h)$ as

$$a_h^{\text{phy}}(\mathbf{u}_h, \mathbf{u}_h) = \int_{\Omega} |\nabla_h \mathbf{u}_h|^2 \, d\mathbf{x} - 2 \sum_{F \in \mathcal{F}_h} \int_F \{ \nabla_h \mathbf{u}_h \} \mathbf{n}_F \cdot \llbracket \mathbf{u}_h \rrbracket \, d\mathbf{s} + \int_{\Omega} |\mathcal{L}(\llbracket \mathbf{u}_h \rrbracket)|^2 \, d\mathbf{x}. \quad (7.11)$$

Let us comment on a few topics. Firstly, the bilinear form a_h^{phy} in (7.11) corresponds to the DG method by Bassi and Rebay [BR97], and can be seen as a central flux approximation to diffusion/viscosity (to the corresponding first-order system). Secondly, note that for SIP a piecewise constant function will not induce physical dissipation if exclusively the broken gradient is used for the definition of a_h^{phy} . In contrast, using the definition (7.10) of a_h^{phy} proposed here, also piecewise constant functions induce physical dissipation.

Moreover, the procedure in the definition of a suitable decomposition of hybrid DG (HDG) methods follows the same reasoning; see Rem. 7.4. In Sec. 7.4, an $\mathbf{H}(\text{div})$ -conforming HDG method will be used for 3D simulations because of its superior effectivity with respect to computational cost; cf. Ch. 3.

7.3 Minimal SIP-DG Penalty Parameter on Hyperrectangles

In this section, we provide the theoretical foundation for the choice of the SIP parameter λ .

7.3.1 Discrete Inverse Trace Inequality and Application

Firstly, let us derive a special discrete inverse trace inequality in 1D, which takes into account *both* end points of the considered interval. Such an estimate is crucial in determining a sharp SIP penalty parameter on hyperrectangles.

Lemma 7.5

Let $I = [a, b]$ be an interval with $h = |b - a|$ and $q \in \mathbb{P}_k(I)$ be a k -th order 1D polynomial. Then,

$$|q(a)|^2 + |q(b)|^2 \leq \frac{C_{\text{tr},k}^2}{h} \int_a^b |q(x)|^2 dx \quad (7.12)$$

holds with $C_{\text{tr},k}^2 = (k+1)(k+2)$.

Proof: In order to prove the claim, consider the shifted Legendre polynomials $L_m(x) = \tilde{L}_m(2x-1)$ on the unit interval $[0, 1]$, where \tilde{L}_m denotes the standard Legendre polynomials defined on $[-1, 1]$. The crucial properties of these polynomials are $L_m(0) = (-1)^m$, $L_m(1) = 1$ and

$$\int_0^1 L_m(x)L_n(x) dx = \frac{1}{2m+1} \delta_{mn}.$$

Thus, using the basis representation $q(x) = \sum_{m=0}^k c_m L_m(x)$, (7.12) can be rewritten as

$$\sum_{m,n=0}^k c_m c_n [(-1)^{m+n} + 1] \leq C_{\text{tr},k}^2 \sum_{m=0}^k c_m^2 \frac{1}{2m+1}.$$

Defining $\mathbf{c} = (c_0, \dots, c_k)^\dagger$, the matrix $\mathbf{B} = (B_{mn})_{m,n=0}^k$ with $B_{mn} = (-1)^{m+n} + 1$, and the matrix $\mathbf{D} = \text{diag}(1/(2m+1))$, one obtains

$$\mathbf{c}^\dagger \mathbf{B} \mathbf{c} \leq C_{\text{tr},k}^2 \mathbf{c}^\dagger \mathbf{D} \mathbf{c} \quad \Leftrightarrow \quad \tilde{\mathbf{c}}^\dagger \mathbf{A} \tilde{\mathbf{c}} \leq C_{\text{tr},k}^2 \tilde{\mathbf{c}}^\dagger \tilde{\mathbf{c}},$$

where $\tilde{\mathbf{c}} = \mathbf{D}^{1/2} \mathbf{c}$ and $\mathbf{A} = \mathbf{D}^{-1/2} \mathbf{B} \mathbf{D}^{-1/2}$ with $\mathbf{D}^{-1/2} = \text{diag}(\sqrt{2m+1})$. The entries A_{mn} of \mathbf{A} are

$$A_{mn} = \begin{cases} 0, & \text{if } m+n \text{ odd,} \\ 4\sqrt{m+1/2}\sqrt{n+1/2}, & \text{otherwise.} \end{cases}$$

Thus, by using the concept of the Rayleigh quotient, determining $C_{\text{tr},k}^2$ reduces to finding the maximum eigenvalue $\lambda_{\max}(\mathbf{A})$ of \mathbf{A} . More precisely, one can verify that

$$C_{\text{tr},k}^2 \geq \lambda_{\max}(\mathbf{A}) = (k+1)(k+2).$$

Applying a scaling argument using the width h , the result can be transferred from $[0, 1]$ to $[a, b]$. Furthermore, $C_{\text{tr},k}^2 = (k+1)(k+2)$ is the smallest possible constant for which (7.12) holds. ■

Note that we verified Lem. 7.5 numerically and observed that the given $C_{\text{tr},k}^2$ is indeed sharp.

The second aim is to apply Lem. 7.5 in the special situation where the normal gradient of the velocity, or the lifting operator, in normal direction on facets has to be estimated. This is the typical application of the discrete trace inequality in DG methods for diffusive problems. As we want to especially treat the Raviart–Thomas $\mathbf{RT}_{[k]}$ case, we exploit the inclusion $\mathbf{Q}_k^{\text{dc}} \subset \mathbf{RT}_{[k]} \subset \mathbf{Q}_{k+1}^{\text{dc}}$ [BBF13].

Lemma 7.6

For all $\mathbf{v}_h \in \mathbf{Q}_{k+1}^{\text{dc}}$ and with $C_{\text{tr},k}^2 = (k+1)(k+2)$, the following discrete trace inequality holds:

$$\|(\nabla \mathbf{v}_h) \mathbf{n}_K\|_{\mathbf{L}^2(\partial K)}^2 \leq \frac{C_{\text{tr},k}^2}{h_K} \|\nabla \mathbf{v}_h\|_{\mathbf{L}^2(K)}^2, \quad \forall K \in \mathcal{T}_h.$$

Proof: This proof is performed for 3D; for 2D and 1D, the same result holds and can be shown as a simplification of the 3D case. Let K be a cube with $K = I_1 \times I_2 \times I_3 = [a_1, b_1] \times [a_2, b_2] \times [a_3, b_3]$ and $h_K = |b_1 - a_1| = |b_2 - a_2| = |b_3 - a_3|$. The boundary of the cube can be decomposed by means of $\partial K = \bigcup_{i=1}^3 \partial K_i$ with $\partial K_i = \{\mathbf{x} \in \partial K : \mathbf{n}_K(\mathbf{x}) \parallel \mathbf{e}_i\}$, where $\mathbf{x} = (x_1, x_2, x_3)^\dagger$ and \mathbf{e}_i denotes the Euclidean unit vector in direction i . Then, one obtains

$$\|(\nabla \mathbf{v}_h) \mathbf{n}_K\|_{\mathbf{L}^2(\partial K)}^2 = \sum_{i=1}^3 \|\partial_{x_i} \mathbf{v}_h\|_{\mathbf{L}^2(\partial K_i)}^2. \quad (7.13)$$

Note that for $\mathbf{v}_h \in \mathbf{Q}_{k+1}^{\text{dc}}$ with $\mathbf{v}_h = (v_1, v_2, v_3)^\dagger$, the charatersiation

$$\mathbf{v}_h|_K \in \text{span} \left\{ \begin{pmatrix} \mathbb{P}_{k+1} \otimes \mathbb{P}_{k+1} \otimes \mathbb{P}_{k+1} \\ \mathbb{P}_{k+1} \otimes \mathbb{P}_{k+1} \otimes \mathbb{P}_{k+1} \\ \mathbb{P}_{k+1} \otimes \mathbb{P}_{k+1} \otimes \mathbb{P}_{k+1} \end{pmatrix} \right\} \Rightarrow (\partial_{x_i} v_m)_{i=1}^3|_K \in \text{span} \left\{ \begin{pmatrix} \mathbb{P}_k \otimes \mathbb{P}_{k+1} \otimes \mathbb{P}_{k+1} \\ \mathbb{P}_{k+1} \otimes \mathbb{P}_k \otimes \mathbb{P}_{k+1} \\ \mathbb{P}_{k+1} \otimes \mathbb{P}_{k+1} \otimes \mathbb{P}_k \end{pmatrix} \right\} \quad (7.14)$$

is valid for all $m = 1, 2, 3$. Now, considering for example $i = 1$ leads to

$$\|\partial_{x_1} \mathbf{v}_h\|_{\mathbf{L}^2(\partial K_1)}^2 = \int_{I_2} \int_{I_3} |\partial_{x_1} \mathbf{v}_h(a_1, x_2, x_3)|^2 + |\partial_{x_1} \mathbf{v}_h(b_1, x_2, x_3)|^2 dx_2 dx_3. \quad (7.15)$$

Fortunately, from (7.14) we can infer that $\partial_{x_1} \mathbf{v}_h(\cdot, x_2, x_3) \in [\mathbb{P}_k(K)]^3$ and thus, the 1D result from Lem. 7.5 can be applied componentwise:

$$|\partial_{x_1} \mathbf{v}_h(a_1, x_2, x_3)|^2 + |\partial_{x_1} \mathbf{v}_h(b_1, x_2, x_3)|^2 \leq \frac{C_{\text{tr},k}^2}{h_K} \int_{I_1} |\partial_{x_1} \mathbf{v}_h(x_1, x_2, x_3)|^2 dx_1.$$

Inserting this estimate into (7.15) leads to

$$\|\partial_{x_1} \mathbf{v}_h\|_{\mathbf{L}^2(\partial K_1)}^2 \leq \frac{C_{\text{tr},k}^2}{h_K} \int_{I_1} \int_{I_2} \int_{I_3} |\partial_{x_1} \mathbf{v}_h(x_1, x_2, x_3)|^2 dx_1 dx_2 dx_3 = \frac{C_{\text{tr},k}^2}{h_K} \|\partial_{x_1} \mathbf{v}_h\|_{\mathbf{L}^2(K)}^2.$$

Finally, using the same arguments also for $i = 2, 3$ and inserting the particular estimates for $\|\partial_{x_i} \mathbf{v}_h\|_{\mathbf{L}^2(\partial K_i)}^2$ into (7.13) concludes the proof. \blacksquare

7.3.2 Non-Negativity of Numerical Viscous Dissipation

We now want to show that provided a certain minimum SIP penalty parameter λ^* is chosen, the numerical viscous dissipation $a_h^{\text{num}}(\mathbf{v}_h, \mathbf{v}_h)$, defined in (7.10), is non-negative for all $\mathbf{v}_h \in \mathbf{V}_h$. Here, only $\mathbf{V}_h = \mathbf{Q}_{k+1}^{\text{dc}}$ is considered, which includes the $\mathbf{RT}_{[k]}$ case. For the sake of brevity, suppose we are working only on meshes containing lines/squares/cubes, then $h_F = h_K$ for all $F \in \mathcal{F}_K$ and for all $K \in \mathcal{T}_h$.

Lemma 7.7

Provided $\lambda \geq \lambda^* = \frac{1}{2} C_{\text{tr},k}^2$, the numerical dissipation of (7.5) is non-negative; that is,

$$a_h^{\text{num}}(\mathbf{v}_h, \mathbf{v}_h) = \sum_{F \in \mathcal{F}_h} \frac{\lambda}{h_F} \int_F |[\![\mathbf{v}_h]\!]|^2 ds - \int_{\Omega} |\mathcal{L}([\![\mathbf{v}_h]\!])|^2 d\mathbf{x} \geq 0, \quad \forall \mathbf{v}_h \in \mathbf{V}_h = \mathbf{Q}_{k+1}^{\text{dc}}.$$

Proof: Rewriting the penalty term from skeleton to boundary element formulation, one obtains

$$a_h^{\text{num}}(\mathbf{v}_h, \mathbf{v}_h) = \sum_{K \in \mathcal{T}_h} \frac{1}{2} \frac{\lambda}{h_K} \int_{\partial K} |[\![\mathbf{v}_h]\!]|^2 ds - \sum_{K \in \mathcal{T}_h} \int_K |\mathcal{L}([\![\mathbf{v}_h]\!])|^2 d\mathbf{x}.$$

Inserting definition (7.7) for the SIP lifting, and using Cauchy–Schwarz and Young ($\varepsilon > 0$), the estimate

$$\begin{aligned} \sum_{K \in \mathcal{T}_h} \int_K |\mathcal{L}([\![\mathbf{v}_h]\!])|^2 d\mathbf{x} &= \sum_{K \in \mathcal{T}_h} \int_{\partial K} [\![\mathbf{v}_h]\!] \cdot \frac{1}{2} \mathcal{L}([\![\mathbf{v}_h]\!]) \mathbf{n}_K ds \\ &\leq \sum_{K \in \mathcal{T}_h} \frac{\varepsilon}{4} \int_{\partial K} |[\![\mathbf{v}_h]\!]|^2 ds + \sum_{K \in \mathcal{T}_h} \frac{1}{4\varepsilon} \int_{\partial K} |\mathcal{L}([\![\mathbf{v}_h]\!]) \mathbf{n}_K|^2 ds \end{aligned}$$

holds. Furthermore, due to the fact that $\mathcal{L}: \mathbf{V}_h|_{\partial K} \rightarrow \nabla_h \mathbf{V}_h|_K$, one can now apply the discrete trace inequality (Lem. 7.6) to infer

$$\int_{\partial K} |\mathcal{L}([\![\mathbf{v}_h]\!]) \mathbf{n}_K|^2 ds \leq \frac{C_{\text{tr},k}^2}{h_K} \|\mathcal{L}([\![\mathbf{v}_h]\!])\|_{\mathbf{L}^2(K)}^2.$$

Choosing $\varepsilon = C_{\text{tr},k}^2/(2h_K)$ and reordering thus yields

$$\sum_{K \in \mathcal{T}_h} \int_K |\mathcal{L}(\llbracket \mathbf{v}_h \rrbracket)|^2 d\mathbf{x} \leq \sum_{K \in \mathcal{T}_h} \frac{C_{\text{tr},k}^2}{4h_K} \int_{\partial K} |\llbracket \mathbf{v}_h \rrbracket|^2 d\mathbf{s}. \quad (7.16)$$

Inserting this estimate into the definition of a_h^{num} leads to

$$\begin{aligned} a_h^{\text{num}}(\mathbf{v}_h, \mathbf{v}_h) &\geq \sum_{K \in \mathcal{T}_h} \frac{1}{2} \frac{\lambda}{h_K} \int_{\partial K} |\llbracket \mathbf{v}_h \rrbracket|^2 d\mathbf{s} - \sum_{K \in \mathcal{T}_h} \frac{C_{\text{tr},k}^2}{4h_K} \int_{\partial K} |\llbracket \mathbf{v}_h \rrbracket|^2 d\mathbf{s} \\ &\geq \sum_{K \in \mathcal{T}_h} \frac{1}{2} \left(\frac{\lambda - \frac{1}{2} C_{\text{tr},k}^2}{h_K} \right) \int_{\partial K} |\llbracket \mathbf{v}_h \rrbracket|^2 d\mathbf{s}. \end{aligned}$$

Concluding, whenever λ is chosen according to $\lambda \geq \lambda^* = \frac{1}{2} C_{\text{tr},k}^2$, a_h^{num} is non-negative. \blacksquare

7.3.3 Minimal SIP Parameter

Lastly, we establish a connection between non-negativity of a_h^{num} and the discrete coercivity (stability) of the corresponding SIP-DG method (7.5).

Lemma 7.8

Provided $\lambda > \lambda^* = \frac{1}{2} C_{\text{tr},k}^2$, the SIP-DG method (7.5) is coercive on $\mathbf{V}_h = \mathbf{Q}_{k+1}^{\text{dc}}$.

Proof: Testing (7.5) symmetrically, inserting the definition of the lifting operator and going over from skeleton to boundary element formulation (using (7.9)) yields

$$\begin{aligned} a_h(\mathbf{v}_h, \mathbf{v}_h) &= \int_{\Omega} |\nabla_h \mathbf{v}_h|^2 d\mathbf{x} - 2 \sum_{F \in \mathcal{F}_h} \int_F \{ \nabla_h \mathbf{v}_h \} \mathbf{n}_F \cdot \llbracket \mathbf{v}_h \rrbracket d\mathbf{s} + \sum_{F \in \mathcal{F}_h} \frac{\lambda}{h_F} \int_F |\llbracket \mathbf{v}_h \rrbracket|^2 d\mathbf{s} \\ &= \sum_{K \in \mathcal{T}_h} \int_K |\nabla \mathbf{v}_h|^2 d\mathbf{x} - 2 \sum_{K \in \mathcal{T}_h} \int_K \nabla \mathbf{u}_h : \mathcal{L}(\llbracket \mathbf{u}_h \rrbracket) d\mathbf{x} + \sum_{K \in \mathcal{T}_h} \frac{1}{2} \frac{\lambda}{h_K} \int_{\partial K} |\llbracket \mathbf{v}_h \rrbracket|^2 d\mathbf{s}. \end{aligned}$$

Applying Cauchy–Schwarz and Young’s inequality ($\varepsilon > 0$) to the problematic middle term, and exploiting the boundedness of the lifting operator (7.16), one obtains

$$\sum_{K \in \mathcal{T}_h} \int_K \nabla \mathbf{u}_h : \mathcal{L}(\llbracket \mathbf{u}_h \rrbracket) d\mathbf{x} \leq \sum_{K \in \mathcal{T}_h} \frac{1}{2\varepsilon} \int_K |\nabla_h \mathbf{v}_h|^2 d\mathbf{x} + \sum_{K \in \mathcal{T}_h} \frac{\varepsilon C_{\text{tr},k}^2}{2} \frac{1}{4h_K} \int_{\partial K} |\llbracket \mathbf{v}_h \rrbracket|^2 d\mathbf{s}.$$

Inserting this estimate leads to

$$a_h(\mathbf{v}_h, \mathbf{v}_h) \geq \left(1 - \frac{1}{\varepsilon} \right) \|\nabla_h \mathbf{v}_h\|_{L^2}^2 + \sum_{K \in \mathcal{T}_h} \frac{1}{2} \left(\frac{\lambda - \frac{\varepsilon}{2} C_{\text{tr},k}^2}{h_K} \right) \int_{\partial K} |\llbracket \mathbf{v}_h \rrbracket|^2 d\mathbf{s}.$$

Choosing $\varepsilon > 0$ infinitesimal, the minimum stabilisation can be achieved by $\lambda > \lambda^* = \frac{1}{2} C_{\text{tr},k}^2$. This coincides with the minimum λ which is needed for non-negativity of a_h^{num} . \blacksquare

7.4 Numerical Demonstration

We consider the classical 3D Taylor–Green vortex (TGV) problem, which is frequently used to investigate the performance of flow solvers for freely decaying turbulence [Bra91; TG37]; much more information will be provided in Sec. 9.1. In the periodic box $\Omega = (0, 2\pi)^3$, the space-periodic initial condition

$$\mathbf{u}_0(\mathbf{x}) = (\cos(x_1) \sin(x_2) \sin(x_3), -\sin(x_1) \cos(x_2) \sin(x_3), 0)^\dagger, \quad (7.17)$$

is the only driving force. For the subsequent simulations, the considered Reynolds number is $\text{Re} = \nu^{-1} = 1600$ and the computations are performed until $T = 20$.

The domain is decomposed into N^3 cubes and the $\mathbf{H}(\text{div})$ -conforming Raviart–Thomas element $\mathbb{RT}_{[k]}$ [BBF13] is employed in an exactly divergence-free HDG framework as explained in Ch. 3. Especially, in order to focus on viscous effects, we do not use any convection stabilisation or additional terms and hence, $c_h(\mathbf{u}_h; \mathbf{u}_h, \mathbf{u}_h) = 0$ and $j_h \equiv 0$. Thus, $-\partial_t \mathcal{K}(\mathbf{u}_h) = \nu a_h(\mathbf{u}_h, \mathbf{u}_h)$ and $\varepsilon_h^{\text{tot}} = \nu a_h^{\text{num}}(\mathbf{u}_h, \mathbf{u}_h)$. Concerning the SIP penalty term, we are interested in the smallest penalty that guarantees non-negative total dissipation. For the (vector-valued) heat equation this constant can be computed explicitly in the case of a periodic Cartesian mesh as $\lambda^* = C_{\text{tr},k} = (k+1)(k+2)$ for the considered $\mathbb{RT}_{[k]}$ -HDG method, or $\lambda^* = k(k+1)/2$ for a \mathbb{Q}_k^{dc} -DG method. The corresponding calculations have been derived in Sec. 7.3. Note that due to the incompressibility constraint, which results in the fact that a_h only acts on the (discretely) divergence-free subspace, the actual minimal penalty parameter can be smaller. A reference solution with $k = 8$ and $N = 16$ has been computed and we focus on the comparison of viscous dissipation in the under-resolved situation $k = 4$, $N = 8$ for different SIP penalties $\lambda \in \{2, 1.5, 1.25, 1\} \lambda^*$.

The upper row of Fig. 7.1 shows that, largely unimpaired by the penalty parameter, the evolution of both the kinetic energy $\mathcal{K}(\mathbf{u}_h)$ and the (negative) total kinetic energy dissipation rate $-\partial_t \mathcal{K}(\mathbf{u}_h)$ is reasonable, although we are strongly under-resolved.

Concerning the viscous dissipation rates, the bottom row shows how the *interpretation* of physical and numerical dissipation differs if broken gradients are used (left) or if our proposed decomposition (7.10) is taken into account (right). Let us stress that the discretisation is the same for both columns and that for $t \leq 4$, the flow seems to be resolved. Thus, in a resolved simulation, the difference between which metric is used becomes irrelevant.

For larger times, however, one can observe that with broken gradients, the perception of the physical dissipation rate strongly depends on the penalty parameter λ , even though the total kinetic energy dissipation rate $-\partial_t \mathcal{K}(\mathbf{u}_h)$ does not change much. Furthermore, if λ is chosen small, but still sufficiently large to guarantee non-increasing kinetic energy, the metric ‘numerical dissipation’ defined by broken gradients (left) can become negative. This suggests that this characterisation acts unreasonably. However, in our opinion, this is not a flaw in the method but rather in the

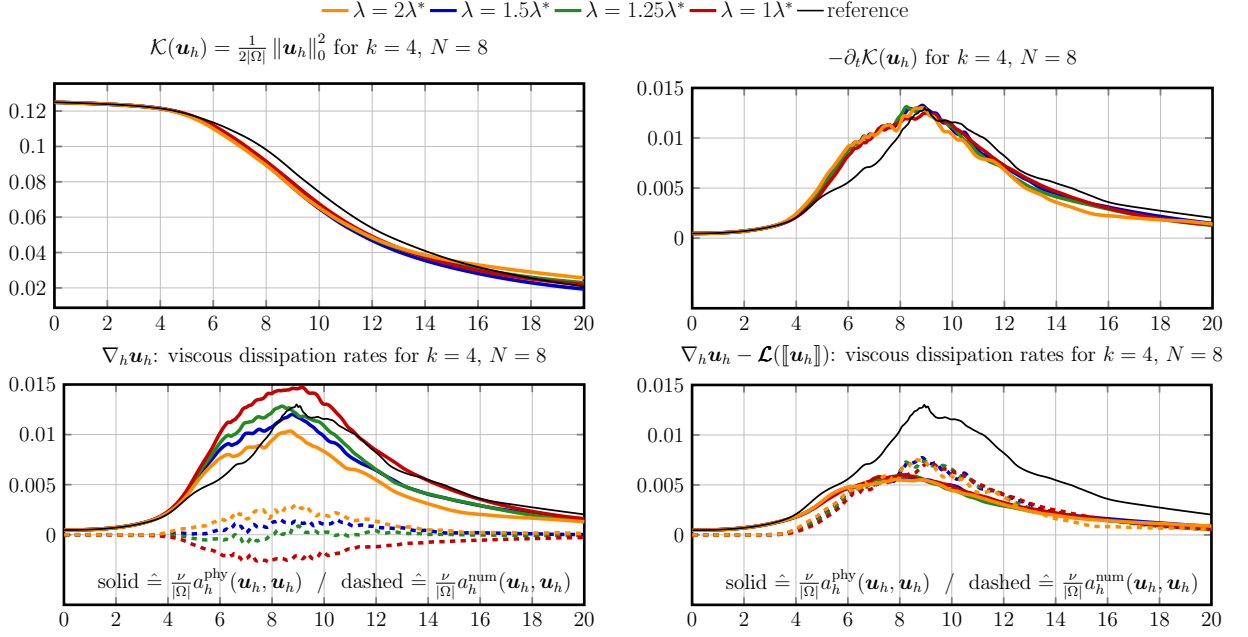


Fig. 7.1: Kinetic energy, kinetic energy dissipation rate and viscous dissipations (physical and numerical) for $t \in [0, 20]$, computed with $k = 4$, $N = 8$. In the bottom row, using the broken gradient $\nabla_h \mathbf{u}_h$ in the definition of the physical dissipation (left) leads to negative numerical viscous dissipation while using σ_h from (7.8) (right) does not.

metric. There is no conclusion that can be drawn from the sign of the broken gradient metric. On the other hand, when our proposed method (7.10) of decomposing the viscous dissipation is used (right), both physical and numerical dissipation are non-negative.

Lastly, concerning the interpretation of the amount of resolution a simulation can offer, the definition with the broken gradients suggests that most of the total dissipation stems from physical dissipation, whereas our proposition (7.10) distributes it more or less evenly between physical and numerical viscous dissipation. In view of a clearly under-resolved simulation for $t > 4$, the latter behaviour is much more natural to us.

2D High-Order CFD Applications

Structure of this chapter: The application of high-order FEM for the simulation of 2D incompressible CFD problems is considered. Beginning with the classical problem of a Kármán vortex street behind an obstacle, we establish a connection between such a flow and pressure-robustness by means of the concept of generalised Beltrami flows. Then, we show results for a Kelvin–Helmholtz instability problem at $\text{Re} = 10\,000$, demonstrate its sensitivity and analyse the occurring convection forces by means of a discrete Helmholtz decomposition. In order to study the self-organisation mechanisms of 2D flows, the last example deals with freely decaying turbulence at various Reynolds numbers. It is intended to build the foundation to emphasise the significantly different physical mechanisms which dominate 2D flows in contrast to the 3D flows considered in the next chapter.

8.1 Vortex Shedding Past Blunt Body	93
8.2 Kelvin–Helmholtz Instability	96
8.2.1 Results for $\text{Re} = 10\,000$	98
8.2.2 Helmholtz Decomposition of Convection Forces	102
8.3 Two-Dimensional Turbulence	105
8.3.1 Results for Different Reynolds Numbers	106
8.3.2 Analysis of Dissipation Processes	109
8.3.3 Long-Time Simulation	111

8.1 Vortex Shedding Past Blunt Body

In Sec. 4.2 it was shown that for generalised Beltrami flows, pressure-robust methods can be much more accurate than non-pressure-robust ones. However, a natural question is whether pressure-robust discretisations are also superior for ‘realistic flows’. Therefore, in this section, we will first investigate to what extent realistic flows are, at least in some parts of the domain, generalised Beltrami flows; see also [DVII]. Secondly, the regions in the flow are identified where p -robust methods are superior compared to non- p -robust ones.

As an example of a practically relevant flow, let us consider the flow around an obstacle ($\mathbf{f} = \mathbf{0}$) in a 2D channel of dimensions $(L, H) = (3, 1.01)$. The obstacle is chosen as a square with side length $r = 0.1$, whose lower left corner is placed at $\mathbf{x} = (0.7, 0.45)^\dagger$. In Fig. 8.1, such a flow can be seen at a time instance where the characteristic vortex shedding of a periodic Kármán vortex street has formed ($t = T = 10$). The Dirichlet inflow BC on the left part of the boundary is given by the parabolic profile $u_1(t, 0, x_2) = 6x_2(H - x_2)/H^2$, which, together with $\nu = 10^{-3}$ leads to the Reynolds number $\text{Re} = \bar{u}r/\nu = 1 \times 0.1 \times 1000 = 100$. On top, bottom and the boundary of the square, no-slip is prescribed and the right part of the boundary represents the outflow boundary (do-nothing).

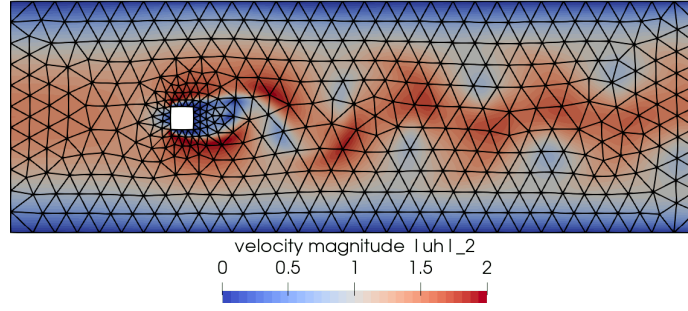


Fig. 8.1: Periodic Kármán vortex shedding in the wake of a square. Visualisation of velocity magnitude $|\mathbf{u}_h|_2$, computational mesh and underlying geometry. Unless stated otherwise, computations are done with $\mathbf{BDM}_4/\mathbb{P}_3^{\text{dc}}$ and upwinding is used ($\theta = 1$).

The most obvious approach for answering where locally the flow behaves like a generalised Beltrami flow is to begin with inspecting the convection term $(\mathbf{u}_h \cdot \nabla_h)\mathbf{u}_h$ in a suitable norm. We have chosen to investigate it in the $\mathbf{L}^{3/2}$ norm, since even for 3D flows the exact nonlinear convection term $(\mathbf{u} \cdot \nabla)\mathbf{u}$ is (for almost all times, in the sense of Bochner spaces) in $\mathbf{L}^{3/2}$.

Fig. 8.2 shows such a qualitative approach, based on the divergence-free $\mathbf{BDM}_4/\mathbb{P}_3^{\text{dc}}$ -SIP-DG method with $\lambda = 8k^2$. At first, we observe that in a large part of the domain the convective term (approximately) vanishes. Wherever $(\mathbf{u}_h \cdot \nabla_h)\mathbf{u}_h \approx \mathbf{0}$, the flow approximates locally a Stokes solution, and is thus trivially a generalised Beltrami flow. However, there are also some regions in the flow where the convection term itself is large (the upstream side of the obstacle and parts of the wake, for instance). These are the regions which are more interesting to us. In the following, proceeding as in Sec. 4.1, we again make use of the discrete Helmholtz projection to investigate them³².

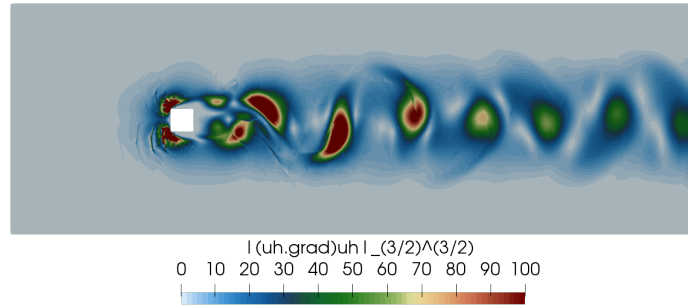


Fig. 8.2: Discrete convection term $|(\mathbf{u}_h \cdot \nabla_h)\mathbf{u}_h|_{3/2}^{3/2}$ computed with $\mathbf{BDM}_4/\mathbb{P}_3^{\text{dc}}$. Note that the colour bar is chosen in such a way that all values above 100 are shown red.

More precisely, the interesting question is where $\mathbf{f}_h = (\mathbf{u}_h \cdot \nabla_h)\mathbf{u}_h$, again computed with the $\mathbf{BDM}_k/\mathbb{P}_{k-1}^{\text{dc}}$ method, is locally a gradient and where its divergence-free part vanishes. After performing the discrete Helmholtz decomposition $\mathbf{f}_h = \mathbb{P}_h^{\text{div}}(\mathbf{f}_h) + \nabla\phi_h$ (see Ch. 3), the divergence-free part of \mathbf{f}_h is encoded in the discrete Helmholtz projection $\mathbb{P}_h^{\text{div}}(\mathbf{f}_h)$, as can be seen in Fig. 8.3 where the colour bar scaling is chosen identically to that of Fig. 8.2. Wherever $\mathbb{P}_h^{\text{div}}(\mathbf{f}_h)$ is small, the

³²Ideally, we would like to perform the Helmholtz decomposition of the exact convection term $(\mathbf{u} \cdot \nabla)\mathbf{u}$ which, of course, is inaccessible to us. Thus, we resort to investigating $(\mathbf{u}_h \cdot \nabla_h)\mathbf{u}_h$ on the assumption that the flow has been approximated reasonably well.

vortex street flow behaves locally like a generalised Beltrami flow. We observe that this is indeed the case at various points in the domain.

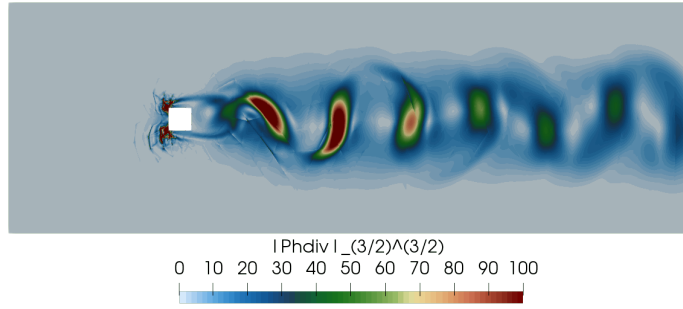


Fig. 8.3: Divergence-free contribution $|\mathbb{P}_h^{\text{div}}(\mathbf{f}_h)|_{3/2}^{3/2}$ of discrete Helmholtz decomposition computed with exactly divergence-free $\mathbf{BDM}_4/\mathbb{P}_3^{\text{dc}}$. Colour bar scaling identically to Fig. 8.2.

On the other hand, the gradient contribution $\nabla\phi_h$ of \mathbf{f}_h can be seen in Fig. 8.4 where, for a better comparison, the colour bar scaling is also chosen identically to that of Fig. 8.2. One can observe that especially in the direct vicinity of the obstacle, there is a significant gradient contribution in $(\mathbf{u}_h \cdot \nabla_h)\mathbf{u}_h$, which indicates that the Kármán vortex street problem might benefit from a pressure-robust discretisation. In the wake, however, mostly the divergence-free contribution $\mathbb{P}_h^{\text{div}}(\mathbf{f}_h)$ seems to dominate the dynamics of the convective part.

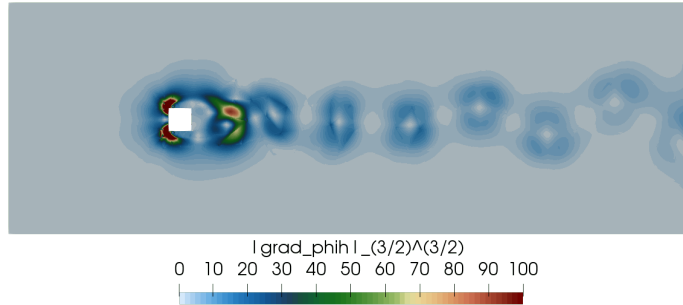


Fig. 8.4: Gradient contribution $|\nabla\phi_h|_{3/2}^{3/2}$ of discrete Helmholtz decomposition computed with exactly divergence-free $\mathbf{BDM}_4/\mathbb{P}_3^{\text{dc}}$. Colour bar scaling identically to Fig. 8.2.

The second question, namely where a p -robust method outperforms a non- p -robust method, can be answered with the help of a second discrete Helmholtz projection, where the same discrete convection term \mathbf{f}_h is decomposed using the non- p -robust discrete Helmholtz projection $\mathbb{P}_h^0(\mathbf{f}_h)$. Note that due to the L^2 -DG Helmholtz projection of the $\mathbb{P}_k^{\text{dc}}/\mathbb{P}_{k-1}^{\text{dc}}$ method, $\mathbb{P}_h^0(\mathbf{f}_h)$ is not exactly divergence-free, even though \mathbf{f}_h has been computed with the div-free $\mathbf{BDM}_4/\mathbb{P}_3^{\text{dc}}$ method.

Now, considering Fig. 8.5, the difference of the two discrete Helmholtz projectors, i.e. $\mathbb{P}_h^{\text{div}}(\mathbf{f}_h) - \mathbb{P}_h^0(\mathbf{f}_h)$ identifies the regions in the flow where a pressure-robust method is more accurate than a non-pressure-robust one. This is due to the fact that a difference between the $\mathbf{H}(\text{div})$ Helmholtz projector $\mathbb{P}_h^{\text{div}}$ and the L^2 Helmholtz projector \mathbb{P}_h^0 indicates that the corresponding non-pressure-

robust $\mathbb{P}_k^{\text{dc}}/\mathbb{P}_{k-1}^{\text{dc}}$ method would see a wrong force locally, which cannot be desired in general.

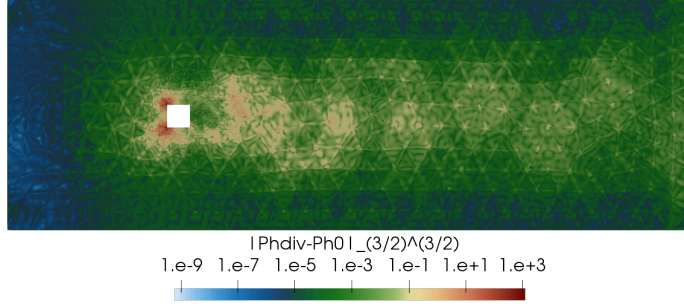


Fig. 8.5: Difference $|\mathbb{P}_h^{\text{div}}(\mathbf{f}_h) - \mathbb{P}_h^0(\mathbf{f}_h)|_{3/2}^{3/2}$ of the two discrete Helmholtz projectors for $k = 4$. High values indicate advantageous regions of the pressure-robust discretisation. Note that the colour scale is chosen logarithmically.

Lastly, the behaviour of the difference of discrete Helmholtz projections under k -refinement is considered. Table 8.1 shows the convergence of the $L^{3/2}$ -norm of the $\mathbf{BDM}_k/\mathbb{P}_{k-1}^{\text{dc}}$ convective term $\mathbf{f}_h = (\mathbf{u}_h \cdot \nabla_h)\mathbf{u}_h$, the discrete Helmholtz projectors $\mathbb{P}_h^{\text{div}}(\mathbf{f}_h)$ and $\mathbb{P}_h^0(\mathbf{f}_h)$, and their difference $\mathbb{P}_h^{\text{div}}(\mathbf{f}_h) - \mathbb{P}_h^0(\mathbf{f}_h)$. One can observe that the difference between the discrete Helmholtz projectors of the L^2 - and the $\mathbf{H}(\text{div})$ -DG methods decreases (although quite slowly due to the sharp corners of the obstacle).

Table 8.1: Convergence behaviour for $L^{3/2}$ -norms of the convection term $\mathbf{f}_h = (\mathbf{u}_h \cdot \nabla_h)\mathbf{u}_h$ and its discrete Helmholtz projections for different polynomial orders $k \in \{2, \dots, 9\}$.

k	2	3	4	5	6	7	8	9
$\ \mathbf{f}_h\ _{L^{3/2}}$	7.823	8.442	8.239	8.045	7.902	7.85	7.831	7.82
$\ \mathbb{P}_h^{\text{div}}(\mathbf{f}_h)\ _{L^{3/2}}$	6.884	7.351	7.181	6.935	6.814	6.784	6.774	6.765
$\ \mathbb{P}_h^0(\mathbf{f}_h)\ _{L^{3/2}}$	7.015	7.381	7.199	6.949	6.824	6.79	6.778	6.767
$\ \mathbb{P}_h^{\text{div}}(\mathbf{f}_h) - \mathbb{P}_h^0(\mathbf{f}_h)\ _{L^{3/2}}$	1.162	0.502	0.303	0.239	0.198	0.159	0.125	0.098

Complementing the observations of Table 8.1, Fig. 8.6 shows some pointwise plots of the difference between the Helmholtz projectors. It is especially interesting that their difference concentrates in the vicinity of the object, which means that pressure-robust methods might have a higher accuracy near objects located in a flow. This is an interesting observation, as important quantities such as drag and lift are measured at the surface of such obstacles.

8.2 Kelvin–Helmholtz Instability

In the literature, the probably most often used example for a high Reynolds number flow in 2D seems to be the Kelvin–Helmholtz (KH) instability, also called mixing layer, problem defined in [LS⁺88]. Numerical investigations can be found in numerous publications; cf., for example, [AC⁺17; BK⁺97; Bur07; DIH; GK00; GWR05; IDD03; Joh05; NW03; OVG07; SF00; V GK97; YBC16]. Starting from a noisy initial condition, small vortices arise which then pair to larger and larger vortices until finally, one vortex remains. Note that such a behaviour of energy transfer from small to large

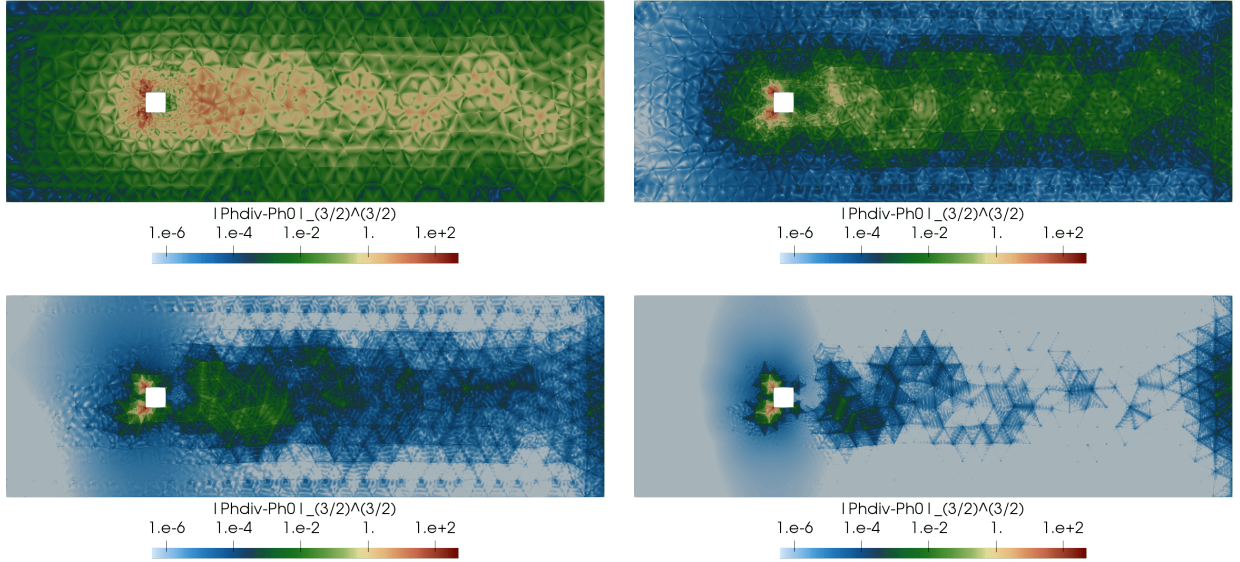


Fig. 8.6: Difference of discrete Helmholtz projectors $|\mathbb{P}_h^{\text{div}}(\mathbf{f}_h) - \mathbb{P}_h^0(\mathbf{f}_h)|_{3/2}^{3/2}$ for different polynomial orders $k \in \{2, 4, 6, 9\}$ (from top left to bottom right).

scales is characteristic for (high Reynolds number) two-dimensional flows. Three-dimensional flows usually cannot reorganise themselves into large structures; see also Sec. 2.4. The KH instability example presents a richness of flow scales and an interesting temporal evolution of the flow field. Furthermore, the mixing layer problem possesses the classical features of deterministic chaos inherent to the Navier–Stokes problem³³. The explanations in this section are based on the (much more detailed) investigations in [DVI]. However, results connected to the discrete Helmholtz decomposition of the (discrete) convection term in Sec. 8.2.2 are original.

The most frequently found setting for a KH instability problem is the evolution of an initial condition in a viscous incompressible Navier–Stokes flow. Due to the fact that no body forces are present, the whole motion is driven only by the initial condition. For the viscosity $\nu > 0$, the time-dependent incompressible Navier–Stokes problem (2.1) with $\mathbf{f} = \mathbf{0}$ is considered. Moreover, $\Omega = (0, 1)^2$ defines the domain where at $x = 0$ and $x = 1$, periodic BCs are used, and at $y = 0$ and $y = 1$, stress-free (free-slip) BCs are prescribed. The initial condition is given by

$$\mathbf{u}_0(x, y) = \begin{bmatrix} u_\infty \tanh\left(\frac{2y-1}{\delta_0}\right) \\ 0 \end{bmatrix} + c_n \begin{bmatrix} \partial_y \psi(x, y) \\ -\partial_x \psi(x, y) \end{bmatrix}, \quad (8.1)$$

with corresponding stream function

$$\psi(x, y) = u_\infty \exp\left(-\frac{(y-0.5)^2}{\delta_0^2}\right) [\cos(8\pi x) + \cos(20\pi x)].$$

Here, $\delta_0 = 1/28$ denotes the initial vorticity thickness, $u_\infty = 1$ is a reference velocity and $c_n = 10^{-3}$ represents a scaling/noise factor.

³³The interaction of deterministic chaos and the concept of 2D self-organisation in flow problems is discussed in more detail in [DVI].

The principal behaviour of the flow is as follows, compare [Les08, Sec. 3.4.1] or, originally [Mic64]. The perturbations prescribed in the right-hand side term of (8.1) are amplified, such that vortices develop. Here, the most amplified mode corresponds to the longitudinal wavelength $\lambda_a = 7\delta_0$. In particular, $n \in \mathbb{N}$ primary vortices develop in a domain with length $n\lambda_a$ in horizontal direction. Hence, due to choosing $\delta_0 = 1/28$, in the numerical simulations, $n = 4$, i.e., so-called ‘4-eddy calculations’ [LS⁺88], are performed. The Reynolds number Re of the KH instability flow is usually calculated on the basis of the characteristic length scale δ_0 , and the characteristic velocity scale u_∞ ; i.e., $\text{Re} = \delta_0 u_\infty / \nu = 1/(28\nu)$ and in this work, exclusively $\text{Re} = 10\,000$ is considered. For the simulations and their evaluation, the time unit $\bar{t} = t \times u_\infty / \delta_0$ is introduced.

8.2.1 Results for $\text{Re} = 10\,000$

In the following, we present results computed with the high-order $\mathbf{RT}_{[8]}^{\text{red}}/\mathbf{F}_8/\mathbb{P}_0^{\text{dc}}$ SIP-HDG ($\lambda = 8k^2$) method on a sequence of square meshes with 16^2 to 256^2 elements. For the time discretisation, a constant time step of size $\Delta t = \delta_0 \times 10^{-3} \approx 3.6 \times 10^{-5}$ is used together with the second-order semi-implicit BDF (SBDF2) method from [ARW95], which combines a second-order BDF scheme for the Stokes subproblem with a second-order accurate extrapolation in time for the nonlinear convection term. A feeling for the computational cost can be obtained from Table 8.2, where the resulting number of degrees of freedom (DOFs) and non-zero entries (NZE) in the system matrix M^* are summarised. Here, the counted DOFs indicate the costs for explicit operator applications (convection), while the NZEs allow to assess the effort involved in implicit linear system solves for the Stokes subproblems. Linear systems are solved with a sparse direct solver (sparse Cholesky from NGSolve [Sch14]) and iterative refinement. For the chosen (relative) tolerance of 10^{-12} (measured in the 2-norm) usually two or three iterative refinements are sufficient. The gain in accuracy due to the iterative refinement proved to be very important for the quite sensitive KH instability problem; see [DVI] for more information.

Table 8.2: Overview of meshes, DOFs and NZEs of M^* based on a discretisation with $\mathbf{RT}_{[8]}^{\text{red}}/\mathbf{F}_8/\mathbb{P}_0^{\text{dc}}$. DOFs are counted before static condensation whereas NZEs from the Schur complement are counted after static condensation. Hybrid facet DOFs of \mathbf{F}_8 are not counted.

Mesh	16^2	32^2	64^2	128^2	256^2
$\#\{\mathbf{u} \text{ DOFs}\}$	21 280	84 544	337 024	1 345 792	5 378 560
$\#\{p \text{ DOFs}\}$	256	1024	4096	16 384	65 536
$\#\{\text{nz}(M^*)\}$	1 075 472	4 292 640	17 152 064	68 571 264	274 211 072

Let us begin with the description of the computational results in Fig. 8.7, which shows vorticity plots on the finest 256^2 mesh illustrating the time evolution and dynamics of the involved vortices. In the first row, the transition from the initial condition to the four primary vortices is shown. At $\bar{t} = 17$, the fine scales of the flow are clearly visible. This is a well-known property of two-dimensional flows for which (in contrast to 3D flows) energy is transferred from small to large scales. In the second row, after the second merging process is completed at $\bar{t} = 56$, we observe

that the two vortices are rotating a very long time, and are still clearly separated at $\bar{t} = 200$. This is a very important difference compared to similar computations in the literature. To the best of our knowledge, until now there are no reliable results available in which the vortices are stable for such a long time. One can see that directly after the merging process to two vortices, they have an ellipsoidal shape and fine scales are clearly visible. As the two vortices rotate, shear forces act dissipatively on the fine scales, thereby smoothing and smearing them out, which has the result that the shape of the vortices becomes more circular. Finally, the two vortices start the pairing process in the third row. Again, the resulting vortex, at first, has many fine scale details which are dissipated over time. Note that the last vortex rotates in the middle of the domain. As has been observed in [DVI], predicting the time instance of the last vortex pairing cannot be done reliably due to the sensitivity of the problem.

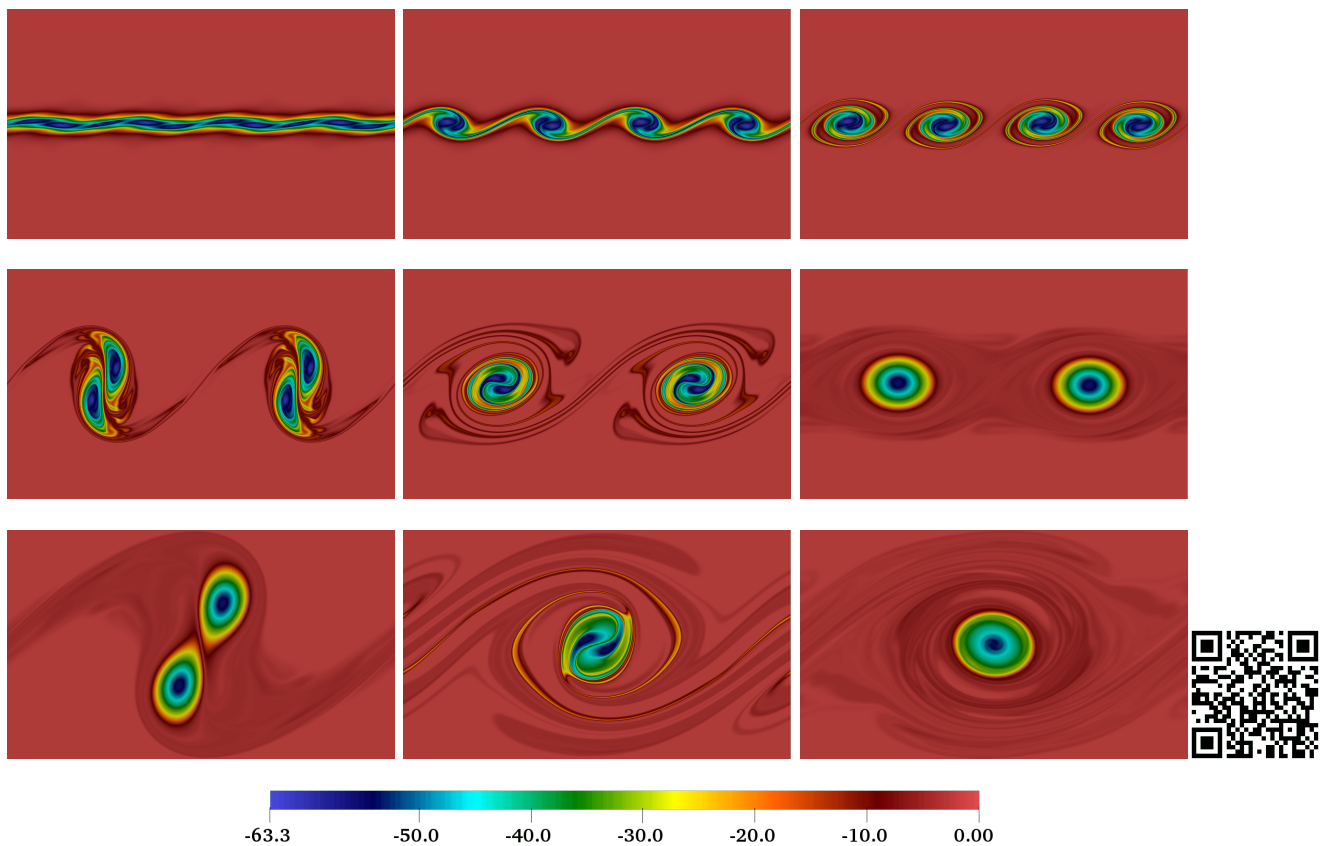


Fig. 8.7: Vorticity $\nabla_h \times \mathbf{u}_h$ for the $\text{Re} = 10000$ Kelvin–Helmholtz instability at (from left to right and top to bottom) $\bar{t} \in \{5, 10, 17, 34, 56, 200, 240, 278, 400\}$. Obtained with div-free $\mathbf{H}(\text{div})$ -HDG method $\mathbf{RT}_{[8]}^{\text{red}}/\mathbf{F}_8/\mathbb{P}_0^{\text{dc}}$ on the finest 256^2 mesh; cf. Table 8.2. (A video of this simulation is available at <https://youtu.be/fXL5ULPNdbU>; note also the QR code.)

More quantitatively, Fig. 8.8 shows the evolution of the resulting kinetic energy for all considered meshes $16^2, \dots, 256^2$. Note that all curves start with the same amount of initial kinetic energy $\mathcal{K}(\mathbf{u}_h(0)) \approx 0.4822$ and, consistent with fluid dynamics theory, all curves are strictly monotonically decreasing. Due to a less dominant role of viscous effects, the flow loses comparably little kinetic energy for this high Reynolds number. In fact, the results show that the kinetic energy loss amounts to only about 0.54% over the course of $\bar{t} = 400$ time units, compared to the energy at $\bar{t} = 0$. Fur-

thermore, one can observe that an essentially mesh-converged state can be reached for basically all considered times $\bar{t} \leq 400$. From our experience, kinetic energy is the quantity of interest which is easiest to compute accurately, even on coarse meshes. Especially, it does not indicate any merging processes of the involved vortices.

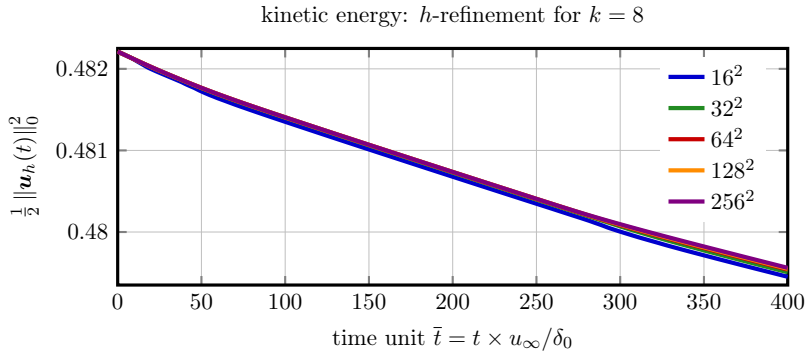


Fig. 8.8: Evolution of kinetic energy for $\text{Re} = 10\,000$ with div-free $\mathbf{RT}_{[8]}^{\text{red}}/\mathbf{F}_8/\mathbb{P}_0^{\text{dc}}$ on a sequence of square meshes.

On the other hand, the evolution of enstrophy, depicted in Fig. 8.9, reveals more insights about the merging processes. At the initial time, one has roughly the same amount of enstrophy $\mathcal{E}(\mathbf{u}_h(0)) \approx 37.63$ for all simulations and, with the possible exception of the very coarse 16^2 simulation, all curves are strictly monotonically decreasing, which is in agreement with the theory in Sec. 2.3. Moreover, equation (2.16) predicts that the decrease in enstrophy is especially strong whenever the palinstrophy is large and, in anticipation of Fig. 8.10, this behaviour is very well observable here. In contrast to the kinetic energy, different meshes result in a different enstrophy but however, the only real difference on fine meshes can be seen in the interval $\bar{t} \in [250, 350]$, where the last pairing of the vortices takes place. This last merging from two vortices to one vortex is very sensitive with respect to perturbations to such an extent that even the two highest resolutions do not show mesh-independence.

Remark 8.1: Note that the desire of having a mesh-converged enstrophy *pointwise in time* is rather ambitious and, in the present situation, not necessarily realistic from an analytical point of view. However, exclusively in the 2D periodic case, one can at least find $L^\infty(\mathbf{H}^1)$ energy estimates for the exact solution \mathbf{u} ; see, for example, [DG95, Sec. 5.4]. Such energy estimates can be extended to FE approximations \mathbf{u}_h , but having control over $\|\mathbf{u} - \mathbf{u}_h\|_{L^\infty(\mathbf{H}^1)}$ by means of *error* estimates with quantitative convergence rates is an open problem and we are not aware of any existing literature in this direction. In fact, numerical error analysis for time-dependent Navier–Stokes flows usually only covers the convergence of the integral quantity $\int_0^t \|\nabla_h[\mathbf{u} - \mathbf{u}_h](\tau)\|_0^2 d\tau$ for $t \in (0, T)$; cf., for example, Cor. 6.13. Here, by choosing a divergence-free method, also on the discrete level, the L^2 -norm of the gradient is identical to the L^2 -norm of the vorticity — the enstrophy. \blacktriangle

Finally, the evolution of the palinstrophy on all meshes is displayed in Fig. 8.10. In contrast to kinetic energy and enstrophy, palinstrophy can increase spontaneously (see (2.17)), and such outbursts always correspond to the merging of vortices in the KH problem. Thus, $\mathcal{P}(\mathbf{u}_h)$ is obviously

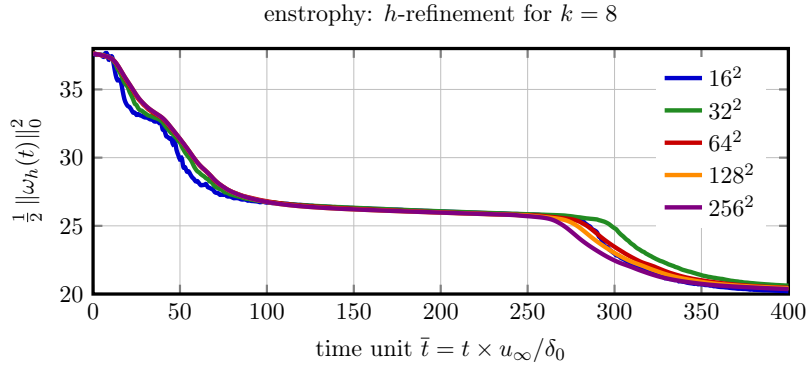


Fig. 8.9: Evolution of enstrophy for $\text{Re} = 10\,000$ with div-free $\mathbf{RT}_{[8]}^{\text{red}}/\mathbf{F}_8/\mathbb{P}_0^{\text{dc}}$ on a sequence of square meshes.

a very sensitive quantity of interest which makes it perfect for comparing results. One can see three time intervals where the palinstrophy has very pronounced local maxima, and these intervals mark the three merging processes of the vortices. Especially, this means that the last merging process does not occur before $\bar{t} = 200$. On the other hand, the time instance of the last pairing cannot be predicted precisely which is due to the sensitivity of the problem; cf. [DVI].

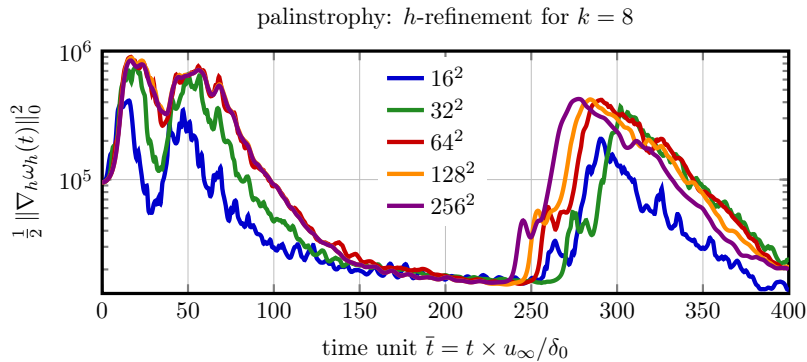


Fig. 8.10: Evolution of palinstrophy for $\text{Re} = 10\,000$ with div-free $\mathbf{RT}_{[8]}^{\text{red}}/\mathbf{F}_8/\mathbb{P}_0^{\text{dc}}$ on a sequence of square meshes.

Remark 8.2: One can evidently see that it is very hard to reliably compute approximate solutions for this problem for times larger than $\bar{t} = 200$. In fact, we want to remark at this point that also numerical error analysis predicts an *exponential* growth in the error for time-dependent Navier–Stokes simulations; cf., for example Thm. 6.11. More precisely, it is shown that, roughly speaking, the error in kinetic energy $\mathcal{K}(\mathbf{u}_h)$ and enstrophy $\mathcal{E}(\mathbf{u}_h)$ can only be controlled up to a factor $\exp(G_{\mathbf{u}}(t))$, where $G_{\mathbf{u}}$ is a Gronwall term which depends on the regularity of the exact solution \mathbf{u} . As $t \rightarrow \infty$, unavoidably, one loses control over the accuracy of any finite element approximation. This might also facilitate the understanding of the difficulties in obtaining a reliable last merging for the KH problem from a theoretical point of view. \blacktriangle

Furthermore, in order to also consider the behaviour of the KH instability problem in the situation that the mesh is fixed and the polynomial order k of the discrete spaces is changed, we provide

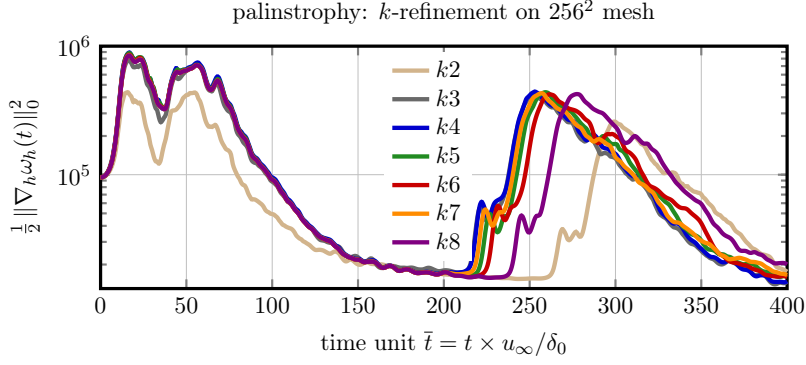


Fig. 8.11: Evolution of palinstrophy for $\text{Re} = 10\,000$ with divergence-free $\mathbb{RT}_{[k]}^{\text{red}}/\mathbb{F}_k/\mathbb{P}_0^{\text{dc}}$ for a sequence of polynomial orders on the 256^2 mesh.

Fig. 8.11. This plot shows the evolution of the palinstrophy, which previously has been identified as the most sensitive quantity of interest, as a function of k where the finest 256^2 mesh has been chosen. Firstly, k -convergence of $\mathcal{P}(\mathbf{u}_h)$ can be observed for $\bar{t} \leq 200$, which is in agreement with the h -refinement study above. Furthermore, $k = 4$ on the 256^2 seems to be the minimum resolution for which reliable results can be computed up to $\bar{t} = 200$. For larger times ($\bar{t} > 200$), the palinstrophy behaves analogously as for the h -refinement study. Namely, the instance in time where the last merging occurs is also very sensitive with respect to the used polynomial degree of the FE spaces.

Remark 8.3: In [DVI] also results for smaller Reynolds numbers are presented, which are less expensive to obtain in terms of necessary computational resources. A corresponding video of simulations comparing the different Reynolds numbers is available at <https://youtu.be/nx4FXAHP7E0>; note also the QR code.



8.2.2 Helmholtz Decomposition of Convection Forces

As already executed in Sec. 4.1 and Sec. 8.1, we now want to take a closer look at the forces acting in this 2D KH problem. Note that in doing so, we consider the fluid problem itself and not (primarily) its discretisation anymore. The interesting force for us is represented by the discrete convection term, computed with the $\mathbb{RT}_{[k]}^{\text{red}}/\mathbb{F}_k/\mathbb{P}_0^{\text{dc}}$ method, and we will again use the discrete Helmholtz projection $\mathbb{P}_h^{\text{div}}$ to obtain the decomposition

$$\mathbf{f}_h = (\mathbf{u}_h \cdot \nabla_h) \mathbf{u}_h = \mathbb{P}_h^{\text{div}}(\mathbf{f}_h) + \nabla \phi_h, \quad (8.2)$$

which is based on the corresponding $\mathbb{RT}_{[k]}/\mathbb{P}_k^{\text{dc}}$ DG method defined by (3.10). In (8.2), $\mathbb{P}_h^{\text{div}}(\mathbf{f}_h)$ represents the divergence-free forces and $\nabla \phi_h$ describes the curl-free gradient forces. Thanks to using a pressure-robust method, the former are cleanly balanced by the discrete velocity and the latter by the discrete pressure. In the following, we only show results for the $16^2, \dots, 128^2$ meshes, because we already saw a satisfactory convergence, at least for $\bar{t} \leq 200$.

The evolution in time of the $\mathbf{L}^{3/2}$ -norm, under mesh-refinement, of the left-hand side of (8.2) (discrete convection term) can be seen in Fig. 8.12. Firstly, one observes that the full convection term

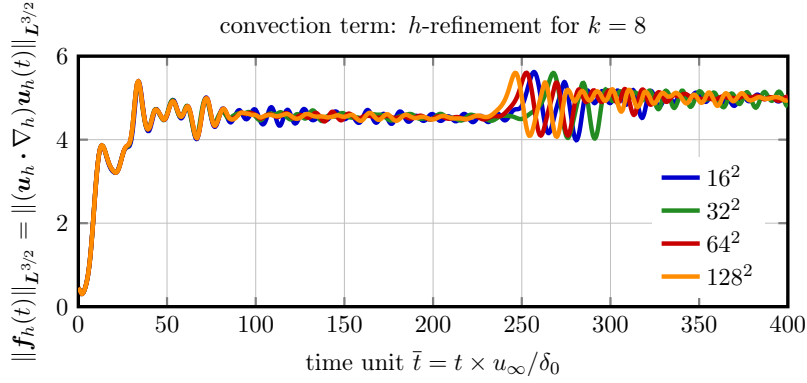


Fig. 8.12: Evolution of $L^{3/2}$ norm of convection term for $\text{Re} = 10000$ with divergence-free $\mathbf{RT}_{[8]}^{\text{red}}/\mathbf{F}_8/\mathbb{P}_0^{\text{dc}}$ on a sequence of square meshes.

is always contributing to the momentum balance, which means that the flow is governed by non-linear mechanisms stemming from the convection term. At no time, the corresponding problem behaves globally like a Stokes problem. However, peaks in $\|\mathbf{f}_h\|_{L^{3/2}}$ can be observed at times which correspond to the previously described merging processes.

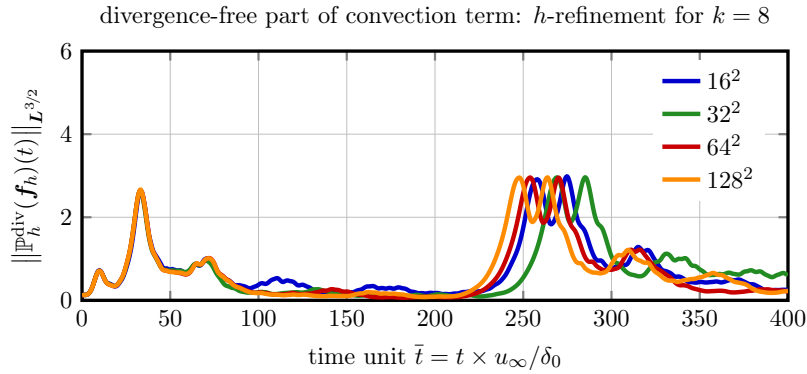


Fig. 8.13: Evolution of divergence-free part of convection term for $\text{Re} = 10000$ with divergence-free $\mathbf{RT}_{[8]}^{\text{red}}/\mathbf{F}_8/\mathbb{P}_0^{\text{dc}}$ on a sequence of square meshes.

Inspecting the right-hand side of (8.2), we consider first the evolution of the divergence-free forces $\|\mathbb{P}_h^{\text{div}}(\mathbf{f}_h)\|_{L^{3/2}}$ in Fig. 8.13. In a pressure-robust method, changes in the divergence-free part of $(\mathbf{u}_h \cdot \nabla_h)\mathbf{u}_h$ affect only the discrete velocity, as already explained above. One can observe distinct peaks of $\|\mathbb{P}_h^{\text{div}}(\mathbf{f}_h)\|_{L^{3/2}}$ locally in time, whenever merging processes occur. Those peaks are directly linked to the peaks observed in the palinstrophy in Fig. 8.10. Whenever vortices are rotating at a fixed position in space (see again Fig. 8.7), $\|\mathbb{P}_h^{\text{div}}(\mathbf{f}_h)\|_{L^{3/2}}$ approaches zero and the flow field of this KH instability is approximately behaving like a generalised Beltrami flow (in time). Because convection is the only acting physical mechanism in this problem, the whole dynamics of the flow can be traced back directly to the divergence-free forces in \mathbf{f}_h .

On the other hand, the evolution of the gradient forces $\|\nabla\phi_h\|_{L^{3/2}}$ in Fig. 8.14 reveals that more dominant forces originating in the convection term are gradient forces, which have to be balanced

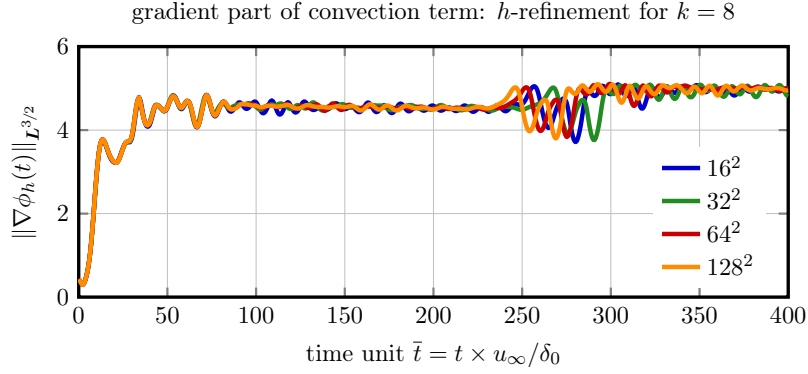


Fig. 8.14: Evolution of gradient part of convection term for $\text{Re} = 10\,000$ with divergence-free $\mathbf{RT}_{[8]}^{\text{red}}/\mathbf{F}_8/\mathbb{P}_0^{\text{dc}}$ on a sequence of square meshes.

by the discrete pressure. This observation can be used to conclude that also for this type of flow problem, a pressure-robust discretisation in general might be superior.

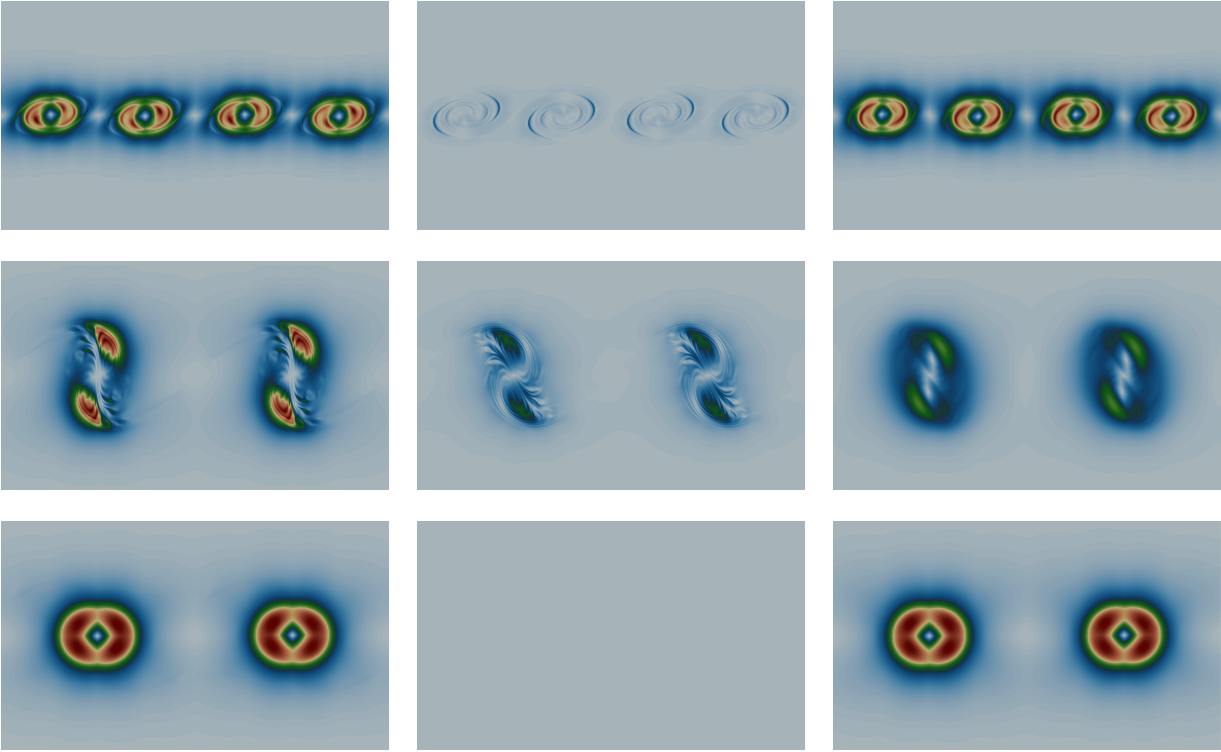


Fig. 8.15: Snapshots of $|\mathbf{u}_h \cdot \nabla_h \mathbf{u}_h|_{3/2}^{3/2}$ (left column), $|\mathbb{P}_h^{\text{div}}(\mathbf{f}_h)|_{3/2}^{3/2}$ (middle column) and $|\nabla\phi_h|_{3/2}^{3/2}$ (right column) for the $\text{Re} = 10\,000$ Kelvin–Helmholtz instability at $\bar{t} = 10$ (top row), $\bar{t} = 34$ (middle row) and $\bar{t} = 200$ (bottom row). Obtained with div-free $\mathbf{H}(\text{div})$ -HDG method $\mathbf{RT}_{[8]}^{\text{red}}/\mathbf{F}_8/\mathbb{P}_0^{\text{dc}}$ on the 128^2 mesh. Colour bar is identical in each row.

Supplementing the quantitative explanations, let us also regard qualitatively how the considered convection forces behave locally. We restrict ourselves to the time interval $\bar{t} \leq 200$ and the 128^2 mesh, for which reliable results can be obtained. Snapshots of the various terms in the discrete Helmholtz decomposition (8.2) at different times can be seen in Fig. 8.15. The left column shows

for different times $\bar{t} \in \{10, 34, 200\}$ that the discrete convection term is locally high exactly where the vortical motion occurs. When the corresponding vortices are rotating at a fixed position, the corresponding curl-free term $\nabla\phi_h$ (right column) is the dominating effect. However, the middle row displays the situation where a merging process is taking place and exactly then, also the divergence-free contribution $\mathbb{P}_h^{\text{div}}(\mathbf{f}_h)$ plays a crucial role. Note that for each fixed \bar{t} (row), the colour bar is chosen identically for all columns.

8.3 Two-Dimensional Turbulence

In this last 2D example, let $\Omega = (0, 1)^2$ and the initial velocity $\mathbf{u}_0 = (\partial_{x_2}\psi, -\partial_{x_1}\psi)^\dagger$ shall represent $n_v^2 = 32^2 = 1024$ pairwise oppositely rotating vortices resulting from the stream function

$$\psi(\mathbf{x}) = \sum_{k,j=1}^{n_v} A_{kj}(-1)^{k+j} \exp\left(-10^4 \left[\left(x_1 - \frac{k}{n_v+1}\right)^2 + \left(x_2 - \frac{j}{n_v+1}\right)^2 \right]\right), \quad (8.3)$$

where $A_{kj} \in \mathbb{R}$ for $k, j = 1, \dots, n_v$ are random samples drawn from a normal (Gaussian) distribution with mean 10^{-2} and standard deviation 10^{-3} ; see also [DIII] where a similar setting has been investigated. Here, \mathbf{u}_0 evolves unimpeded; thus $\mathbf{f} = \mathbf{0}$ and therefore we are dealing with a freely decaying problem. The domain is equipped with periodic boundary conditions on the vertical and horizontal parts of $\partial\Omega$ ³⁴. In using this initial condition, we intentionally impose both a high frequency instability by means of the slightly different peaks of the vortices, and a low frequency instability since the vortices are not distributed equidistantly, i.e. the distance of vortices across the periodic boundaries is larger than in the ‘interior’ of the domain. A corresponding display of the initial state of the problem can be seen in Fig. 8.16.

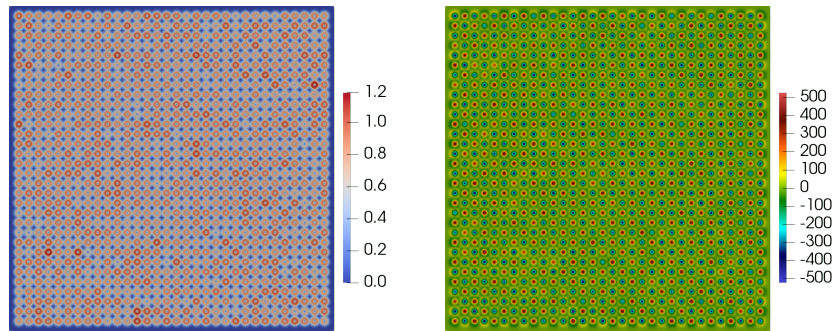


Fig. 8.16: Initial velocity magnitude $|\mathbf{u}_h(0)|$ (left) and vorticity $\nabla_h \times \mathbf{u}_h(0)$ (right) for all freely decaying 2D turbulence simulations.

A flow with such an initial condition, especially for high Reynolds numbers, is very unstable and tends to evolve into a rather chaotic motion. This phenomenon is known as two-dimensional turbulence; we refer to Sec. 2.4 and [BE12; Tab02] for more information. 2D turbulence follows the Kraichnan–Batchelor–Leith (KBL) theory [Dav04], and typical properties of freely decaying flows are the energy spectrum $E(\kappa) \sim \kappa^{-3}$ and, in stark contrast to 3D turbulence, the self-organisation

³⁴Thus, the pressure has to be determined uniquely by means of, for example, the zero-mean condition.

of small-scale features of the flow into constantly growing large-scale coherent vortices; cf. [Van88].

Studying such problems is not novel; see, for example, [BM⁺00a] where freely decaying 2D turbulence has been studied in the vorticity-stream function formulation. Also, we would like to mention [SS12], where a comparison of different numerical schemes (no FEM, though) for the DNS of freely decaying 2D turbulence in ω/ψ -formulation has been presented. Moreover, in the context of atmospheric flows, the transfer of energy and enstrophy between scales is very important, and a comparable flow configuration for the study of freely decaying 2D turbulence can be found in [TKW14] (also in ω/ψ -formulation).

In contrast to the experiments in [DIII], our intention here is to use high-order methods to compute the evolution of such a turbulent freely decaying 2D flow. For the computations, the $\mathbf{RT}_{[8]}^{\text{red}}/\mathbf{F}_k/\mathbb{P}_0^{\text{dc}}$ $\mathbf{H}(\text{div})$ - \mathbf{H}^1 -lifting-HDG method ($\lambda = k$, $\lambda_\ell = 2$) has been used on a single mesh³⁵ consisting of 64^2 square elements (Table 8.2 is also valid here). The time-stepping is performed up to $T = 24$, using a constant time step $\Delta t = 10^{-4}$ with the second-order RK variant ARS(2,2,2) of the implicit-explicit (IMEX) method introduced in [ARS97]. It is especially interesting to investigate the behaviour of the resulting flow for different Reynolds numbers, as the particular difference can be seen very instructively. Thus, in the following, we consider the three cases $\nu \in \{10^{-4}, 2 \times 10^{-5}, 10^{-6}\}$.

8.3.1 Results for Different Reynolds Numbers

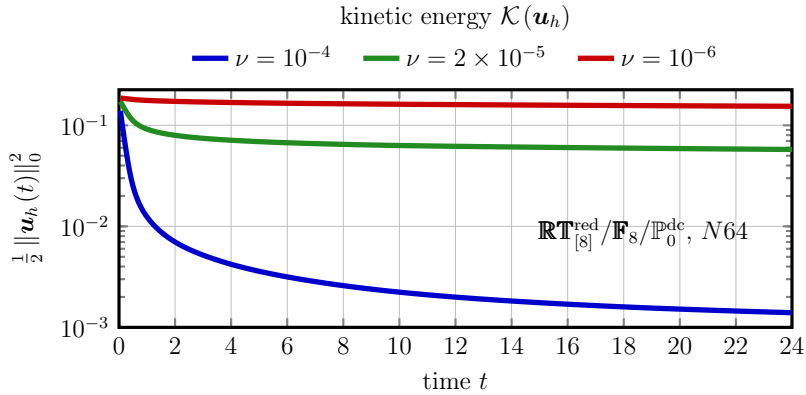


Fig. 8.17: Evolution of kinetic energy for $\nu \in \{10^{-4}, 2 \times 10^{-5}, 10^{-6}\}$, computed with the divergence-free $\mathbf{RT}_{[8]}^{\text{red}}/\mathbf{F}_8/\mathbb{P}_0^{\text{dc}}$ $\mathbf{H}(\text{div})$ - \mathbf{H}^1 -lifting-HDG method on a 64^2 mesh.

First of all, Fig. 8.17 and Fig. 8.18 show the evolution of the kinetic energy and enstrophy for the three different viscosities. We observe the expected behaviour that with decreasing ν , $\mathcal{K}(\mathbf{u}_h)$ also decays much more slowly. For $\nu = 10^{-6}$, kinetic energy seems to be fairly constant over time. More interesting is the behaviour of the enstrophy $\mathcal{E}(\mathbf{u}_h)$. Especially for the smallest viscosity, one can observe a small initial range up to $t \approx 0.75$ where the enstrophy decays only slowly. In accordance with [Dav04, Ch. 10] this describes a transition zone in which 2D turbulence develops out of the ordered initial condition. After that, a stronger decay in $\mathcal{E}(\mathbf{u}_h)$ can be observed, which corresponds

³⁵As can be seen from the subsequent analysis in Sec. 8.3.2, this is already a rather sufficient resolution for resolving the most important flow characteristics in this 2D example.

to fully developed 2D turbulence.

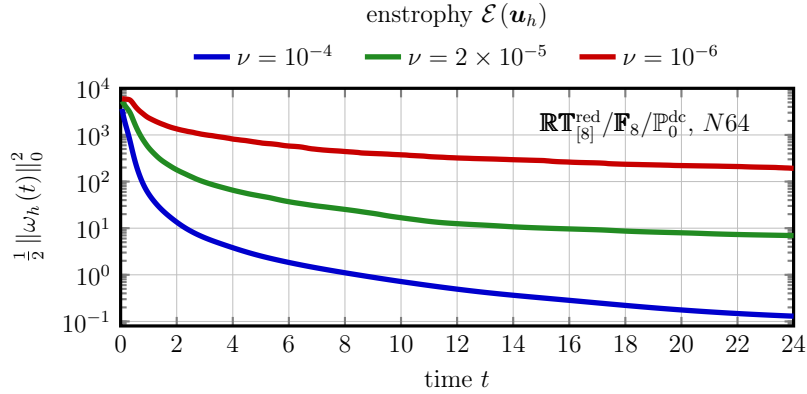


Fig. 8.18: Evolution of enstrophy for $\nu \in \{10^{-4}, 2 \times 10^{-5}, 10^{-6}\}$, computed with the divergence-free $\mathbf{RT}_{[8]}^{\text{red}}/\mathbf{F}_8/\mathbb{P}_0^{\text{dc}}$ $\mathbf{H}(\text{div})$ - \mathbf{H}^1 -lifting-HDG method on a 64^2 mesh.

Additionally, in Fig. 8.19 one can look at the evolution of the palinstrophy over time. While the largest viscosity $\nu = 10^{-4}$ leads to a strictly decreasing palinstrophy, the two smaller viscosities show a small increase in $\mathcal{P}(\mathbf{u}_h)$ at the beginning of the simulation. Moreover, it can be seen that over time, the palinstrophy indeed spontaneously increases.

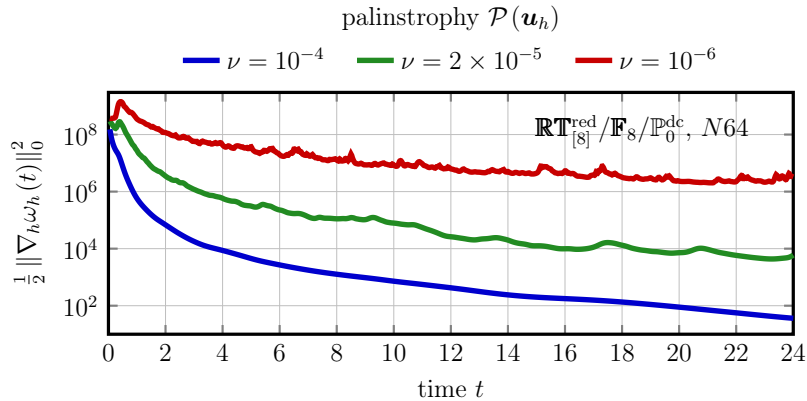


Fig. 8.19: Evolution of palinstrophy for $\nu \in \{10^{-4}, 2 \times 10^{-5}, 10^{-6}\}$, computed with the divergence-free $\mathbf{RT}_{[8]}^{\text{red}}/\mathbf{F}_8/\mathbb{P}_0^{\text{dc}}$ $\mathbf{H}(\text{div})$ - \mathbf{H}^1 -lifting-HDG method on a 64^2 mesh.

In Fig. 8.20, snapshots of the vorticity can be seen for the different viscosities (columns) at certain time instances (rows). At first, it becomes clear how viscous forces attack the initial vorticity field, consisting of 1024 clearly separated vortices, and therefore, depending on which ν is considered, a more or less chaotic motion can be observed. Here, a smaller viscosity leads to a more small-scale structure of the flow. As time proceeds, one can directly observe that while the multitude of vortices moves through the domain, like-signed vortices merge and oppositely rotating vortices repel each other. One can see clearly that over time, the flow tends to self-organise itself into large-scale structures; see also [Van88]. Furthermore, a smaller viscosity implies less molecular diffusion and, therefore, the colour bars show that the absolute value of the vorticity is considerably higher than

for larger viscosities.

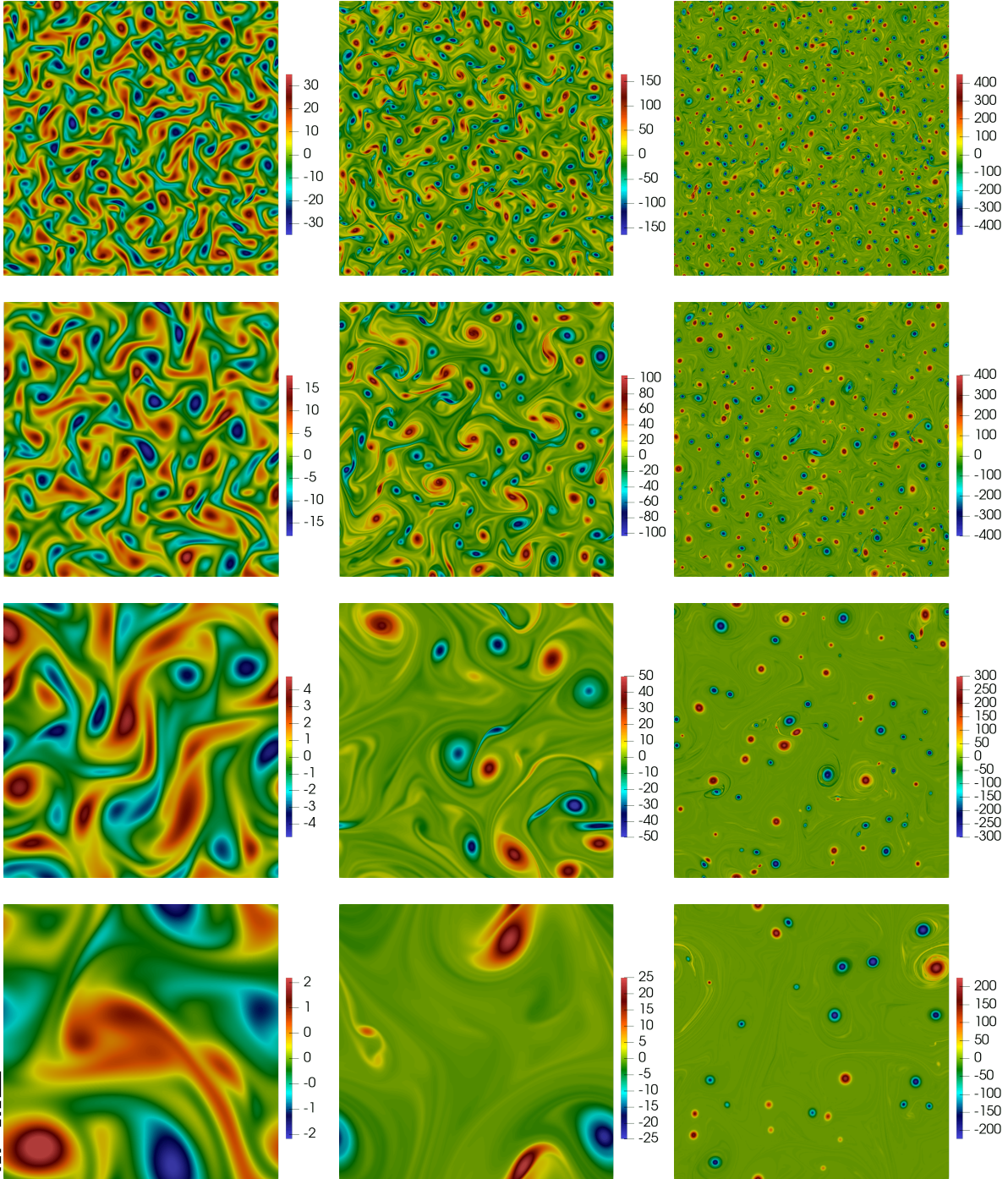


Fig. 8.20: Vorticity $\nabla_h \times \mathbf{u}_h(t)$ for freely decaying 2D turbulence with $\nu \in \{10^{-4}, 2 \times 10^{-5}, 10^{-6}\}$ (from left to right) at $t \in \{1, 2, 8, 24\}$ (from top to bottom). Obtained with div-free $\mathbf{H}(\text{div})$ -HDG method $\mathbf{RT}_{[8]}^{\text{red}}/\mathbf{F}_8/\mathbb{P}_0^{\text{dc}}$ on a 64^2 mesh. (A video of this simulation is available at <https://youtu.be/0zUCPAD4YDQ>; note also the QR code.)

A more quantitative comparison of the (time-dependent) distribution of small- and large-scale structures can be obtained by considering the energy spectra; see Fig. 8.21. There, a mutual characteristic of all simulations is that kinetic energy, which is initially concentrated in high wavenumbers

(small eddies), over time is transferred to smaller wavenumbers (large eddies). Note that this is exactly in agreement with the observations from Fig. 8.20. The spectra show a decaying evolution from which, with decreasing viscosity (increasing Reynolds number), the classical $E(\kappa) \sim \kappa^{-3}$ slope can be determined in a certain inertial range. However, the slope is sometimes slightly steeper and thus shows more a κ^{-4} behaviour at some later time instances. A similar phenomenon of a slope between κ^{-3} and κ^{-4} has also been observed for the KH instability problem [LS⁺88].

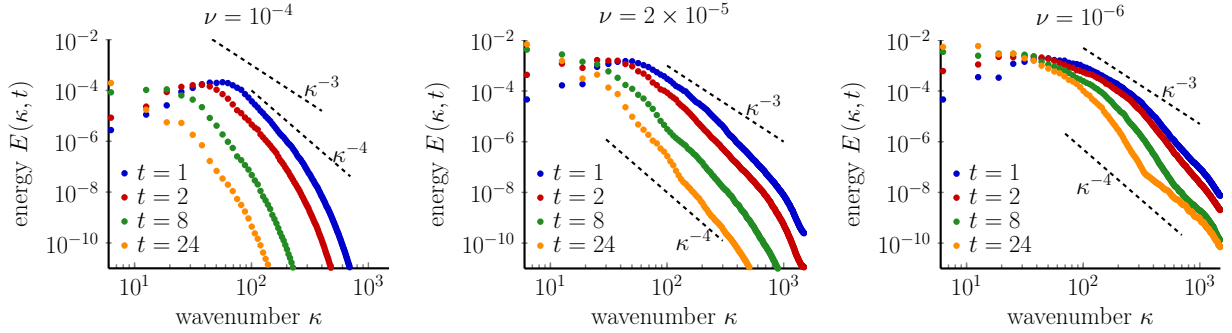


Fig. 8.21: Energy spectra for freely decaying 2D turbulence with $\nu \in \{10^{-4}, 2 \times 10^{-5}, 10^{-6}\}$ (from left to right) at times corresponding to Fig. 8.20. Obtained with div-free $\mathbf{H}(\text{div})$ -HDG method $\mathbf{RT}_{[8]}^{\text{red}}/\mathbf{F}_8/\mathbb{P}_0^{\text{dc}}$ on a 64^2 mesh.

In view of Rem. 2.16, Fig. 8.21 can also be used to draw conclusions concerning the regularity of the particular flows. First, one can observe that for each fixed viscosity, the spectra become steeper as time increases. This means that locally in time, the regularity of the corresponding flows increases, which seems meaningful as the flow obviously becomes less complicated over time. Furthermore, the decay of the spectrum is steeper for larger viscosities; hence, flows at smaller Reynolds numbers are smoother than flows at higher Reynolds numbers. Intuitively, this conclusion makes sense as well.

8.3.2 Analysis of Dissipation Processes

In this section, we want to take up the explanations from Ch. 7 and apply them in the situation of 2D freely decaying homogeneous turbulence, computed with a *hybrid* DG method. The main questions which arise are the following. How much of the total kinetic energy dissipation can be attributed to physical (molecular) dissipation? How large is the contribution from numerical dissipation based on the discretisation of the diffusion and the convection term? How does this distribution evolve over time?

Remembering (7.3), the (negative) total kinetic energy dissipation $-\partial_t \mathcal{K}(\mathbf{u}_h)$ is given by

$$-\frac{d}{dt} \frac{1}{2} \|\mathbf{u}_h\|_{\mathbf{L}^2(\Omega)}^2 = \nu a_h(\mathbf{u}_h, \mathbf{u}_h) + c_h(\mathbf{u}_h; \mathbf{u}_h, \mathbf{u}_h) + j_h(\mathbf{u}_h, \mathbf{u}_h) \quad (-\text{dt_ekin}),$$

where, for our chosen method, $j_h \equiv 0$. Using the decomposition (7.10) with $\boldsymbol{\sigma}_h(\mathbf{u}_h) = \nabla_h \mathbf{u}_h -$

$\mathcal{L}(\llbracket \mathbf{u}_h \rrbracket_\tau)$ (see Rem. 7.4), one can define the different dissipation mechanisms as follows:

$$\begin{aligned} \nu a_h^{\text{phy}}(\mathbf{u}_h, \mathbf{u}_h) &= \nu \|\boldsymbol{\sigma}_h\|_{L^2}^2 && (\text{phy_diss}), \\ \nu a_h^{\text{num}}(\mathbf{u}_h, \mathbf{u}_h) &= \nu a_h(\mathbf{u}_h, \mathbf{u}_h) - \nu a_h^{\text{phy}}(\mathbf{u}_h, \mathbf{u}_h) && (\text{num_diss_visc}), \\ c_h(\mathbf{u}_h; \mathbf{u}_h, \mathbf{u}_h) &= |\mathbf{u}_h|_{\mathbf{u}_h, \text{upw}}^2 && (\text{num_diss_upw}). \end{aligned}$$

In the remainder of this section, we analyse how these four dissipation processes behave over the course of the 2D turbulence simulations for different viscosities $\nu \in \{10^{-4}, 2 \times 10^{-5}, 10^{-6}\}$.

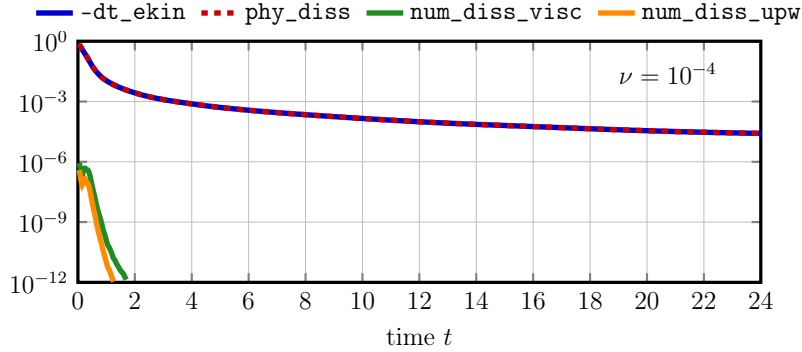


Fig. 8.22: Evolution of dissipations for $\nu = 10^{-4}$ with div-free $\mathbf{RT}_{[8]}^{\text{red}}/\mathbf{F}_8/\mathbb{P}_0^{\text{dc}}$ on a 64^2 mesh.

Beginning with the lowest Reynolds number case, in Fig. 8.22 the respective dissipation quantities are monitored over time for $\nu = 10^{-4}$. One can observe that most of the total dissipation $-\partial_t \mathcal{K}(\mathbf{u}_h)$ originates from physical dissipation $\nu a_h^{\text{phy}}(\mathbf{u}_h, \mathbf{u}_h)$. The numerical contributions are only relevant at the beginning of the simulation ($t < 2$), where the initial 1024 vortices undergo the transition to 2D turbulence. There, the numerical viscous dissipation seems to be slightly larger than the one caused by upwinding. For larger times, numerical dissipation is below 10^{-12} , and thus not plotted anymore.

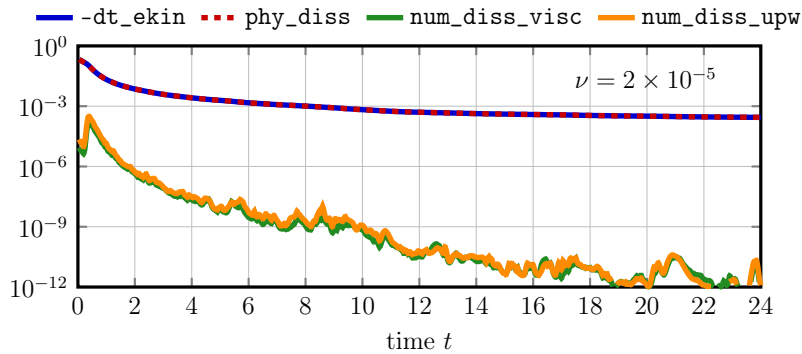


Fig. 8.23: Evolution of dissipations for $\nu = 2 \times 10^{-5}$ with div-free $\mathbf{RT}_{[8]}^{\text{red}}/\mathbf{F}_8/\mathbb{P}_0^{\text{dc}}$ on a 64^2 mesh.

Increasing the Reynolds number, Fig. 8.23 shows the evolution of dissipation quantities for $\nu = 2 \times 10^{-5}$. While the difference between total dissipation and physical dissipation is again not clearly visible, the amount of numerical dissipation is, in general, much larger here. Thus, numerical dissipation

pation indeed plays an increasingly important role in dissipating energy for increasingly less-resolved simulations. Note that viscous numerical dissipation and upwind dissipation contribute basically the same amount of dissipation.

For the highest Reynolds number resulting from $\nu = 10^{-6}$, one can see that the role of numerical dissipation increases considerably, see Fig. 8.24. Over the whole simulation, both viscous numerical dissipation and upwind dissipation can be observed, where the upwind dissipation seems to be more dominant. However, the major part of the dissipation rate can still be attributed to physical/resolved dissipation.

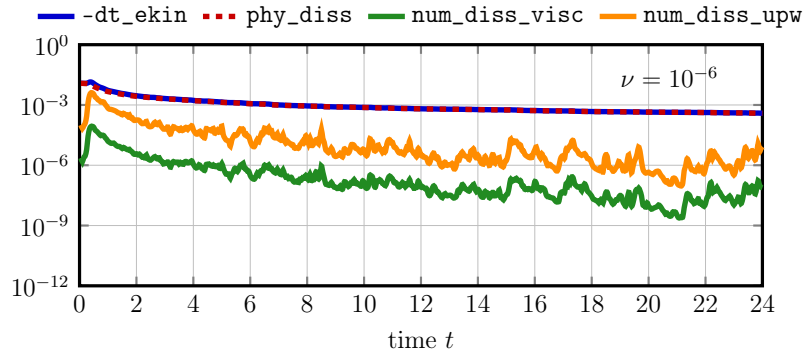


Fig. 8.24: Evolution of dissipations for $\nu = 10^{-6}$ with div-free $\mathbf{RT}_{[8]}^{\text{red}}/\mathbb{F}_8/\mathbb{P}_0^{\text{dc}}$ on a 64^2 mesh.

In retrospect, it becomes apparent that the chosen spatial resolution $k = 8$ on a 64^2 mesh results in a comparably low amount of numerical dissipation for all considered viscosities $\nu \in \{10^{-4}, 2 \times 10^{-5}, 10^{-6}\}$. Hence, this choice seems to lead to a sufficiently fine resolution for capturing the essential physical characteristics of the underlying flow problem.

8.3.3 Long-Time Simulation

Finally, let us consider the long-time behaviour of turbulent freely decaying 2D flows; see also [MS⁺91; Tab02]. A second look at Fig. 8.20 for $\nu = 2 \times 10^{-5}$ at $t = 24$ reveals that there are basically only two counter-rotating vortices left for the moderately small viscosity. Actually, taking into account the self-organisation properties of 2D flows, one would expect that the same holds true also for $\nu = 10^{-6}$. However, in order to observe such a final state with a high Reynolds number, a long-time simulation has to be carried out. Thus, we repeat the above simulation for $\nu = 10^{-6}$, but this time compute ten times longer, up to $T = 240$.

In Fig. 8.25, corresponding snapshots of the vorticity can be seen for $t \in \{30, 40, 60, 100, 160, 240\}$; for $t \leq 24$, the flow of course behaves qualitatively the same as depicted in Fig. 8.20. And indeed, one can observe that more and more merging process reduce the overall number of vortices and for $t \geq 160$, only two counter-rotating vortices are left. The end of the last merging process of the vortices with positive vorticity can actually be seen at $t = 100$. After a final dipole vortex state has formed, the two vortices only travel through the domain with a comparatively small amount of interaction, as can for example be seen at $t = 240$. If the computation were to be carried out for

yet a longer time, the flow would very slowly dissipate to the zero no-flow solution.

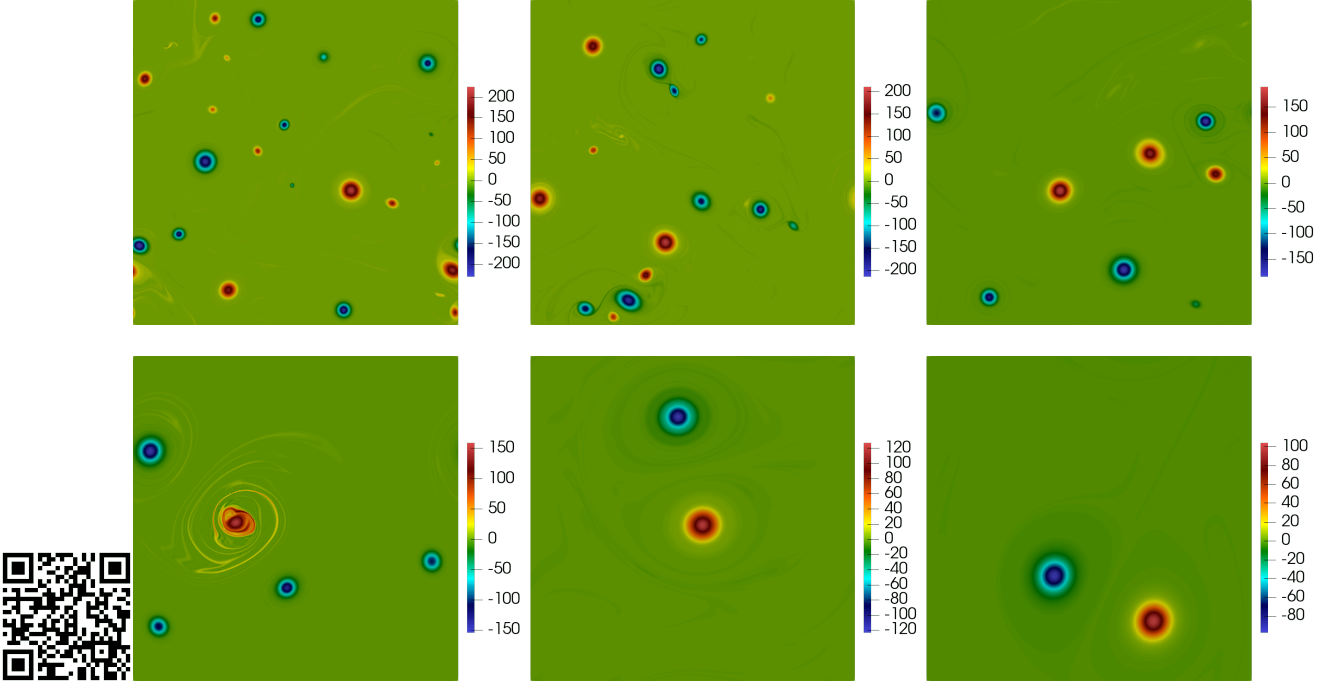


Fig. 8.25: Long-time simulation: vorticity $\nabla_h \times \mathbf{u}_h(t)$ for freely decaying 2D turbulence with $\nu = 10^{-6}$ at $t \in \{30, 40, 60, 100, 160, 240\}$ (from left to right and top to bottom). Obtained with div-free $\mathbf{H}(\text{div})$ -HDG method $\mathbf{RT}_{[8]}^{\text{red}}/\mathbf{F}_8/\mathbb{P}_0^{\text{dc}}$ on a 64^2 mesh. (A video is available at <https://youtu.be/Q1yhhF1hI0I>; note also the QR code.)

Concerning kinetic energy spectra, the distribution of energy in wave-space can be seen in Fig. 8.26 at times corresponding to Fig. 8.25. Overall, and as expected, the amount of energy in fine scales decreases over time, because the number of merging processes decreases as well. However, for example at $t = 100$, the last merging of vortices with positive vorticity results in a visible sudden increase in fine-scale structures.

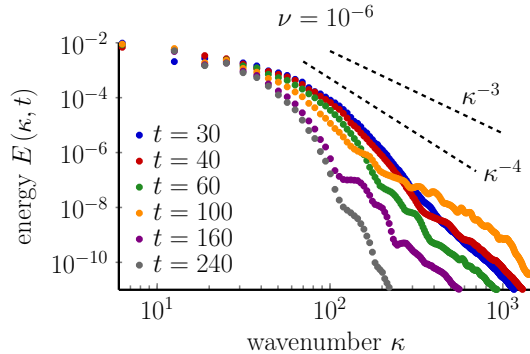


Fig. 8.26: Long-time simulation: energy spectra for freely decaying 2D turbulence with $\nu = 10^{-6}$ at times corresponding to Fig. 8.25. Obtained with div-free $\mathbf{H}(\text{div})$ -HDG method $\mathbf{RT}_{[8]}^{\text{red}}/\mathbf{F}_8/\mathbb{P}_0^{\text{dc}}$ on a 64^2 mesh.

For the sake of completeness, the long-time evolution of kinetic energy, enstrophy and palinstrophy is shown in Fig. 8.27. The palinstrophy is again the most interesting quantity. Every local-in-time outburst of palinstrophy indicates merging processes of the vortices. As we know that at $t = 100$, the last like-signed positive vortices merge, the peaks of palinstrophy for $120 < t < 150$ show the instance in time where the last negative-signed vortices merge. Both kinetic energy and enstrophy are strictly monotonically decreasing at all times.

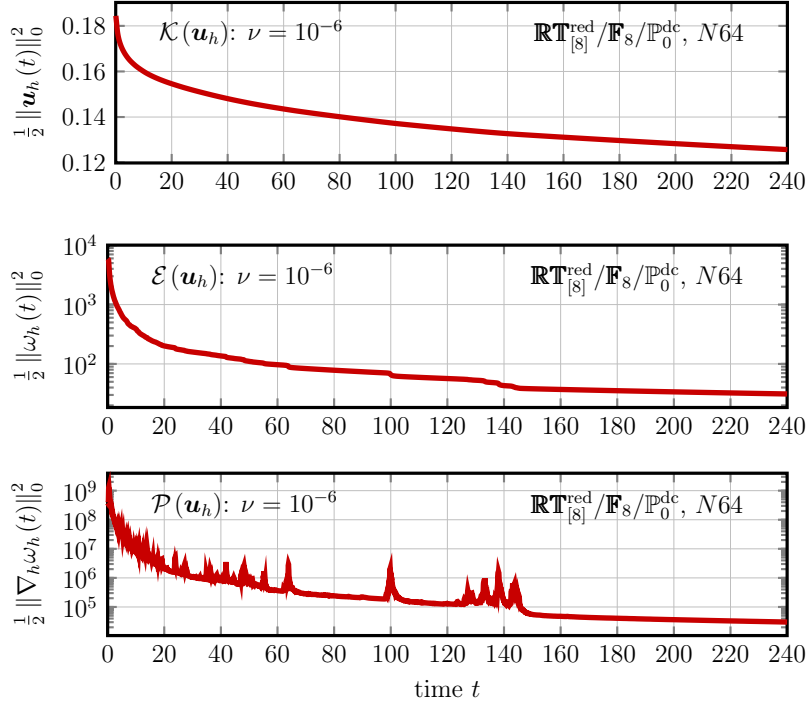


Fig. 8.27: Long-time evolution of kinetic energy (top), enstrophy (middle) and palinstrophy (bottom) for $\nu = 10^{-6}$, computed with the divergence-free $\mathbf{RT}_{[s]}^{\text{red}}/\mathbf{F}_8/\mathbb{P}_0^{\text{dc}}$ $\mathbf{H}(\text{div})$ - \mathbf{H}^1 -lifting-HDG method on a 64^2 mesh.

Lastly, let us also consider the distribution of numerical and physical dissipation processes in Fig. 8.28. For $t > 160$, the dipole solution can obviously be resolved comparably well as there is only a small (decreasing in time) amount of numerical dissipation present. However, one can again see very clearly that whenever merging processes occur, for example at $t = 100$, numerical dissipation also spontaneously increases. This is a response of the numerical method to an increasing amount of not necessarily resolved small-scale features which are present in the flow.

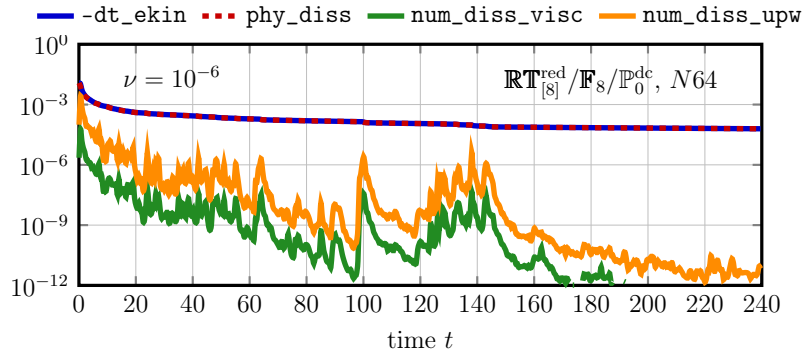


Fig. 8.28: Long-time evolution of physical and numerical dissipation(s) for $\nu = 10^{-6}$ with divergence-free $\mathbb{RT}_{[s]}^{\text{red}}/\mathbb{F}_8/\mathbb{P}_0^{\text{dc}}$ $\mathbf{H}(\text{div})\text{-}\mathbf{H}^1$ -lifting-HDG method on a 64^2 mesh.

3D High-Order CFD Applications

Structure of this chapter: This chapter considers the application of high-order divergence-free $\mathbf{H}(\text{div})$ -FEM to the simulation of 3D incompressible CFD problems in the context of implicit large eddy simulation (ILES). The two limit cases of the Taylor–Green vortex (freely decaying homogeneous turbulence) and the turbulent channel flow (wall-bounded attached turbulence) are examined. For the former problem, also results for the limit case as $\text{Re} \rightarrow \infty$ are presented and the latter is computed for varying friction Reynolds numbers Re_τ . Both examples are equipped with investigations aimed at emphasising the importance of the concept of generalised Beltrami flows for such considerably more complicated flows involving turbulence.

9.1	Homogeneous Isotropic Turbulence: Taylor–Green Vortex	115
9.1.1	TGV Flow Topology and Characteristics for $\text{Re} = 1600$	116
9.1.2	Some Aspects of Implicit Large Eddy Simulation	119
9.1.3	Towards the Inviscid Euler Limit Case as $\text{Re} \rightarrow \infty$	123
9.1.4	Helmholtz Decomposition of Convection Forces	128
9.2	Turbulent Channel Flow	129
9.2.1	Simulations for $\text{Re}_\tau = 180$	132
9.2.2	Simulations for $\text{Re}_\tau = 395$	135
9.2.3	Simulations for $\text{Re}_\tau = 950$	138
9.2.4	Simulations for $\text{Re}_\tau = 2000$	139

9.1 Homogeneous Isotropic Turbulence: Taylor–Green Vortex

In the box $\Omega = (0, 2\pi)^3$, equipped with periodic boundary conditions on all faces, consider the case $\mathbf{f} \equiv \mathbf{0}$ and the space-periodic initial condition [Bra91; TG37]

$$\mathbf{u}_0(\mathbf{x}) = \begin{pmatrix} \cos(x_1) \sin(x_2) \sin(x_3) \\ -\sin(x_1) \cos(x_2) \sin(x_3) \\ 0 \end{pmatrix}. \tag{9.1}$$

This initial condition is imposed, and the evolving flow is monitored over time. The resulting Taylor–Green vortex (TGV) problem describes the transition of large-scale to small-scale features [Kol41a; Kol41b], and the associated (viscous) decay which is characteristic for freely decaying homogeneous isotropic turbulence. It is possibly the easiest flow system for which one can observe the key physical mechanisms inherent to turbulence: transition, vortex roll-up, 3D vortex stretching and interaction, and finally, in the viscous case, molecular energy dissipation. Therefore, it is very frequently investigated in the CFD literature (both compressible and incompressible), mostly in the context of explicit and implicit large eddy simulation (LES) [Ber05; CH⁺13; DeB13; DF⁺07;

EC⁺18; FLD09; FWK18b; GB12; HSF18; PMB18; RKR17; SD⁺15; vOY⁺17; vRL⁺11; YBC16].

9.1.1 TGV Flow Topology and Characteristics for $\text{Re} = 1600$

In this subsection, results are presented only for the upwind-stabilised SIP $\mathbf{RT}_{[k]}^{\text{red}}/\mathbf{F}_k/\mathbb{P}_0^{\text{dc}}$ $\mathbf{H}(\text{div})$ -HDG method with penalty parameter $\lambda = 6(k+1)^2$ (see (3.36) for the Stokes part) on structured cube meshes with N elements in each space direction. The time-stepping is performed up to $T = 20$ using a constant time step $\Delta t = 0.01$ with the second-order Runge–Kutta variant ARS(2,2,2) of the implicit-explicit (IMEX) method introduced in [ARS97]. Again, the Stokes subproblem is treated implicitly and convection is treated explicitly. Our results are compared to the reference DNS data provided by [FWK18a] ($k = 7$, $N = 128$).

At first, we want to consider the evolution of kinetic energy $\mathcal{K}(\mathbf{u}_h)$ and (negative) total kinetic energy dissipation rate $-\partial_t \mathcal{K}(\mathbf{u}_h)$ under h -refinement. In Fig. 9.1 both quantities are displayed for $k = 8$ on a sequence of meshes with $N \in \{4, 8, 16\}$, which correspond to strongly under-resolved, moderately resolved and essentially resolved simulations³⁶. While on the coarse mesh, the results obviously differ from the reference DNS results, they are basically identical on the finest mesh. Note the peak in energy dissipation at around $t \approx 9$. Moreover, it is comparably easy to obtain a good approximation for the kinetic energy, even in a strongly under-resolved situation, but in order to capture the total dissipation rate accurately, significantly more resolution is necessary.

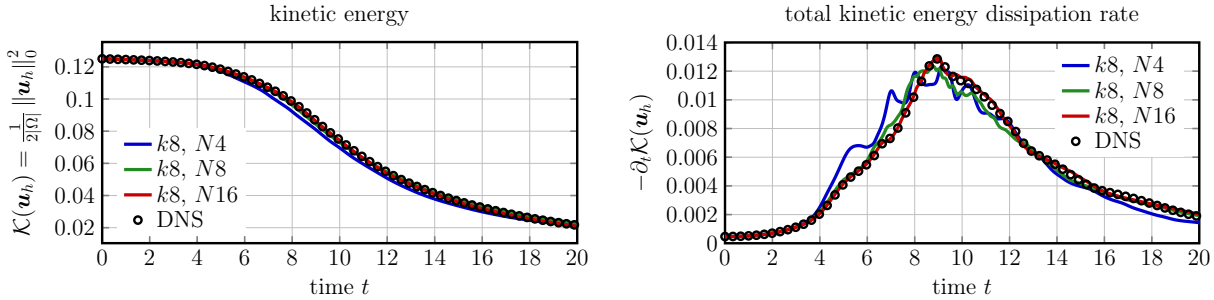


Fig. 9.1: Upwind-stabilised high-order SIP $\mathbf{RT}_{[8]}^{\text{red}}/\mathbf{F}_8/\mathbb{P}_0^{\text{dc}}$ $\mathbf{H}(\text{div})$ -HDG results for the simulation of the $\text{Re} = 1600$ TGV under h -refinement. Evolution of kinetic energy (left) and total kinetic energy dissipation rate (right) on different meshes with $N \in \{4, 8, 16\}$.

For the purpose of identifying vortical structures, we make use of the popular (discrete) Q -criterion [Hal05; HWM88; JH95] ($\nabla \mathbf{u} = \mathbb{D}(\mathbf{u}) + \mathbb{S}(\mathbf{u}) = \frac{1}{2} [\nabla \mathbf{u} + (\nabla \mathbf{u})^\dagger] + \frac{1}{2} [\nabla \mathbf{u} - (\nabla \mathbf{u})^\dagger]$)

$$Q(\mathbf{u}_h) = \left\{ \mathbf{x} \in \Omega : \frac{1}{2} \left[|\mathbb{S}(\mathbf{u}_h)|^2 - |\mathbb{D}(\mathbf{u}_h)|^2 \right] > 0 \right\}; \quad (9.2)$$

that is, we define the neighbourhood of a vortex as the set of points in a flow for which the Euclidean norm of the spin tensor (local rigid body rotation) dominates the deformation tensor (shearing).

³⁶For $\mathbf{RT}_{[k]}$, the corresponding number of velocity DOFs amounts to $N^d d(k+1)^d$.

Based on the SIP- $\mathbf{RT}_{[8]}^{\text{red}}/\mathbf{F}_8/\mathbb{P}_0^{\text{dc}}$ simulation with $N = 16$ and using the Q -criterion, Fig. 9.2 shows how the TGV flow behaves over time; see also [BM+83] for a more detailed description. The first row show the early-time behaviour, which is basically dominated by inviscid motion for $t < 4$. Between $t = 4$ and $t = 9$, a vortex roll-up can be observed, the structures undergo transition and are elongated due to vortex stretching. At approximately $t \approx 9$, corresponding to the dissipation peak, the coherent structures break down and for $t \geq 10$, fully turbulent structures characterise the freely decaying flow. Note the diametrically opposed behaviour compared to the 2D case in Ch. 8; see also Sec. 2.4.

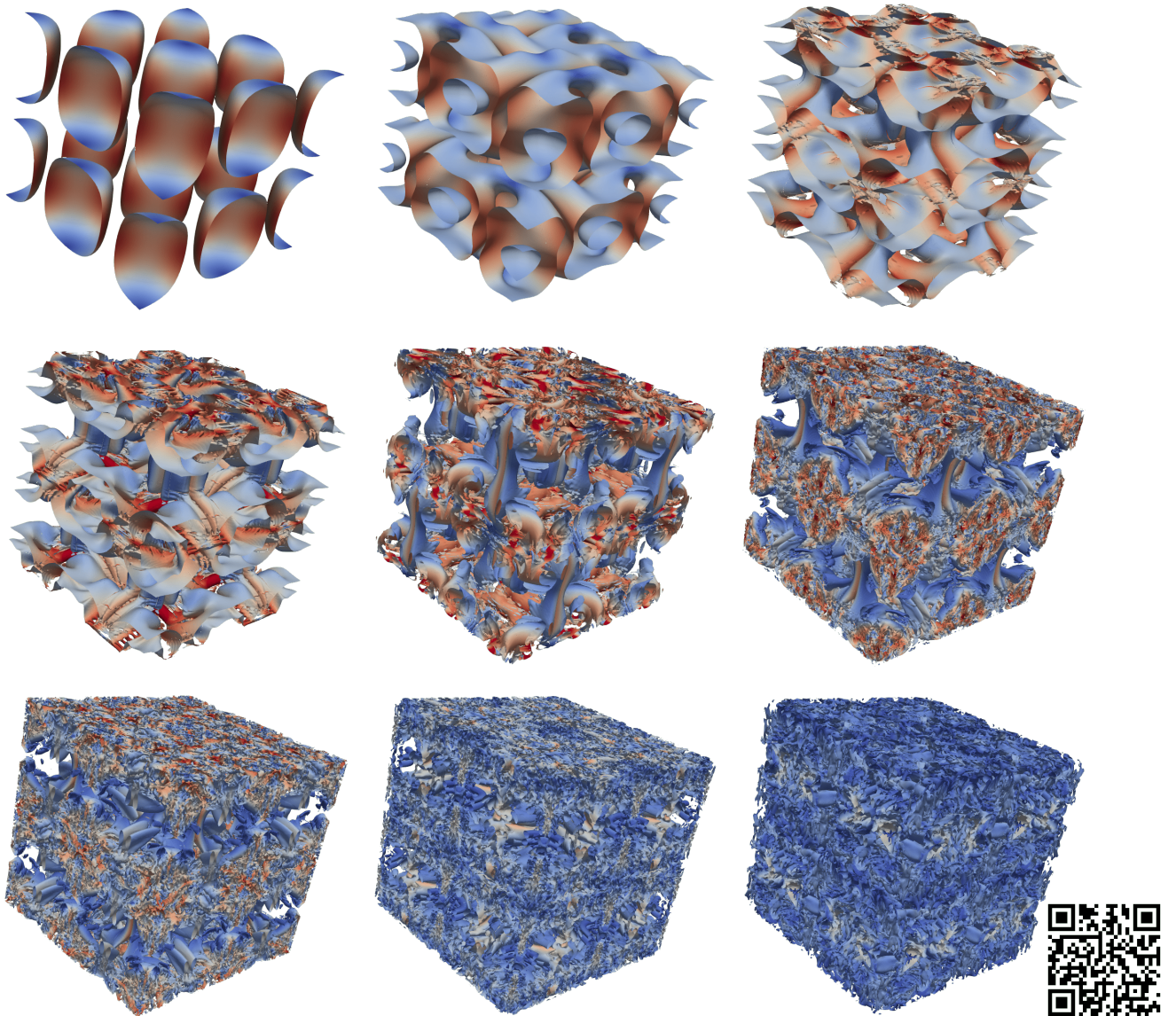


Fig. 9.2: $\text{Re} = 1600$ TGV: Evolution of 0.1-isosurface of $Q(\mathbf{u}_h)$ -criterion coloured with velocity magnitude $|\mathbf{u}_h|$, where blue corresponds to zero and red to everything above unity. Obtained with the SIP $\mathbf{RT}_{[8]}^{\text{red}}/\mathbf{F}_8/\mathbb{P}_0^{\text{dc}}$ method on a mesh with $N = 16$ cubical elements in each direction. Time instances from left to right and top to bottom: $t = 0, 2, 4, 5, 7, 9, 10, 14, 20$. (A video of this simulation is available at <https://youtu.be/ENjjDUrrhwE>; note also the QR code.)

Concerning the distribution of energy $E(\kappa)$ over different wavenumbers κ , Fig. 9.3 shows the kinetic energy spectrum at $t = 10$ (shortly after the dissipation peak) on the different meshes. Referring to Sec. 2.4, one can see that for this Reynolds number, the flow exhibits only a comparably small inertial range where the Kolmogorov $-5/3$ rule can be observed (but it grows for larger N). However, one can also deduce that for an increasing resolution, more energy in the fine scales gets dissipated as a consequence of better resolved viscous effects. On the coarse mesh, the resolution is not sufficient to accurately dissipate the fine-scale features on the molecular level. Note that the resolution threshold wavenumber $N(k+1)$, under which the flow is frequently considered resolved, is also indicated for the different meshes. Above this threshold the flow is not resolved, which makes it difficult to expect an highly accurate behaviour.

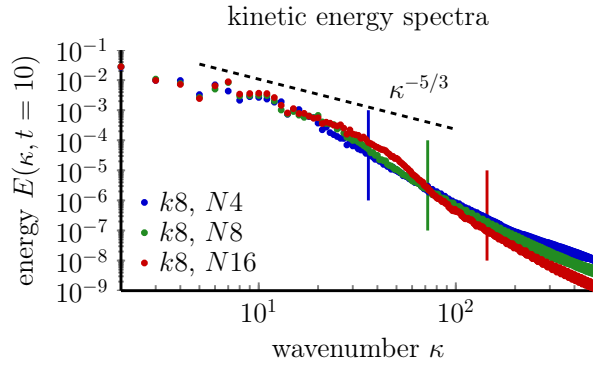


Fig. 9.3: $\text{Re} = 1600$ TGV: kinetic energy spectra at $t = 10$ for $\mathbb{RT}_{[8]}^{\text{red}}/\mathbb{F}_8/\mathbb{P}_0^{\text{dc}}$ on different meshes with $N \in \{4, 8, 16\}$. Vertical lines correspond to $N(k+1)$, respectively.

Furthermore, let us regard the 1-isosurface of the $Q(\mathbf{u}_h)$ -criterion at $t = 20$ under h -refinement in Fig. 9.4. While only few vortical structures are visible for the most under-resolved simulation with $N = 4$, increasing the resolution leads to the appearance and visibility of more and more vortical structures. In contrast to Fig. 9.2, this is a different isosurface of the Q -criterion and accordingly, the structures also look differently. Note that the colour code is chosen differently for each plot.

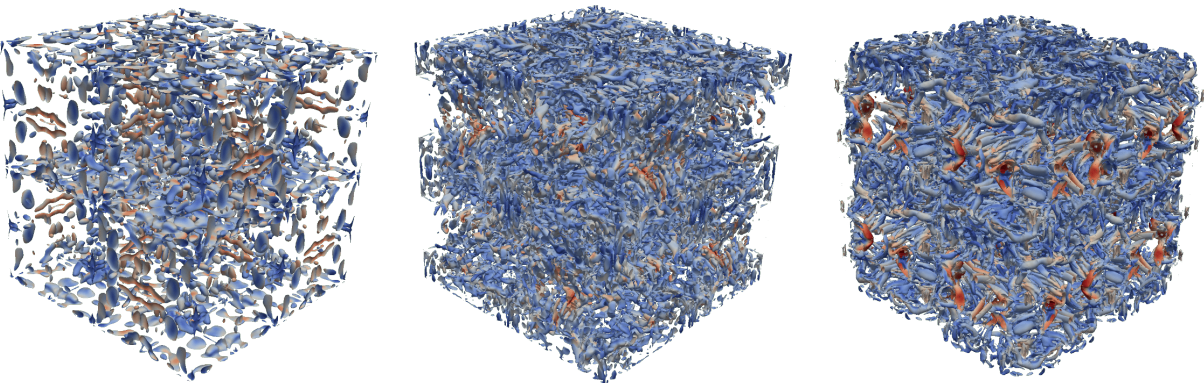


Fig. 9.4: Upwind-stabilised high-order SIP $\mathbb{RT}_{[8]}^{\text{red}}/\mathbb{F}_8/\mathbb{P}_0^{\text{dc}}$ $\mathbf{H}(\text{div})$ -HDG results for the simulation of the $\text{Re} = 1600$ TGV under h -refinement. 1-isosurface of the $Q(\mathbf{u}_h)$ -criterion coloured with velocity magnitude $|\mathbf{u}_h|$ at $t = 20$ on different meshes with $N \in \{4, 8, 16\}$.

Finally, let us also consider the under-resolved setting by fixing the order/mesh combinations $(k, N) = (8, 4), (4, 8), (2, 16)$. This choice leads to roughly comparable approximation properties, while of course, not to the same amount of computational effort. Then, Fig. 9.5 (left) shows that even such under-resolved lower-order $\mathbf{H}(\text{div})$ -based simulations can reflect a satisfying behaviour of the kinetic energy. Therefore, in the following, we will not discuss the evolution of kinetic energy anymore, but instead focus on the more demanding energy dissipation rate. However, Fig. 9.5 (right) reveals that even in the under-resolved setting, regarding only the total dissipation rate $\partial_t \mathcal{K}(\mathbf{u}_h)$ does not allow to obtain more insight into the question where low- and high-order results differ. The next section will address this question more systematically.

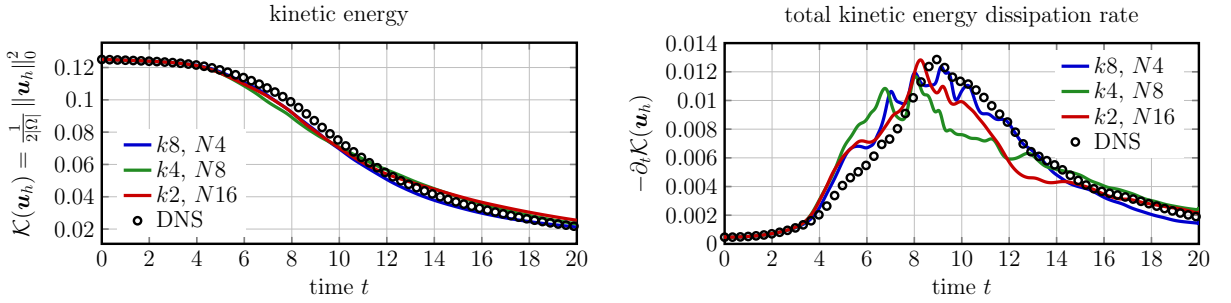


Fig. 9.5: Upwind-stabilised SIP $\mathbb{RT}_{[k]}^{\text{red}}/\mathbb{F}_k/\mathbb{P}_0^{\text{dc}}$ $\mathbf{H}(\text{div})$ -HDG results for the simulation of the $\text{Re} = 1600$ TGV with a fixed, strong under-resolution. Evolution of kinetic energy (left) and total kinetic energy dissipation rate (right).

9.1.2 Some Aspects of Implicit Large Eddy Simulation

Recalling our explanations in Ch. 7 and Sec. 8.3.2, using the decomposition (7.10) with $\sigma_h(\mathbf{u}_h) = \nabla_h \mathbf{u}_h - \mathcal{L}(\llbracket \mathbf{u}_h \rrbracket_\tau)$ (see Rem. 7.4), the total numerical dissipation can be decomposed as

$$\underbrace{\varepsilon_h^{\text{tot}}(\mathbf{u}_h)}_{\text{num_diss_tot}} = \underbrace{-\partial_t \mathcal{K}(\mathbf{u}_h)}_{-\text{dt_ekin}} - \underbrace{\nu \|\sigma_h\|_{L^2}^2}_{\text{phy_diss}} = \underbrace{\nu a_h^{\text{num}}(\mathbf{u}_h, \mathbf{u}_h)}_{\text{num_diss_visc}} + \underbrace{\theta |\mathbf{u}_h|_{\mathbf{u}_h, \text{upw}}^2}_{\text{num_diss_upw}}, \quad (9.3)$$

where $\theta = 1$ if upwinding is used, and $\theta = 0$ if no convection stabilisation is applied. In this situation, our understanding of implicit LES is the following: $\varepsilon_h^{\text{tot}}(\mathbf{u}_h)$ can indeed be large in the under-resolved situation, but one has to ‘hope’ that the (implicitly) introduced numerical dissipations $\nu a_h^{\text{num}}(\mathbf{u}_h, \mathbf{u}_h)$ and $\theta |\mathbf{u}_h|_{\mathbf{u}_h, \text{upw}}^2$, and the physically resolved dissipation $\nu \|\sigma_h\|_{L^2}^2$ complement each other well such that the (negative) total dissipation of kinetic energy $-\partial_t \mathcal{K}(\mathbf{u}_h)$ overall shows a reasonable behaviour.

The evolution of $-\partial_t \mathcal{K}(\mathbf{u}_h)$ (`-dt_ekin`) has already been shown to be reasonable by means of Fig. 9.1. Thus, we will now inspect the remaining terms in (9.3) more systematically. In the under-resolved setting, the left-hand side of Fig. 9.6 shows that the amount of total numerical dissipation $\varepsilon_h^{\text{tot}}(\mathbf{u}_h)$ (`num_diss_visc` + `num_diss_upw`) is in fact not small compared to the physically resolved dissipation $\nu \|\sigma_h\|_{L^2}^2$ (`phy_diss`). However, because the total dissipation rate $-\partial_t \mathcal{K}(\mathbf{u}_h)$ is qualitatively meaningful, and $\varepsilon_h^{\text{tot}}(\mathbf{u}_h) \rightarrow 0$ as $h \rightarrow 0$ (see the middle and right-hand side plots), one can

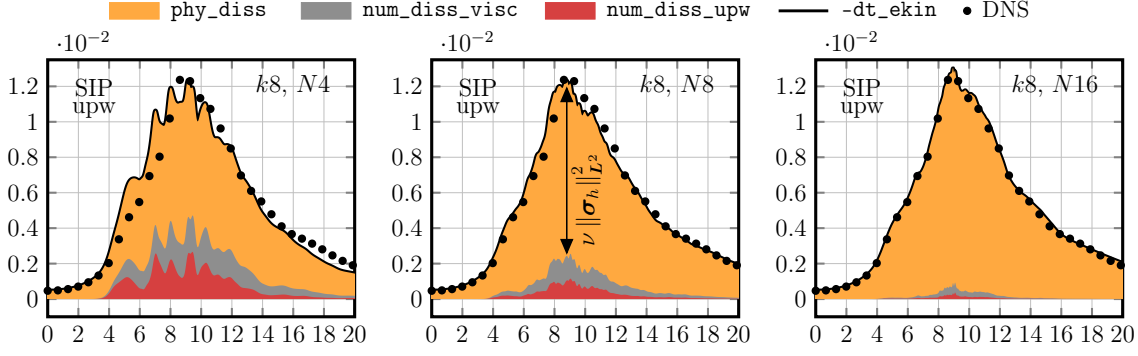


Fig. 9.6: High-order upwind-stabilised SIP $\mathbf{RT}_{[8]}^{\text{red}}/\mathbf{F}_8/\mathbb{P}_0^{\text{dc}}$ $\mathbf{H}(\text{div})$ -HDG implicit LES mechanisms for the simulation of the $\text{Re} = 1600$ TGV under h -refinement.

deduce that the implicit LES strategy is indeed successful here. We remark that both the viscous numerical dissipation and the numerical dissipation due to upwinding seem to be approximately balanced in the sense that they contribute equally to the total dissipation rate.

Associated to the previous investigation of lower-order methods in the under-resolved setting, see Fig. 9.5, the preceding decomposition of the total energy dissipation rate should of course also be done. Correspondingly, Fig. 9.7 shows the decomposition of total energy dissipation into its physical and numerical components for a fixed level of under-resolution. The most important observation is that the dissipation of lower-order methods relies significantly more on numerical dissipation than high-order methods'. This is the reason why we believe that higher-order methods are superior for this test scenario. Therefore, in the remainder of this section, results are presented only for the high-order case $k = 8$, but we expect that no general differences would appear for lower-order choices. For lower-order methods, numerical dissipation is only more pronounced, which is a well-known fact in the CFD community.

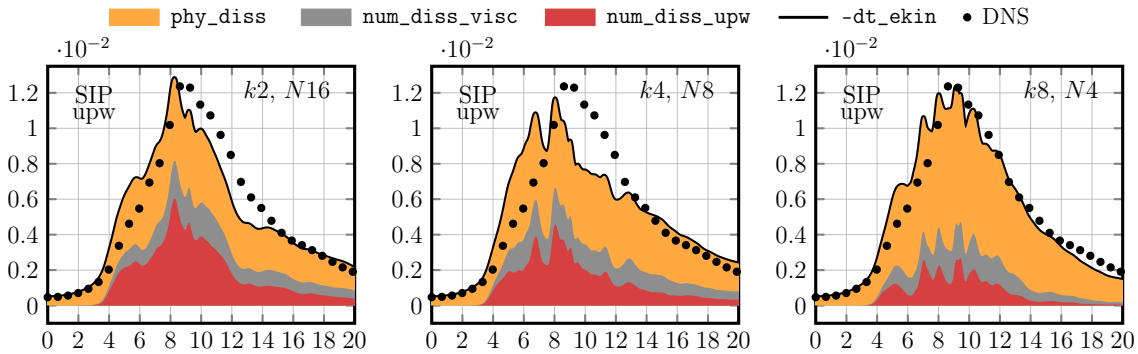


Fig. 9.7: High-order upwind-stabilised SIP $\mathbf{RT}_{[k]}^{\text{red}}/\mathbf{F}_k/\mathbb{P}_0^{\text{dc}}$ $\mathbf{H}(\text{div})$ -HDG implicit LES mechanisms for the simulation of the $\text{Re} = 1600$ TGV with a fixed level of under-resolution.

Our next step is to investigate the impact of upwinding on the dissipation behaviour of the simulations with the high-order SIP- $\mathbf{RT}_{[8]}^{\text{red}}/\mathbf{F}_8/\mathbb{P}_0^{\text{dc}}$ method. Fig. 9.8 shows the results of the computations without any kind of convection stabilisation ($\theta = 0$), where one has to notice that $\varepsilon_h^{\text{tot}}(\mathbf{u}_h) = \nu a_h^{\text{num}}(\mathbf{u}_h, \mathbf{u}_h)$ (num_diss_visc). First of all, for the better resolved cases $N = 8$ and

$N = 16$, basically no difference can be observed compared to the simulations with upwinding above. Only in the strongly under-resolved situation with $N = 4$, the total dissipation rate is slightly different in the vicinity of the dissipation peak ($t \approx 8 - 9$) compared to the results with upwinding in Fig. 9.6. Therefore, we infer that in the present setting with SIP, the influence of convection stabilisation plays only a subordinate role.

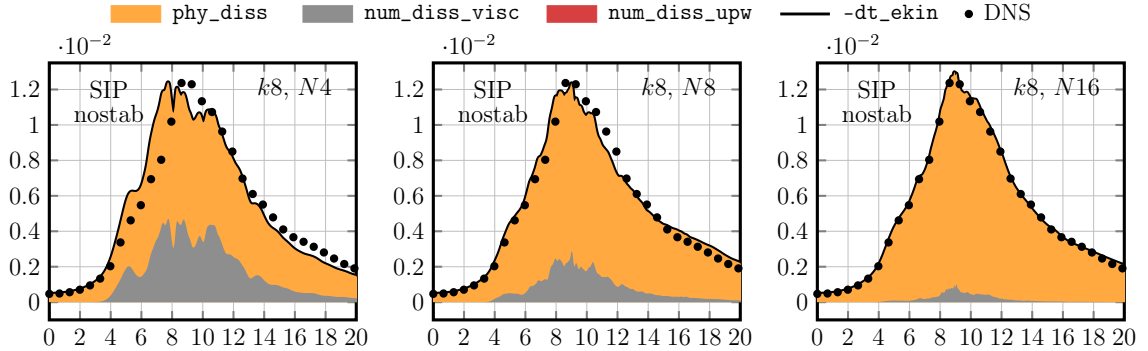


Fig. 9.8: No upwinding: High-order SIP $\mathbb{RT}_{[8]}^{\text{red}}/\mathbb{F}_8/\mathbb{P}_0^{\text{dc}}$ $\mathbf{H}^1(\text{div})$ -HDG implicit LES mechanisms for the simulation of the $\text{Re} = 1600$ TGV under h -refinement.

After having considered the impact of convection stabilisation on the dissipation behaviour for the SIP method, we now also compare different treatments of the viscosity term. In this context, Fig. 9.9 shows the various dissipation rates under h -refinement when the \mathbf{H}^1 -lifting mechanism with $\lambda = k$ and $\lambda_\ell = 2$ (see (3.38) for the Stokes part) is used instead of the SIP method. More or less by construction, the \mathbf{H}^1 -lifting variant introduces less numerical viscous dissipation (`num_diss_visc`) than SIP, because the corresponding penalty parameter(s) can be chosen comparably smaller. Surprisingly, the corresponding total energy dissipation rates (`-dt_ekin`) do not show significant differences. The particular contributions from the numerical dissipation, on the other hand, reveal that first, the treatment of the viscosity in the \mathbf{H}^1 -lifting method certainly is less dissipative but second, the upwinding dissipation (`num_diss_upw`) is considerably larger. Phrased differently, when the viscosity discretisation is carried out with a small amount of numerical dissipation, the convection stabilisation seems to take over a dominating role within this particular implicit LES approach. Consequently, based on the TGV problem, whether the SIP or the \mathbf{H}^1 -lifting technique is superior cannot be determined in general.

This conclusion immediately leads to the last experiment. How important is upwinding for this freely decaying turbulence simulation when the less dissipative \mathbf{H}^1 -lifting is used for the viscosity treatment? A corresponding comparison for the most under-resolved situation with $N = 4$ can be found in Fig. 9.10, where results for all the above considered methods are shown. Note that only the lower right plot is new; the others are plotted additionally in order to provide a better and more compact presentation.

One can observe that, similar to the SIP method without upwinding, the \mathbf{H}^1 -lifting method without any convection stabilisation behaves basically the same with respect to the total dissipation

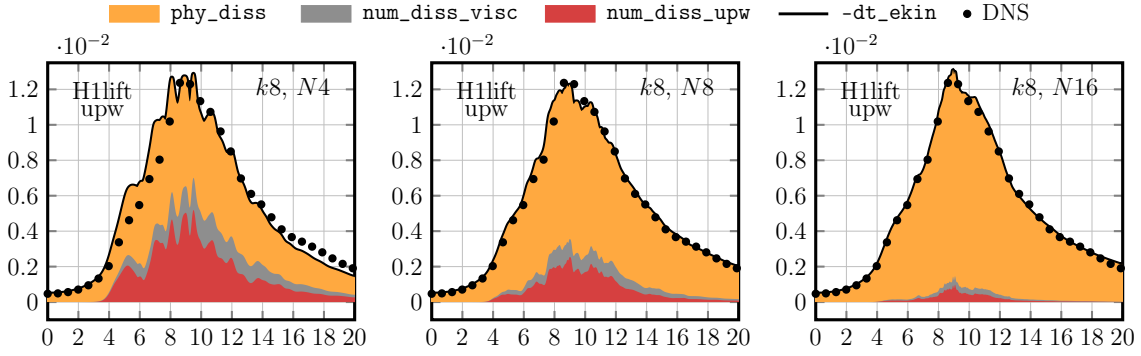


Fig. 9.9: High-order upwind-stabilised H^1 -lifting $\mathbb{RT}_{[8]}^{\text{red}}/\mathbb{F}_8/\mathbb{P}_0^{\text{dc}}$ $H(\text{div})$ -HDG implicit LES mechanisms for the simulation of the $\text{Re} = 1600$ TGV under h -refinement.

rate. In fact, none of the considered methods can be singled out as superior. This actually goes so far that upwinding does not play an important role, even when the viscous term is treated with the less dissipative H^1 -lifting technique.

In other words, based on a simulation without convection stabilisation, adding upwinding does not result in a simple superposition of numerical dissipation. Instead, both the stabilisation provided by the treatment of the viscous term and upwinding obviously interact with each other. Such a discovery might be unexpected intuitively, not least because while the viscous stabilisation inherent in the SIP or H^1 -lifting method acts isotropically in each direction, the upwind mechanism only penalises (tangential) jumps when the normal velocity on facets is large; see Ch. 3.

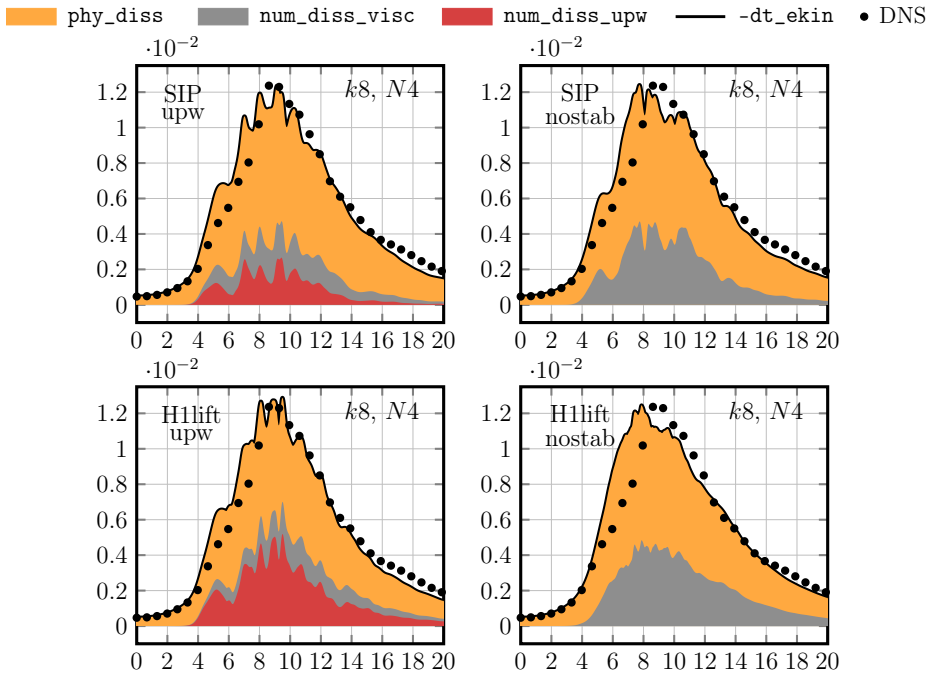


Fig. 9.10: High-order $\mathbb{RT}_{[8]}^{\text{red}}/\mathbb{F}_8/\mathbb{P}_0^{\text{dc}}$ $H(\text{div})$ -HDG implicit LES mechanisms for the under-resolved simulation of the $\text{Re} = 1600$ TGV with $N = 4$. Comparison of SIP and H^1 -lifting results, with and without upwinding, respectively.

9.1.3 Towards the Inviscid Euler Limit Case as $\text{Re} \rightarrow \infty$

In this section, we want to increase the Reynolds number from $\text{Re} = 1600$ to $\text{Re} = 3000$, $\text{Re} = 5000$, $\text{Re} = 10\,000$, $\text{Re} = 100\,000$ and finally to $\text{Re} = \infty$ (incompressible Euler). Especially the inviscid limit is numerically interesting, since the lack of viscous dissipation leads to small scales in the flow which become arbitrarily small over time. The inviscid TGV is also frequently considered in the literature [Ber05; BM⁺83; FMB03; Ker93; SD⁺05; WM⁺18], mostly in order to test the dissipation properties of the underlying convection stabilisation and/or turbulence model. For the investigations in this subsection, we restrict ourselves to using the moderate order $k = 4$.

Whenever $\text{Re} < \infty$, the same upwind-stabilised SIP $\mathbb{RT}_{[k]}^{\text{red}}/\mathbb{F}_k/\mathbb{P}_0^{\text{dc}}$ $\mathbf{H}(\text{div})$ -HDG method with the same IMEX time-stepping as in Sec. 9.1.1 is used. For the inviscid Euler case ($\text{Re} = \infty$), on the other hand, no viscosity is present and it is reasonable to use an explicit method in which no hybrid facet variable for the velocity is needed anymore; cf., for example, [Leh10, Rem. 3.2.1] or [Fu19]. Here, we decide on employing the third-order total variation diminishing Runge–Kutta method (TVD-RK3) from [GS98; SO88] with a constant time step $\Delta t = 0.001$ (this time step is ten times smaller than the one used for $\text{Re} < \infty$), and the abbreviation for the method is simply $\mathbb{RT}_{[k]}^{\text{red}}/\mathbb{P}_0^{\text{dc}}$. In the following, the explicit method will be used with and without upwinding.

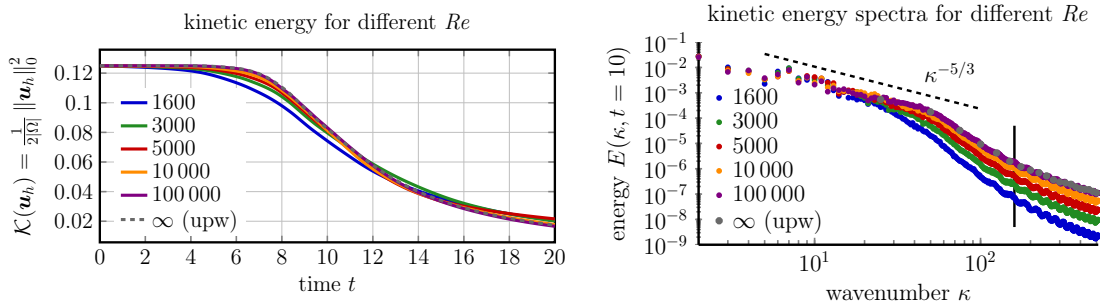


Fig. 9.11: Upwind-stabilised SIP $\mathbb{RT}_{[4]}^{\text{red}}/\mathbb{F}_4/\mathbb{P}_0^{\text{dc}}$ $\mathbf{H}(\text{div})$ -HDG ($\text{Re} < \infty$) and upwind-stabilised $\mathbb{RT}_{[4]}^{\text{red}}/\mathbb{P}_0^{\text{dc}}$ $\mathbf{H}(\text{div})$ -DG ($\text{Re} = \infty$) results for the simulation of the TGV with $N = 32$. Evolution of kinetic energy (left) and kinetic energy spectra at $t = 10$ (right). The vertical line corresponds to $N(k + 1)$ and, for better clarity, for $\text{Re} = \infty$ only some spectrum values with upwinding are displayed.

Let us begin with considering the kinetic energy quantities in Fig. 9.11. On the left-hand side, the evolution of $\mathcal{K}(\mathbf{u}_h)$ is shown for an ascending sequence of Reynolds numbers, where $\text{Re} = \infty$ has been computed with upwinding. One can observe that as $\text{Re} \rightarrow \infty$, the first phase of the TGV, which is dominated by inviscid motion, extends in time since the kinetic energy starts to decrease later. Furthermore, no clear difference between $\text{Re} = 100\,000$ and $\text{Re} = \infty$ (with upwinding) can be discerned. From the right-hand side of Fig. 9.11 ($t = 10$ fixed), it becomes clear that as $\text{Re} \rightarrow \infty$, the inertial range where the Kolmogorov $-5/3$ spectrum can be observed is growing. Again, basically no difference between $\text{Re} = 100\,000$ and $\text{Re} = \infty$ (with upwinding) can be observed. The vertical line indicates the threshold wavenumber $N(k + 1)$.

We have seen that due to a decreasing role of viscosity, the fine scales are dissipated less and less as $Re \rightarrow \infty$ in the TGV problem. In the style of Sec. 9.1.2, Fig. 9.12 confirms this statement by investigating the energy dissipation balance (9.3). For lower Reynolds numbers, we can conclude that the physical viscous dissipation plays the dominant role. As Re increases, however, the dissipative character of the upwind stabilisation is clearly noticeable. In this portrayal, one can observe that, as opposed to $Re = \infty$ (with upwinding), for $Re = 100\,000$ still a small amount of viscous dissipation is responsible for energy dissipation. Note that as the Reynolds number increases, the simulations become more and more under-resolved.

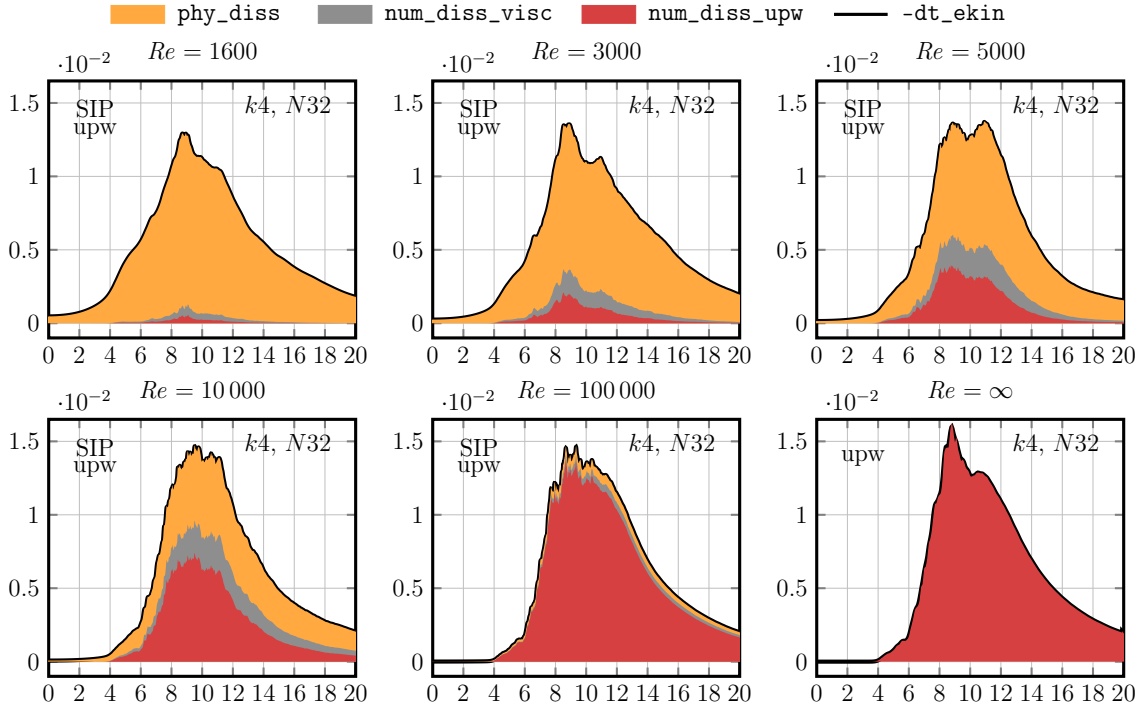


Fig. 9.12: Implicit LES mechanisms for upwind-stabilised SIP $\mathbb{RT}_{[4]}^{\text{red}}/\mathbb{F}_4/\mathbb{P}_0^{\text{dc}}$ $\mathbf{H}(\text{div})$ -HDG ($Re < \infty$) and upwind-stabilised $\mathbb{RT}_{[4]}^{\text{red}}/\mathbb{P}_0^{\text{dc}}$ $\mathbf{H}(\text{div})$ -DG ($Re = \infty$) for the simulation of the TGV at different Reynolds numbers with a fixed $N = 32$ mesh.

Complementing the presentation of results for the increasing sequence of Reynolds numbers, Fig. 9.13 shows the 1-isosurface of the Q -criterion at $t = 20$ for the different simulations corresponding to Fig. 9.12. One can observe that while for the lowest Reynolds number $Re = 1600$, the flow shows relatively large vortical structures, increasing the Reynolds number leads to increasingly more small-scale structures. This observation is completely consistent with the expectation; see again the energy spectra in Fig. 9.11. Note that the colour code for $|\mathbf{u}_h|$ is chosen differently for each plot.

Another important observation concerns the fact that the TGV problem originally is intended to result in freely decaying *homogeneous isotropic* turbulence. However, from Fig. 9.13 one can get the impression that this assumption might be problematic, at least for smaller Reynolds numbers. Indeed, even at $t = 20$, the flow is certainly not invariant against translation and/or rotation of the coordinate system for $Re \leq 10\,000$. This problem could be solved, for example, by simulating

the flow for an even longer time. We conjecture that the structure preserving properties of our divergence-free $\mathbf{H}(\text{div})$ method are responsible for preserving the symmetric structure of the initial condition even for such long times.

At this point, let us also mention that by choosing different isosurfaces of the Q -criterion, the perception of the vortical motion for the TGV can change dramatically. In this sense, plots of the Q -criterion have to be considered with a grain of salt. They always provide a biased point of view.

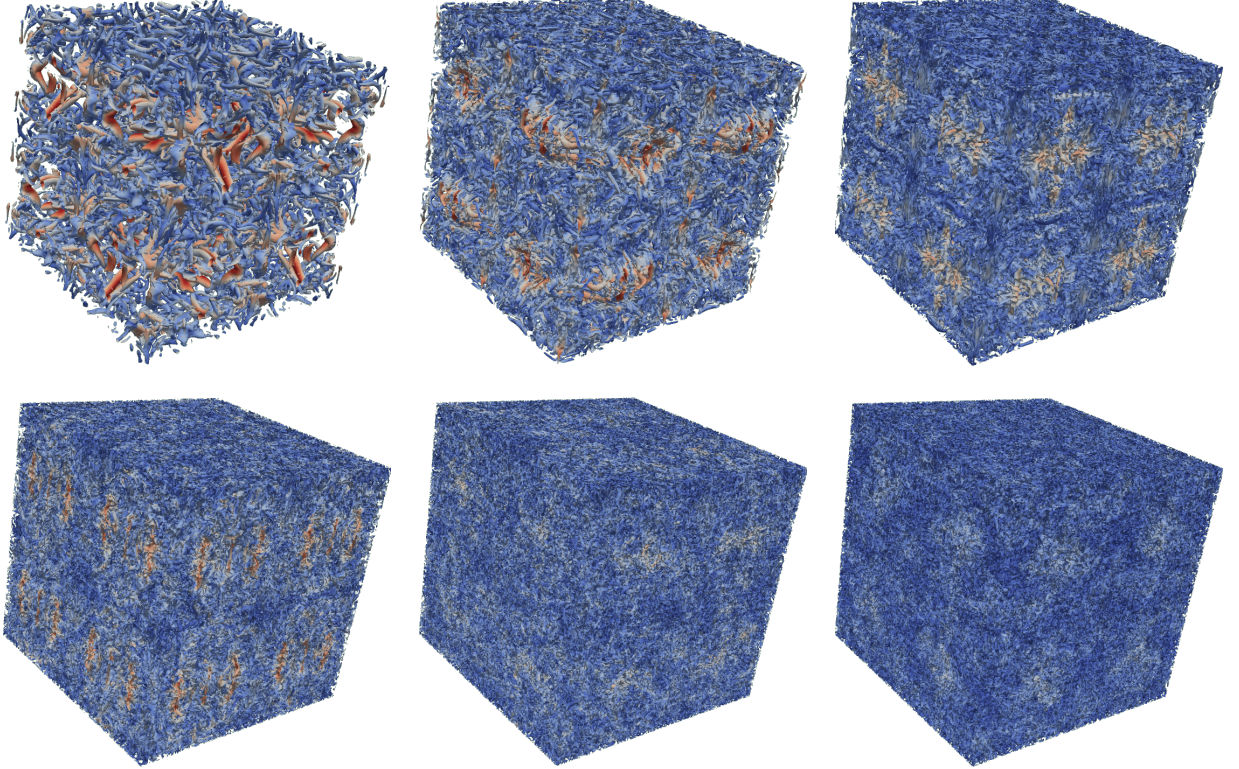


Fig. 9.13: Upwind-stabilised SIP $\mathbb{RT}_{[4]}^{\text{red}}/\mathbb{F}_4/\mathbb{P}_0^{\text{dc}}$ $\mathbf{H}(\text{div})$ -HDG ($\text{Re} < \infty$) and upwind-stabilised $\mathbb{RT}_{[4]}^{\text{red}}/\mathbb{P}_0^{\text{dc}}$ $\mathbf{H}(\text{div})$ -DG ($\text{Re} = \infty$) for the simulation of the TGV at different Reynolds numbers with a fixed $N = 32$ mesh. 1-isosurface of the $Q(\mathbf{u}_h)$ -criterion coloured with velocity magnitude $|\mathbf{u}_h|$ at $t = 20$ for $\text{Re} \in \{1600, 3000, 5000, 10\,000, 100\,000, \infty\}$ (from left to right and top to bottom).

For the Euler problem on the continuous level, one can easily show that energy is conserved exactly for all times, provided enough regularity is assumed; see Rem. 2.9. Thus, the following observations concerning the dissipative character of upwinding inevitably lead to the question whether it is possible to compute the inviscid Euler problem without any convection stabilisation. This is done in the hope that the numerical results come closer to the expectations of the continuous problem.

And indeed, as shown qualitatively in Fig. 9.14, the exactly divergence-free $\mathbf{H}(\text{div})$ -DG method $\mathbb{RT}_{[4]}^{\text{red}}/\mathbb{P}_0^{\text{dc}}$ on the $N = 32$ mesh is perfectly able to simulate the inviscid Euler-TGV problem without any stabilisation. This figure shows instantaneous states of the Q -criterion analogous to the

ones displayed in Fig. 9.2 for $\text{Re} = 1600$. One can observe that, as expected, the absence of viscosity in the Euler case leads to a flow topology with a significantly increased amount of fine-scale structures compared to $\text{Re} = 1600$.

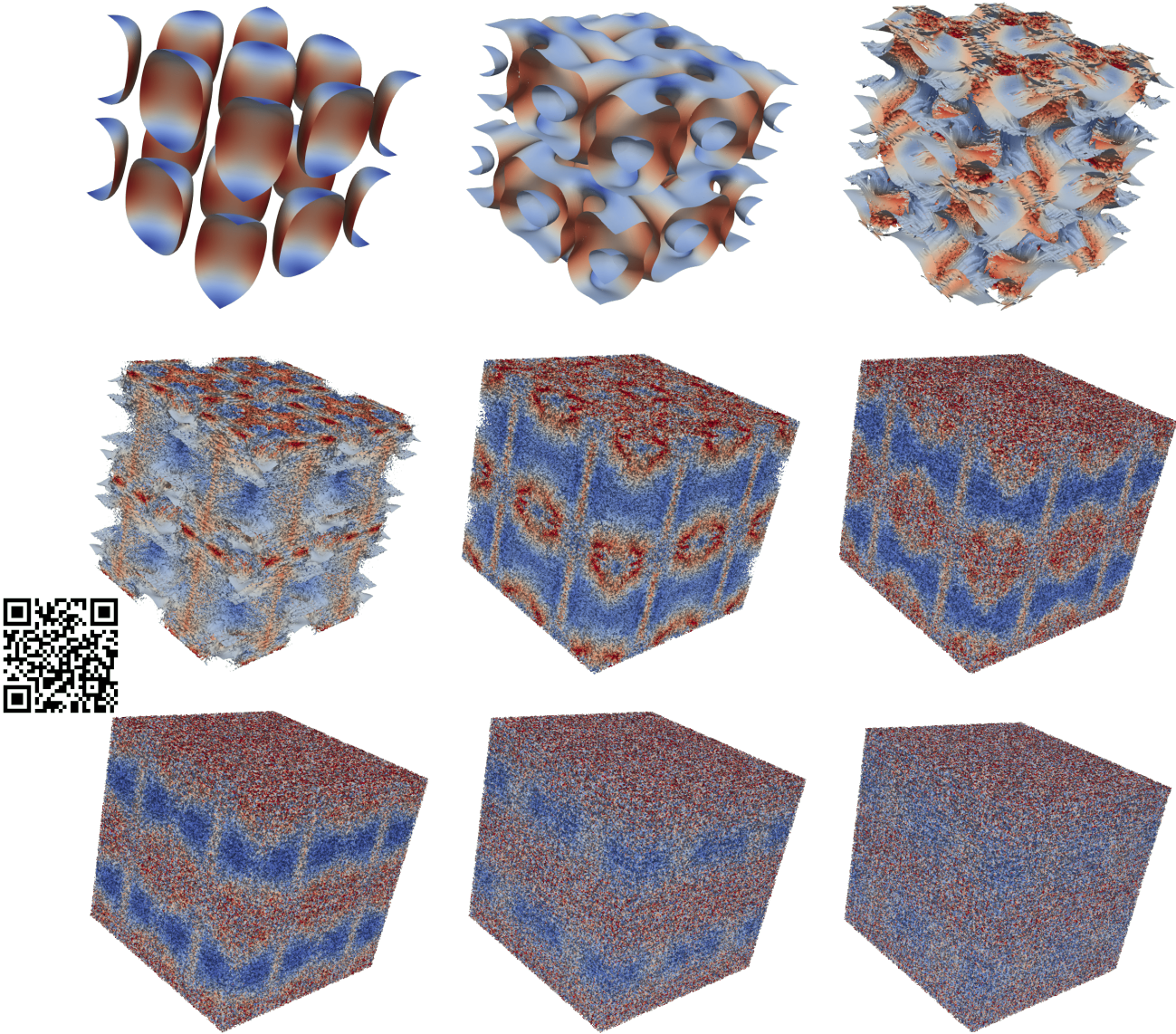


Fig. 9.14: Inviscid TGV: Evolution of 0.1-isosurface of $Q(\mathbf{u}_h)$ -criterion coloured with velocity magnitude $|\mathbf{u}_h|$, where blue corresponds to zero and red to everything above unity. Obtained with the unstabilised $\mathbf{RT}_{[4]}^{\text{red}}/\mathbb{P}_0^{\text{dc}}$ method on a mesh with $N = 32$ cubical elements in each direction. Time instances from left to right and top to bottom: $t = 0, 2, 4, 5, 7, 9, 10, 14, 20$. (A video of this simulation is available at <https://youtu.be/cDXLFnR4468>; note also the QR code.)

Finally, let us examine closer the differences between the results for $\text{Re} = \infty$, computed with and without upwinding. The left-hand side of Fig. 9.15 shows that without upwinding, irrespective of the degree of resolution, the kinetic energy stays approximately constant over the time interval $t \in [0, 20]$. Hence, it becomes clear that by using upwinding, in principle, a simulation with an effectively smaller Reynolds number is performed. In view of the characteristics of the continuous

problem, we hence infer that the simulation without upwinding might be superior. It is interesting to observe that for this pure convection problem, no stabilisation is required. We conjecture that the reason for this is the clean energy balance of exactly divergence-free methods.

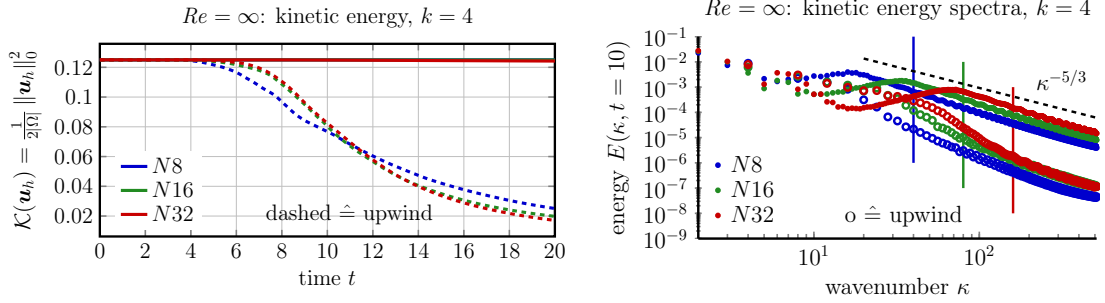


Fig. 9.15: Comparison of kinetic energy (left) and kinetic energy spectra at $t = 10$ (right), with and without upwinding for the inviscid Euler-TGV. Computed with the $\mathbf{RT}_{[4]}^{\text{red}}/\mathbb{P}_0^{\text{dc}}$ $\mathbf{H}(\text{div})$ -DG method on different meshes. For better clarity, not all spectrum values for the upwinding simulations are displayed. Vertical lines correspond to $N(k + 1)$, respectively.

The right-hand side of Fig. 9.15 shows the corresponding energy spectra at $t = 10$. One can see clearly that upwinding dissipates energy from the small-scale features (large wavenumbers) of the turbulent flow. The results without upwinding show that on finer meshes, the amount of energy in the large scales (small wavenumbers) decreases. A possible explanation for this behaviour is that a finer resolution naturally allows for the presence of finer scales which, under (approximate) energy conservation, leads to less energy being present in large scales. Note that the cut-off for $\kappa > 512$ is connected to the maximum resolution *used for sampling/post-processing* the velocity field; it does not indicate that there exists a sudden drop in energy *in the solution*. Recalling Onsager’s conjecture (Rem. 2.9), the decay of the energy spectrum according to $\kappa^{-5/3}$, for sufficiently large wavenumbers, indicates that the inviscid Euler flow possesses at least $C^{0,1/3}$ regularity; see Rem. 2.16. Hence, one can expect that this flow is not prone to anomalous dissipation phenomena.

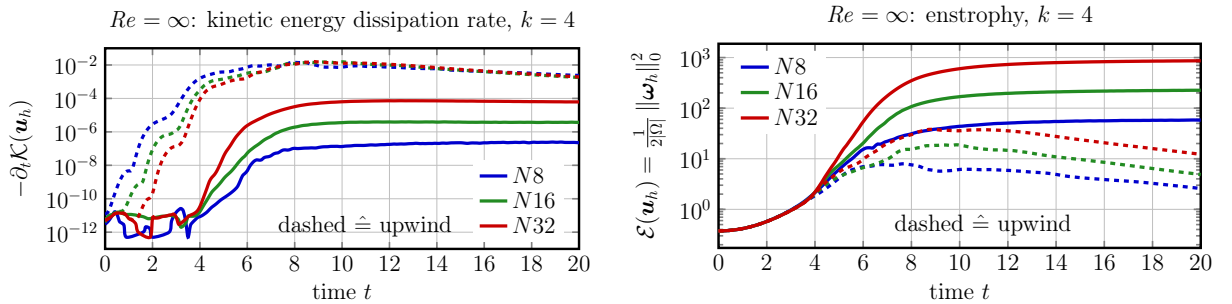


Fig. 9.16: Comparison of total kinetic energy dissipation rate (left) and enstrophy (right), with and without upwinding, for the inviscid Euler-TGV. Computed with the $\mathbf{RT}_{[4]}^{\text{red}}/\mathbb{P}_0^{\text{dc}}$ $\mathbf{H}(\text{div})$ -DG method on different meshes.

Concerning the total dissipation rate, Fig. 9.16 (left) shows $-\partial_t \mathcal{K}(\mathbf{u}_h)$ on different meshes with and

without upwinding. As expected, the simulations with upwinding dissipate more energy (dashed lines). Interestingly enough, the results without upwinding show that increasing the resolution actually leads to slightly more energy dissipation. Moreover, as can be seen from the enstrophy on the right-hand side of Fig. 9.16, a more resolved simulation also leads to a higher enstrophy in the flow. Note, however, that even in the most resolved situation we consider here, the enstrophy actually does not show any signs of mesh-convergence, which can be expected in light of potentially infinitesimal small structures in the (continuous) problem.

Remark 9.1: A video comparing the $Re = 1600$ TGV with the inviscid TGV side-by-side is available at <https://youtu.be/XEEmFvmnYJU>; note also the QR code. In this direct comparison, one can observe very well that the Euler problem leads to much more dominant fine-scale structures, which are dissipated by molecular viscosity in the Navier–Stokes case. ▲



9.1.4 Helmholtz Decomposition of Convection Forces

The last investigation concerning the TGV is to deal with the Helmholtz decomposition of the convection forces in the two cases $Re = 1600$ and $Re = \infty$ (without upwinding). The underlying question is the following. Is there any difference between the distribution of divergence-free and curl-free forces for different Reynolds numbers? As in Sec. 8.2.2, we use

$$\mathbf{f}_h = (\mathbf{u}_h \cdot \nabla_h) \mathbf{u}_h = \mathbb{P}_h^{\text{div}}(\mathbf{f}_h) + \nabla \phi_h,$$

which is based on the corresponding $\mathbb{RT}_{[4]}/\mathbb{P}_4^{\text{dc}}$ DG method defined by (3.10). Here, $\mathbb{P}_h^{\text{div}}(\mathbf{f}_h)$ represents the divergence-free forces and $\nabla \phi_h$ describes the curl-free gradient forces. Thanks to using a pressure-robust method, the former are cleanly balanced by the discrete velocity and the latter by the discrete pressure.

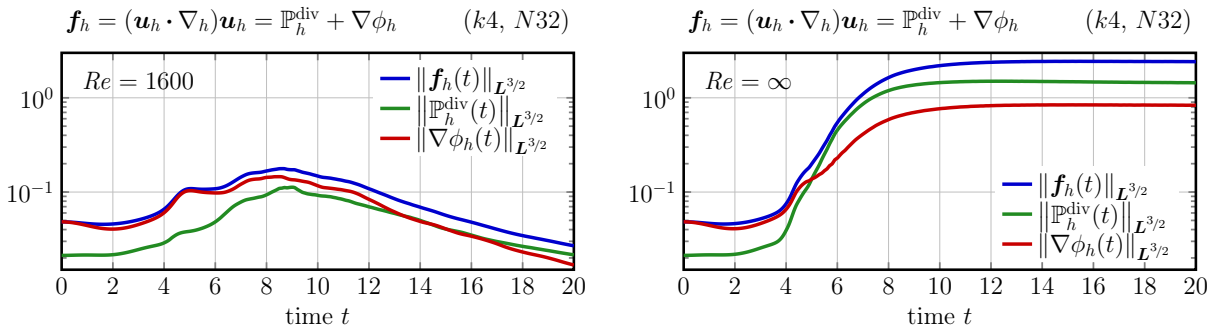


Fig. 9.17: Evolution of Helmholtz decomposition of convection forces for $Re = 1600$ (left) and inviscid Euler limit $Re = \infty$ (right). Computed with upwind-stabilised SIP $\mathbb{RT}_{[4]}^{\text{red}}/\mathbb{F}_4/\mathbb{P}_0^{\text{dc}}$ ($Re = 1600$) and unstabilised $\mathbb{RT}_{[4]}^{\text{red}}/\mathbb{P}_0^{\text{dc}}$ ($Re = \infty$); both on a $N = 32$ mesh. All norms are normalised by the box volume $|\Omega| = (2\pi)^3$.

In Fig. 9.17, the evolutions of the $L^{3/2}$ -norms of the total convection force \mathbf{f}_h , its divergence-free part $\mathbb{P}_h^{\text{div}}(\mathbf{f}_h)$ and its curl-free part $\nabla \phi_h$ are displayed for $Re = 1600$ and $Re = \infty$ (without upwinding). At first, one can see that at the beginning of the simulation (approx. $t < 4$), where

the motion is dominated by inviscid behaviour, the gradient part is clearly dominating the flow for both Reynolds numbers. Thus, as long as there is no turbulence, the force $\nabla\phi_h$ tries to preserve the large-scale vortex structure imposed by the initial condition. As transition sets in (approx. $t \in [4, 10]$), however, the divergence-free force $\mathbb{P}_h^{\text{div}}(\mathbf{f}_h)$ increases considerably to such an extent that at the dissipation peak ($t \approx 9$), it is almost as large ($\text{Re} = 1600$) and larger ($\text{Re} = \infty$) as the gradient part, respectively. Finally, in the fully turbulent regime up to $t = 20$, the situation is no longer changing, apart from the fact that viscous effects dampen the flow for $\text{Re} = 1600$, which is not the case for $\text{Re} = \infty$ (without upwinding).

9.2 Turbulent Channel Flow

The 3D turbulent channel flow problem is a frequently used benchmark problem for assessing the ability of flow solvers to deal with wall-bounded turbulence [KMM87; MK82; MKM99]. As the domain for all channel flows we consider the rectangular cuboid $\Omega = (0, L_x) \times (0, L_y) \times (0, L_z)$ with $L_x = 2\pi\delta_c$, $L_y = 2\delta_c$, $L_z = \pi\delta_c$ and channel half-width $\delta_c = 1$. In x - (streamwise) and z -direction (spanwise) periodic BCs are prescribed, whereas for $y \in \{0, L_y\}$ the no-slip condition $\mathbf{u} = \mathbf{0}$ is imposed. Due to sharp velocity gradients, it is common practice to stretch the mesh in y -direction (wall normal direction). We choose the stretching function $f: [0, 1] \rightarrow [0, L_y]$,

$$y \mapsto \delta_c \frac{\tanh(C[2y - 1])}{\tanh(C)} + \delta_c, \quad (9.4)$$

with a constant $C = 1.8$ for all simulations. Therefore, given a mesh with N elements in each direction, the resulting meshes for the channel flow problem consist of N^3 hexahedra (cuboids), which will be equidistant in x - and z -direction and stretched in y -direction. Usually, the whole motion is driven solely by a constant pressure gradient source term $\mathbf{f} = (f_p, 0, 0)^\dagger$, acting in the streamwise direction; cf., for example, [CL14, Sec. 13.4].

Note that a feeling for how the stretching (9.4) works can be obtained from regarding Fig. 9.24, where the corresponding stretched meshes for $N \in \{4, 8, 16\}$ are shown. In this context, it is important to emphasise that the subsequent numerical results in this section are intentionally provided also for (strongly) under-resolved settings. Indeed, we are again interested in how our $\mathbf{H}(\text{div})$ -based methods perform in such unfavourable situations.

In order to distinguish different turbulent channel flow settings, the *friction Reynolds number* Re_τ is considered most frequently; cf., for example, [BIL06, Sec. 12.2]. It is defined as $\text{Re}_\tau = u_\tau \delta_c / \nu$, where u_τ denotes the so-called wall friction velocity which, in turn, depends on the wall shear stress τ_w as $u_\tau^2 = \tau_w / \rho$. Under the assumption of a statistically steady state flow, and with $\rho = 1$, one has $\tau_w = f_p \delta_c$; see [DJT99, Sec. 2.3]. Then, by choosing $f_p = 1$, one obtains $u_\tau = 1$ and hence, friction Reynolds number and viscosity are connected by the simple relation $\nu = 1/\text{Re}_\tau$.

The relevant quantities of interest for the channel flow involve averaging in time $\langle \cdot \rangle_t$ and in spatial directions of homogeneity $\langle \cdot \rangle_s$, where the abbreviation $\langle \cdot \rangle = \langle \langle \cdot \rangle_s \rangle_t$ is used [Joh16]. Then, we

consider the following normalised quantities:

$$\begin{aligned}
 \text{mean velocities:} & \quad \langle u_i \rangle^+ = \langle u_i \rangle / u_\tau, \\
 \text{Reynolds stresses:} & \quad \langle u'_i u'_j \rangle^+ = \langle u_i u_j \rangle / u_\tau^2 - \langle u_i \rangle \langle u_j \rangle / u_\tau^2, \\
 \text{turbulent kinetic energy:} & \quad k^+ = 0.5 \left[\langle u'_1 u'_1 \rangle^+ + \langle u'_2 u'_2 \rangle^+ + \langle u'_3 u'_3 \rangle^+ \right], \\
 \text{rms turbulence intensities:} & \quad u_{i,\text{rms}}^+ = \left| \langle u'_i u'_i \rangle^+ - 2k^+ / 3 \right|^{1/2}.
 \end{aligned}$$

Furthermore, instead of the physical distance y , so-called *wall units* $y^+ = y u_\tau / \nu$ for $y \in [0, \delta_c]$ are frequently used. Note that defined in such a way, $y^+ = \text{Re}_\tau$ refers to the middle of the channel.

Remark 9.2: A different possible definition of the Reynolds number in channel flows is the *bulk Reynolds number* $\text{Re}_m = u_m (2\delta_c) / \nu$, where the main difference lies in the definition of the reference velocity u_m [Pop00, Sec. 7.1.1]. For computing Re_m , the following (averaged) bulk velocity is used:

$$u_m = \frac{1}{\delta_c} \int_0^{\delta_c} \langle u_1 \rangle(y) dy.$$

For $\text{Re}_m < 1350$ the flow is laminar; it is fully turbulent for $\text{Re}_m > 1800$ [Pop00, Sec. 7.1.1]. We are not aware of an analogous characterisation based on Re_τ . ▲

Concerning the practical realisation of the following simulations, averages (statistics) always have been recorded over a time period of 20 time units, whenever a fully turbulent flow was present. The time-stepping is again based on the second-order RK variant ARS(2,2,2) of the IMEX method introduced in [ARS97], where a constant time step (different for each simulation) has been chosen in order to fulfil the CFL stability criterion. Here, only the pressure-velocity coupling is involved in the implicit treatment, whereas both viscosity and convection are treated explicitly. Therefore, no hybridisation is necessary and the underlying SIP- $\mathbf{H}(\text{div})$ -DG method is $\mathbf{RT}_{[k]}^{\text{red}} / \mathbb{P}_0^{\text{dc}}$ with $\lambda = 3(k+1)^2$; cf. Sec. 3.3. A fully turbulent velocity solution from a coarser mesh is used as initial condition for the next finer mesh.

A sketch of the main difference between laminar and turbulent channel flows can be seen in Fig. 9.18. While for the laminar profile usually a quadratic profile occurs at instantaneous observations, a turbulent channel flow, after averaging, is characterised by a much more flat profile. An instantaneous snapshot of a turbulent channel flow, on the other hand, typically reveals its underlying non-deterministic motion; cf. Fig. 9.24.

Moreover, for turbulent channel flows there exists a certain notion of (empirically-determined) self similarity in the averaged streamwise velocity profiles for different Reynolds numbers; cf., for example, [SG00, Sec. 17.1.2], [Pop00, Sec. 7.1] or [Wil06, Sec. 1.3.5] for more details on the derivation of the following statements. Close to the wall, the region where $y^+ \lesssim 5$ holds is called *viscous sublayer*. In the viscous sublayer the flow is dominated by viscous effects, and one can show that $\langle u_1(y) \rangle^+ \approx y^+$. On the other hand, in the so-called *log layer* region where $y^+ \gtrsim 30$, the relationship $\langle u_1(y) \rangle^+ \approx 1/\kappa^+ \ln(y^+) + C^+$ holds. Here, the von Kármán constant $\kappa^+ \approx 0.41$ and the

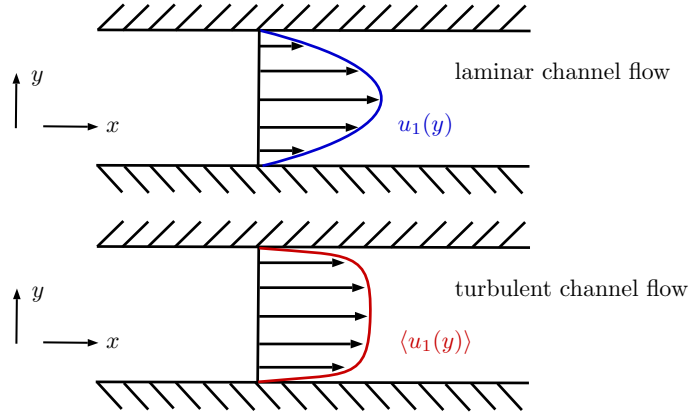


Fig. 9.18: Sketch of streamwise profiles for laminar (top) and turbulent (bottom) channel flow. Note that the laminar profile occurs in the instantaneous flow, whereas the turbulent profile can be seen only after suitable averaging $\langle \cdot \rangle$.

constant $C^+ \approx 5.17$ are usually determined from experiments. In the log layer, viscosity effects can be neglected to a certain extent. With a slight abuse of naming, we will refer to the introduced characterisation for $\langle u_1(y) \rangle$ as the *law of the wall*. Note that all the above statements are only approximately correct and thus, all numbers have to be handled very carefully. Moreover, the region between the viscous sublayer and the log layer is called *buffer layer*, and it describes the region where viscosity-dominated ($y^+ \lesssim 5$) and turbulence-dominated ($y^+ \gtrsim 30$) parts of the flow come together. Therefore, in the buffer layer, neither of the two characterisations for $\langle u_1 \rangle^+$ is valid. Lastly, there exists also the so-called *defect layer* for large y^+ , but since it is not universal for every flow, we will not discuss it here.

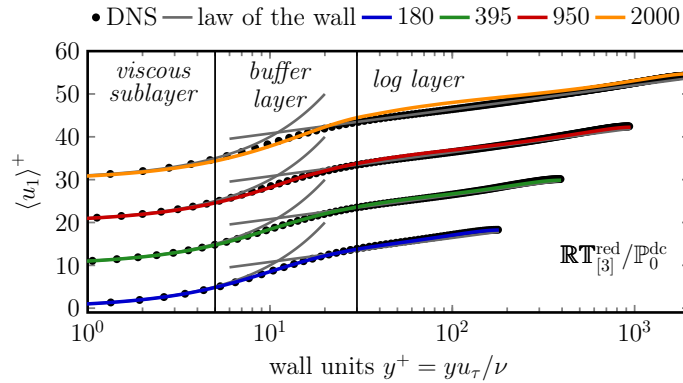


Fig. 9.19: Streamwise velocity profiles $\langle u_1 \rangle^+$ computed with the $\mathbf{RT}_{[3]}^{\text{red}}/\mathbb{P}_0^{\text{dc}}$ method for different friction Reynolds numbers $\text{Re}_\tau \in \{180, 395, 950, 2000\}$, together with corresponding DNS results and the law of the wall. For $\text{Re}_\tau > 180$, the results are each vertically shifted by 10 units in order to ensure better visibility.

In anticipation of the subsequent results, Fig. 9.19 (logarithmic scaling of abscissa) shows the law of the wall for different friction Reynolds numbers. The universal validity of the law of the wall can be confirmed, because the curves for all Reynolds numbers collapse (without the vertical shifting for better visibility). The only difference is that for higher Reynolds numbers, the log layer simply

gets larger, which means that the maximum mean velocity increases slightly. On top of that, the validity of the law of the wall is underlined by means of available DNS results and our own computed streamwise velocity profiles $\langle u_1 \rangle^+$, computed with the $\mathbb{RT}_{[3]}^{\text{red}}/\mathbb{P}_0^{\text{dc}}$ method on the respective finest mesh (more details can be found in the following subsections). In the viscous sublayer and in the log layer the DNS data matches the law of the wall for all Reynolds numbers. One can already suspect, however, that our simulation for $\text{Re}_\tau = 2000$ does not resolve the flow completely, since at the beginning of the log layer, the velocity is slightly over-predicted. Note that, as frequently done in this context, the profiles are only plotted up to the middle of the channel.

Remark 9.3 (Boussinesq’s conjecture): Before considering our numerical experiments in detail, we want to comment on Boussinesq’s conjecture from 1877, which states that turbulent fluctuations are dissipative on the mean flow. In order to explain this, with an abuse of notation, denote by $\langle \cdot \rangle$ a suitable averaging operator; usually ensemble averaging is used, but long-time averages are in principal valid as well. Note that averaging over several flow-through times for turbulent channel flow simulations can be thought of as a possibility to obtain ensemble averages; hence the placement of this remark in this section. Then, turbulent fluctuations are defined as $\mathbf{u}' = \mathbf{u} - \langle \mathbf{u} \rangle$, and averaging the Navier–Stokes equations (2.1) results in the non-closed problem

$$\begin{cases} \partial_t \langle \mathbf{u} \rangle + (\langle \mathbf{u} \rangle \cdot \nabla) \langle \mathbf{u} \rangle - \nu \Delta \langle \mathbf{u} \rangle - \nabla \cdot \mathbb{R}_s(\mathbf{u}, \mathbf{u}) + \nabla \langle p \rangle = \mathbf{f} & \text{in } \Omega, \\ \nabla \cdot \langle \mathbf{u} \rangle = 0 & \text{in } \Omega. \end{cases} \quad (9.5a)$$

$$(9.5b)$$

Here, $\mathbb{R}_s(\mathbf{u}, \mathbf{u}) = -\langle \mathbf{u}' \otimes \mathbf{u}' \rangle = \langle \mathbf{u} \rangle \otimes \langle \mathbf{u} \rangle - \langle \mathbf{u} \otimes \mathbf{u} \rangle$ denotes the *Reynolds stress tensor*. One obtains the energy budget by dotting $\langle \mathbf{u} \rangle$ into (9.5), integration over Ω and integration by parts:

$$\frac{1}{2} \frac{d}{dt} \|\langle \mathbf{u} \rangle\|_{L^2}^2 + \nu \|\nabla \langle \mathbf{u} \rangle\|_{L^2}^2 + \int_{\Omega} \mathbb{R}_s(\mathbf{u}, \mathbf{u}) : \nabla \langle \mathbf{u} \rangle \, d\mathbf{x} = \int_{\Omega} \mathbf{f} \cdot \langle \mathbf{u} \rangle \, d\mathbf{x}.$$

The integral involving $\mathbb{R}_s(\mathbf{u}, \mathbf{u})$ describes the effect of fluctuations on the kinetic energy of the mean flow. Now, following [JL16], denoting by LIM a generalised limit, the following mathematical phrasing of Boussinesq’s conjecture holds for strong solutions which are regular enough to fulfil energy equality, and as long as the ensemble is generated by different initial conditions only:

$$\text{LIM}_{T \rightarrow \infty} \frac{1}{T} \int_0^T \int_{\Omega} \mathbb{R}_s(\mathbf{u}, \mathbf{u}) : \nabla \langle \mathbf{u} \rangle \, d\mathbf{x} \, d\tau = \text{LIM}_{T \rightarrow \infty} \frac{\nu}{T} \|\nabla \mathbf{u}'\|_{L^2}^2 \, d\tau \geq 0.$$

See also [CL14, Thm. 3.5], where a similar result has been proven for long-time averaging. ▲

9.2.1 Simulations for $\text{Re}_\tau = 180$

Let us begin with the comparably small Reynolds number $\text{Re}_\tau = 180$ for which DNS results are available from [MKM99]. Using the DNS data, in terms of the bulk Reynolds number, this corresponds to $\text{Re}_m \approx 5585$.

In Fig. 9.20, the statistics resulting from a $\mathbb{RT}_{[3]}^{\text{red}}/\mathbb{P}_0^{\text{dc}}$ method are shown on different meshes. One can observe that while the coarsest $N = 4$ mesh already leads to satisfying results concerning

the mean velocity $\langle u_1 \rangle^+$, both the cross-Reynolds stress $\langle u'_1 u'_2 \rangle^+$ and the rms turbulence intensity $u_{1,\text{rms}}^+$ need at least the resolution provided by the $N = 8$ mesh. Moreover, the upper two plots show the streamwise mean profile $\langle u_1 \rangle^+$ in linear and logarithmic scaling, respectively; note the similarity to the turbulent flow displayed in Fig. 9.18. As the clarity of the presentation reduces for increasing Reynolds numbers with linear scaling, the logarithmic scaling is usually the favoured choice for presenting velocity profiles.

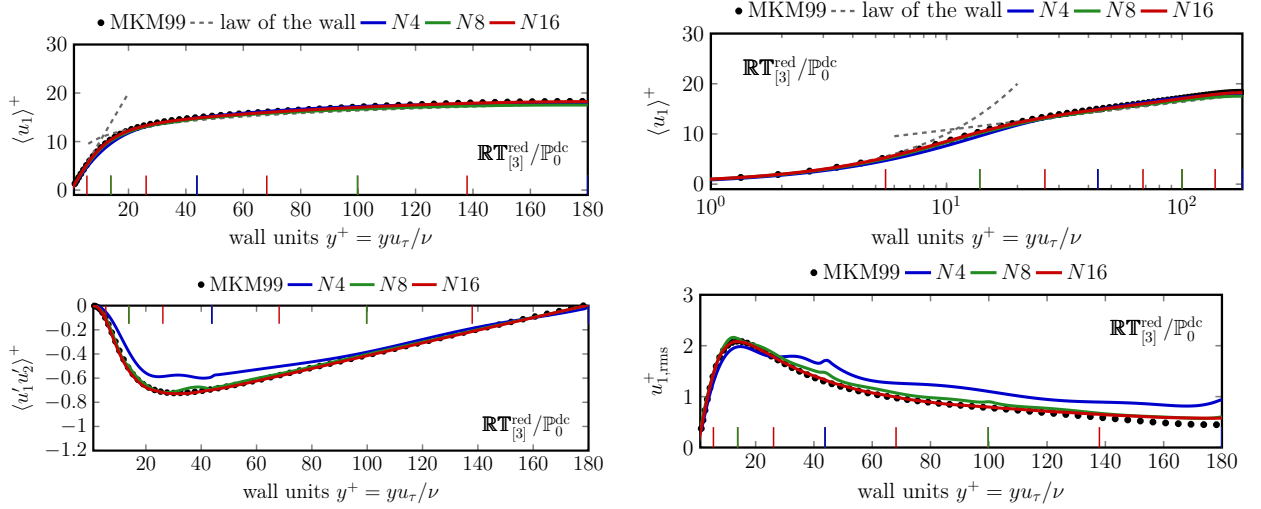


Fig. 9.20: $\text{Re}_\tau = 180$ mean velocity $\langle u_1 \rangle^+$ with linear (top left) and logarithmic (top right) scaling, cross-Reynolds stress $\langle u'_1 u'_2 \rangle^+$ (bottom left) and rms turbulence intensity $u_{1,\text{rms}}^+$ (bottom right), computed with $\mathbf{RT}_{[3]}^{\text{red}}/\mathbb{P}_0^{\text{dc}}$ on different meshes with $N \in \{4, 8, 16\}$. The indicated vertical lines visualise the underlying mesh spacing in wall-normal direction.

Furthermore, concerning the placement of the first off-wall mesh point, one can deduce from Fig. 9.20 that for this Reynolds number, a relatively coarse mesh is perfectly sufficient in order to achieve meaningful results.

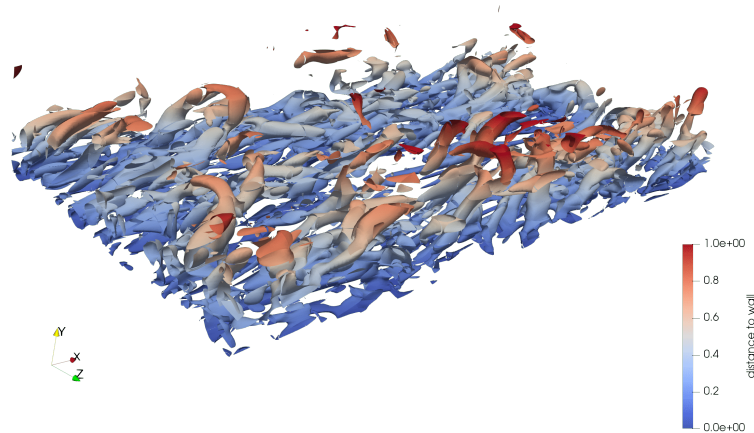


Fig. 9.21: $\text{Re}_\tau = 180$ channel flow: 200-isosurface of $Q(\mathbf{u}_h)$ -criterion, coloured with the distance to the lower wall. Computation: $\mathbf{RT}_{[3]}^{\text{red}}/\mathbb{P}_0^{\text{dc}}$ with $N = 16$.

An instantaneous impression of the flow can be obtained from Fig. 9.21, where the Q -criterion shows that there are large-scale structures in turbulent channel flows and our implicit LES approach does not suppress them.

Interestingly, also the lower order method $\mathbf{RT}_{[2]}^{\text{red}}/\mathbb{P}_0^{\text{dc}}$ yields meaningful results for this low Reynolds number; see Fig. 9.22. However, the simulations with $N = 4$ now show rather large oscillations for the Reynolds stress and the turbulence intensity. On the fine $N = 16$ mesh, on the other hand, the statistics are in no way inferior to the results of the $\mathbf{RT}_{[3]}^{\text{red}}/\mathbb{P}_0^{\text{dc}}$ method. Nevertheless, to be on the safe side, in the following we will limit ourselves to higher-order methods with $k \geq 3$.

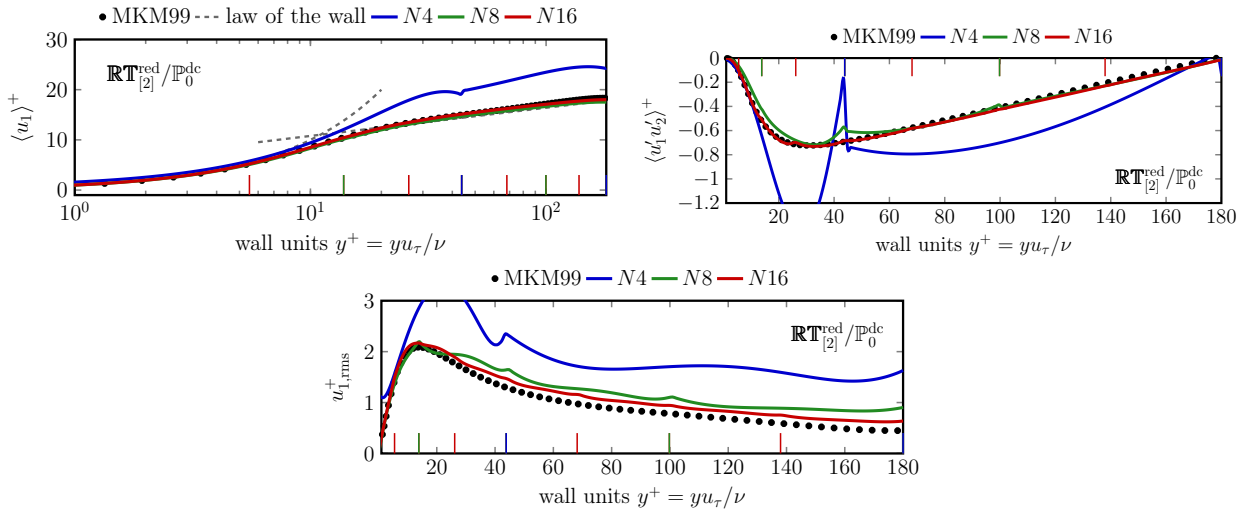


Fig. 9.22: $\text{Re}_\tau = 180$ mean velocity $\langle u_1 \rangle^+$ (top left), cross-Reynolds stress $\langle u_1' u_2' \rangle^+$ (top right) and rms turbulence intensity $u_{1,\text{rms}}^+$ (bottom), computed with $\mathbf{RT}_{[2]}^{\text{red}}/\mathbb{P}_0^{\text{dc}}$ on different meshes with $N \in \{4, 8, 16\}$. The indicated vertical lines visualise the underlying mesh spacing in wall-normal direction.

The quality of our results for $\text{Re}_\tau = 180$ is comparable to the one achieved by a stabilised \mathbf{L}^2 -based ILES-DG method [FWK18b] and much better than, for example, results with a projection-based variational multiscale (VMS) $k = 2$ FEM [JR07]. Especially the under-resolved simulation with $k = 3$ and $N = 8$ still shows a very reasonable behaviour, also in terms of Reynolds stress and turbulence intensity.

Also for the turbulent channel flow the question of the distribution of forces in the (discrete) convection term is interesting. Thus, as in Sec. 8.2.2, we consider the Helmholtz decomposition

$$\mathbf{f}_h = (\mathbf{u}_h \cdot \nabla_h) \mathbf{u}_h = \mathbb{P}_h^{\text{div}}(\mathbf{f}_h) + \nabla \phi_h,$$

which is based on the corresponding $\mathbf{RT}_{[k]}/\mathbb{P}_k^{\text{dc}}$ DG method defined by (3.10). Then, Fig. 9.23 shows the temporal evolution over 25 time units of the $\mathbf{L}^{3/2}$ -norms of particular terms in the decomposition. The data has been collected in the fully developed turbulent channel flow with $\text{Re}_\tau = 180$ using the $\mathbf{RT}_{[3]}^{\text{red}}/\mathbb{P}_0^{\text{dc}}$ method on the $N = 16$ mesh. One can observe that the convection term is

clearly dominated by divergence-free forces $\mathbb{P}_h^{\text{div}}(\mathbf{f}_h)$. Thus, this $\text{Re}_\tau = 180$ turbulent channel flow does not seem to possess characteristics of a (generalised) Beltrami flow in time.

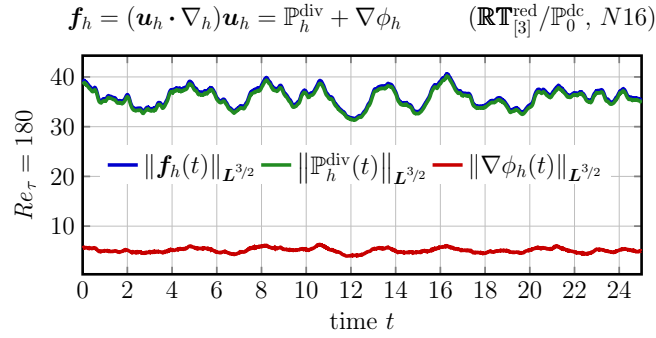


Fig. 9.23: Evolution of Helmholtz decomposition of convection forces in fully developed turbulent channel flow for $\text{Re}_\tau = 180$, computed with $\mathbb{RT}_{[3]}^{\text{red}}/\mathbb{P}_0^{\text{dc}}$ on the $N = 16$ mesh. All norms are normalised by the channel volume $|\Omega| = L_x L_y L_z$.

9.2.2 Simulations for $\text{Re}_\tau = 395$

Increasing the friction Reynolds number to $\text{Re}_\tau = 395$, DNS results are also available from [MKM99]. Using the DNS data, this corresponds to a bulk Reynolds number of $\text{Re}_m \approx 13\,763$.

As for the $\text{Re}_\tau = 180$ case, the problem is computed with $k = 3$ on a sequence of meshes with $N \in \{4, 8, 16\}$. Correspondingly, Fig. 9.24 presents snapshots of the instantaneous velocity magnitude for $\text{Re}_\tau = 395$, which show that a turbulent channel flow is characterised by largely varying fluctuations which become finer as the resolution is increased. Note that the wall-near elements, even for the finest $N = 16$ mesh, are only moderately anisotropic.

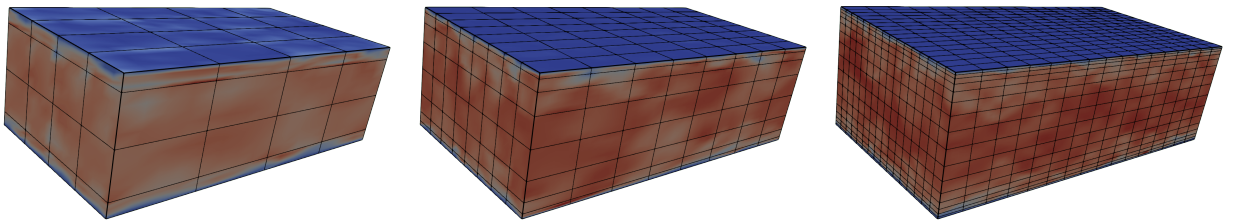


Fig. 9.24: Instantaneous snapshots of velocity magnitude $|\mathbf{u}_h|$ for $\text{Re}_\tau = 395$, computed with $\mathbb{RT}_{[3]}^{\text{red}}/\mathbb{P}_0^{\text{dc}}$ on different meshes with $N \in \{4, 8, 16\}$ (from left to right). Blue colour indicates low velocity and red high velocity.

While Fig. 9.24 gives an impression of how a fully turbulent channel flows looks like, it is also very interesting to take a closer look at the transition from laminar to turbulent flow. Fig. 9.25 gives an impression of this process by visualising velocity magnitude (top) and Q -criterion (bottom) at two time instances directly in the transition to turbulence. Prior to the left-hand side time instance, the flow is laminar with the characteristic deterministic laminar quadratic profile (see Fig. 9.18). However, this laminar profile is unstable for large Reynolds numbers and as a consequence, the

flow begins to develop wave-like structures directly in the boundary layer. The corresponding vortical motion, which develops from this perturbation in the boundary layer, can be seen very well by means of the Q -criterion. Afterwards, turbulence spreads from the boundary layer into the domain. One can see the vortices travel towards the centre of the channel, accompanied by clearly visible Q -isosurfaces. After the right-hand side time instance, the flow transitions into fully developed turbulence (see e.g. Fig. 9.24). In our opinion, it is remarkable that even with such a relatively coarse resolution, these qualitatively consistent flow phenomena can be observed from the numerical solution.

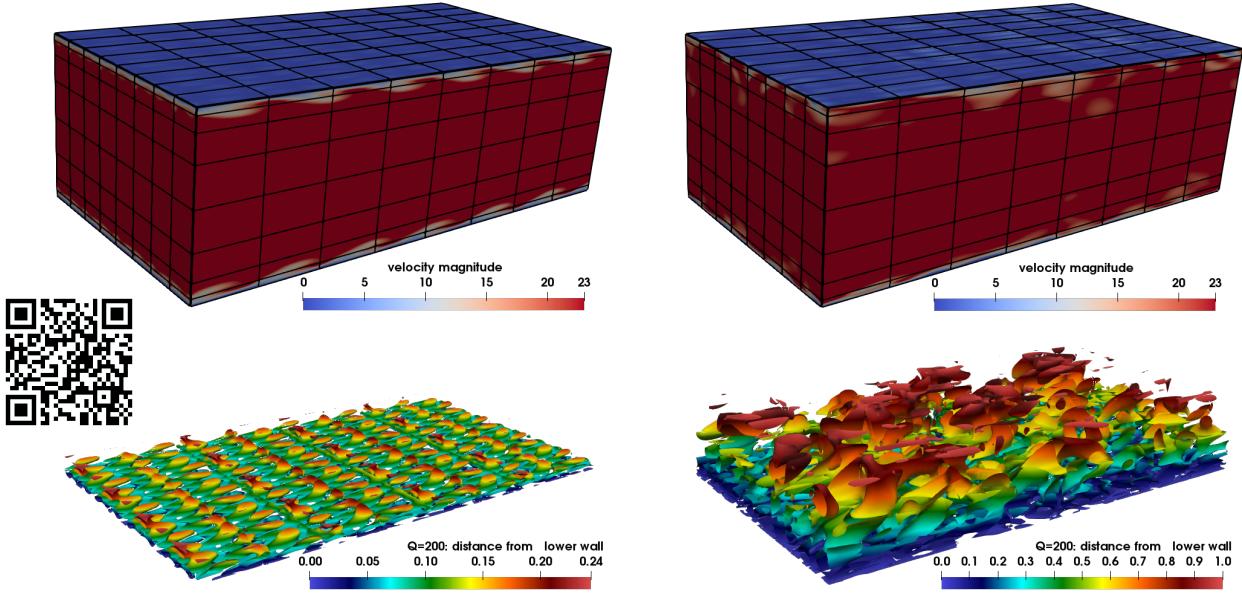


Fig. 9.25: Transition from laminar to turbulent flow: instantaneous snapshots (at the same time instances) of velocity magnitude $|\mathbf{u}_h|$ for $\text{Re}_\tau = 395$ (top) and 200-isosurface of the Q -criterion (bottom; coloured with distance from lower wall), computed with $\text{RT}_{[3]}^{\text{red}}/\mathbb{P}_0^{\text{dc}}$ with $N = 8$. (A video of this simulation is available at <https://youtu.be/XBwqvVxg6Dk>; note also the QR code.)

More quantitatively, the resulting statistics for $\text{Re}_\tau = 395$ and $k = 3$ can be seen in Fig. 9.26. Not surprisingly, the extremely under-resolved simulation with $(k, N) = (3, 4)$ does not match the DNS data. However, at least in the direct vicinity of the wall ($y^+ \lesssim 10$), the mean velocity profile $\langle u_1 \rangle^+$, the cross-Reynolds stress $\langle u'_1 u'_2 \rangle^+$ and the rms turbulence intensity $u_{1,\text{rms}}^+$ are not completely useless. As the mesh is refined, the results improve, and for $N = 16$, both DNS data and the law of the wall can actually be reproduced. Note that this is still not a very fine mesh (or high polynomial order), but the results are already convincing.

Concerning the question whether high-order methods are superior for turbulent channel flows, let us double the polynomial degree to $k = 6$, while at the same time halving the mesh sizes and recompute the turbulent channel flow problem at $\text{Re}_\tau = 395$. The corresponding results can be seen in Fig. 9.27. Note that for $(k, N) = (6, 2)$ the first off-wall mesh point is located at $y^+ = \text{Re}_\tau$, the middle of the channel. One can observe that, compared to $k = 3$, the high-order results are

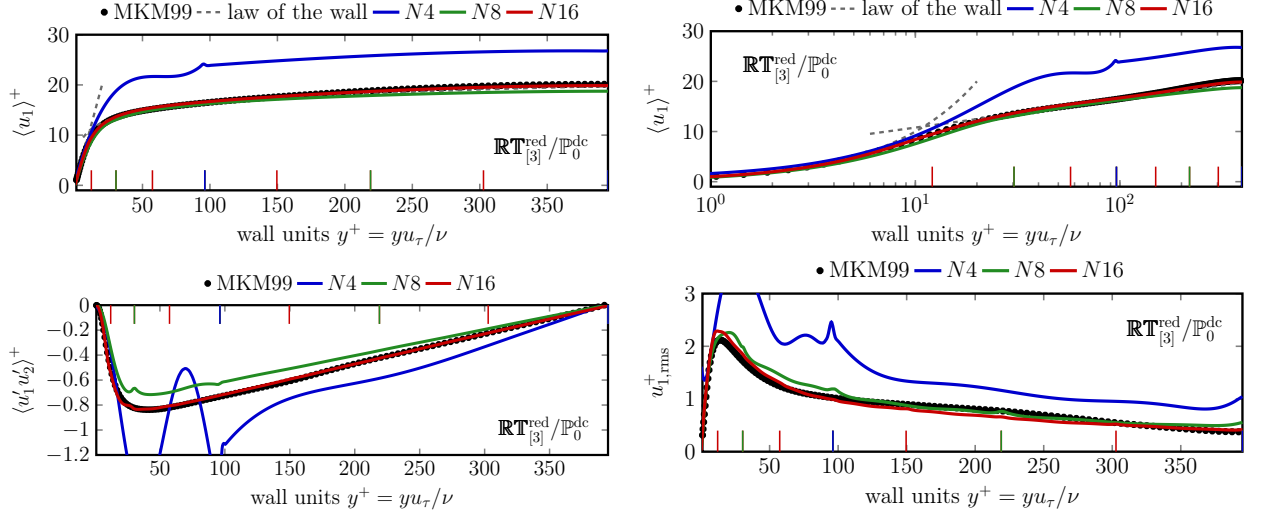


Fig. 9.26: $Re_\tau = 395$ mean velocity $\langle u_1 \rangle^+$ with linear (top left) and logarithmic (top right) scaling, cross-Reynolds stress $\langle u'_1 u'_2 \rangle^+$ (bottom left) and rms turbulence intensity $u_{1,rms}^+$ (bottom right), computed with $\mathbf{RT}_{[3]}^{\text{red}}/\mathbb{P}_0^{\text{dc}}$ on different meshes with $N \in \{4, 8, 16\}$. The indicated vertical lines visualise the underlying mesh spacing in wall-normal direction.

in no way superior. A similar observation for $Re_\tau = 180$ can be found in [FWK18b]. Therefore, and in contrast to decaying turbulence (see Sec. 9.1.2), we conclude that turbulent channel flow simulations, in general, cannot benefit from high-order discretisations. Thus, in the following, we restrict ourselves to $k = 3$.

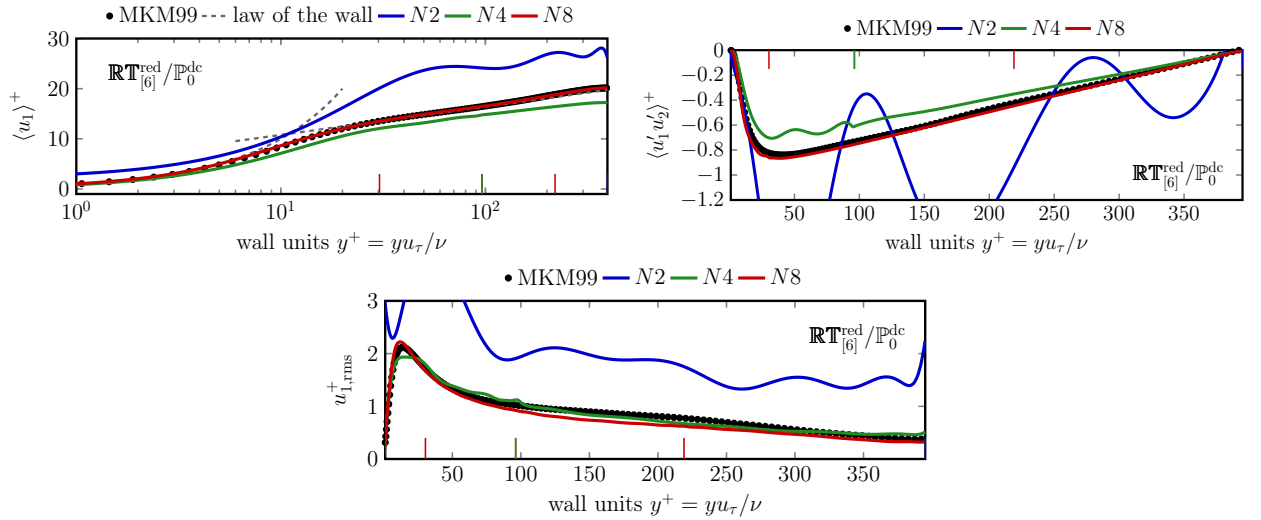


Fig. 9.27: $Re_\tau = 395$ mean velocity $\langle u_1 \rangle^+$ (top left), cross-Reynolds stress $\langle u'_1 u'_2 \rangle^+$ (top right) and rms turbulence intensity $u_{1,rms}^+$ (bottom), computed with $\mathbf{RT}_{[6]}^{\text{red}}/\mathbb{P}_0^{\text{dc}}$ on different meshes with $N \in \{4, 8, 16\}$. The indicated vertical lines visualise the underlying mesh spacing in wall-normal direction.

Irrespective of k , the quality of our results for $Re_\tau = 395$ is comparable to the ones achieved by an isogeometric divergence-conforming VMS method [vOY⁺17] and residual-based NURBS-VMS

[BC⁺07]. Moreover, they seem to be superior to the $k = 1$ FE-RANS-based results from [AKL08], and the finite volume results with explicit LES modelling presented in [KZ⁺10].

9.2.3 Simulations for $\text{Re}_\tau = 950$

Next, for the friction Reynolds number $\text{Re}_\tau = 950$, DNS results can be found in [HJ06; HJ08]; using the DNS data, this corresponds to a bulk Reynolds number of $\text{Re}_m \approx 37\,037$. Owing to the fact that naturally, in order to accurately compute flows at higher Reynolds numbers, a higher resolution is necessary, we now slightly refine the underlying meshes to $N \in \{8, 16, 24\}$.

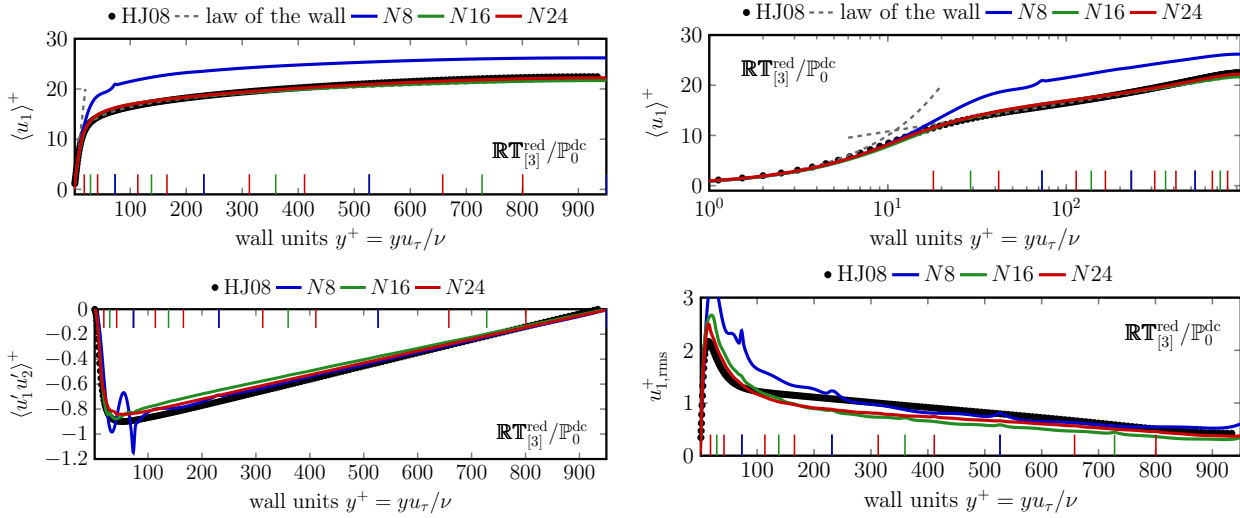


Fig. 9.28: $\text{Re}_\tau = 950$ mean velocity $\langle u_1 \rangle^+$ with linear (top left) and logarithmic (top right) scaling, cross-Reynolds stress $\langle u'_1 u'_2 \rangle^+$ (bottom left) and rms turbulence intensity $u_{1,\text{rms}}^+$ (bottom right), computed with $\mathbf{RT}_{[3]}^{\text{red}}/\mathbb{P}_0^{\text{pdc}}$ on different meshes with $N \in \{8, 16, 24\}$. The indicated vertical lines visualise the underlying mesh spacing in wall-normal direction.

The resulting statistics can be found in Fig. 9.28. While the mean velocity $\langle u_1 \rangle^+$ seems to be relatively easy to capture, the other quantities are actually not so harmless. For the cross-Reynolds stress $\langle u'_1 u'_2 \rangle^+$, an obvious tendency of convergence to the DNS data can be observed, but even for $N = 24$ our results are not identical to them. Even worse, our approximations to the rms turbulence intensity $u_{1,\text{rms}}^+$ seem to converge even slower to the DNS data. It is noticeable that the region in the log layer, where approximately $100 \lesssim y^+ \lesssim 400$, seems to be especially hard to capture in under-resolved simulations. Nonetheless, our results still altogether show a very reasonable behaviour. Indeed, the accuracy of our results for $\text{Re}_\tau = 950$ is comparable to the one achieved by the stabilised L^2 -based ILES-DG methods proposed in [CH⁺15; FWK18b]. On the other hand, the results from [RG13], computed with a $k = 1$ multifractal subgrid-scale VMS LES method, only match the DNS data for higher resolutions.

Another question which may arise is the importance of upwinding for turbulent channel flow problems. In order to make an assessment of the role of convection stabilisation in this context, the previous computations are repeated without upwinding ($\theta = 0$). Fig. 9.29 shows that on the

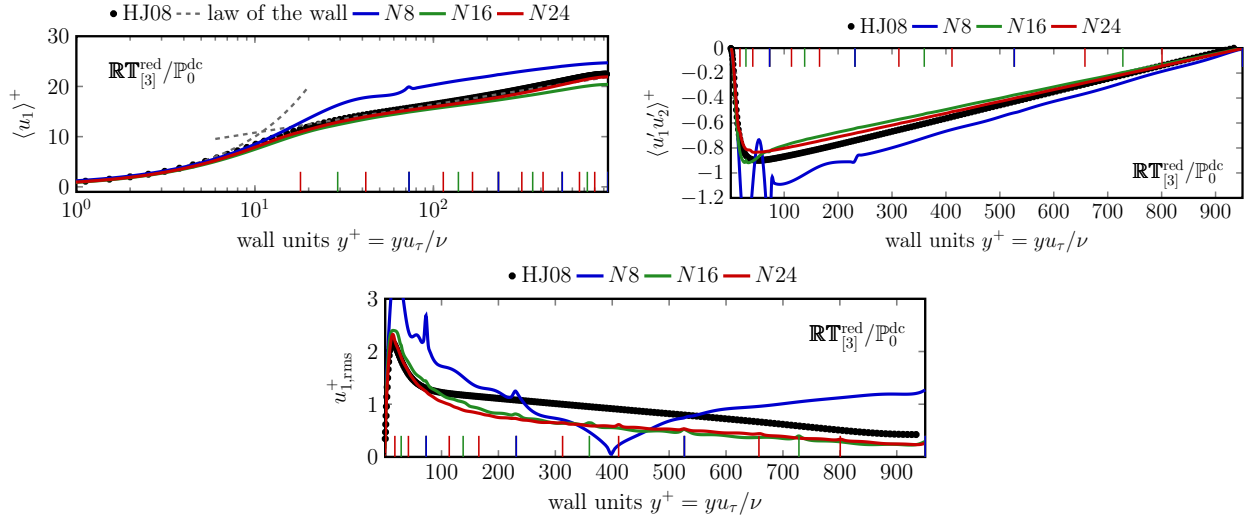


Fig. 9.29: No upwinding: $\text{Re}_\tau = 950$ mean velocity $\langle u_1 \rangle^+$ (top left), cross-Reynolds stress $\langle u'_1 u'_2 \rangle^+$ (top right) and rms turbulence intensity $u_{1,\text{rms}}^+$ (bottom), computed with $\mathbf{RT}_{[3]}^{\text{red}}/\mathbb{P}_0^{\text{dc}}$ on different meshes with $N \in \{8, 16, 24\}$.

coarsest $N = 8$ mesh, the simulation without upwinding behaves unreasonable, especially for the rms turbulence intensity $u_{1,\text{rms}}^+$. Moreover, also the other quantities obviously benefit from the additional dissipation provided by upwinding. Therefore, and in contrast to the TGV problem in Sec. 9.1, convection stabilisation by upwinding seems to be beneficial for turbulent channel flows.

9.2.4 Simulations for $\text{Re}_\tau = 2000$

The highest Reynolds number considered in this work is $\text{Re}_\tau = 2000$, for which DNS results are also reported in [HJ06; HJ08]. By (numerical) integration of the DNS data, one obtains the corresponding bulk Reynolds number $\text{Re}_m \approx 87123$. An impression for the resulting flow can be obtained from the (instantaneous) snapshots provided in Fig. 9.30. Along with the $N = 24$ mesh (this is also the finest mesh we use here, similarly as in the $\text{Re}_\tau = 950$ case), one can anticipate the amount of fine-scale structures which are present in such a flow.

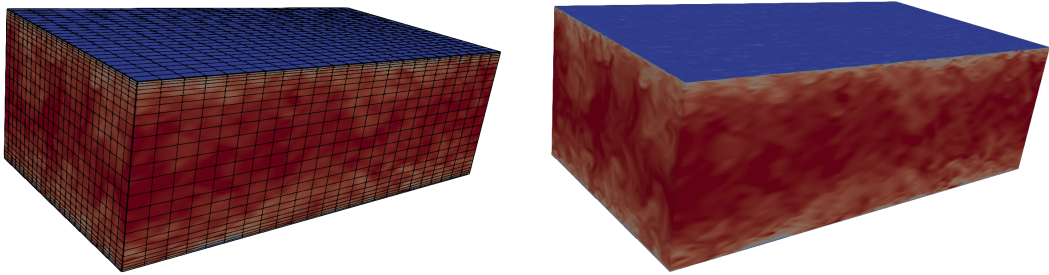


Fig. 9.30: Instantaneous snapshots of velocity magnitude $|\mathbf{u}_h|$ for $\text{Re}_\tau = 2000$, computed with $\mathbf{RT}_{[3]}^{\text{red}}/\mathbb{P}_0^{\text{dc}}$ on a $N = 24$ mesh. Left: with underlying mesh; right: without mesh. Blue colour indicates low velocity and red high velocity.

Fig. 9.31 shows the Q -criterion, coloured with the distance from the lower wall, for a particular time instance. This illustration gives a clear idea of the richness of (local) vortical motion and, as

compared to Fig. 9.21 for $\text{Re}_\tau = 180$, shows that the amount of those structures increases significantly with increasing Reynolds number. Moreover, they are getting much denser in the vicinity of the wall, which confirms that they emerge mainly as a result of interactions with solid boundaries.

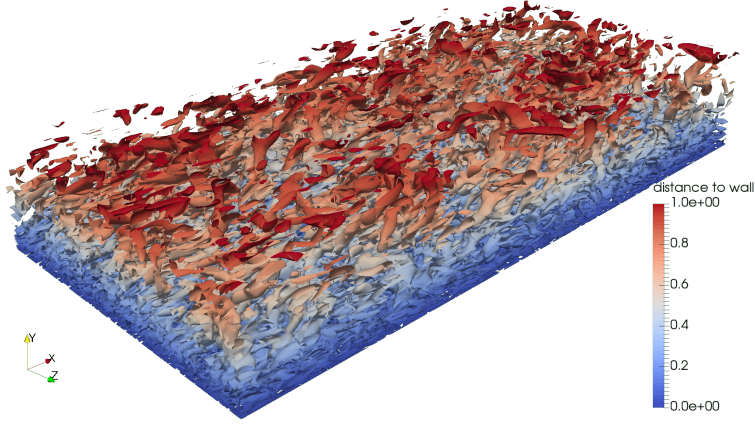


Fig. 9.31: $\text{Re}_\tau = 2000$ channel flow: 200-isosurface of $Q(\mathbf{u}_h)$ -criterion, coloured with the distance to the lower wall. Computation: $\mathbb{RT}_{[3]}^{\text{red}}/\mathbb{P}_0^{\text{dc}}$ with $N = 24$.

More quantitatively, the resulting statistics for the $\mathbb{RT}_{[3]}^{\text{red}}/\mathbb{P}_0^{\text{dc}}$ method under mesh-refinement are shown in Fig. 9.32. Now, even on the finest mesh, not even our computed mean velocity $\langle u_1 \rangle^+$ matches the DNS everywhere; in the log layer, the range between $y^+ \approx 20$ and $y^+ \approx 200$ seems too hard to capture accurately. Predicting the cross-Reynolds stress $\langle u'_1 u'_2 \rangle^+$ and the rms turbulence intensity $u_{1,\text{rms}}^+$ is, of course, even more complicated. The main problem, even on the finest mesh, seems to be to reproduce the peaks near the wall accurately. However, our results are again very much reasonable, even in this extremely under-resolved setting.

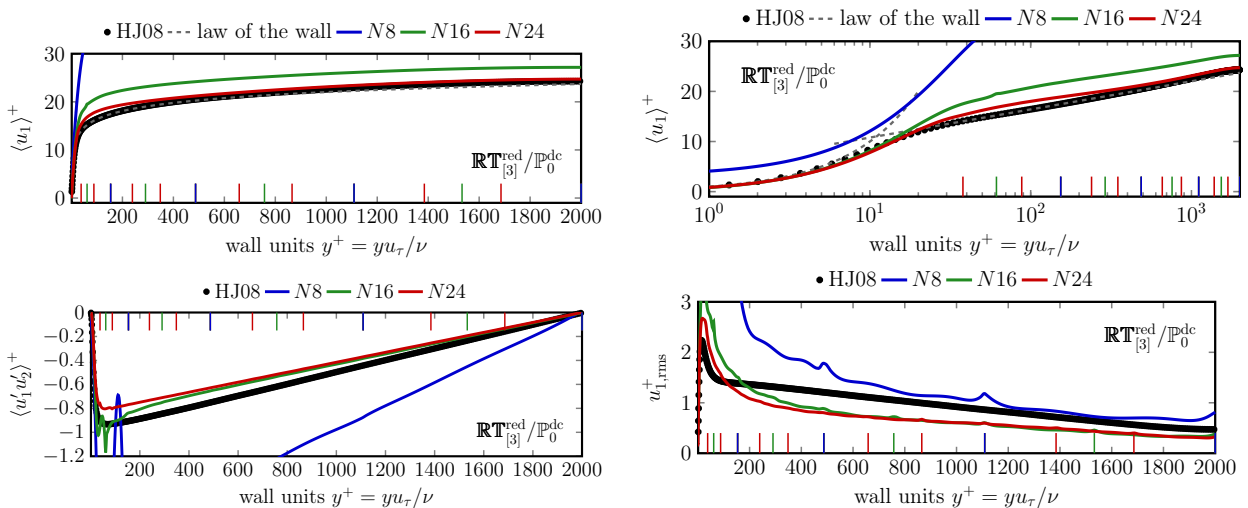


Fig. 9.32: $\text{Re}_\tau = 2000$ mean velocity $\langle u_1 \rangle^+$ with linear (top left) and logarithmic (top right) scaling, cross-Reynolds stress $\langle u'_1 u'_2 \rangle^+$ (bottom left) and rms turbulence intensity $u_{1,\text{rms}}^+$ (bottom right), computed with $\mathbb{RT}_{[3]}^{\text{red}}/\mathbb{P}_0^{\text{dc}}$ on different meshes with $N \in \{8, 16, 24\}$.

The last investigation with regard to the turbulent channel concerns the Helmholtz decomposition of the discrete convective term. For the relatively low Reynolds number $\text{Re}_\tau = 180$, Fig. 9.33 reveals that divergence-free forces dominate the convection term. As shown in Fig. 9.23, the situation does not change for $\text{Re}_\tau = 2000$. Only the magnitude of the involved norms increases noticeably.

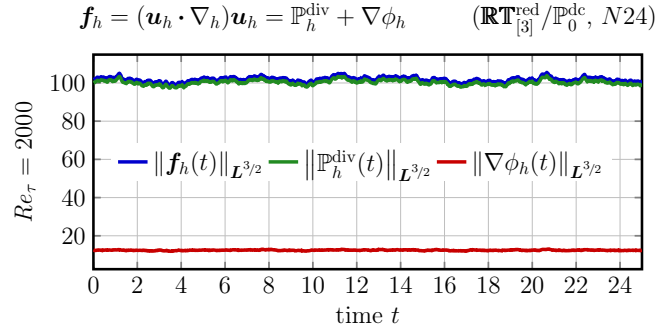


Fig. 9.33: Evolution of Helmholtz decomposition of convection forces in fully developed turbulent channel flow for $\text{Re}_\tau = 2000$, computed with $\mathbf{RT}_{[3]}^{\text{red}} / \mathbb{P}_0^{\text{dc}}$ on the $N = 24$ mesh. All norms are normalised by the channel volume $|\Omega| = L_x L_y L_z$.

Summary, Conclusions and Future Work

Let us directly provide the (condensed) main conclusion of this thesis in advance:

High-order exactly divergence-free $\mathbf{H}(\text{div})$ -based methods are extremely well suited for the simulation of incompressible computational fluid dynamics (CFD) problems. They are conceptually convincing due to exact mass conservation, pressure-robustness and a clean energy balance, versatile with regard to geometry and meshing, can deal with convection dominated problems naturally and can be made computationally efficient by hybridisation. In the practically most relevant situation of not being able to resolve all flow features, as for example in large-eddy simulation of turbulent flows, they robustly deliver trustworthy and accurate results superior to a vast majority of other methods. Such a successful simulation of under-resolved incompressible flows is directly related to the usage of a pressure-robust method.

In addition to this statement, in the following, each previous chapter is summarised separately and set into context. Furthermore, the most important conclusions of this work are repeated in detail, and possible future research directions are outlined.

Ch. 2: Incompressible Fluid Dynamics

This chapter has been dedicated to incompressible fluid dynamics on the continuous level. After motivating the incompressibility (divergence-free) constraint, the Navier–Stokes equations (NSEs) have been introduced, and what is known concerning well-posedness so far has been discussed. Thereafter, in order to guarantee a setting in which the NSEs provide a unique and well-behaved solution, the essential regularity assumption $\nabla \mathbf{u} \in L^1(\mathbf{L}^\infty)$ has been introduced and motivated (Asm. B). Note, however, that while this assumption surely is essential for a meaningful numerical error analysis, it is by no means obvious to what extent practically relevant (turbulent) flows comply with it.

Moreover, it has been shown using the Helmholtz decomposition that only divergence-free forces can have an impact on the velocity, while gradient forces (curl-free) exclusively affect the pressure. This idea, and its consequences for numerical approximations, has been an ever-recurring topic in this work which is directly related to the concept of pressure-robustness.

Afterwards, important characteristic quantities of flows, namely kinetic energy, energy dissipation rate, enstrophy and palinstrophy have been defined and their qualitative behaviour has been clarified on the basis of evolution equations. These balance statements, for example, are most important in the context of turbulent flows, because they give prominence to the influence of vortex stretching in 3D flows, and reveal fundamental differences between 2D and 3D flows. Finally, basic characteristics of turbulent flows have been indicated together with considerations of spectral analysis

as, for example, the celebrated Kolmogorov $-5/3$ law for the inertial range of the kinetic energy spectrum of 3D flows.

Ch. 3: Inf-Sup Stable Finite Element Methods

Everything that is needed for the understanding of finite element methods (FEMs) in the context of the present work has been provided in this chapter. Starting from fully discontinuous \mathbf{L}^2 -based Discontinuous Galerkin (DG) methods, our favourite choice of $\mathbf{H}(\text{div})$ methods has been introduced, which leads to the possibility of obtaining exactly divergence-free velocity solutions. By further increasing the regularity, classical \mathbf{H}^1 -conforming FEM can be recovered. Both simplicial and tensor-product elements have been considered.

In order to make DG methods computationally efficient, the concept of hybridisation has been explained, thereby leading to Hybrid DG (HDG) methods where, for example, static condensation turns out to be crucial. Especially, relying on the FE library `NGSolve`, all explained methods have been used practically in a high-order framework in this thesis. Concerning the particular treatment of diffusion phenomena, the focus has been laid on the symmetric interior penalty (SIP) method; but in the context of HDG methods, lifting techniques have been introduced and evaluated as well.

Ch. 4: Essential Robustness Concepts

The essential robustness concepts which have played a major role in the present thesis are structure preservation, pressure-robustness and Reynolds-semi-robustness. In this chapter, the ability of a numerical method to preserve large-scale structures has been related to its ability to treat divergence-free and curl-free forces accurately (Helmholtz decomposition). This investigation served as a motivation and has been based on a 2D moving Gresho vortex; it would be interesting to extend these ideas to 3D in the future.

Afterwards, the ability of handling different forces correctly has been linked to pressure-robustness. Following an introduction, it has been shown that pressure-robust methods can outperform non-pressure-robust ones dramatically whenever large gradient forces, as for example the pressure, are present. For example, it turned out that this is the case for potential flows, which then have been embedded into the large class of generalised Beltrami flows. The superiority of p -robust methods has been demonstrated to be especially striking for under-resolved flow simulations. Exactly divergence-free methods are automatically pressure-robust. Maybe most instructive, it has been emphasised that even the situation where a flow at rest is simulated can lead to huge errors, when non- p -robust methods are used.

A numerical method is called Reynolds-semi-robust when its error does not explicitly depend on negative powers of the viscosity ν (positive powers of the Reynolds number Re). Finally, a numerical experiment, called ‘planar lattice flow’, has been conducted which showed that non- Re -semi-robust methods are practically useless for $\text{Re} \gg 1$, because they might blow up after a short time. Furthermore, it has been made clear that inevitably, simulating the nonlinear Navier–Stokes problem

always entails the occurrence of an exponentially increasing error in time, where one can only hope to control its slope. Not even the usage of high-order methods, despite exponential convergence in this situation, can rectify this issue.

Ch. 5: Stokes Analysis with Emphasis on Pressure-Robustness

Driven by the wish to understand better why p -robust methods can be so much more accurate, numerical analysis for the stationary Stokes problem has been provided in this chapter. In doing so, pressure-robust error estimates for exactly divergence-free \mathbf{H}^1 - and $\mathbf{H}(\text{div})$ -methods have been provided which, in the context of the so-called Stokes projector, have also been used for the Navier–Stokes analysis in the next chapter. The most important characteristic of p -robust estimates is the complete absence of the pressure in the velocity error estimates, hence the name.

Furthermore, the Gresho vortex in Ch. 4 revealed that non- p -robust L^2 -based methods can actually be stabilised in order to be approximately p -robust. Such a stabilisation, called DG-grad-div stabilisation, has been analysed in this chapter for the Stokes problem. It turned out that in the limit case as the stabilisation parameter tends to infinity, the solution of an exactly divergence-free and pressure-robust $\mathbf{H}(\text{div})$ -conforming method is recovered.

Ch. 6: Transient Navier–Stokes: Robust Numerical Analysis

An extension of the \mathbf{H}^1 - and $\mathbf{H}(\text{div})$ -conforming pressure-robust numerical analysis in the direction of the nonlinear and time-dependent Navier–Stokes equations has been presented in this chapter. Deriving Reynolds-semi-robust error estimates for the kinetic energy, the (discrete) dissipation rate and the max-norm has been possible. However, the validity of stability and linear convergence for the L^∞ -error of the $\mathbf{H}(\text{div})$ Stokes projection (Asm. D) remains an open problem. Nevertheless, the expected convergence rate of the methods has been shown under the usual regularity assumptions, which are stronger than $\nabla \mathbf{u} \in L^1(L^\infty)$ introduced in Ch. 2. Future research could potentially be conducted by using the discrete Helmholtz projector, instead of the discrete Stokes projector, for the error analysis. In this way, the presence of time derivatives of the approximation error in error estimates could be avoided.

Note that while it is certainly necessary to have a solid numerical error analysis, the involved regularity assumptions are rather restrictive from a practical point of view. Especially, one cannot expect that a 3D turbulent flow is very regular, neither in space nor in time. Therefore, balance considerations for kinetic energy and energy dissipation rate, energy spectra, as well as structure preservation examinations are probably more relevant in this context than rigorous mathematical error analysis.

Ch. 7: Viscous Dissipation in DG Methods

Fortunately, exactly divergence-free FEM are naturally energy-stable and numerical dissipation originating in convection stabilisation can be identified easily. On the other hand, for DG methods,

separating physical from numerical dissipation for the treatment of viscous terms is not so straightforward. This chapter has been provided in order to obtain more insights into this admittedly subtle topic.

After an introduction to the problem, which also explains why the method of separating physical and numerical viscous dissipation in DG methods by means of broken gradients used so far in the community can be misleading, an alternative more suitable decomposition has been proposed. This decomposition is based on well-known arguments from dual mixed methods, and includes the lifting $\mathcal{L}(\llbracket \mathbf{u}_h \rrbracket)$ of inter-element jumps which are natural for DG methods. As a result, it has been suggested to define the physical dissipation inherent in a DG method as $\nu \|\boldsymbol{\sigma}_h\|_{\mathbf{L}^2}^2$, where $\boldsymbol{\sigma}_h = \nabla_h \mathbf{u}_h - \mathcal{L}(\llbracket \mathbf{u}_h \rrbracket)$ is the discrete diffusive flux. Validity and meaningfulness of this measure have then been demonstrated on the basis of a 3D numerical experiment for freely decaying turbulence. Furthermore, sharp estimates for the minimum SIP parameter on hyperrectangles have been provided.

Ch. 8: 2D High-Order CFD Applications

This chapter considered the use of exactly divergence-free $\mathbf{H}(\text{div})$ methods for 2D CFD applications. Beginning with the classical example of a flow past an obstacle, the importance of pressure-robustness also for such more complicated flows has been illustrated. Even though the associated vortex street is not globally a generalised Beltrami flow, it has been shown that it can behave like one at least locally in space.

Moreover, computations for a Kelvin–Helmholtz instability problem have been carried out. It has been shown that while the first merging processes of the corresponding flow can be predicted accurately, 2D flows are extremely sensitive to perturbations. These perturbations have been identified to be responsible for making it very difficult to reliably simulate 2D flows at high Reynolds numbers over a long period of time. Another aspect has been revealed by considering the interplay between fluid flow and the Helmholtz decomposition of the (discrete) convection force: whenever the corresponding flow shows a stable motion with mainly large-scale structures, the corresponding divergence-free force is comparably small and the flow behaves like a generalised Beltrami flow in time. This also underlined the conclusion that curl-free forces are responsible for maintaining large-scale structures, and that pressure-robust methods are especially well suited for this task.

The last 2D application considered here was 2D freely decaying turbulence which highlighted the fundamental characteristic of 2D flows: they tend to reorganise themselves into large-scale structures. Such a behaviour has been shown for different Reynolds numbers. In this context, the behaviour of numerical dissipation for divergence-free $\mathbf{H}(\text{div})$ -HDG methods has been investigated, using the concepts introduced in Ch. 7.

Ch. 9: 3D High-Order CFD Applications

In the last chapter, two fundamental 3D turbulent flows have been investigated: the Taylor–Green vortex (TGV) as an example of freely decaying turbulence, and the wall-bounded turbulence occurring in channel flows. For different Reynolds numbers, high-order exactly divergence-free $\mathbf{H}(\text{div})$ - $(\mathbf{H})\text{DG}$ methods have been used to simulate these standard CFD test cases. This chapter actually represents the synthesis of all accumulated insights from previous chapters, and can therefore be considered as the most auspicious contribution of the present thesis.

For the TGV, it has been observed that even in under-resolved simulations, comparably accurate results can be obtained. Based on $\text{Re} = 1600$ simulations, the detailed investigation of the underlying implicit LES mechanisms (using Ch. 7) revealed that high-order methods, compared to low-order ones, are superior for freely decaying flows. Furthermore, a comparison of the SIP mechanism with the less dissipative \mathbf{H}^1 -lifting method, both used with and without upwinding, has been provided. The main conclusion here is that upwinding does not play a crucial role for the TGV problem, and the particular choice of stabilisation in the viscous treatment also does not seem to be particularly decisive. Interestingly, even the limit case of the inviscid Euler TGV as $\text{Re} \rightarrow \infty$ can be simulated easily with div-free $\mathbf{H}(\text{div})$ methods. In this context, the dissipative character of upwinding has been emphasised. Concerning the distribution of convection forces, the TGV problem has lastly been used to verify that gradient (curl-free) forces play the most important role when it comes to preserving large-scale structures. When the flow is fully turbulent, on the other hand, divergence-free forces are large as well.

For the turbulent channel flow problem, flows with friction Reynolds number Re_τ ranging from 180 to 2000 have been investigated. The corresponding sections have demonstrated that, compared to accurate DNS data and the law of the wall, a satisfying agreement in terms of the mean velocity can be achieved for all Reynolds numbers. Note that a comparably coarse resolution has been used, which results in the fact that as Re_τ increases, our under-resolved results and the DNS results do not coincide anymore. Nonetheless the $\mathbf{H}(\text{div})$ -based method is always able to deliver meaningful results. Additionally, investigations concerning the distribution of convection forces have shown that channel flows are clearly dominated by div-free forces. Comparisons of the used polynomial degree indicate that for channel flow problems, high-order methods might not necessarily be advantageous. Together with the fact that upwinding turned out to be helpful here, this leads to the conjecture that for channel flow problems, more numerical dissipation seems to be needed than for freely decaying turbulence. In order to better resolve the flow in the vicinity of the wall, a slight mesh-stretching has always been used. It would be interesting to see if such an approach could be (partially) avoided if instead, locally near the wall, the FE space would be enriched with higher-order polynomials.

Recommendations and Further Outlook

Finally, concerning the question of which order is ‘high-enough’: as a general recommendation, we believe that in most applications choosing $k = 4$ will be sufficient to ensure accurate results, which will be superior to comparable low-order results. In addition, we recommend to always use

upwinding in the context of DG methods for Navier–Stokes flows, because in our experience, it is never disadvantageous but only increases the robustness of the method.

With a view to future work, application and assessment of the performance of exactly div-free $\mathbf{H}(\text{div})$ methods for 3D turbulent flows with separation and (re-)attachment phenomena is still pending and potentially very interesting. Secondly, in our opinion, the exact interrelation between pressure-robust methods and exactly divergence-free methods is still not entirely understood. For example, would a non-pressure-robust but exactly divergence-free method be less accurate for turbulent flows? Or does energy conservation become more and more important, especially when the flow exhibits a particularly large amount of divergence-free forces?

On a different note, exploring possibilities of combining knowledge from experimental fluid dynamics (for example, optical methods for flow visualisation like particle image velocimetry) with results from CFD could be promising. Moreover, leaving the incompressible sector, it would also be interesting to consider weakly compressible flows. In this context, as a first step, the DG-grad-div stabilisation analysed in Ch. 5 could be used to ensure approximate $\mathbf{H}(\text{div})$ -conformity in the limit as the Mach number tends to zero.

References

- [AB⁺02] D. N. Arnold, F. Brezzi, B. Cockburn, and L. D. Marini. Unified analysis of discontinuous Galerkin methods for elliptic problems. *SIAM J. Numer. Anal.*, **39**(5):1749–1779, 2002.
- [AC⁺17] N. Ahmed, T. Chacón Rebollo, V. John, and S. Rubino. Analysis of a full space-time discretization of the Navier–Stokes equations by a local projection stabilization method. *IMA J. Numer. Anal.*, **37**(3):1437–1467, 2017.
- [Ach90] D. J. Acheson. *Elementary Fluid Dynamics*. Oxford University Press, 1990.
- [ADL15] D. Arndt, H. Dallmann, and G. Lube. Local projection FEM stabilization for the time-dependent incompressible Navier–Stokes problem. *Numer. Methods Partial Differential Equations*, **31**(4):1224–1250, 2015.
- [AKL08] T. Apel, T. Knopp, and G. Lube. Stabilized finite element methods with anisotropic mesh refinement for the Oseen problem. *Appl. Numer. Math.*, **58**(12):1830–1843, 2008.
- [ALM17] N. Ahmed, A. Linke, and C. Merdon. Towards pressure-robust mixed methods for the incompressible Navier–Stokes equations. *Comput. Methods Appl. Math.*, **18**(3):353–372, 2017.
- [And95] J. D. Anderson. *Computational Fluid Dynamics: The Basics with Applications*. McGraw-Hill Inc., 1995.
- [AP14a] D. Ayala and B. Protas. Maximum palinstrophy growth in 2D incompressible flows. *J. Fluid Mech.*, **742**:340–367, 2014.
- [AP14b] D. Ayala and B. Protas. Vortices, maximum growth and the problem of finite-time singularity formation. *Fluid Dyn. Res.*, **46**(3):031404, 2014.
- [ARS97] U. M. Ascher, S. J. Ruuth, and R. J. Spiteri. Implicit-explicit Runge–Kutta methods for time-dependent partial differential equations. *Appl. Numer. Math.*, **25**(2–3):151–167, 1997.
- [ARW95] U. Ascher, S. Ruuth, and B. Wetton. Implicit-explicit methods for time-dependent partial differential equations. *SIAM J. Numer. Anal.*, **32**(3):797–823, 1995.
- [Bat69] G. K. Batchelor. Computation of the energy spectrum in homogeneous two-dimensional turbulence. *Phys. Fluids*, **12**:II233–II239, 1969.
- [BBF13] D. Boffi, F. Brezzi, and M. Fortin. *Mixed Finite Element Methods and Applications*. Springer-Verlag Berlin Heidelberg, 2013.
- [BC⁺06] F. Brezzi, B. Cockburn, L. Marini, and E. Süli. Stabilization mechanisms in discontinuous Galerkin finite element methods. *Comput. Methods Appl. Mech. Engrg.*, **195**(25–28):3293–3310, 2006.
- [BC⁺07] Y. Bazilevs, V. M. Calo, J. A. Cottrell, T. J. R. Hughes, A. Reali, and G. Scovazzi. Variational multiscale residual-based turbulence modeling for large eddy simulation of incompressible flows. *Comput. Methods Appl. Mech. Engrg.*, **197**(1–4):173–201, 2007.
- [BdFS11] A. Buffa, C. de Falco, and G. Sangalli. IsoGeometric analysis: stable elements for the 2D Stokes equation. *Int. J. Numer. Meth. Fluids*, **65**(11–12):1407–1422, 2011.
- [BE12] G. Boffetta and R. E. Ecke. Two-dimensional turbulence. *Annu. Rev. Fluid Mech.*, **44**:427–451, 2012.
- [Ber05] L. C. Berselli. On the large eddy simulation of the Taylor–Green vortex. *J. Math. Fluid Mech.*, **7**(S2):S164–S191, 2005.
- [Ber88] A. L. Bertozzi. Heteroclinic orbits and chaotic dynamics in planar fluid flows. *SIAM J. Math. Anal.*, **19**(6):1271–1294, 1988.
- [BF⁺16] A. D. Beck, D. G. Flad, C. Tonhäuser, G. Gassner, and C.-D. Munz. On the influence of polynomial de-aliasing on subgrid scale models. *Flow Turbul. Combust.*, **97**(2):475–511, 2016.

- [BF07] E. Burman and M. A. Fernández. Continuous interior penalty finite element method for the time-dependent Navier–Stokes equations: space discretization and convergence. *Numer. Math.*, **107**(1):39–77, 2007.
- [BF13] F. Boyer and P. Fabrie. *Mathematical Tools for the Study of the Incompressible Navier–Stokes Equations and Related Models*. Springer-Verlag New York, 2013.
- [BIL06] L. C. Berselli, T. Iliescu, and W. J. Layton. *Mathematics of Large Eddy Simulation of Turbulent Flows*. Springer-Verlag Berlin Heidelberg, 2006.
- [BK⁺97] B. J. Boersma, M. N. Kooper, F. T. M. Nieuwstadt, and P. Wesseling. Local grid refinement in large-eddy simulations. *J. Engrg. Math.*, **32**(2–3):161–175, 1997.
- [BL⁺18] T. Buckmaster, C. D. Lellis, L. Székelyhidi, and V. Vicol. Onsager’s conjecture for admissible weak solutions. *Commun. Pure Appl. Math.*, **72**(2):229–274, 2018.
- [BM⁺00a] A. Bracco, J. C. McWilliams, G. Murante, A. Provenzale, and J. B. Weiss. Revisiting freely decaying two-dimensional turbulence at millennial resolution. *Phys. Fluids*, **12**(11):2931–2941, 2000.
- [BM⁺00b] F. Brezzi, G. Manzini, D. Marini, P. Pietra, and A. Russo. Discontinuous Galerkin approximations for elliptic problems. *Numer. Methods Partial Differential Equations*, **16**(4):365–378, 2000.
- [BM⁺83] M. E. Brachet, D. I. Meiron, S. A. Orszag, B. G. Nickel, R. H. Morf, and U. Frisch. Small-scale structure of the Taylor–Green vortex. *J. Fluid Mech.*, **130**:411–452, 1983.
- [BR97] F. Bassi and S. Rebay. A high-order accurate discontinuous finite element method for the numerical solution of the compressible Navier–Stokes equations. *J. Comput. Phys.*, **131**(2):267–279, 1997.
- [Bra07] D. Braess. *Finite Elements: Theory, Fast Solvers, and Applications in Solid Mechanics*. Cambridge University Press, 3rd edition, 2007.
- [Bra91] M. E. Brachet. Direct simulation of three-dimensional turbulence in the Taylor–Green vortex. *Fluid Dyn. Res.*, **8**(1–4):1–8, 1991.
- [BT13] C. W. Bardos and E. S. Titi. Mathematics and turbulence: where do we stand? *J. Turbul.*, **14**(3):42–76, 2013.
- [Bur07] E. Burman. Interior penalty variational multiscale method for the incompressible Navier–Stokes equation: Monitoring artificial dissipation. *Comput. Methods Appl. Mech. Engrg.*, **196**(41–44):4045–4058, 2007.
- [BV19] T. Buckmaster and V. Vicol. Convex integration and phenomenologies in turbulence. [arXiv:1901.09023 \[math.AP\]](https://arxiv.org/abs/1901.09023), 2019. URL: <https://arxiv.org/abs/1901.09023>.
- [CC⁺08] A. Cheskidov, P. Constantin, S. Friedlander, and R. Shvydkoy. Energy conservation and Onsager’s conjecture for the Euler equations. *Nonlinearity*, **21**(6):1233–1252, 2008.
- [CCQ17] A. Cesmelioglu, B. Cockburn, and W. Qiu. Analysis of a hybridizable discontinuous Galerkin method for the steady-state incompressible Navier–Stokes equations. *Math. Comp.*, **86**(306):1643–1670, 2017.
- [CET94] P. Constantin, W. E, and E. S. Titi. Onsager’s conjecture on the energy conservation for solutions of Euler’s equation. *Commun. Math. Phys.*, **165**(1):207–209, 1994.
- [CG05a] B. Cockburn and J. Gopalakrishnan. Incompressible finite elements via hybridization. Part I: The Stokes system in two space dimensions. *SIAM J. Numer. Anal.*, **43**(4):1627–1650, 2005.
- [CG05b] B. Cockburn and J. Gopalakrishnan. Incompressible finite elements via hybridization. Part II: The Stokes system in three space dimensions. *SIAM J. Numer. Anal.*, **43**(4):1651–1672, 2005.
- [CG09] B. Cockburn and J. Gopalakrishnan. The derivation of hybridizable discontinuous Galerkin methods for Stokes flow. *SIAM J. Numer. Anal.*, **47**(2):1092–1125, 2009.

- [CGL09] B. Cockburn, J. Gopalakrishnan, and R. Lazarov. Unified hybridization of discontinuous Galerkin, mixed, and continuous Galerkin methods for second order elliptic problems. *SIAM J. Numer. Anal.*, **47**(2):1319–1365, 2009.
- [CH⁺13] C. Carton de Wiart, K. Hillewaert, M. Duponcheel, and G. Winckelmans. Assessment of a discontinuous Galerkin method for the simulation of vortical flows at high Reynolds number. *Int. J. Numer. Meth. Fluids*, **74**(7):469–493, 2013.
- [CH⁺15] C. Carton de Wiart, K. Hillewaert, L. Briceux, and G. Winckelmans. Implicit LES of free and wall-bounded turbulent flows based on the discontinuous Galerkin/symmetric interior penalty method. *Int. J. Numer. Meth. Fluids*, **78**(6):335–354, 2015.
- [CH⁺17] S. Charnyi, T. Heister, M. A. Olshanskii, and L. G. Rebholz. On conservation laws of Navier–Stokes Galerkin discretizations. *J. Comput. Phys.*, **337**:289–308, 2017.
- [CH17] K. Chrysafinos and L. S. Hou. Analysis and approximations of the evolutionary Stokes equations with inhomogeneous boundary and divergence data using a parabolic saddle point formulation. *ESAIM: M2AN*, **51**(4):1501–1526, 2017.
- [CKS05] B. Cockburn, G. Kanschat, and D. Schötzau. A locally conservative LDG method for the incompressible Navier–Stokes equations. *Math. Comp.*, **74**(251):1067–1095, 2005.
- [CKS07] B. Cockburn, G. Kanschat, and D. Schötzau. A note on discontinuous Galerkin divergence-free solutions of the Navier–Stokes equations. *J. Sci. Comput.*, **31**(1–2):61–73, 2007.
- [CL14] T. Chacón Rebollo and R. Lewandowski. *Mathematical and Numerical Foundations of Turbulence Models and Applications*. Birkhäuser Basel, 2014.
- [CM88] P. Constantin and A. Majda. The Beltrami spectrum for incompressible fluid flows. *Commun. Math. Phys.*, **115**(3):435–456, 1988.
- [CMvH99] H. J. H. Clercx, S. R. Maassen, and G. J. F. van Heijst. Decaying two-dimensional turbulence in square containers with no-slip or stress-free boundaries. *Phys. Fluids*, **11**(3):611–626, 1999.
- [Coc09] B. Cockburn. Two new techniques for generating exactly incompressible approximate velocities. In *Computational Fluid Dynamics 2006*, pages 1–11. Springer Berlin Heidelberg, 2009.
- [Coc16] B. Cockburn. Static condensation, hybridization, and the devising of the HDG methods. In *Lecture Notes in Computational Science and Engineering*, pages 129–177. Springer International Publishing, 2016.
- [CvH17] H. J. H. Clercx and G. J. F. van Heijst. Dissipation of coherent structures in confined two-dimensional turbulence. *Phys. Fluids*, **29**(11):111103, 2017.
- [DI] P. W. Schroeder and G. Lube. Stabilised dG-FEM for incompressible natural convection flows with boundary and moving interior layers on non-adapted meshes. *J. Comput. Phys.*, **335**:760–779, 2017. URL: <https://doi.org/10.1016/j.jcp.2017.01.055>.
- [DX] N. Fehn, M. Kronbichler, C. Lehrenfeld, G. Lube, and P. W. Schroeder. High-order DG solvers for under-resolved turbulent incompressible flows: A comparison of L^2 and $H(\text{div})$ methods, 2019. (in preparation).
- [DII] P. W. Schroeder and G. Lube. Pressure-robust analysis of divergence-free and conforming FEM for evolutionary incompressible Navier–Stokes flows. *J. Numer. Math.*, **25**(4):249–276, 2017. URL: <https://doi.org/10.1515/jnma-2016-1101>.
- [DIII] P. W. Schroeder and G. Lube. Divergence-free $H(\text{div})$ -FEM for time-dependent incompressible flows with applications to high Reynolds number vortex dynamics. *J. Sci. Comput.*, **75**(2):830–858, 2018. URL: <https://doi.org/10.1007/s10915-017-0561-1>.
- [DIV] P. W. Schroeder, C. Lehrenfeld, A. Linke, and G. Lube. Towards computable flows and robust estimates for inf-sup stable FEM applied to the time-dependent incompressible Navier–Stokes equations. *SeMA J.*, **75**(4):629–653, 2018. URL: <https://doi.org/10.1007/s40324-018-0157-1>.
- [DV] M. Akbas, A. Linke, L. G. Rebholz, and P. W. Schroeder. The analogue of grad-div stabilization in DG methods for incompressible flows: Limiting behavior and extension to tensor-product

- meshes. *Comput. Methods Appl. Mech. Engrg.*, **341**:917–938, 2018. URL: <https://doi.org/10.1016/j.cma.2018.07.019>.
- [DVI] P. W. Schroeder, V. John, P. L. Lederer, C. Lehrenfeld, G. Lube, and J. Schöberl. On reference solutions and the sensitivity of the 2D Kelvin–Helmholtz instability problem. *Comput. Math. Appl.*, **77**(4):1010–1028, 2019. URL: <https://doi.org/10.1016/j.camwa.2018.10.030>.
- [DVII] N. R. Gauger, A. Linke, and P. W. Schroeder. On high-order pressure-robust space discretisations, their advantages for incompressible high Reynolds number generalised Beltrami flows and beyond. *arXiv:1808.10711 [math.NA]*, 2018. URL: <https://arxiv.org/abs/1808.10711>.
- [DVIII] G. Lube and P. W. Schroeder. Implicit LES with high-order $H(\text{div})$ -conforming FEM for incompressible Navier–Stokes flows. *arXiv:1809.06558 [math.NA]*, 2018. URL: <https://arxiv.org/abs/1809.06558>. (accepted for BAIL Proceedings 2018).
- [DIX] C. Lehrenfeld, G. Lube, and P. W. Schroeder. A natural decomposition of viscous dissipation in DG methods for turbulent incompressible flows. *arXiv:1811.12769 [math.NA]*, 2018. URL: <https://arxiv.org/abs/1811.12769>.
- [DA16] H. Dallmann and D. Arndt. Stabilized finite element methods for the Oberbeck–Boussinesq model. *J. Sci. Comput.*, **69**(1):244–273, 2016.
- [Dav04] P. A. Davidson. *Turbulence: An Introduction for Scientist and Engineers*. Oxford University Press, 2004.
- [DE12] D. A. Di Pietro and A. Ern. *Mathematical Aspects of Discontinuous Galerkin Methods*. Springer-Verlag Berlin Heidelberg, 2012.
- [DeB13] J. DeBonis. Solutions of the Taylor–Green vortex problem using high-resolution explicit finite difference methods. In *51st AIAA Aerospace Sciences Meeting including the New Horizons Forum and Aerospace Exposition*, 2013.
- [DF⁺07] D. Drikakis, C. Fureby, F. F. Grinstein, and D. Youngs. Simulation of transition and turbulence decay in the Taylor–Green vortex. *J. Turbul.*, **8**(20), 2007.
- [dFG⁺18a] J. de Frutos, B. García-Archilla, V. John, and J. Novo. Analysis of the grad-div stabilization for the time-dependent Navier–Stokes equations with inf-sup stable finite elements. *Adv. Comput. Math.*, **44**(1):195–225, 2018.
- [dFG⁺18b] J. de Frutos, B. García-Archilla, V. John, and J. Novo. Error analysis of non inf-sup stable discretizations of the time-dependent Navier–Stokes equations with local projection stabilization. *IMA J. Numer. Anal.*, 2018. URL: <https://doi.org/10.1093/imanum/dry044>. (in press).
- [DG95] C. R. Doering and J. D. Gibbon. *Applied Analysis of the Navier–Stokes Equations*. Cambridge University Press, 1995.
- [DJT99] T. Dubois, F. Jauberteau, and R. Temam. *Dynamic Multilevel Methods and the Numerical Simulation of Turbulence*. Cambridge University Press, 1999.
- [Doe09] C. R. Doering. The 3D Navier–Stokes problem. *Annu. Rev. Fluid Mech.*, **41**:109–128, 2009.
- [DR06] P. G. Drazin and N. Riley. *The Navier–Stokes Equations: A Classification of Flows and Exact Solutions*. Cambridge University Press, Cambridge, 2006.
- [Dur08] F. Durst. *Fluid Mechanics: An Introduction to the Theory of Fluid Flows*. Springer-Verlag Berlin Heidelberg, 2008.
- [EC⁺18] J. A. Evans, C. Coley, R. M. Aronson, C. L. Wetterer-Nelson, and Y. Bazilevs. Residual-based large eddy simulation with isogeometric divergence-conforming discretizations. In *Frontiers in Computational Fluid-Structure Interaction and Flow Simulation*, pages 91–130. Birkhäuser, Cham, 2018.
- [EG04] A. Ern and J.-L. Guermond. *Theory and Practice of Finite Elements*. Springer New York, 2004.
- [EH13a] J. A. Evans and T. J. R. Hughes. IsoGeometric divergence-conforming B-splines for the steady Navier–Stokes equations. *Math. Models Methods Appl. Sci.*, **23**(8):1421–1478, 2013.

- [EH13b] J. A. Evans and T. J. R. Hughes. Isogeometric divergence-conforming B-splines for the unsteady Navier–Stokes equations. *J. Comput. Phys.*, **241**:141–167, 2013.
- [ES94] C. R. Ethier and D. A. Steinman. Exact fully 3D Navier–Stokes solutions for benchmarking. *Int. J. Numer. Meth. Fluids*, **19**(5):369–375, 1994.
- [Eva10] L. C. Evans. *Partial Differential Equations*. American Mathematical Society, 2nd edition, 2010.
- [Eva11] J. A. Evans. *Divergence-free B-spline Discretizations for Viscous Incompressible Flows*. PhD thesis, The University of Texas at Austin, 2011.
- [Eyi94] G. L. Eyink. Energy dissipation without viscosity in ideal hydrodynamics I. Fourier analysis and local energy transfer. *Physica D*, **78**(3–4):222–240, 1994.
- [FLD09] D. Fauconnier, C. D. Langhe, and E. Dick. Construction of explicit and implicit dynamic finite difference schemes and application to the large-eddy simulation of the Taylor–Green vortex. *J. Comput. Phys.*, **228**(21):8053–8084, 2009.
- [FMB03] U. Frisch, T. Matsumoto, and J. Bec. Singularities of Euler flow? Not out of the blue! *J. Stat. Phys.*, **113**(5/6):761–781, 2003.
- [Fri95] U. Frisch. *Turbulence*. Cambridge University Press, 1995.
- [Fu19] G. Fu. An explicit divergence-free DG method for incompressible flow. *Comput. Methods Appl. Mech. Engrg.*, **345**:502–517, 2019.
- [FWK18a] N. Fehn, W. A. Wall, and M. Kronbichler. Efficiency of high-performance discontinuous Galerkin spectral element methods for under-resolved turbulent incompressible flows. *Int. J. Numer. Meth. Fluids*, **88**(1):32–54, 2018.
- [FWK18b] N. Fehn, W. A. Wall, and M. Kronbichler. Robust and efficient discontinuous Galerkin methods for under-resolved turbulent incompressible flows. *J. Comput. Phys.*, **372**:667–693, 2018.
- [Gal11] G. P. Galdi. *An Introduction to the Mathematical Theory of the Navier–Stokes Equations*. Springer-Verlag New York, 2nd edition, 2011.
- [GB12] G. J. Gassner and A. D. Beck. On the accuracy of high-order discretizations for underresolved turbulence simulations. *Theor. Comput. Fluid Dyn.*, **27**(3–4):221–237, 2012.
- [GC90] P. M. Gresho and S. T. Chan. On the theory of semi-implicit projection methods for viscous incompressible flow and its implementation via a finite element method that also introduces a nearly consistent mass matrix. Part 2: Implementation. *Int. J. Numer. Meth. Fluids*, **11**(5):621–659, 1990.
- [GK00] M. Griebel and F. Koster. Adaptive wavelet solvers for the unsteady incompressible Navier–Stokes equations. In pages 67–118. J. Málek, J. Nečas, M. Rokyta (eds) *Advances in Mathematical Fluid Mechanics*. Springer, Berlin, Heidelberg, 2000.
- [GKM14] H. Grimm-Strele, F. Kupka, and H. Muthsam. Curvilinear grids for WENO methods in astrophysical simulations. *Comput. Phys. Commun.*, **185**(3):764–776, 2014.
- [GLS18] J. Gopalakrishnan, P. L. Lederer, and J. Schöberl. A mass conserving mixed stress formulation for the Stokes equations. [arXiv:1806.07173 \[math.NA\]](https://arxiv.org/abs/1806.07173), 2018. URL: <https://arxiv.org/abs/1806.07173>.
- [GM⁺18] T. H. Gibson, L. Mitchell, D. A. Ham, and C. J. Cotter. A domain-specific language for the hybridization and static condensation of finite element methods. [arXiv:1802.00303 \[cs.MS\]](https://arxiv.org/abs/1802.00303), 2018. URL: <https://arxiv.org/abs/1802.00303>.
- [GNS15] V. Girault, R. H. Nochetto, and L. R. Scott. Max-norm estimates for Stokes and Navier–Stokes approximations in convex polyhedra. *Numer. Math.*, **131**(4):771–822, 2015.
- [GR86] V. Girault and P.-A. Raviart. *Finite Element Methods for Navier–Stokes Equations*. Springer Berlin Heidelberg, 1986.
- [GS98] S. Gottlieb and C.-W. Shu. Total variation diminishing Runge–Kutta schemes. *Math. Comp.*, **67**(221):73–85, 1998.

- [GSS11] F. Gargano, M. Sammartino, and V. Sciacca. High Reynolds number Navier–Stokes solutions and boundary layer separation induced by a rectilinear vortex. *Comput. & Fluids*, **52**:73–91, 2011.
- [GSS17] J. Guzmán, C.-W. Shu, and F. A. Sequeira. H(div) conforming and DG methods for incompressible Euler’s equations. *IMA J. Numer. Anal.*, **37**(4):1733–1771, 2017.
- [Gud10] T. Gudi. A new error analysis for discontinuous finite element methods for linear elliptic problems. *Math. Comp.*, **79**(272):2169–2189, 2010.
- [Guy65] R. J. Guyan. Reduction of stiffness and mass matrices. *AIAA J.*, **3**(2):380–380, 1965.
- [GWR05] V. Gravemeier, W. A. Wall, and E. Ramm. Large eddy simulation of turbulent incompressible flows by a three-level finite element method. *Int. J. Numer. Meth. Fluids*, **48**(10):1067–1099, 2005.
- [Hal05] G. Haller. An objective definition of a vortex. *J. Fluid Mech.*, **525**:1–26, 2005.
- [HG⁺13] N. Happenhofer, H. Grimm-Strele, F. Kupka, B. Löw-Baselli, and H. Muthsam. A low Mach number solver: Enhancing applicability. *J. Comput. Phys.*, **236**:96–118, 2013.
- [Hil13] K. Hillewaert. *Development of the Discontinuous Galerkin Method for High-Resolution, Large Scale CFD and Acoustics in Industrial Geometries*. PhD thesis, Université catholique de Louvain, 2013.
- [HJ06] S. Hoyas and J. Jiménez. Scaling of the velocity fluctuations in turbulent channels up to $Re_\tau = 2003$. *Phys. Fluids*, **18**(1):011702, 2006.
- [HJ08] S. Hoyas and J. Jiménez. Reynolds number effects on the Reynolds-stress budgets in turbulent channels. *Phys. Fluids*, **20**(10):101511, 2008.
- [HKR90] W. D. Henshaw, H. O. Kreiss, and L. G. Reyna. Smallest scale estimates for the Navier–Stokes equations for incompressible fluids. *Arch. Ration. Mech. Anal.*, **112**(1):21–44, 1990.
- [HSF18] I. Huismann, J. Stiller, and J. Fröhlich. Scaling to the stars – a linearly scaling elliptic solver for p -multigrid. [arXiv:1808.03595 \[math.NA\]](https://arxiv.org/abs/1808.03595), 2018. URL: <https://arxiv.org/abs/1808.03595>.
- [HWM88] J. C. R. Hunt, A. A. Wray, and P. Moin. Eddies, streams, and convergence zones in turbulent flows. *Center for Turbulence Research Report*, **CTR-S88**, 1988.
- [IDD03] P. Iannelli, F. M. Denaro, and G. De Stefano. A deconvolution-based fourth-order finite volume method for incompressible flows on non-uniform grids. *Int. J. Numer. Meth. Fluids*, **43**(4):431–462, 2003.
- [Ing13] R. Ingram. Unconditional convergence of high-order extrapolations of the Crank–Nicolson, finite element method for the Navier–Stokes equations. *Int. J. Numer. Anal. Model.*, **10**(2):257–297, 2013.
- [Iro65] B. Irons. Structural eigenvalue problems - elimination of unwanted variables. *AIAA J.*, **3**(5):961–962, 1965.
- [JH95] J. Jeong and F. Hussain. On the identification of a vortex. *J. Fluid Mech.*, **285**:69–94, 1995.
- [JL⁺17] V. John, A. Linke, C. Merdon, M. Neilan, and L. G. Rebholz. On the divergence constraint in mixed finite element methods for incompressible flows. *SIAM Rev.*, **59**(3):492–544, 2017.
- [JL16] N. Jiang and W. Layton. Algorithms and models for turbulence not at statistical equilibrium. *Comput. Math. Appl.*, **71**(11):2352–2372, 2016.
- [Joh05] V. John. An assessment of two models for the subgrid scale tensor in the rational LES model. *J. Comput. Appl. Math.*, **173**(1):57–80, 2005.
- [Joh16] V. John. *Finite Element Methods for Incompressible Flow Problems*. Springer International Publishing, 2016.

- [JR07] V. John and M. Roland. Simulations of the turbulent channel flow at $Re_\tau = 180$ with projection-based finite element variational multiscale methods. *Int. J. Numer. Meth. Fluids*, **55**(5):407–429, 2007.
- [Ker93] R. M. Kerr. Evidence for a singularity of the three-dimensional, incompressible Euler equations. *Phys. Fluids A*, **5**(7):1725–1746, 1993.
- [KF⁺17] B. Krank, N. Fehn, W. A. Wall, and M. Kronbichler. A high-order semi-explicit discontinuous Galerkin solver for 3D incompressible flow with application to DNS and LES of turbulent channel flow. *J. Comput. Phys.*, **348**:634–659, 2017.
- [KI⁺03] Y. Kaneda, T. Ishihara, M. Yokokawa, K. Itakura, and A. Uno. Energy dissipation rate and energy spectrum in high resolution direct numerical simulations of turbulence in a periodic box. *Phys. Fluids*, **15**(2):L21–L24, 2003.
- [KMM87] J. Kim, P. Moin, and R. Moser. Turbulence statistics in fully developed channel flow at low Reynolds number. *J. Fluid Mech.*, **177**:133–166, 1987.
- [Kol41a] A. N. Kolmogorov. Dissipation of energy in the locally isotropic turbulence. *Dokl. Akad. Nauk SSSR*, **32**(1), 1941.
- [Kol41b] A. N. Kolmogorov. The local structure of turbulence in incompressible viscous fluid for very large Reynolds numbers. *Dokl. Akad. Nauk SSSR*, **30**(4), 1941.
- [Kop17] D. A. Kopriva. Stability of overintegration methods for nodal discontinuous Galerkin spectral element methods. *J. Sci. Comput.*, **76**(1):426–442, 2017.
- [KS05] G. E. Karniadakis and S. J. Sherwin. *Spectral/hp Element Methods for Computational Fluid Dynamics*. Oxford University Press, Oxford, 2nd edition, 2005.
- [KZ⁺10] T. Knopp, X. Zhang, R. Kessler, and G. Lube. Enhancement of an industrial finite-volume code for large-eddy-type simulation of incompressible high Reynolds number flow using near-wall modelling. *Comput. Methods Appl. Mech. Engrg.*, **199**(13–16):890–902, 2010.
- [Lay08] W. Layton. *Introduction to the Numerical Analysis of Incompressible Viscous Flows*. SIAM Philadelphia, 2008.
- [Leh10] C. Lehrenfeld. *Hybrid Discontinuous Galerkin methods for solving incompressible flow problems*. Master’s thesis, Rheinisch-Westfälische Technische Hochschule Aachen, 2010. URL: https://www.igpm.rwth-aachen.de/Download/reports/lehrenfeld/DA_HDG4NSE_1_0.pdf.
- [Leh16] C. Lehrenfeld. Removing the stabilization parameter in fitted and unfitted symmetric Nitsche formulations. In *Proceedings of the VII European Congress on Computational Methods in Applied Sciences and Engineering (ECCOMAS Congress 2016)*, pages 373–383, 2016.
- [Les08] M. Lesieur. *Turbulence in Fluids*. Springer Netherlands, 4th edition, 2008.
- [Lin09] A. Linke. Collision in a cross-shaped domain – A steady 2d Navier–Stokes example demonstrating the importance of mass conservation in CFD. *Comput. Methods Appl. Mech. Engrg.*, **198**(41–44):3278–3286, 2009.
- [LLS18a] P. L. Lederer, C. Lehrenfeld, and J. Schöberl. Hybrid discontinuous Galerkin methods with relaxed H(div)-conformity for incompressible flows. Part I. *SIAM J. Numer. Anal.*, **56**(4):2070–2094, 2018.
- [LLS18b] P. L. Lederer, C. Lehrenfeld, and J. Schöberl. Hybrid discontinuous Galerkin methods with relaxed H(div)-conformity for incompressible flows. Part II. *ESAIM: M2AN*, 2018. URL: <https://doi.org/10.1051/m2an/2018054>. (in press).
- [LM16] A. Linke and C. Merdon. Pressure-robustness and discrete Helmholtz projectors in mixed finite element methods for the incompressible Navier–Stokes equations. *Comput. Methods Appl. Mech. Engrg.*, **311**:304–326, 2016.
- [LS⁺88] M. Lesieur, C. Staquet, P. Le Roy, and P. Comte. The mixing layer and its coherence examined from the point of view of two-dimensional turbulence. *J. Fluid Mech.*, **192**:511–534, 1988.

- [LS16] C. Lehrenfeld and J. Schöberl. High order exactly divergence-free hybrid discontinuous Galerkin methods for unsteady incompressible flows. *Comput. Methods Appl. Mech. Engrg.*, **307**:339–361, 2016.
- [LS18] P. L. Lederer and J. Schöberl. Polynomial robust stability analysis for $H(\text{div})$ -conforming finite elements for the Stokes equations. *IMA J. Numer. Anal.*, **38**(4):1832–1860, 2018.
- [LW03] R. Liska and B. Wendroff. Comparison of several difference schemes on 1D and 2D test problems for the Euler equations. *SIAM J. Sci. Comput.*, **25**(3):995–1017, 2003.
- [LW12] R. J. Labeur and G. N. Wells. Energy stable and momentum conserving hybrid finite element method for the incompressible Navier–Stokes equations. *SIAM J. Sci. Comput.*, **34**(2):A889–A913, 2012.
- [MB02] A. J. Majda and A. L. Bertozzi. *Vorticity and Incompressible Flow*. Cambridge University Press, 2002.
- [MFH08] A. Montlaur, S. Fernandez-Mendez, and A. Huerta. Discontinuous Galerkin methods for the Stokes equations using divergence-free approximations. *Int. J. Numer. Meth. Fluids*, **57**(9):1071–1092, 2008.
- [Mic64] A. Michalke. On the inviscid instability of the hyperbolic-tangent velocity profile. *J. Fluid Mech.*, **19**(4):543–556, 1964.
- [MK82] P. Moin and J. Kim. Numerical investigation of turbulent channel flow. *J. Fluid Mech.*, **118**:341–377, 1982.
- [MKM99] R. D. Moser, J. Kim, and N. N. Mansour. Direct numerical simulation of turbulent channel flow up to $Re_\tau = 590$. *Phys. Fluids*, **11**(4):943–945, 1999.
- [MS⁺91] W. H. Matthaeus, W. T. Stribling, D. Martinez, S. Oughton, and D. Montgomery. Decaying, two-dimensional, Navier–Stokes turbulence at very long times. *Physica D*, **51**(1–3):531–538, 1991.
- [NC18] A. Natale and C. J. Cotter. A variational $H(\text{div})$ finite-element discretization approach for perfect incompressible fluids. *IMA J. Numer. Anal.*, **38**(3):1388–1419, 2018.
- [NW03] S. Nägele and G. Wittum. Large-eddy simulation and multigrid methods. *Electron. Trans. Numer. Anal.*, **15**:152–164, 2003.
- [Oik10] I. Oikawa. Hybridized discontinuous Galerkin method with lifting operator. *JSIAM Lett.*, **2**:99–102, 2010.
- [Ons49] L. Onsager. Statistical hydrodynamics. *Il Nuovo Cimento*, **6**(S2):279–287, 1949.
- [OVG07] E. Oñate, A. Valls, and J. García. Computation of turbulent flows using a finite calculus–finite element formulation. *Int. J. Numer. Meth. Fluids*, **54**(6–8):609–637, 2007.
- [Pan13] R. L. Panton. *Incompressible Flow*. John Wiley & Sons Inc., 4th edition, 2013.
- [PKvdW02] B. R. Pearson, P.-Å. Krogstad, and W. van de Water. Measurements of the turbulent energy dissipation rate. *Phys. Fluids*, **14**(3):1288–1290, 2002.
- [PL⁺75] A. Pouquet, M. Lesieur, J. C. André, and C. Basdevant. Evolution of high Reynolds number two-dimensional turbulence. *J. Fluid Mech.*, **72**(2):305–319, 1975.
- [PMB18] M. Piatkowski, S. Müthing, and P. Bastian. A stable and high-order accurate discontinuous Galerkin based splitting method for the incompressible Navier–Stokes equations. *J. Comput. Phys.*, **356**:220–239, 2018.
- [Pop00] S. B. Pope. *Turbulent Flows*. Cambridge University Press, 2000.
- [PY⁺85] R. B. Pelz, V. Yakhot, S. A. Orszag, L. Shtilman, and E. Levich. Velocity-vorticity patterns in turbulent flow. *Phys. Rev. Lett.*, **54**:2505–2508, 1985.
- [Qin94] J. Qin. *On the Convergence of Some Low Order Mixed Finite Elements for Incompressible Fluids*. PhD thesis, Pennsylvania State University, 1994.

- [RG13] U. Rasthofer and V. Gravemeier. Multifractal subgrid-scale modeling within a variational multiscale method for large-eddy simulation of turbulent flow. *J. Comput. Phys.*, **234**:79–107, 2013.
- [Riv08] B. Rivière. *Discontinuous Galerkin Methods for Solving Elliptic and Parabolic Equations*. SIAM, 2008.
- [RKR17] M. E. Rafei, L. Könözy, and Z. Rana. Investigation of numerical dissipation in classical and implicit large eddy simulations. *Aerospace*, **4**(4):59, 2017.
- [RST08] H.-G. Roos, M. Stynes, and L. Tobiska. *Robust Numerical Methods for Singularly Perturbed Differential Equations: Convection-Diffusion-Reaction and Flow Problems*. Springer-Verlag Berlin Heidelberg, 2nd edition, 2008.
- [RW17] S. Rhebergen and G. N. Wells. Analysis of a hybridized/interface stabilized finite element method for the Stokes equations. *SIAM J. Numer. Anal.*, **55**(4):1982–2003, 2017.
- [RW18] S. Rhebergen and G. N. Wells. A hybridizable discontinuous Galerkin method for the Navier–Stokes equations with pointwise divergence-free velocity field. *J. Sci. Comput.*, **76**(3):1484–1501, 2018.
- [Saf93] P. G. Saffman. *Vortex Dynamics*. Cambridge University Press, 1993.
- [Sal16] S. Salsa. *Partial Differential Equations in Action*. Springer International Publishing, 3rd edition, 2016.
- [Sch14] J. Schöberl. C++11 Implementation of Finite Elements in NGSolve. ASC Report 30/2014, Institute for Analysis and Scientific Computing, Vienna University of Technology, 2014. URL: <https://www.asc.tuwien.ac.at/~schoeberl/wiki/publications/ngs-cpp11.pdf>.
- [Sch97] J. Schöberl. NETGEN An advancing front 2D/3D-mesh generator based on abstract rules. *Comput. Vis. Sci.*, **1**(1):41–52, 1997.
- [SD⁺05] C.-W. Shu, W.-S. Don, D. Gottlieb, O. Schilling, and L. Jameson. Numerical convergence study of nearly incompressible, inviscid Taylor–Green vortex flow. *J. Sci. Comput.*, **24**(1):1–27, 2005.
- [SD⁺15] F. S. Schraner, J. A. Domaradzki, S. Hickel, and N. A. Adams. Assessing the numerical dissipation rate and viscosity in numerical simulations of fluid flows. *Comput. & Fluids*, **114**:84–97, 2015.
- [SF00] K. Schneider and M. Farge. Numerical simulation of a mixing layer in an adaptive wavelet basis. *C. R. Acad. Sci. Paris Sér. IIB*, **328**(3):263–269, 2000.
- [SG00] H. Schlichting and K. Gersten. *Boundary-Layer Theory*. Springer-Verlag Berlin Heidelberg, 8th edition, 2000.
- [SL13] J. Schöberl and C. Lehrenfeld. Domain decomposition preconditioning for high order hybrid discontinuous Galerkin methods on tetrahedral meshes. In *Advanced Finite Element Methods and Applications*, pages 27–56. Springer Berlin Heidelberg, 2013.
- [SO88] C.-W. Shu and S. Osher. Efficient implementation of essentially non-oscillatory shock-capturing schemes. *J. Comput. Phys.*, **77**(2):439–471, 1988.
- [Soh01] H. Sohr. *The Navier–Stokes Equations: An Elementary Functional Analytic Approach*. Birkhäuser Basel, 2001.
- [Spr10] V. Springel. E pur si muove: Galilean-invariant cosmological hydrodynamical simulations on a moving mesh. *Mon. Not. R. Astron. Soc.*, **401**(2):791–851, 2010.
- [SS12] O. San and A. E. Staples. High-order methods for decaying two-dimensional homogeneous isotropic turbulence. *Comput. & Fluids*, **63**:105–127, 2012.
- [SV85] L. R. Scott and M. Vogelius. Norm estimates for a maximal right inverse of the divergence operator in spaces of piecewise polynomials. *ESAIM: M2AN*, **19**(1):111–143, 1985.
- [SZ05] J. Schöberl and S. Zaglmayr. High order Nédélec elements with local complete sequence properties. *COMPEL*, **24**(2):374–384, 2005.

- [Tab02] P. Tabeling. Two-dimensional turbulence: a physicist approach. *Phys. Rep.*, **362**(1):1–62, 2002.
- [TG37] G. I. Taylor and A. E. Green. Mechanism of the production of small eddies from large ones. *Proceedings of the Royal Society A: Mathematical, Physical and Engineering Sciences*, **158**(895):499–521, 1937.
- [TKW14] J. Thuburn, J. Kent, and N. Wood. Cascades, backscatter and conservation in numerical models of two-dimensional turbulence. *Quart. J. Roy. Meteor. Soc.*, **140**(679):626–638, 2014.
- [TM⁺92] T. Tezduyar, S. Mittal, S. Ray, and R. Shih. Incompressible flow computations with stabilized bilinear and linear equal-order-interpolation velocity-pressure elements. *Comput. Methods Appl. Mech. Engrg.*, **95**(2):221–242, 1992.
- [Tri88] D. J. Tritton. *Physical Fluid Dynamics*. Oxford University Press New York, 2nd edition, 1988.
- [Van88] E. Van Groesen. Time-asymptotics and the self-organization hypothesis for 2D Navier–Stokes equations. *Physica A*, **148**(1–2):312–330, 1988.
- [VGK97] B. Vreman, B. Geurts, and H. Kuerten. Large-eddy simulation of the turbulent mixing layer. *J. Fluid Mech.*, **339**:357–390, 1997.
- [vOY⁺17] T. M. van Opstal, J. Yan, C. Coley, J. A. Evans, T. Kvamsdal, and Y. Bazilevs. Isogeometric divergence-conforming variational multiscale formulation of incompressible turbulent flows. *Comput. Methods Appl. Mech. Engrg.*, **316**:859–879, 2017.
- [vRL⁺11] W. M. van Rees, A. Leonard, D. I. Pullin, and P. Koumoutsakos. A comparison of vortex and pseudo-spectral methods for the simulation of periodic vortical flows at high Reynolds numbers. *J. Comput. Phys.*, **230**(8):2794–2805, 2011.
- [vWah18] H. von Wahl. *Implicit-Explicit Time Splitting Schemes for Incompressible Navier–Stokes Flows*. Master’s thesis, Georg-August-Universität Göttingen, 2018. URL: <https://num.math.uni-goettingen.de/picap/pdf/E908.pdf>.
- [Wie74] K. Wiegardt. *Theoretische Strömungslehre*. B. G. Teubner Stuttgart, 2nd edition, 1974.
- [Wil06] D. C. Wilcox. *Turbulence Modeling for CFD*. DCW Industries, 3rd edition, 2006.
- [WM⁺18] A. R. Winters, R. C. Moura, G. Mengaldo, G. J. Gassner, S. Walch, J. Peiro, and S. J. Sherwin. A comparative study on polynomial dealiasing and split form discontinuous Galerkin schemes for under-resolved turbulence computations. *J. Comput. Phys.*, **372**:1–21, 2018.
- [WMZ06] J.-Z. Wu, H.-Y. Ma, and M.-D. Zhou. *Vorticity and Vortex Dynamics*. Springer-Verlag Berlin Heidelberg, 2006.
- [XC⁺18] H. Xu, C. D. Cantwell, C. Monteserin, C. Eskilsson, A. P. Engsig-Karup, and S. J. Sherwin. Spectral/*hp* element methods: Recent developments, applications, and perspectives. *J. Hydrodyn.*, **30**(1):1–22, 2018.
- [YBC16] L. Yang, S. Badia, and R. Codina. A pseudo-compressible variational multiscale solver for turbulent incompressible flows. *Comput. Mech.*, **58**(6):1051–1069, 2016.
- [YO87] V. Yakhot and S. A. Orszag. Renormalization group and local order in strong turbulence. *Nucl. Phys. B - Proc. Suppl.*, **2**:417–440, 1987.
- [Zag06] S. Zaglmayr. *High Order Finite Element Methods for Electromagnetic Field Computation*. PhD thesis, Johannes Kepler Universität Linz, 2006.
- [Zha05] S. Zhang. A new family of stable mixed finite elements for the 3D Stokes equations. *Math. Comp.*, **74**(250):543–554, 2005.
- [Zha11] S. Zhang. Divergence-free finite elements on tetrahedral grids for $k \geq 6$. *Math. Comp.*, **80**(274):669–669, 2011.

Lebenslauf

Persönliche Daten

Name	Philipp W. Schroeder
Geboren	am 28. April 1991 in Goslar
Familienstand	ledig
Staatsangehörigkeit	deutsch

Bildungsweg

04/2016 – 03/2019	GAUSS-Promotion „Mathematical Sciences“, Universität Göttingen
09/2017	Forschungsaufenthalt, Clemson University (South Carolina/USA)
10/2013 – 03/2016	M.Sc. Mathematik, Universität Göttingen
WS 2013/2014	Auslandssemester, Swansea University (Wales/UK)
10/2010 – 09/2013	B.Sc. Mathematik, Universität Göttingen
08/2007 – 06/2010	Abitur, Niedersächsisches Internatsgymnasium Bad Harzburg

Vorträge

- 2018 Weierstraß-Institut für Angewandte Analysis und Stochastik, Berlin, 5.–7. Dezember
13th International Workshop on Variational Multiscale and Stabilized Finite Elements
- Universität der Bundeswehr München, Neubiberg, 30. Oktober
Kolloquium Angewandte Mathematik
- Technische Universität Chemnitz, 24.–26. September
31st Chemnitz Finite Element Symposium 2018
- Georg-August-Universität Göttingen, 4.–6. Juli
2nd NGSolve User Meeting 2018
- University of Strathclyde, Glasgow, Großbritannien, 18.–22. Juni
International Conference on Boundary and Interior Layers (BAIL 2018)
- Ruprecht-Karls-Universität Heidelberg, 8.–9. Juni
16th European Finite Element Fair (EFEF 2018)
- 2017 Universität La Sapienza, Rom, Italien, 5.–7. April
19th International Conference on Finite Elements in Flow Problems (FEF 2017)
- Weierstraß-Institut für Angewandte Analysis und Stochastik, Berlin, 9. Februar
Forschungsseminar der Forschungsgruppe 3
- 2016 Rheinisch-Westfälische Technische Hochschule Aachen, 27.–28. Juni
Workshop on Multiscale Modeling and Model Reduction (CompSE)
- Brunel University London, Großbritannien, 14.–17. Juni
The Mathematics of Finite Elements and Applications (MAFELAP 2016)
- Otto-von-Guericke-Universität Magdeburg, 16.–18. März
11th International Workshop on Variational Multiscale and Stabilized Finite Elements

Veröffentlichungen

- N. Fehn, M. Kronbichler, C. Lehrenfeld, G. Lube, and P. W. Schroeder. High-order DG solvers for under-resolved turbulent incompressible flows: A comparison of L^2 and $H(\text{div})$ methods, 2019. (in preparation)
- C. Lehrenfeld, G. Lube, and P. W. Schroeder. A natural decomposition of viscous dissipation in DG methods for turbulent incompressible flows. *arXiv:1811.12769 [math.NA]*, 2018. URL: <https://arxiv.org/abs/1811.12769>
- G. Lube and P. W. Schroeder. Implicit LES with high-order $H(\text{div})$ -conforming FEM for incompressible Navier–Stokes flows. *arXiv:1809.06558 [math.NA]*, 2018. URL: <https://arxiv.org/abs/1809.06558>. (accepted for BAIL Proceedings 2018)
- N. R. Gauger, A. Linke, and P. W. Schroeder. On high-order pressure-robust space discretisations, their advantages for incompressible high Reynolds number generalised Beltrami flows and beyond. *arXiv:1808.10711 [math.NA]*, 2018. URL: <https://arxiv.org/abs/1808.10711>
- P. W. Schroeder, V. John, P. L. Lederer, C. Lehrenfeld, G. Lube, and J. Schöberl. On reference solutions and the sensitivity of the 2D Kelvin–Helmholtz instability problem. *Comput. Math. Appl.*, **77**(4):1010–1028, 2019. URL: <https://doi.org/10.1016/j.camwa.2018.10.030>
- M. Akbas, A. Linke, L. G. Rebholz, and P. W. Schroeder. The analogue of grad-div stabilization in DG methods for incompressible flows: Limiting behavior and extension to tensor-product meshes. *Comput. Methods Appl. Mech. Engrg.*, **341**:917–938, 2018. URL: <https://doi.org/10.1016/j.cma.2018.07.019>
- P. W. Schroeder, C. Lehrenfeld, A. Linke, and G. Lube. Towards computable flows and robust estimates for inf-sup stable FEM applied to the time-dependent incompressible Navier–Stokes equations. *SeMA J.*, **75**(4):629–653, 2018. URL: <https://doi.org/10.1007/s40324-018-0157-1>
- P. W. Schroeder and G. Lube. Divergence-free $H(\text{div})$ -FEM for time-dependent incompressible flows with applications to high Reynolds number vortex dynamics. *J. Sci. Comput.*, **75**(2):830–858, 2018. URL: <https://doi.org/10.1007/s10915-017-0561-1>
- P. W. Schroeder and G. Lube. Pressure-robust analysis of divergence-free and conforming FEM for evolutionary incompressible Navier–Stokes flows. *J. Numer. Math.*, **25**(4):249–276, 2017. URL: <https://doi.org/10.1515/jnma-2016-1101>
- P. W. Schroeder and G. Lube. Stabilised dG-FEM for incompressible natural convection flows with boundary and moving interior layers on non-adapted meshes. *J. Comput. Phys.*, **335**:760–779, 2017. URL: <https://doi.org/10.1016/j.jcp.2017.01.055>